

AD-A222 462

DTIC EDITION 2000

(2)

NUMERICAL INVESTIGATION OF LAMINAR-TURBULENT  
TRANSITION IN A FLAT PLATE WAKE

by

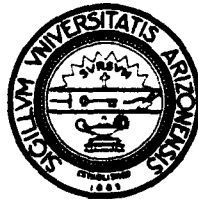
David I. Dratler and Hermann F. Fasel

DTIC  
ELECTED  
MAY 25 1990  
S D  
D S

Prepared from work done under Grant

ONR-N00014-85-K-0412

DISTRIBUTION STATEMENT A  
Approved for public release  
Distribution Unlimited



Department of Aerospace and Mechanical Engineering

University of Arizona

Tucson, Arizona 85721

February 1990

90 05 22 122

Unclassified

SECURITY CLASSIFICATION OF THIS PAGE

## REPORT DOCUMENTATION PAGE

1a. REPORT SECURITY CLASSIFICATION Unclassified		1b. RESTRICTIVE MARKINGS													
2a. SECURITY CLASSIFICATION AUTHORITY		3. DISTRIBUTION/AVAILABILITY OF REPORT  N/A													
2b. DECLASSIFICATION/DOWNGRADING SCHEDULE															
4. PERFORMING ORGANIZATION REPORT NUMBER(S)		5. MONITORING ORGANIZATION REPORT NUMBER(S)  N/A													
6a. NAME OF PERFORMING ORGANIZATION  University of Arizona	6b. OFFICE SYMBOL (if applicable)	7a. NAME OF MONITORING ORGANIZATION  N/A													
6c. ADDRESS (City, State and ZIP Code)  Department of Aerospace & Mechanical Engrg. Tucson, Arizona 85721		7b. ADDRESS (City, State and ZIP Code)													
8a. NAME OF FUNDING/SPONSORING ORGANIZATION  Office of Naval Research	8b. OFFICE SYMBOL (if applicable)	9. PROCUREMENT INSTRUMENT IDENTIFICATION NUMBER													
8c. ADDRESS (City, State and ZIP Code)  Mechanics Division, Code 1513:LHO 800 Quincy Street Arlington, VA 22217-5000		10. SOURCE OF FUNDING NOS.  PROGRAM ELEMENT NO.      PROJECT NO.      TASK NO.      WORK UNIT NO.													
11. TITLE (Include Security Classification)  Coherent Structures, Chaos, and the Role of Modern Dynamics in Turbulent Shear Flows															
12. PERSONAL AUTHOR(S) Hermann F. Fasel and Alan C. Newell															
13a. TYPE OF REPORT  Final (Supplement)	13b. TIME COVERED  FROM 3/1/88 TO 2/28/89	14. DATE OF REPORT (Yr., Mo., Day)  March 2, 1990	15. PAGE COUNT  108												
16. SUPPLEMENTARY NOTATION															
17. COSATI CODES  <table border="1"><tr><th>FIELD</th><th>GROUP</th><th>SUB. GR.</th></tr><tr><td></td><td></td><td></td></tr><tr><td></td><td></td><td></td></tr><tr><td></td><td></td><td></td></tr></table>	FIELD	GROUP	SUB. GR.										18. SUBJECT TERMS (Continue on reverse if necessary and identify by block number)		
FIELD	GROUP	SUB. GR.													
19. ABSTRACT (Continue on reverse if necessary and identify by block number)  Laminar-turbulent transition of high-deficit flat plate wakes is investigated by direct numerical simulations using the complete Navier-Stokes equations. The simulations are based on a spatial model so that both the base flow and the disturbance flow can develop in the downstream direction. The Navier-Stokes equations are used in a vorticity-velocity form and are solved using a combination of finite-difference and spectral approximations. Fourier series are used in the spanwise direction. Second-order finite-differences are used to approximate the spatial derivatives in the streamwise and transverse directions. For the temporal discretion, a combination of ADI, Crank-Nicolson, and Adams-Bashforth methods is employed. The discretized velocity equations are solved using fast Helmholtz solvers. Code validation is accomplished by comparison of the numerical results to both linear stability theory and to experiments.															
(over)															
20. DISTRIBUTION/AVAILABILITY OF ABSTRACT  UNCLASSIFIED/UNLIMITED <input checked="" type="checkbox"/> SAME AS RPT. <input type="checkbox"/> DTIC USERS <input type="checkbox"/>		21. ABSTRACT SECURITY CLASSIFICATION  N/A													
22a. NAME OF RESPONSIBLE INDIVIDUAL  Dr. Michael M. Reischmann		22b. TELEPHONE NUMBER (Include Area Code)  (202) 696-4406	22c. OFFICE SYMBOL  ONR												

Calculations of two- and/or three-dimensional sinuous mode disturbances in the wake of a flat plate are undertaken. For calculations of two-dimensional disturbances, the wake is forced at an amplitude level so that nonlinear disturbance development may be observed. In addition, the forcing amplitude is varied in order to determine its effect on the disturbance behavior. To investigate the onset of three-dimensionality, the wake is forced with a small-amplitude three-dimensional disturbance and a larger amplitude two-dimensional disturbance. The two-dimensional forcing amplitude is varied in order to determine its influence on the three-dimensional flow field.

Two-dimensional disturbances are observed to grow exponentially at small amplitude levels. At higher amplitude levels, nonlinear effects become important and the disturbances saturate. The saturation of the fundamental disturbance appears to be related to the stability characteristics of the mean flow. Large forcing amplitudes result in the earlier onset of nonlinear effects and saturation. At large amplitude levels, a Karman vortex street pattern develops.

When the wake is forced with both two- and three-dimensional disturbances strong interaction between these disturbances is observed. The saturation of the two-dimensional disturbance causes the three-dimensional disturbance to saturate. However, this is followed by a resumption of strong three-dimensional growth that may be due to a secondary instability mechanism. Larger two-dimensional forcing amplitudes accelerate the saturation of the two-dimensional and three-dimensional disturbances as well as accelerate the resumption of strong three-dimensional growth. These interactions also result in complicated distributions of vorticity and in a significant increase in the wake width.

## ACKNOWLEDGEMENTS

This work was carried out in the transition research group in the Department of Aerospace and Mechanical Engineering at the University of Arizona. Support was also provided by the NASA Graduate Student Researchers Program (NASA Grant Number NGT-50074) and by the Office of Naval Research (ONR Grant Number N00014-85-K-0412).

Accession For	
NTIS	<input checked="" type="checkbox"/>
DTIC	<input type="checkbox"/>
Unannounced	<input type="checkbox"/>
Justification:	
By <i>per call</i>	
Distribution:	
Availability Codes	
Dist	<input checked="" type="checkbox"/> Audit and/or Special
<b>A-1</b>	

STATEMENT "A" per S. Lekoudis  
 ONR/1132F  
 TELECON

5/23/90 VG



**TABLE OF CONTENTS**

	<b>Page</b>
<b>LIST OF ILLUSTRATIONS . . . . .</b>	<b>7</b>
<b>ABSTRACT . . . . .</b>	<b>16</b>
<b>1. INTRODUCTION . . . . .</b>	<b>18</b>
1.1 The Linear Region of Transition . . . . .	19
1.2 The Nonlinear Region of Transition . . . . .	21
1.3 The Three-Dimensional Region of Transition . . . . .	25
<b>2. PROBLEM STATEMENT . . . . .</b>	<b>26</b>
<b>3. GOVERNING EQUATIONS . . . . .</b>	<b>29</b>
3.1 The Navier-Stokes Equations . . . . .	29
3.2 Nondimensionalization . . . . .	31
<b>4. BOUNDARY AND INITIAL CONDITIONS . . . . .</b>	<b>34</b>
4.1 Spatial Domain . . . . .	34
4.2 Temporal Domain . . . . .	35
4.3 Boundary and Initial Conditions for the Undisturbed Flow . . . . .	35
4.4 Boundary and Initial Conditions for the Disturbed Flow . . . . .	41
<b>5. NUMERICAL METHOD . . . . .</b>	<b>50</b>
5.1 Spanwise Spectral Approximation . . . . .	50
5.1.1 Fourier Representation of the Boundary and Initial Conditions for the Undisturbed Flow . . . . .	53
5.1.2 Fourier Representation of the Boundary and Initial Conditions for the Disturbed Flow . . . . .	55
5.2 Computational Domain . . . . .	60
5.3 Discretization of Spatial Derivatives . . . . .	61
5.4 Discretized Vorticity Equations . . . . .	61

5.4.1	Discretized Boundary and Initial Conditions for the Undisturbed Vorticity . . . . .	65
5.4.2	Discretized Boundary and Initial Conditions for the Disturbed Vorticity . . . . .	66
5.4.3	Equation Systems for the Calculation of the Vorticity . .	67
5.5	Discretized Velocity Equations . . . . .	71
5.5.1	Discretized Boundary and Initial Conditions for the Undisturbed Velocity . . . . .	72
5.5.2	Discretized Boundary and Initial Conditions for the Disturbed Velocity . . . . .	74
5.5.3	Equation Systems for the Calculation of the Velocity . .	77
5.6	Evaluation of the Nonlinear Terms . . . . .	87
5.7	Consistency, Stability, and Convergence of the Numerical Method . . . . .	89
6.	RESULTS . . . . .	92
6.1	Investigations of Two-Dimensional Disturbance Development .	95
6.2	Investigations of Three-Dimensional Disturbance Development .	115
7.	CONCLUSIONS . . . . .	128
	FIGURES . . . . .	131
	APPENDIX A: SOLUTION OF THE THREE-DIMENSIONAL ORR-SOMMERFELD EQUATION . . . . .	264
	APPENDIX B: INFLUENCE OF THE GRID INCREMENT ON THE NUMERICAL SOLUTION . . . . .	273
	REFERENCES . . . . .	277

## LIST OF ILLUSTRATIONS

Figure	Page
2.1 Spatial domain . . . . .	131
5.1 Discretization of the spatial computational domain . . . . .	132
6.1 Base flow streamwise velocity $U^0$ for Case-1 . . . . .	133
6.2 Sinuous mode eigenfunctions of the two-dimensional Orr-Sommerfeld equation corresponding to $\beta = .317$ and $Re_\theta = \frac{\bar{\theta}_{1e} \bar{U}_\infty}{\nu} = 594$ .	
a) amplitudes of $U^0$ , $V^0$ , and $\Omega_z^0$ ; . . . . .	134
b) phases of $U^0$ , $V^0$ , and $\Omega_z^0$ . . . . .	135
6.3 Comparison of amplification curves based on the kinetic energy $\hat{E}^0(x, F)$ to linear stability theory. Case-1: $A_2 = .001$ , $A_3 = 0$ , and $\beta = .317$ . . . . .	136
6.4 Comparison of the amplitude distributions of the fundamental disturbance ( $F = 1$ ) to linear stability theory. Case-1: $A_2 = .001$ , $A_3 = 0$ , and $\beta = .317$ .	
a) streamwise velocity, $U^0$ ; . . . . .	137
b) transverse velocity, $V^0$ ; . . . . .	138
c) spanwise vorticity, $\Omega_z^0$ . . . . .	139
6.5 Comparison of the phase distributions of the fundamental disturbance ( $F = 1$ ) to linear stability theory. Case-1: $A_2 = .001$ , $A_3 = 0$ , and $\beta = .317$ .	
a) streamwise velocity, $U^0$ ; . . . . .	140
b) transverse velocity, $V^0$ ; . . . . .	141
c) spanwise vorticity, $\Omega_z^0$ . . . . .	142
6.6 Comparison of the streamwise variation of $\alpha_r$ , $\alpha_i$ , and $c_p$ for the fundamental disturbance ( $F = 1$ ) to linear stability theory. Case-1: $A_2 = .001$ , $A_3 = 0$ , and $\beta = .317$ .	
a) streamwise wavenumber, $\alpha_r$ ; . . . . .	143
b) amplification rate, $\alpha_i$ ; . . . . .	144
c) phase velocity, $c_p$ . . . . .	145

6.7	Comparison of a Gaussian streamwise velocity distribution to experimental data and to the similarity solution of Goldstein (1929), reproduced from Sato and Kuriki (1961) . . . . .	146
6.8	Base flow streamwise velocity $U^0$ for Case-2 . . . . .	147
6.9	Comparison of the base flow centerline streamwise velocity $U^0$ for Case-2 to the similarity solution of Goldstein (1929) . . . . .	148
6.10	Orr-Sommerfeld eigenvalues for the sinuous mode (mode-1) and the varicose mode (mode-2), corresponding to the streamwise velocity distribution at the inflow boundary (Case-2) and $Re_\theta = \frac{\bar{\theta}_L U_\infty}{\nu} = 594$ .	
a)	streamwise wavenumber, $\alpha_r$ ; . . . . .	149
b)	amplification rate, $\alpha_i$ ; . . . . .	150
c)	phase velocity, $c_p$ . . . . .	151
6.11	Sinuous mode eigenfunctions of the two-dimensional Orr-Sommerfeld equation corresponding to $\beta = .51$ and $Re_\theta = \frac{\bar{\theta}_L U_\infty}{\nu} = 594$ .	
a)	amplitudes of $U^0$ , $V^0$ , and $\Omega_z^0$ ; . . . . .	152
b)	phases of $U^0$ , $V^0$ , and $\Omega_z^0$ . . . . .	153
6.12	Comparison of streamwise velocity amplitude distributions of the fundamental disturbance ( $F = 1$ ) to experimental data.	
a)	Case-2: $A_2 = .000667$ , $A_3 = 0$ , and $\beta = .51$ ; . . . . .	154
b)	experimental, reproduced from Sato (1970) . . . . .	154
6.13	Comparison of the streamwise variation of the mean streamwise centerline velocity $U^0$ and the mean wake half-width to experimental data.	
a)	Case-2: $A_2 = .000667$ , $A_3 = 0$ , and $\beta = .51$ ; . . . . .	155
b)	experimental, reproduced from Sato (1970) . . . . .	155
6.14	Contours of $U^0$ , $V^0$ , and $\Omega_z^0$ for $t = 2176\Delta t$ . Case-3: $A_2 = .001$ , $A_3 = 0$ , and $\beta = .51$ . Twenty contour intervals between the minimum and maximum values. Solid lines denote positive vorticity and dashed lines denote negative vorticity.	
a)	streamwise velocity, $U^0$ ; . . . . .	156
b)	transverse velocity, $V^0$ ; . . . . .	157
c)	spanwise vorticity, $\Omega_z^0$ . . . . .	158

6.15	Contours of spanwise vorticity $\Omega_z^0$ for $t = 2176\Delta t$ . Case-3: $A_2 = .001$ , $A_3 = 0$ , and $\beta = .51$ . Thirty contour intervals between the minimum and maximum values. Solid lines denote positive vorticity and dashed lines denote negative vorticity.	
a)	$0 \leq z/\Delta z \leq 512$ , . . . . .	159
b)	$0 \leq z/\Delta z \leq 340$ . . . . .	160
6.16	Contours of spanwise vorticity $\Omega_z^0$ for $t = 2176\Delta t$ . Case-3: $A_2 = .001$ , $A_3 = 0$ , and $\beta = .51$ . Thirty contour intervals between the minimum and maximum values. Solid lines denote positive vorticity and dashed lines denote negative vorticity.	
a)	$0 \leq z/\Delta z \leq 128$ , . . . . .	161
b)	$128 \leq z/\Delta z \leq 256$ , . . . . .	162
c)	$256 \leq z/\Delta z \leq 384$ , . . . . .	163
d)	$384 \leq z/\Delta z \leq 512$ . . . . .	164
6.17	Amplification curves of the kinetic energy $\hat{E}^0(z, F)$ obtained from the time interval $13T_F < t \leq 15T_F$ . Case-3: $A_2 = .001$ , $A_3 = 0$ , and $\beta = .51$ . . . . .	165
6.18	Temporal variation of the centerline transverse velocity $V^0$ in the time interval $13T_F < t \leq 15T_F$ . Case-3: $A_2 = .001$ , $A_3 = 0$ , and $\beta = .51$ . . . . .	166
6.19	Streamwise variation of the centerline streamwise velocity $U^0$ for the mean flow and the base flow. Case-3: $A_2 = .001$ , $A_3 = 0$ , and $\beta = .51$ . . . . .	167
6.20	Streamwise variation of the wake half-width $b$ for the mean flow and the base flow. Case-3: $A_2 = .001$ , $A_3 = 0$ , and $\beta = .51$ . . . . .	168
6.21	Streamwise variation of $\alpha_r$ and $c_p$ for the fundamental disturbance component ( $F = 1$ ). Case-3: $A_2 = .001$ , $A_3 = 0$ , and $\beta = .51$ .	
a)	streamwise wavenumber, $\alpha_r$ ; . . . . .	169
b)	phase velocity, $c_p$ . . . . .	170
6.22	Amplification curves of the kinetic energy $\hat{E}^0(z, F)$ for Case-3 ( $A_2 = .001$ ) and Case-4 ( $A_2 = .01$ ).	
a)	$F = 0$ , . . . . .	171
b)	$F = 1$ , . . . . .	172
c)	$F = 2$ . . . . .	173

6.23	Comparison of the mean centerline streamwise velocity $U^0$ for Case-3 ( $A_2 = .001$ ) and Case-4 ( $A_2 = .01$ ) . . . . .	174
6.24	Comparison of the streamwise variation of the mean half-width $b$ for Case-3 ( $A_2 = .001$ ) and Case-4 ( $A_2 = .01$ ) . . . . .	175
6.25	Comparison of the base flow centerline streamwise velocity $U^0$ for Case-3 ( $N = 1024$ ) and Case-5 ( $N = 1536$ ) . . . . .	176
6.26	Contours of spanwise vorticity $\Omega_z^0$ for Case-5. $A_2 = .001$ , $A_3 = 0$ , $\beta = .51$ . Solid lines denote positive vorticity and dashed lines denote negative vorticity. a) $t = 2176\Delta t$ and $0 \leq z/\Delta z \leq 1024$ , twenty contour intervals; . . . . . b) $t = 3200\Delta t$ and $0 \leq z/\Delta z \leq 1536$ , ten contour intervals . . . . .	177 178
6.27	Comparison of amplification curves of the kinetic energy $\hat{E}^0(x, F)$ for Case-3 ( $N = 1024$ ) and Case-5 ( $N = 1536$ ). a) $F = 0$ , . . . . . b) $F = 1$ , . . . . . c) $F = 2$ . . . . .	179 180 181
6.28	Amplification curves of the kinetic energy $\hat{E}^0(x, F)$ obtained from the time interval $23T_F < t \leq 25T_F$ . Case-5: $A_2 = .001$ , $A_3 = 0$ , and $\beta = .51$ . . . . .	182
6.29	Temporal variation of the centerline transverse velocity $V^0$ in the time interval $23T_F < t \leq 25T_F$ . Case-5: $A_2 = .001$ , $A_3 = 0$ , and $\beta = .51$ . . . . .	183
6.30	Sinusoidal mode eigenfunctions of the three-dimensional Orr- Sommerfeld equation corresponding to $\beta = .28$ , $\gamma = .5$ , and $Re_\theta = \frac{\bar{U}_\infty \bar{U}_\infty}{\gamma} = 594$ . a) amplitudes of $U^1$ , $V^1$ , and $W^1$ ; . . . . . b) amplitudes of $\Omega_x^1$ , $\Omega_y^1$ , and $\Omega_z^1$ ; . . . . . c) phases of $U^1$ , $V^1$ , and $W^1$ ; . . . . . d) phases of $\Omega_x^1$ , $\Omega_y^1$ , and $\Omega_z^1$ . . . . .	184 185 186 187
6.31	Comparison of amplification curves of the kinetic energy $\hat{E}^1(x, F)$ to linear stability theory. Case-6: $A_2 = 0$ , $A_3 = .001$ , $\beta = .28$ , and $\gamma = .5$ . . . . .	188

6.32	Comparison of the amplitude distributions of the fundamental disturbance ( $F = 1, k = 1$ ) to linear stability theory. Case-6: $A_2 = 0, A_3 = .001, \beta = .28$ , and $\gamma = .5$ .	
	a) streamwise velocity, $U^1$ ; . . . . .	189
	b) transverse velocity, $V^1$ ; . . . . .	190
	c) spanwise velocity, $W^1$ . . . . .	191
6.33	Comparison of the phase distributions of the fundamental disturbance ( $F = 1, k = 1$ ) to linear stability theory. Case-6: $A_2 = 0, A_3 = .001, \beta = .28$ , and $\gamma = .5$ .	
	a) streamwise velocity, $U^1$ ; . . . . .	192
	b) transverse velocity, $V^1$ ; . . . . .	193
	c) spanwise velocity, $W^1$ . . . . .	194
6.34	Sinuous mode eigenfunctions of the three-dimensional Orr-Sommerfeld equation corresponding to $\beta = .51, \gamma = .5$ , and $Re_\theta = \frac{\bar{\theta}_{1\ell} \bar{U}_\infty}{\nu} = 594$ .	
	a) amplitudes of $U^1, V^1$ , and $W^1$ ; . . . . .	195
	b) amplitudes of $\Omega_x^1, \Omega_y^1$ , and $\Omega_z^1$ ; . . . . .	196
	c) phases of $U^1, V^1$ , and $W^1$ ; . . . . .	197
	d) phases of $\Omega_x^1, \Omega_y^1$ , and $\Omega_z^1$ . . . . .	198
6.35	Amplification curves of the kinetic energy $\hat{E}^1(x, F)$ . Case-7: $A_2 = 0, A_3 = .001, \beta = .51$ , and $\gamma = .5$ .	
	a) $6T_F < t \leq 8T_F$ , . . . . .	199
	b) $8T_F < t \leq 10T_F$ . . . . .	200
6.36	Contours of streamwise vorticity $\omega_z$ in the $yz$ -plane for $t = 4096\Delta t$ . Case-7: $A_2 = 0, A_3 = .001, \beta = .51$ , and $\gamma = .5$ . Twenty contour intervals between the minimum and maximum values. Solid lines denote positive vorticity and dashed lines denote negative vorticity.	
	a) $x = .030$ , . . . . .	201
	b) $x = .146$ . . . . .	202
6.37	Contours of streamwise vorticity $\omega_z$ in the $yz$ -plane, reproduced from Meiburg and Lasheras (1988) . . . . .	203
6.38	Amplification curves of the kinetic energy $\hat{E}^k(x, 1)$ . Case-8: $A_2 = .01, A_3 = .001, \beta = .51$ , and $\gamma = .5$ . . . . .	204

6.39	Amplification curves of the kinetic energy $\hat{E}^k(x, 1)$ . Case-9: $A_2 = .05, A_3 = .001, \beta = .51$ , and $\gamma = .5$	205
6.40	Amplification curves of the kinetic energy $\hat{E}^1(x, F)$ . Case-9: $A_2 = .05, A_3 = .001, \beta = .51$ , and $\gamma = .5$ .	
a)	$N = 256$	206
b)	$N = 512$	207
6.41	Temporal variation of two-dimensional and three-dimensional disturbance kinetic energy in a free shear layer, reproduced from Metcalfe et. al (1987)	208
6.42	Contours of streamwise vorticity $\omega_z$ in the $yz$ -plane for $t = 4096\Delta t$ . $z = .146$ . Twenty contour intervals between the minimum and maximum values. Solid lines denote positive vorticity and dashed lines denote negative vorticity.	
a)	Case-8, $A_2 = 0.01$ and $A_3 = 0.001$	209
b)	Case-9, $A_2 = 0.05$ and $A_3 = 0.001$	210
6.43	Contours of spanwise vorticity $\omega_z$ in the $yz$ -plane for $t = 4096\Delta t$ . $z = .146$ . Twenty contour intervals between the minimum and maximum values. Solid lines denote positive vorticity and dashed lines denote negative vorticity.	
a)	Case-7, $A_2 = 0.00$ and $A_3 = 0.001$	211
b)	Case-8, $A_2 = 0.01$ and $A_3 = 0.001$	212
c)	Case-9, $A_2 = 0.05$ and $A_3 = 0.001$	213
6.44	Contours of streamwise vorticity $\omega_z$ in the $xy$ -plane for $t = 4096\Delta t$ . $z = \pi/2$ . Twenty contour intervals between the minimum and maximum values. Solid lines denote positive vorticity and dashed lines denote negative vorticity.	
a)	Case-7, $A_2 = 0.00$ and $A_3 = 0.001$	214
b)	Case-8, $A_2 = 0.01$ and $A_3 = 0.001$	215
c)	Case-9, $A_2 = 0.05$ and $A_3 = 0.001$	216
6.45	Contours of spanwise vorticity $\omega_z$ in the $xy$ -plane for $t = 4096\Delta t$ . $z = 0$ . Twenty contour intervals between the minimum and maximum values. Solid lines denote positive vorticity and dashed lines denote negative vorticity.	
a)	Case-7, $A_2 = 0.00$ and $A_3 = 0.001$	217
b)	Case-8, $A_2 = 0.01$ and $A_3 = 0.001$	218
c)	Case-9, $A_2 = 0.05$ and $A_3 = 0.001$	219

6.46	Contours of spanwise vorticity $\omega_z$ in the $xy$ -plane for $t = 4096\Delta t$ and $z = 0$ . Case-8: $A_2 = .01$ , $A_3 = .001$ , $\beta = .51$ , and $\gamma = .5$ . Thirty contour intervals between the minimum and maximum values. Solid lines denote positive vorticity and dashed lines denote negative vorticity . . . . .	220
6.47	Contours of spanwise vorticity $\omega_z$ in the $zz$ -plane for $t = 4096\Delta t$ . Case-8: $A_2 = .01$ , $A_3 = .001$ , $\beta = .51$ , and $\gamma = .5$ . Thirty contour intervals between the minimum and maximum values. Solid lines denote positive vorticity and dashed lines denote negative vorticity.	
a)	$y = 2$ ( $y/\Delta y = 72$ ), . . . . .	221
b)	$y = -2$ ( $y/\Delta y = 56$ ) . . . . .	222
6.48	Contours of streamwise vorticity $\omega_x$ in the $zz$ -plane for $t = 4096\Delta t$ . Case-8: $A_2 = .01$ , $A_3 = .001$ , $\beta = .51$ , and $\gamma = .5$ . Thirty contour intervals between the minimum and maximum values. Solid lines denote positive vorticity and dashed lines denote negative vorticity.	
a)	$y = 2$ ( $y/\Delta y = 72$ ), . . . . .	223
b)	$y = -2$ ( $y/\Delta y = 56$ ) . . . . .	224
6.49	Contours of spanwise vorticity $\omega_z$ in the $yz$ -plane for $t = 4096\Delta t$ . Case-8: $A_2 = .01$ , $A_3 = .001$ , $\beta = .51$ , and $\gamma = .5$ . Thirty contour intervals between the minimum and maximum values. Solid lines denote positive vorticity and dashed lines denote negative vorticity.	
a)	$x = .172$ ( $x/\Delta x = 110$ ), . . . . .	225
b)	$x = .160$ ( $x/\Delta x = 101$ ) . . . . .	226
6.50	Contours of streamwise vorticity $\omega_x$ in the $yz$ -plane for $t = 4096\Delta t$ . Case-8: $A_2 = .01$ , $A_3 = .001$ , $\beta = .51$ , and $\gamma = .5$ . Thirty contour intervals between the minimum and maximum values. Solid lines denote positive vorticity and dashed lines denote negative vorticity.	
a)	$x = .172$ ( $x/\Delta x = 110$ ), . . . . .	227
b)	$x = .160$ ( $x/\Delta x = 101$ ) . . . . .	228
6.51	Vorticity amplitude distributions for $F = 1$ . Case-7: $A_2 = 0$ , $A_3 = .001$ , $\beta = .51$ , and $\gamma = .5$ .	
a)	spanwise vorticity, $\Omega_z^0$ ; . . . . .	229
b)	spanwise vorticity, $\Omega_z^1$ ; . . . . .	230
c)	streamwise vorticity, $\Omega_x^1$ . . . . .	231

6.52	Vorticity amplitude distributions for $F = 1$ . Case-8: $A_2 = .01$ , $A_3 = .001$ , $\beta = .51$ , and $\gamma = .5$ .	
a)	spanwise vorticity, $\Omega_z^0$ ; . . . . .	232
b)	spanwise vorticity, $\Omega_z^1$ ; . . . . .	233
c)	streamwise vorticity, $\Omega_z^1$ . . . . .	234
6.53	Vorticity amplitude distributions for $F = 1$ . Case-9: $A_2 = .05$ , $A_3 = .001$ , $\beta = .51$ , and $\gamma = .5$ .	
a)	spanwise vorticity, $\Omega_z^0$ ; . . . . .	235
b)	spanwise vorticity, $\Omega_z^1$ ; . . . . .	236
c)	streamwise vorticity, $\Omega_z^1$ . . . . .	237
6.54	Streamwise variation of the wake half-width $b$ for Case-4, $A_2 = 0.01$ , $A_3 = 0.00$ ; Case-7, $A_2 = 0.00$ , $A_3 = 0.001$ ; and Case-8, $A_2 = 0.01$ , $A_3 = 0.001$ . . . . .	238
6.55	Streamwise variation of the wake half-width $b$ for Case-8, $A_2 = 0.01$ , $A_3 = 0.001$ ; and Case-9, $A_2 = 0.05$ , $A_3 = 0.001$ . . . . .	239
B.1	Influence of the grid increment on the amplification of the kinetic energy $\hat{E}^0(x, F = 1)$ for Case-1.	
a)	$M = 64$ with $N = 64$ , $N = 128$ , and $N = 256$ ; . . . . .	240
b)	$N = 128$ with $M = 32$ , $M = 64$ , and $M = 128$ . . . . .	241
B.2	Influence of the grid increment on the amplitude distributions of the fundamental disturbance ( $F = 1$ ) of the streamwise velocity for Case-1.	
a)	$M = 64$ with $N = 64$ , $N = 128$ , and $N = 256$ ; . . . . .	242
b)	$N = 128$ with $M = 32$ , $M = 64$ , and $M = 128$ . . . . .	243
B.3	Influence of the grid increment on the phase distributions of the fundamental disturbance ( $F = 1$ ) of the streamwise velocity for Case-1.	
a)	$M = 64$ with $N = 64$ , $N = 128$ , and $N = 256$ ; . . . . .	244
b)	$N = 128$ with $M = 32$ , $M = 64$ , and $M = 128$ . . . . .	245
B.4	Influence of the streamwise grid increment on the amplification of the kinetic energy $\hat{E}^0(x, F)$ . Case-2: $M = 256$ with $N = 512$ , $N = 768$ , and $N = 1024$ .	
a)	the mean component, $F = 0$ ; . . . . .	246
b)	the fundamental component, $F = 1$ ; . . . . .	247
c)	the second harmonic, $F = 2$ . . . . .	248

B.5	Influence of the transverse grid increment on the amplification of the kinetic energy $\hat{E}^0(x, F)$ . Case-2: $N = 1024$ with $M = 128$ , $M = 192$ , and $M = 256$ .	
a)	the mean component, $F = 0$ ; . . . . .	249
b)	the fundamental component, $F = 1$ ; . . . . .	250
c)	the second harmonic, $F = 2$ . . . . .	251
B.6	Influence of the streamwise grid increment on the amplitude distributions of the streamwise velocity. Case-2: $M = 256$ with $N = 512$ , $N = 768$ , and $N = 1024$ .	
a)	the mean component, $F = 0$ ; . . . . .	252
b)	the fundamental component, $F = 1$ ; . . . . .	253
c)	the second harmonic, $F = 2$ . . . . .	254
B.7	Influence of the transverse grid increment on the amplitude distributions of the streamwise velocity. Case-2: $N = 1024$ with $M = 128$ , $M = 192$ , and $M = 256$ .	
a)	the mean component, $F = 0$ ; . . . . .	255
b)	the fundamental component, $F = 1$ ; . . . . .	256
c)	the second harmonic, $F = 2$ . . . . .	257
B.8	Influence of the streamwise grid increment on the phase distributions of the streamwise velocity. Case-2: $M = 256$ with $N = 512$ , $N = 768$ , and $N = 1024$ .	
a)	the mean component, $F = 0$ ; . . . . .	258
b)	the fundamental component, $F = 1$ ; . . . . .	259
c)	the second harmonic, $F = 2$ . . . . .	260
B.9	Influence of the transverse grid increment on the phase distributions of the streamwise velocity. Case-2: $N = 1024$ with $M = 128$ , $M = 192$ , and $M = 256$ .	
a)	the mean component, $F = 0$ ; . . . . .	261
b)	the fundamental component, $F = 1$ ; . . . . .	262
c)	the second harmonic, $F = 2$ . . . . .	263

## ABSTRACT

Laminar-turbulent transition of high-deficit flat plate wakes is investigated by direct numerical simulations using the complete Navier-Stokes equations. The simulations are based on a spatial model so that both the base flow and the disturbance flow can develop in the downstream direction. The Navier-Stokes equations are used in a vorticity-velocity form and are solved using a combination of finite-difference and spectral approximations. Fourier series are used in the spanwise direction. Second-order finite-differences are used to approximate the spatial derivatives in the streamwise and transverse directions. For the temporal discretization, a combination of ADI, Crank-Nicolson, and Adams-Basforth methods is employed. The discretized velocity equations are solved using fast Helmholtz solvers. Code validation is accomplished by comparison of the numerical results to both linear stability theory and to experiments.

Calculations of two- and/or three-dimensional sinuous mode disturbances in the wake of a flat plate are undertaken. For calculations of two-dimensional disturbances, the wake is forced at an amplitude level so that nonlinear disturbance development may be observed. In addition, the forcing amplitude is varied in order to determine its effect on the disturbance behavior. To investigate the onset of three-dimensionality, the wake is forced with a small-amplitude three-dimensional disturbance and a larger amplitude two-dimensional disturbance. The two-dimensional forcing amplitude is varied in order to determine its influence on the three-dimensional flow field.

Two-dimensional disturbances are observed to grow exponentially at small amplitude levels. At higher amplitude levels, nonlinear effects become important and the disturbances saturate. The saturation of the fundamental disturbance

appears to be related to the stability characteristics of the mean flow. Larger forcing amplitudes result in the earlier onset of nonlinear effects and saturation. At large amplitude levels, a Kármán vortex street pattern develops.

When the wake is forced with both two- and three-dimensional disturbances, strong interactions between these disturbances is observed. The saturation of the two-dimensional disturbance causes the three-dimensional disturbance to saturate. However, this is followed by a resumption of strong three-dimensional growth that may be due to a secondary instability mechanism. Larger two-dimensional forcing amplitudes accelerate the saturation of the two-dimensional and three-dimensional disturbances as well as accelerate the resumption of strong three-dimensional growth. These interactions also result in complicated distributions of vorticity and in a significant increase in the wake width.

## CHAPTER 1

### INTRODUCTION

According to Sato and Kuriki (1961), in the laminar-turbulent transition of a flat plate wake three distinct regions can be identified: a linear region, a nonlinear region, and a three-dimensional region. In the linear region, small disturbances in the background flow trigger two-dimensional wave-like fluctuations. Sato and Kuriki's measurements indicate that the frequency of the dominant fluctuation in the wake corresponds to the frequency of the most amplified disturbance predicted by linear stability theory. Once present in the wake, these fluctuations grow exponentially in the downstream direction and are well described by linear stability theory.

Due to the large amplification rates associated with wakes, the amplitudes of the disturbances rapidly become quite large and nonlinear interactions between the disturbances become important. The behavior of the disturbances deviate from linear stability theory predictions but the wake remains two-dimensional (Sato and Kuriki, 1961). In this region, the disturbances grow at rates significantly less than those predicted by linear stability theory and harmonics of the fundamental disturbances are generated. Also due to nonlinear effects, the mean flow is altered. As verified by several researchers (Zabusky and Deem, 1971; Aref and Siggia, 1981; and Meiburg and Lasheras, 1988), this sequence of events leads to the well known Kármán vortex streets that are observed in flat plate wakes.

Finally, three dimensionality becomes important. The work of Robinson and Saffman (1982) indicates that the two-dimensional Kármán vortex street is unstable with respect to three-dimensional disturbances. As a consequence of this

instability, three-dimensional lambda vortex patterns are formed in the region between consecutive Kármán vortices of opposite sign (Meiburg and Lasheras, 1988).

### 1.1 The Linear Region of Transition

Linear stability theory describes the behavior of small amplitude disturbances in parallel shear flows. In nonparallel shear flows, linear stability theory is not strictly applicable but can still be a useful model of small amplitude disturbance development. The streamfunction  $\psi$  of a disturbance described by linear stability theory has the form

$$\psi(x, y, z, t) = \text{Real}(\phi(y)e^{i(\alpha z + \gamma z - \beta t)}) \quad (1.1)$$

where the variables  $\mathbf{x} = (x, y, z)$  and  $t$  are the spatial position vector and time respectively. The amplitude  $\phi(y)$  is an eigenfunction of the Orr-Sommerfeld equation

$$(U - c)(\phi'' - (\alpha^2 + \gamma^2)\phi) - U''\phi + \frac{i}{\alpha Re}(\phi''' - 2(\alpha^2 + \gamma^2)\phi'' + (\alpha^2 + \gamma^2)^2\phi) = 0 \quad (1.2)$$

where primes denotes differentiation with respect to  $y$ . In equation (1.2),  $U = U(y)$  is the streamwise velocity distribution of the undisturbed flow,  $\alpha$  is the streamwise wave number of the disturbance,  $\gamma$  is the spanwise wave number of the disturbance, and  $\beta$  is the temporal frequency of the disturbance. The phase velocity of the disturbance is  $c = \beta/\alpha$  and  $Re$  is the Reynolds number of the undisturbed flow. In general,  $\alpha$  and  $\beta$  are complex and  $\gamma$  is real. However, interest is usually confined to two cases, namely, to the case of spatially growing disturbances for which  $\alpha = (\alpha_r, \alpha_i)$  is complex and  $\beta$  is real, and to the case of temporally growing disturbances for which  $\beta = (\beta_r, \beta_i)$  is complex and  $\alpha$  is real. A complete derivation of equation (1.2) is given by White (1974).

Wakes are inviscidly unstable due to the inflection points in their velocity profile. As is characteristic of flows with inflectional profiles, the disturbances observed in wakes have high amplification rates. Also, because the streamwise velocity distribution of wakes has two inflection points, two different instability modes exist. The sinuous mode (mode-1) is highly amplified with an anti-symmetric streamwise velocity distribution. The varicose mode (mode-2) is less amplified (at most frequencies) than the sinuous mode and has a symmetric streamwise velocity distribution. Because of the higher amplification rates associated with the sinuous mode, it is this mode that is usually observed in experiments (Sato and Kuriki, 1961; Sato, 1970; Miksad et al., 1982).

The validity of linear stability theory in describing the initial stages of transition in near wakes has been verified experimentally. Sato and Kuriki (1961) studied the transition of a flat plate wake subject to acoustical excitation. The results of these experiments were compared to linear stability calculations of temporally-amplifying, sinuous mode disturbances. The temporal amplification rates  $\beta_i$ , obtained from linear stability theory, were converted into spatial amplification rates  $\frac{a\beta_i}{\beta_r}$  using a phase velocity transformation. The theoretical eigenfunctions compared very well with those obtained experimentally. However, the experimental amplification rates did not compare as well with those predicted by linear stability theory because the phase velocity transformation is not accurate enough for dispersive waves.

Mattingly and Criminale (1972) experimentally investigated the behavior of small amplitude disturbances in the near wake of a thin airfoil (NACA 0003) and compared their results to both spatial and temporal linear stability theory. For comparison of temporal amplification rates to experimentally obtained amplification rates, the Gaster transformation (Gaster, 1962) was employed. The ex-

perimentally obtained amplitude distributions and amplification rates compared well to spatial linear stability theory predictions. The assumption of temporally-amplifying disturbances, and using the Gaster transformation, did not produce as good an agreement with the experimental results. The lack of agreement can be explained by the fact that the Gaster transformation is based on the assumption of small amplification rates  $|\alpha_i| \ll 1$ , which is not satisfied for high-deficit wakes. From their results, Mattingly and Criminale concluded that spatial stability theory is more accurate than temporal stability theory in predicting the behavior of small amplitude disturbances in the near wake of a thin airfoil.

Mattingly and Criminale also found that the stability characteristics of a spatially varying wake could be computed by the use of a quasi-uniform (quasi-parallel) assumption, i.e. the wake is assumed to be locally parallel. The stability characteristics of the local mean velocity profile are then computed using the Orr-Sommerfeld equation. Then, the streamwise wave number  $\alpha$  is obtained as a function of streamwise distance.

Miksad et al. (1982) have shown that linear stability theory is also valid when there is more than one dominant disturbance in the wake. They experimentally studied the early development of two small amplitude sinuous mode disturbances, of different frequencies, in the wake of a thin airfoil. Their results indicated that, at small amplitudes, both disturbances grew exponentially at rates predicted by linear stability theory.

### 1.2 The Nonlinear Region of Transition

Due to the large amplification rates associated with high-deficit wakes, the linear region of transition in these flows is usually quite small. With the appearance of large amplitude disturbances, nonlinear effects become important and linear stability theory is no longer applicable. In contrast to the linear region where

the disturbances grew quite rapidly, the disturbances evolve more gradually in the nonlinear region. This is also in contrast with the development in boundary layer flows where rapid transition to turbulence occurs once nonlinear effects and three-dimensionality become important.

Sato and Kuriki (1961) found that the early (upstream) part of the nonlinear region is similar in some respects to the linear region of transition. Although the amplification rates of the disturbances are significantly lower than those observed in the linear region, their experimental results indicate that the amplitude distribution of the fundamental disturbance does not change significantly until the nonlinearity has persisted for some distance downstream. However, harmonics of the fundamental disturbance are generated and the second harmonic becomes the dominant disturbance component near the wake centerline (Sato and Kuriki, 1961). Nonlinear effects also change the mean flow, leading to rapid increases in the mean centerline velocity and the mean wake half-width (Sato, 1970). The resulting mean streamwise velocity distribution is much fuller than that of the undisturbed flow, indicating a greater degree of fluid mixing.

As the disturbances travel farther downstream in the nonlinear region, the amplitude distribution of the fundamental disturbance deviates from the shape predicted by linear theory. The measurements of Sato (1970) indicate that the peaks in the streamwise velocity amplitude distribution of the fundamental disturbance shift towards the outer edge of the wake and also decrease in magnitude with increasing downstream distance. The peak value in the streamwise velocity amplitude distribution of the second harmonic component, which initially grew rapidly, also begins to decrease. Sato speculates that the energy lost by the fluctuations might be transferred to the mean flow. Sato's measurements also show that the mean half-width and the mean centerline velocity, which initially increased in

the nonlinear region, begin to decrease when the fundamental streamwise velocity fluctuation begins to decrease. Sato showed that the production of fluctuation energy

$$-\overline{u'v'} \frac{\partial \bar{u}}{\partial y} , \quad (1.3)$$

where  $u'$  and  $v'$  are the time fluctuating components of the streamwise and transverse velocities,  $\overline{u'v'}$  is the Reynolds stress associated with the disturbances, and  $\bar{u}$  is the mean streamwise velocity, has the same sign as the mean centerline velocity gradient. Therefore, when the mean centerline velocity increases the fluctuation energy should increase, and when the mean centerline velocity decreases the fluctuation energy should decrease. Also in this region, Sato and Kuriki (1961) observed velocity "over-shoots" near the outer edge of the wake so that the mean streamwise velocity attained values greater than its freestream value.

Motivated by the appearance of vortices in wakes, Sato and Kuriki proposed a "double row vortex model" as a way of explaining the nonlinear behavior of wake disturbances. In this model, the vortices alternate in sign and are arranged in a staggered fashion on each side of the wake centerline. The velocity induced by this vortex pattern does indeed capture some of the features observed in wakes such as the second harmonic near the wake centerline, the velocity over-shoots near the outer edge of the wake, and the decrease of the mean centerline velocity far downstream.

Several different numerical investigations support the double row vortex model. Zabusky and Deem (1971) performed Navier-Stokes simulations of the temporal evolution of an unstable disturbance in a parallel wake. Their results indicate that the saturation of the fundamental disturbance in plane wakes leads to the development of a vortex street pattern. Phenomena similar to those observed by

Sato and Kuriki, such as the velocity over-shoots, were observed in the numerical results. Aref and Siggia (1981) and Meiburg and Lasheras (1988) studied the temporal development of vortex rows using inviscid vortex dynamics. They modeled a plane wake as two vortex sheets of opposite sign. When the vortex sheets were perturbed, they evolved into a two-dimensional vortex street.

Several researchers including Sato and Onda (1970), Sato (1970), Motohashi (1979) and Miksad et al. (1982) have experimentally investigated the behavior of wakes that were disturbed at two different frequencies. By perturbing the wake with disturbances at two different frequencies, these researchers hoped to gain insight into the complex nonlinear interactions that take place in natural transition. Sato and Saito (1975) performed experiments to study the interaction of a discrete frequency disturbance with the broad band background fluctuations that were naturally present in the flow. In their experiments, Sato (1970) and Sato and Onda (1970) found that the nonlinear interactions between the two disturbances generated the expected higher harmonics as well as a difference frequency. This difference frequency is similar to the low frequency fluctuations observed in natural transition. In natural transition, the low frequency component is not a single frequency but a narrow band of frequencies. The conjecture is that these low frequencies are generated by interactions between the higher frequency fluctuations that result from the linear instability.

Miksad et al. (1982) found that interactions between the difference frequency and the two fundamental frequencies produced sidebands in the spectrum. These sidebands modulate the amplitude of the fundamental fluctuations. Amplitude modulation in combination with the dispersion relation of the fluctuations produces phase modulation of the fluctuations. Miksad et al. indicate that this mod-

ulation has an important role in spectral broadening, that is in the redistribution of energy from a small number of frequencies to a larger number of frequencies.

### 1.3 The Three-Dimensional Region of Transition

Investigations of laminar-turbulent transition in plane wakes have dealt mainly with two-dimensional instability mechanisms. Notable exceptions are the numerical work of Meiburg and Lasheras (1987 and 1988), the experimental investigations of Breidenthal (1980), and the theoretical work of Robinson and Saffman (1982).

Robinson and Saffman (1982) theoretically investigated the stability of vortex arrays to small amplitude two- and three-dimensional disturbances. They found that the staggered pattern of the Kármán vortex street is most unstable with respect to three-dimensional, spanwise-periodic disturbances. This implies that the breakdown of the vortex streets observed in flat plate wakes should be of a three-dimensional nature.

Breidenthal (1980) experimentally investigated the three-dimensional behavior of a turbulent flat plate wake. The plate trailing edge varied periodically in the spanwise direction in order to induce three-dimensional disturbances in the wake. Under the influence of this three-dimensional perturbation, the wake was observed to form a spanwise periodic array of interconnecting vortex loops.

Meiburg and Lasheras (1987 and 1988) numerically investigated the interaction of a large amplitude, three-dimensional disturbance with a smaller amplitude, two-dimensional disturbance. They found that the two-dimensional disturbance led to the formation of a vortex street. The three-dimensional disturbance, through an interaction with the two-dimensional vortex street, formed lambda vortices similar to those found in boundary layers. Further interaction between the lambda vortices and the two-dimensional structures led to the development of closed vortex loops similar to those observed by Breidenthal.

## CHAPTER 2

### PROBLEM STATEMENT

In this work, laminar-turbulent transition of an incompressible high-deficit flat plate wake is investigated by direct numerical simulations using the complete Navier-Stokes equations. Research efforts are initially focused on the early stages of transition where two-dimensional disturbances are dominant. Of primary interest is the role of nonlinear effects in the development of disturbances. Subsequently, the focus is on the early stages of three-dimensional breakdown where both two- and three-dimensional disturbances play an important role. The onset of this three-dimensionality is investigated by simulating the interaction of two-dimensional and three-dimensional disturbances. Investigations of these interactions might explain how three-dimensional disturbances, which according to linear stability theory are more stable than two-dimensional disturbances, eventually dominate the wake development.

The numerical simulations are designed to model the physical experiments of Sato and Kuriki (1961) and Sato (1970). The results of these simulations may then be compared to the results of the physical experiments. The wake that is studied is shown in Figure 2.1. The wake is generated by a thin flat plate aligned parallel to a uniform stream. The boundary layers on the plate are assumed to be laminar and steady over the entire length of the plate, and hence form a laminar wake when they merge at the plate trailing edge. The wake evolves rapidly downstream of the plate.

The spatial domain in which the numerical simulations take place lies downstream of the flat plate trailing edge. The domain is placed near the plate so that

it will contain the high-deficit region of the wake. However, the domain does not include the trailing edge of the plate. The plate trailing edge is of primary interest in studies of receptivity and in studies of absolute instabilities. Although, these are both important aspects of wake transition, they are not the main focus of this research.

The calculations are undertaken using a numerical method that is designed to solve both the two-dimensional and three-dimensional Navier-Stokes equations. Because of the spanwise periodicity of disturbances that was observed in experiments, the spanwise variation of the wake is represented by finite Fourier series. Second-order finite-differences are used to approximate the spatial derivatives in the streamwise and transverse directions. Time integration of the Navier-Stokes equations is accomplished using a hybrid scheme that is second-order time-accurate.

The results of many experimental investigations (Sato and Kuriki, 1961; Sato, 1970; Mattingly and Criminale, 1972) indicate that transition in wakes is the result of a spatial instability rather than a temporal instability. Furthermore, Mattingly and Criminale (1972) showed that the use of the Gaster transformation (1962) to convert temporal stability results into spatial stability results is invalid for high-deficit wakes. Therefore, in this work spatial amplification and temporal periodicity of wake disturbances is assumed. To correctly model disturbances of this type, the boundary conditions employed in these simulations must be of the inflow-outflow type. Spatially growing disturbances are induced in the wake by time-periodic excitation at the inflow boundary of the spatial domain.

The remaining chapters describe in more detail other important aspects of this work. In Chapter 3, the governing equations of these simulations are discussed. The length, time, and velocity scales that are used to nondimensionalize

the governing equations are also discussed. The boundary and initial conditions that are required to complete the mathematical formulation of the physical problem are outlined in Chapter 4. The method used to obtain numerical solutions of the governing equations is discussed in Chapter 5. Chapter 6 contains a discussion of the results of the numerical simulations. Finally, in Chapter 7 significant conclusions are presented.

## CHAPTER 3

### GOVERNING EQUATIONS

The Navier-Stokes equations govern momentum transfer in a viscous fluid. These equations are derived by applying Newton's second law of motion to a fluid particle. The assumptions required to obtain these equations are that the fluid is a continuum and that its stress-strain relationship is Newtonian.

#### 3.1 The Navier-Stokes Equations

The numerical method is based on the Navier-Stokes equations for incompressible flow. In vector form they can be written as

$$\frac{\partial \bar{u}}{\partial \bar{t}} + \bar{u} \cdot \bar{\nabla} \bar{u} = -\frac{1}{\bar{\rho}} \bar{\nabla} \bar{p} + \bar{\nu} \bar{\nabla}^2 \bar{u} . \quad (3.1)$$

The continuity equation for incompressible flow is

$$\bar{\nabla} \cdot \bar{u} = 0 . \quad (3.2)$$

The independent variables in equations (3.1) and (3.2) are time  $\bar{t}$  and the spatial position vector  $\bar{x} = (\bar{x}, \bar{y}, \bar{z})$ . The dependent variables are the Eulerian velocity vector field  $\bar{u} = (\bar{u}, \bar{v}, \bar{w})$  and the fluid pressure  $\bar{p}$ . These variables depend on  $\bar{x}$  and  $\bar{t}$ . The three coordinate directions  $\bar{x}$ ,  $\bar{y}$ , and  $\bar{z}$  and the corresponding fluid velocity components  $\bar{u}$ ,  $\bar{v}$ , and  $\bar{w}$  are shown in Figure 2.1. The fluid density  $\bar{\rho}$  and the kinematic viscosity of the fluid  $\bar{\nu}$  are assumed to be constant. Variables with over-bars denote dimensional quantities, while bold-face variables represent vector quantities.

The operator  $\bar{\nabla}$  is a vector which in Cartesian coordinates is of the form

$$\bar{\nabla} = \left( \frac{\partial}{\partial \bar{x}}, \frac{\partial}{\partial \bar{y}}, \frac{\partial}{\partial \bar{z}} \right) . \quad (3.3)$$

The Laplacian operator  $\bar{\nabla}^2$  is

$$\bar{\nabla}^2 = \frac{\partial^2}{\partial \bar{x}^2} + \frac{\partial^2}{\partial \bar{y}^2} + \frac{\partial^2}{\partial \bar{z}^2} \quad (3.4a)$$

and the operator  $\bar{u} \cdot \bar{\nabla}$  is

$$\bar{u} \cdot \bar{\nabla} = \bar{u} \frac{\partial}{\partial \bar{x}} + \bar{v} \frac{\partial}{\partial \bar{y}} + \bar{w} \frac{\partial}{\partial \bar{z}} . \quad (3.4b)$$

Equations (3.1) together with (3.2) lead to four scalar equations which in principle can be numerically solved for the four dependent variables  $(\bar{u}, \bar{v}, \bar{w})$  and  $\bar{p}$  as functions of  $(\bar{x}, \bar{y}, \bar{z})$  and  $\bar{t}$ . However, one difficulty with solving these equations is formulating boundary conditions for the pressure. This difficulty is avoided by solving an alternate formulation of the Navier-Stokes equations in which the pressure does not appear. This formulation of the Navier-Stokes equations is obtained by taking the curl of equation (3.1) and simplifying the result with the appropriate vector identities. The resulting vector equation (Batchelor, 1967) is

$$\frac{\partial \bar{\omega}}{\partial \bar{t}} - \nu \bar{\nabla}^2 \bar{\omega} = \bar{\omega} \cdot \bar{\nabla} \bar{u} - \bar{u} \cdot \bar{\nabla} \bar{\omega} . \quad (3.5)$$

The Eulerian vorticity vector field  $\bar{\omega} = (\bar{\omega}_x, \bar{\omega}_y, \bar{\omega}_z)$  is defined by the relation

$$\bar{\omega} = -\bar{\nabla} \times \bar{u} \quad (3.6)$$

and the operator  $\bar{\omega} \cdot \bar{\nabla}$  is

$$\bar{\omega} \cdot \bar{\nabla} = \bar{\omega}_x \frac{\partial}{\partial \bar{x}} + \bar{\omega}_y \frac{\partial}{\partial \bar{y}} + \bar{\omega}_z \frac{\partial}{\partial \bar{z}} . \quad (3.7)$$

It is noted that the vorticity vector as defined by equation (3.6) is the negative of the usual definition of vorticity,  $\bar{\omega} = \bar{\nabla} \times \bar{u}$ . However, throughout this work the term vorticity will be used to denote the flow variable defined by equation (3.6).

Furthermore, because of the negative sign in equation (3.6), the direction of fluid rotation associated with the vorticity vector  $\bar{\omega} = -\bar{\nabla} \times \bar{u}$  is given by a left-hand rule instead of the usual right-hand rule.

Equation (3.5) is the Navier-Stokes equation in vorticity-velocity formulation, or alternatively the vorticity transport equation. Coupled to equation (3.5) is the Poisson equation

$$\bar{\nabla}^2 \bar{u} = \bar{\nabla} \times \bar{\omega} \quad (3.8)$$

which is derived from the definition of vorticity ( $\bar{\omega} = -\bar{\nabla} \times \bar{u}$ ) using the continuity equation (3.2). The vorticity  $\bar{\omega}$  is also a function of the independent variables  $\bar{x}$  and  $\bar{t}$ .

Equations (3.5) and (3.8) are a system of six scalar equations which can be solved subject to appropriate boundary and initial conditions. As desired, equations (3.5) and (3.8) also do not contain the fluid pressure  $\bar{p}$  as an unknown variable. However, in contrast to equations (3.1) and (3.2), now six scalar equations must be solved instead of four.

### 3.2 Nondimensionalization

Equations (3.5) through (3.8) are nondimensionalized using appropriate length, time, and velocity scales. The independent variables are nondimensionalized using the following formulas:

$$x = \frac{\bar{x}}{\bar{l}} , \quad y = \frac{\bar{y}}{\theta_{te}} , \quad z = \bar{z} \bar{\gamma} , \quad \text{and} \quad t = \frac{\bar{t} \bar{U}_\infty}{\bar{l}} \quad (3.9)$$

where the variables without overbars are dimensionless. The streamwise length scale  $\bar{l}$  is the length of the flat plate. In the transverse direction the length scale is  $\theta_{te}$  which is the momentum thickness of the wake at the trailing edge of the flat plate. The length scale that is used in the spanwise direction is  $1/\bar{\gamma}$  where  $\bar{\gamma}$  is the

spanwise wavenumber of the three-dimensional disturbance that results from the excitation at the inflow boundary. The time scale is the ratio of the streamwise length scale  $\bar{l}$  to the freestream velocity  $\bar{U}_\infty$ .

The dependent variables  $\bar{\mathbf{u}} = (\bar{u}, \bar{v}, \bar{w})$  and  $\bar{\boldsymbol{\omega}} = (\bar{\omega}_x, \bar{\omega}_y, \bar{\omega}_z)$  are nondimensionalized as follows:

$$u = \frac{\bar{u}}{\bar{U}_\infty} , \quad v = \frac{\bar{v}}{\bar{U}_\infty r_2} , \quad w = \frac{\bar{w}}{\bar{U}_\infty r_3} , \quad (3.10a)$$

and

$$\omega_x = \frac{\bar{\omega}_x \bar{\theta}_{te}}{\bar{U}_\infty} , \quad \omega_y = \frac{\bar{\omega}_y \bar{\theta}_{te}}{\bar{U}_\infty r_2} , \quad \omega_z = \frac{\bar{\omega}_z \bar{\theta}_{te}}{\bar{U}_\infty r_3} . \quad (3.10b)$$

The parameter  $r_2$  is the ratio of the transverse length scale  $\bar{\theta}_{te}$  to the streamwise length scale  $\bar{l}$ :  $r_2 = \bar{\theta}_{te}/\bar{l}$ . Similarly, the parameter  $r_3$  is the ratio of the spanwise length scale  $1/\bar{\gamma}$  to the streamwise length scale  $\bar{l}$ :  $r_3 = 1/(\bar{\gamma}\bar{l})$ .

With this nondimensionalization, equations (3.5) and (3.8) become

$$\frac{\partial \boldsymbol{\omega}}{\partial t} - \frac{1}{Re} \nabla^2 \boldsymbol{\omega} = \mathbf{f} \quad (3.11a)$$

and

$$\nabla^2 \mathbf{u} = \mathbf{g} \quad (3.11b)$$

which are solved for the six unknown variables  $\mathbf{u} = (u, v, w)$  and  $\boldsymbol{\omega} = (\omega_x, \omega_y, \omega_z)$  as functions of the dimensionless spatial position vector  $\mathbf{x} = (x, y, z)$  and dimensionless time  $t$ . The right hand side of equation (3.11a), the vector  $\mathbf{f} = (f_x, f_y, f_z)$ , is the dimensionless version of  $\boldsymbol{\omega} \cdot \nabla \mathbf{u} - \mathbf{u} \cdot \nabla \boldsymbol{\omega}$  which appears on the right hand side of equation (3.5). The three components of  $\mathbf{f}$  are

$$f_x = \omega_x \frac{\partial u}{\partial x} + \omega_y \frac{\partial u}{\partial y} + \omega_z \frac{\partial u}{\partial z} - u \frac{\partial \omega_x}{\partial x} - v \frac{\partial \omega_x}{\partial y} - w \frac{\partial \omega_x}{\partial z} , \quad (3.12a)$$

$$f_y = \omega_x \frac{\partial v}{\partial x} + \omega_y \frac{\partial v}{\partial y} + \omega_z \frac{\partial v}{\partial z} - u \frac{\partial \omega_y}{\partial x} - v \frac{\partial \omega_y}{\partial y} - w \frac{\partial \omega_y}{\partial z} , \quad (3.12b)$$

$$\text{and } f_z = \omega_x \frac{\partial w}{\partial x} + \omega_y \frac{\partial w}{\partial y} + \omega_z \frac{\partial w}{\partial z} - u \frac{\partial \omega_z}{\partial x} - v \frac{\partial \omega_z}{\partial y} - w \frac{\partial \omega_z}{\partial z} . \quad (3.12c)$$

The right hand side equation (3.11b), the vector  $\mathbf{g} = (g_x, g_y, g_z)$ , is the dimensionless version of  $\bar{\nabla} \times \bar{\omega}$  which appears in equation (3.8). The three components of  $\mathbf{g}$  are

$$g_x = \frac{r_3}{r_2^2} \frac{\partial \omega_z}{\partial y} - \frac{1}{r_3} \frac{\partial \omega_y}{\partial z}, \quad (3.13a)$$

$$g_y = \frac{1}{r_3 r_2^2} \frac{\partial \omega_x}{\partial z} - \frac{r_3}{r_2^2} \frac{\partial \omega_z}{\partial x}, \quad (3.13b)$$

$$\text{and } g_z = \frac{1}{r_3} \frac{\partial \omega_y}{\partial x} - \frac{1}{r_3 r_2^2} \frac{\partial \omega_x}{\partial y}. \quad (3.13c)$$

The dimensionless Laplacian has the form

$$\nabla^2 = \frac{\partial^2}{\partial x^2} + \frac{1}{r_2^2} \frac{\partial^2}{\partial y^2} + \frac{1}{r_3^2} \frac{\partial^2}{\partial z^2} \quad (3.14)$$

and the parameter  $Re$  is the Reynolds number  $Re = \frac{\bar{U}_\infty l}{\nu}$ .

Equations (3.11) serve as the basic equations for the simulations described in this work. Use of such a vorticity-velocity formulation for transition simulations was suggested by Fasel (1976) and used successfully for both two-dimensional (1976) and three-dimensional simulations of transition in boundary layers. The same formulation was also successfully employed by Pruett (1986) for two- and three-dimensional transition studies in free shear layers.

## CHAPTER 4

### BOUNDARY AND INITIAL CONDITIONS

The governing equations (3.11) represent a set of partial differential equations. This equation system is parabolic with respect to the time variable  $t$  and is elliptic with respect to the spatial variables  $x$ ,  $y$ , and  $z$ . Solution of equations (3.11) requires specification of suitable spatial and temporal domains. Furthermore, the unknown variables  $\omega$  and  $u$  must be specified at some initial time. Finally, boundary conditions must be specified along the entire boundary of the spatial domain.

#### 4.1 Spatial Domain

The governing equations are solved in a three-dimensional rectangular region in space that is downstream of the flat plate. The domain extends downstream from near the trailing edge of the plate and is assumed to extend in the streamwise direction for several disturbance wavelengths. The transverse thickness of the domain is assumed to be much wider than the vorticity disturbances that are present in the wake. The domain extends into the irrotational region of the flow field above and below the wake. The spanwise extent of the domain is equal to one nondimensional spanwise disturbance wavelength  $\lambda_z = 2\pi$ .

The spatial domain and coordinate system are shown in Figure 2.1. The  $x$  direction corresponds to the streamwise direction which is parallel to the freestream velocity  $\bar{U}_\infty$ . The transverse direction is denoted by the independent variable  $y$ . The third coordinate direction  $z$  corresponds to the spanwise direction and is parallel to the trailing edge of the flat plate. For convenience, the origin of the coordinate system is placed at the trailing edge of the flat plate. The spatial

domain extends in the streamwise direction from  $x_0$  to  $x_N$ , in the transverse direction from  $y_0$  to  $y_M$ , and in the spanwise direction from  $z = 0$  to  $z = 2\pi$ . The spatial domain is then given by

$$x_0 \leq x \leq x_N , \quad (4.1a)$$

$$y_0 \leq y \leq y_M , \quad (4.1b)$$

$$\text{and } 0 \leq z \leq 2\pi . \quad (4.1c)$$

#### 4.2 Temporal Domain

The time integration of the governing equations is divided into two separate procedures or steps. In the first step, the governing equations are solved to obtain the steady laminar wake that appears behind the flat plate. This is done by integrating the governing equations (3.11) with respect to time, subject to time-independent boundary conditions (no forcing), until a steady state solution is obtained. This calculation begins at an initial time  $t = t_{L_1} < 0$  for which initial values of the dependent variables  $u(x, y, z, t_{L_1})$  and  $\omega(x, y, z, t_{L_1})$  are specified. The calculation ends at time  $t = 0$ , at which time the steady solution is obtained. This steady wake is referred to as the base flow.

In the second step of the calculation, the response of the wake to time-dependent excitations that are introduced at the inflow boundary is investigated. The governing equations are integrated in time from  $t = 0$  to  $t = t_{L_2}$ . The initial values of the dependent variables at time  $t = 0$  are given by the base flow.

#### 4.3 Boundary and Initial Conditions for the Undisturbed Flow

The undisturbed wake is assumed to be two-dimensional, so that

$$w(x, y, z, t) = \omega_x(x, y, z, t) = \omega_y(x, y, z, t) = 0 . \quad (4.2)$$

The remaining flow variables  $u(x, y, z, t)$ ,  $v(x, y, z, t)$ , and  $\omega_z(x, y, z, t)$  are solutions of the governing equations (3.11). Restricted to two-dimensional flows, the governing equations become

$$\frac{\partial \omega_z}{\partial t} + u \frac{\partial \omega_z}{\partial x} + v \frac{\partial \omega_z}{\partial y} = \frac{1}{Re} \left( \frac{\partial^2 \omega_z}{\partial x^2} + \frac{1}{r_2^2} \frac{\partial^2 \omega_z}{\partial y^2} \right) , \quad (4.3a)$$

$$\frac{\partial^2 u}{\partial x^2} + \frac{1}{r_2^2} \frac{\partial^2 u}{\partial y^2} = \frac{r_3}{r_2^2} \frac{\partial \omega_z}{\partial y} , \quad (4.3b)$$

$$\text{and } \frac{\partial^2 v}{\partial x^2} + \frac{1}{r_2^2} \frac{\partial^2 v}{\partial y^2} = -\frac{r_3}{r_2^2} \frac{\partial \omega_z}{\partial x} . \quad (4.3c)$$

Because the base flow is two-dimensional, the spatial domain reduces from a three-dimensional region to a two-dimensional plane that is perpendicular to the  $z$  axis. Boundary conditions for the unknown variables  $u$ ,  $v$ , and  $\omega_z$  need to be specified along the boundaries of this plane. These boundary conditions are independent of time and are chosen such that the solution of equations (4.3) represents a laminar, high-deficit, flat plate wake.

#### Inflow Boundary ( $x = x_0$ )

The inflow boundary of the spatial domain is located downstream of the flat plate trailing edge. Therefore, the velocity and vorticity distributions at this boundary should correspond to those of a spatially-developing, high-deficit wake. For most of the calculations in this work, a Gaussian distribution is used to represent the streamwise velocity at the inflow boundary. The Gaussian distribution compares reasonably well to experimentally obtained streamwise velocity profiles (Sato and Kuriki, 1961). In a few other calculations, a hyperbolic secant function is used to represent the inflow streamwise velocity. The hyperbolic secant distribution also compares reasonable well with experimentally obtained streamwise velocity profiles (Mattingly and Criminale, 1972)

With the use of either a Gaussian distribution or a hyperbolic secant distribution, the streamwise velocity is then known as a function of  $y$  at the inflow boundary. However, since the  $x$  dependence of the streamwise velocity is unknown, being given by the solution of the Navier-Stokes equations, the transverse velocity cannot be related to the streamwise velocity using the continuity equation (3.2). Instead,  $v$  must be given an arbitrary value. In this work, the Reynolds number of the wake  $Re = \frac{U_\infty l}{\nu}$  is large. Therefore, except for very near the flat plate trailing edge, the transverse velocity is much smaller than the streamwise velocity and can be set to zero at the inflow boundary with reasonable accuracy.

For the base flow calculation, the inflow boundary condition is

$$u(x_0, y, z, t) = u^I(y) , \quad (4.4a)$$

$$v(x_0, y, z, t) = 0 , \quad (4.4b)$$

$$\text{and } \omega_z(x_0, y, z, t) = \omega_z^I(y) \quad (4.4c)$$

where the superscript  $( )^I$  refers to the fact that the functions  $u^I(y)$  and  $\omega_z^I(y)$  are the streamwise velocity and spanwise vorticity distributions at the inflow boundary. If the streamwise velocity is specified to have a Gaussian distribution, then  $u^I(y)$  is given by

$$u^I(y) = 1 - (1 - U_c)e^{-\sigma y^2} \quad (4.5a)$$

where

$$\sigma = \frac{\ln(2)}{b^2} . \quad (4.5b)$$

Alternatively,  $u^I(y)$  can be given by

$$u^I(y) = 1 - (1 - U_c)\operatorname{sech}^2(\sigma y) \quad (4.6a)$$

where

$$\sigma = \frac{\operatorname{arccosh}(\sqrt{2})}{b^2} . \quad (4.6b)$$

The spanwise vorticity is given by

$$\omega_z^I(y) = \frac{du^I(y)}{dy} . \quad (4.7)$$

In equations (4.5) and (4.6),  $U_c$  is the centerline velocity of the wake at the inflow boundary and  $b$  is the wake half-width at the inflow boundary. The parameters  $U_c$  and  $b$  are chosen so that the resulting base flow closely models the high-deficit wakes observed in experiments.

#### Outflow Boundary ( $x = x_N$ )

For spatially-developing wakes, a proper outflow boundary condition is not easily found since the flow condition at this location would be obtained by the solution of the governing equations and is therefore not known *a priori*. However, it is possible to determine an outflow boundary condition without requiring advance knowledge of the solution. Suppose the two-dimensional version of equations (3.5) and (3.8) are nondimensionalized using the boundary layer scaling

$$x = \frac{\bar{x}}{\bar{l}}, \quad y = \frac{\bar{y}}{\bar{l}} Re^{\frac{1}{2}}, \quad u = \frac{\bar{u}}{\bar{U}_\infty}, \quad v = \frac{\bar{v}}{\bar{U}_\infty} Re^{\frac{1}{2}}, \quad \text{and} \quad \omega_z = \frac{\bar{\omega}_z \bar{l}}{\bar{U}_\infty Re^{\frac{1}{2}}} . \quad (4.8)$$

The parameters  $\bar{l}$ ,  $\bar{U}_\infty$ , and  $Re$  are defined in section 3.2. The resulting dimensionless equations, for steady flow, are

$$u \frac{\partial \omega_z}{\partial x} + v \frac{\partial \omega_z}{\partial y} = \frac{1}{Re} \frac{\partial^2 \omega_z}{\partial x^2} + \frac{\partial^2 \omega_z}{\partial y^2} , \quad (4.9a)$$

$$\frac{1}{Re} \frac{\partial^2 u}{\partial x^2} + \frac{\partial^2 u}{\partial y^2} = \frac{\partial \omega_z}{\partial y} , \quad (4.9b)$$

$$\text{and} \quad \frac{1}{Re} \frac{\partial^2 v}{\partial x^2} + \frac{\partial^2 v}{\partial y^2} = -\frac{\partial \omega_z}{\partial x} . \quad (4.9c)$$

For high Reynolds number flows  $Re \gg 1$ , as in these investigations, the streamwise diffusion term is the smallest term in each of the three equations (4.9a) through (4.9c). Therefore, the streamwise diffusion terms are set equal to zero, resulting in the outflow boundary conditions

$$\frac{\partial^2 u}{\partial x^2}(x_N, y, z, t) = 0 , \quad (4.10a)$$

$$\frac{\partial^2 v}{\partial x^2}(x_N, y, z, t) = 0 , \quad (4.10b)$$

$$\text{and } \frac{\partial^2 \omega_z}{\partial x^2}(x_N, y, z, t) = 0 . \quad (4.10c)$$

These boundary conditions were first proposed by Fasel (1976).

#### Freestream Boundaries ( $y = y_0$ ) and ( $y = y_M$ )

As stated previously, the base flow is assumed to be a high Reynolds number flow. Therefore, the rotational part of the wake is confined to a region very near to its centerline and the streamwise velocity rapidly approaches its freestream value as  $y \rightarrow \pm\infty$ . The boundary conditions that satisfy these assumptions are, for the lower freestream boundary,

$$u(x, y_0, z, t) = 1 , \quad (4.11a)$$

$$\frac{\partial v}{\partial y}(x, y_0, z, t) = 0 , \quad (4.11b)$$

$$\text{and } \omega_z(x, y_0, z, t) = 0 . \quad (4.11c)$$

Similarly, for the upper freestream boundary:

$$u(x, y_M, z, t) = 1 , \quad (4.12a)$$

$$\frac{\partial v}{\partial y}(x, y_M, z, t) = 0 , \quad (4.12b)$$

$$\text{and } \omega_z(x, y_M, z, t) = 0 . \quad (4.12c)$$

Equations (4.11b) and (4.12b) follow directly from the conditions (4.11a) and (4.12a) using the continuity equation.

#### Auxiliary Condition ( $y = 0$ )

The boundary conditions described up to this point are sufficient to ensure the uniqueness of the solution of the vorticity equation (4.3a) and the Poisson equation for the streamwise velocity, equation (4.3b). However, these boundary conditions are not sufficient to ensure the uniqueness of solutions of the transverse velocity equation (4.3c). This was shown by Pruett (1986) who notes that if a function  $V(x, y)$  is a solution of equation (4.3c), subject to the boundary conditions described previously in this section, then the function

$$V(x, y) + c(x - x_0) \quad (4.13)$$

where  $c$  is a constant, is also a solution of equation (4.3c). Therefore, an infinite number of solutions satisfy equation (4.3c) and the boundary conditions described in this section.

Therefore, an additional condition has to be specified that will ensure that the solution of equation (4.3c) is unique. Experimental evidence indicates that the steady streamwise velocity is symmetric with respect to the wake centerline ( $y = 0$ ). Therefore, the transverse velocity  $v$  is antisymmetric with respect to the wake centerline ( $y = 0$ ) and is equal to zero at the centerline. The transverse velocity  $v$  is therefore required to satisfy the condition

$$v(x, 0, z, t) = 0 \quad (4.14)$$

at the wake centerline.

### Initial Conditions ( $t = t_{L_1}$ )

This calculation starts at time  $t = t_{L_1}$ , for which initial values of the unknown variables  $u$ ,  $v$ , and  $\omega_z$  are specified. In this work, the initial conditions are chosen such that the flow profile is independent of  $x$  and is identical to that of the inflow boundary. These conditions are

$$u(x, y, z, t_{L_1}) = u^I(y) , \quad (4.15a)$$

$$v(x, y, z, t_{L_1}) = 0 , \quad (4.15b)$$

$$\text{and } \omega_z(x, y, z, t_{L_1}) = \omega_z^I(y) . \quad (4.15c)$$

### 4.4 Boundary and Initial Conditions for the Disturbed Flow

For calculations of the disturbed flow, which may be three-dimensional, boundary conditions have to be specified for all boundaries of the three-dimensional domain.

#### Inflow Boundary ( $x = x_0$ )

In a physical experiment, disturbances in wakes may originate from a variety of sources. Wake disturbances may arise from freestream turbulence, roughness on the flat plate, sound, etc. Disturbances can also be artificially introduced into wakes through loudspeakers, flaps at the plate trailing edge, or through heater strips on the plate. In this work, the disturbances are introduced at the inflow boundary. For this purpose, solutions of the Orr-Sommerfeld equation are used.

Thus, the velocity and vorticity components at the inflow boundary are a combination of those of the steady base flow discussed in the previous section and of time varying components that then excite the disturbances in the wake. The inflow boundary conditions are of the form

$$u(x_0, y, z, t) = u_{ss}(x_0, y) + P_u^{2d}(x_0, y, t) + P_u^{3d}(x_0, y, t)\cos(z) , \quad (4.16a)$$

$$v(x_0, y, z, t) = 0 + P_v^{2d}(x_0, y, t) + P_v^{3d}(x_0, y, t)\cos(z), \quad (4.16b)$$

$$w(x_0, y, z, t) = 0 + P_w^{3d}(x_0, y, t)\cos(z), \quad (4.16c)$$

$$\omega_z(x_0, y, z, t) = 0 + P_{\omega_z}^{3d}(x_0, y, t)\cos(z), \quad (4.16d)$$

$$\omega_y(x_0, y, z, t) = 0 + P_{\omega_y}^{3d}(x_0, y, t)\cos(z), \quad (4.16e)$$

$$\text{and } \omega_z(x_0, y, z, t) = \omega_{zSS}(x_0, y) + P_{\omega_z}^{2d}(x_0, y, t) + P_{\omega_z}^{3d}(x_0, y, t)\cos(z). \quad (4.16f)$$

The functions  $u_{SS}(x_0, y)$  and  $\omega_{zSS}(x_0, y)$  are the streamwise velocity and spanwise vorticity components of the base flow at the inflow boundary. The functions  $P_u^{2d}(x_0, y, t)$ ,  $P_v^{2d}(x_0, y, t)$ , and  $P_{\omega_z}^{2d}(x_0, y, t)$  are two-dimensional disturbances obtained from the Orr-Sommerfeld equation. These functions are

$$P_u^{2d}(x_0, y, t) = r(t)A_2 u_A^{2d}(y)\cos(\alpha_r^{2d}x_0 - \beta t + \phi_u^{2d}(y)), \quad (4.17a)$$

$$P_v^{2d}(x_0, y, t) = r(t)A_2 v_A^{2d}(y)\cos(\alpha_r^{2d}x_0 - \beta t + \phi_v^{2d}(y)), \quad (4.17b)$$

$$\text{and } P_{\omega_z}^{2d}(x_0, y, t) = r(t)A_2 \omega_{zA}^{2d}(y)\cos(\alpha_r^{2d}x_0 - \beta t + \phi_{\omega_z}^{2d}(y)). \quad (4.17c)$$

The functions  $P_u^{3d}(x_0, y, t)$ ,  $P_v^{3d}(x_0, y, t)$ ,  $P_w^{3d}(x_0, y, t)$ ,  $P_{\omega_z}^{3d}(x_0, y, t)$ ,  $P_{\omega_y}^{3d}(x_0, y, t)$ , and  $P_{\omega_z}^{3d}(x_0, y, t)$  are three-dimensional disturbances obtained from the three-dimensional Orr-Sommerfeld equation. These functions are

$$P_u^{3d}(x_0, y, t) = r(t)A_3 u_A^{3d}(y)\cos(\alpha_r^{3d}x_0 - \beta t + \phi_u^{3d}(y)), \quad (4.18a)$$

$$P_v^{3d}(x_0, y, t) = r(t)A_3 v_A^{3d}(y)\cos(\alpha_r^{3d}x_0 - \beta t + \phi_v^{3d}(y)), \quad (4.18b)$$

$$P_w^{3d}(x_0, y, t) = r(t)A_3 w_A^{3d}(y)\cos(\alpha_r^{3d}x_0 - \beta t + \phi_w^{3d}(y)), \quad (4.18c)$$

$$P_{\omega_z}^{3d}(x_0, y, t) = r(t)A_3 \omega_{zA}^{3d}(y)\cos(\alpha_r^{3d}x_0 - \beta t + \phi_{\omega_z}^{3d}(y)), \quad (4.18d)$$

$$P_{\omega_y}^{3d}(x_0, y, t) = r(t)A_3 \omega_{yA}^{3d}(y)\cos(\alpha_r^{3d}x_0 - \beta t + \phi_{\omega_y}^{3d}(y)), \quad (4.18e)$$

$$\text{and } P_{\omega_z}^{3d}(x_0, y, t) = r(t)A_3 \omega_{zA}^{3d}(y)\cos(\alpha_r^{3d}x_0 - \beta t + \phi_{\omega_z}^{3d}(y)). \quad (4.18f)$$

For the three-dimensional disturbances, a superposition of two oblique waves of equal and opposite spanwise wavenumbers is used.

In the preceding paragraph, the parameter  $\alpha_r^{2d}$  was the real part of the eigenvalue of the two-dimensional Orr-Sommerfeld equation corresponding to the frequency  $\beta$ . The parameter  $\alpha_r^{3d}$  was the real part of the eigenvalue of the three-dimensional Orr-Sommerfeld equation corresponding to the frequency  $\beta$  and the nondimensional spanwise wavenumber  $\gamma = 1$ . The functions  $(u_A^{2d}(y), \phi_u^{2d}(y))$ ,  $(v_A^{2d}(y), \phi_v^{2d}(y))$ , and  $(\omega_z A^{2d}(y), \phi_{\omega_z}^{2d}(y))$  are the amplitudes and phases of the eigenfunction of the two-dimensional Orr-Sommerfeld equation corresponding to the frequency  $\beta$ . The functions  $(u_A^{3d}(y), \phi_u^{3d}(y))$ ,  $(v_A^{3d}(y), \phi_v^{3d}(y))$ ,  $(w_A^{3d}(y), \phi_w^{3d}(y))$ ,  $(\omega_x A^{3d}(y), \phi_{\omega_x}^{3d}(y))$ ,  $(\omega_y A^{3d}(y), \phi_{\omega_y}^{3d}(y))$ , and  $(\omega_z A^{3d}(y), \phi_{\omega_z}^{3d}(y))$  are the amplitudes and phases of the eigenfunction of the three-dimensional Orr-Sommerfeld equation corresponding to the frequency  $\beta$  and the nondimensional spanwise wavenumber  $\gamma = 1$ . Both the two-dimensional and the three-dimensional eigensolutions correspond to the streamwise location  $x_0$  at which the steady streamwise velocity distribution is  $u_{SS}(x_0, y)$ . The amplitude of the disturbances at the inflow boundary is controlled by the parameters  $A_2$  and  $A_3$ . The solution procedure used to obtain eigensolutions of the Orr-Sommerfeld equation is discussed in Appendix A.

The function  $r(t)$  that appears in equations (4.17) and (4.18) is chosen to minimize any transient disturbance that might arise when the excitation is initiated. The function  $r(t)$  has the values

$$r(t) = \begin{cases} \sin^2(\frac{\beta t}{2}), & \text{if } 0 \leq t < \pi/\beta; \\ 1, & \text{if } t \geq \pi/\beta. \end{cases} \quad (4.19)$$

#### Outflow Boundary ( $x = x_N$ )

For numerical simulations of spatially-amplifying disturbances in shear flows, the specification of appropriate outflow boundary conditions represents a major

difficulty. Numerical simulations of spatially-periodic, temporally amplifying disturbances avoid this problem because then periodic inflow-outflow boundary conditions can be employed.

For the numerical simulation of two-dimensional, spatially-amplifying, small-amplitude disturbances in a flat plate boundary layer, Fasel (1976) employed the condition

$$\frac{\partial^2 u'}{\partial x^2} = -\alpha_r^2 u' \quad (4.20)$$

at the outflow boundary. In equation (4.20),  $u' = u - u_{ss}$  is the streamwise perturbation velocity and  $\alpha_r$  is the real part of the disturbance wavenumber. Similar conditions were used for the other flow variables. In Fasel's numerical simulations, the boundary condition (4.20) allowed small-amplitude disturbances to pass unreflected through the outflow boundary. However, equation (4.20) is formally exact only for small amplitude neutrally stable disturbances. Therefore, while equation (4.20) is a suitable approximation for the slowly amplifying disturbances that are observed in flat plate boundary layers, it is definitely not appropriate when disturbances are highly amplified, as in high-deficit wakes.

Pruett (1986) attempted to use outflow boundary conditions that were similar to equation (4.20) for the simulation of spatially-amplifying disturbances in free shear layers. However, as Pruett notes, amplification rates are quite large in free shear layers, and therefore the previous condition is not valid. Pruett found that boundary conditions similar to equation (4.20) allowed the fundamental disturbance component to pass through the boundary unreflected, but reflected any nonlinearly generated harmonics of the fundamental fluctuation.

As an alternative to boundary conditions such as equation (4.20), Pruett employed a moving outflow boundary for his calculations. The moving outflow

boundary is implemented in the following manner. First, the base flow is computed in the entire spatial domain for which  $x_0 \leq x \leq x_N$ . Then, the disturbed flow is calculated in a smaller subset of the spatial domain bounded by  $x = x_0$  and  $x = x_{MB}(t) < x_N$  where  $x = x_{MB}(t)$  is the instantaneous location of the moving boundary. The moving boundary is initially located at a specified distance downstream of the inflow boundary. As the calculation progresses and the disturbances propagate downstream, the moving boundary propagates downstream ahead of the disturbances so that the flow remains undisturbed at this boundary. As a consequence, Dirichlet boundary conditions that enforce an undisturbed flow can be employed at the location of the moving boundary. When the moving boundary reaches the fixed outflow boundary at  $x = x_N$ , the calculation is stopped.

For the present simulations, boundary conditions similar to those used by Pruett are employed. However, instead of using a moving outflow boundary, the undisturbed flow condition is enforced at the outflow boundary located at  $x = x_N$ . The disturbed flow is then calculated in the entire spatial domain. Furthermore, the domain is specified to be large enough so that the disturbances do not reach the outflow boundary before the calculation is stopped. The resulting boundary conditions are

$$u(x_N, y, z, t) = u_{SS}(x_N, y) , \quad (4.21a)$$

$$v(x_N, y, z, t) = v_{SS}(x_N, y) , \quad (4.21b)$$

$$w(x_N, y, z, t) = 0 , \quad (4.21c)$$

$$\omega_z(x_N, y, z, t) = 0 , \quad (4.21d)$$

$$\omega_y(x_N, y, z, t) = 0 , \quad (4.21e)$$

$$\text{and } \omega_z(x_N, y, z, t) = \omega_{zSS}(x_N, y) . \quad (4.21f)$$

As before, the subscript ( )<sub>SS</sub> denotes the steady state wake or base flow.

Freestream Boundaries ( $y = y_0$ ) and ( $y = y_M$ )

The freestream boundary conditions are based on the assumption that disturbances at these locations decay exponentially at rates predicted by linear stability theory. These boundary conditions are now derived.

An equation for the streamwise perturbation velocity  $u' = u - u_{SS}$  can be obtained by subtracting the base flow streamwise velocity equation (4.3b) from the streamwise component of equation (3.11b). The resulting equation is

$$\frac{\partial^2 u'}{\partial x^2} + \frac{1}{r_2^2} \frac{\partial^2 u'}{\partial y^2} + \frac{1}{r_3^2} \frac{\partial^2 u'}{\partial z^2} = \frac{r_3}{r_2^2} \frac{\partial \omega_z'}{\partial y} - \frac{1}{r_3} \frac{\partial \omega_y}{\partial z} \quad (4.22)$$

where the spanwise perturbation vorticity  $\omega_z - \omega_{zSS}$  is denoted by  $\omega_z'$ . Assuming that the velocity and vorticity fluctuations at the freestream boundaries are described by linear stability theory, then

$$u'(x, y, z, t) = \text{Real}(\hat{u}(y)e^{i(\alpha x + z - \beta t)}) \quad (4.23)$$

and analogous formulas are valid for the other velocity and vorticity components.

Then, from Squire's equation

$$\hat{\omega}_y'' - (\alpha^2 + 1 + i\alpha Re(U - c)) \hat{\omega}_y = -i Re U' \hat{v} \quad (4.24)$$

it can be shown that for  $Re \gg 1$ ,  $\hat{\omega}_y \simeq 0$  for  $|y| \gg 1$ . Furthermore, from the continuity equation and the definition of  $\hat{\omega}_x$  and  $\hat{\omega}_z$ , it can also be shown that for velocity fluctuations that decay exponentially when  $|y| \gg 1$ , then  $\hat{\omega}_x \simeq 0$  and  $\hat{\omega}_z \simeq 0$  for  $|y| \gg 1$ . Combining equation (4.22) with equation (4.23), and assuming that the vorticity fluctuations are negligible for large  $|y|$ , then the equation

$$\frac{\partial^2 \hat{u}(y)}{\partial y^2}(y) = r_2^2 \left( \alpha_r^2 + \frac{1}{r_3^2} \right) \hat{u}(y) \quad (4.25)$$

is valid if the disturbance is assumed to neutrally stable ( $\alpha_i = 0$ ). In reality however, wake disturbances are usually highly amplified and therefore equation (4.25) is not strictly applicable. However, for the calculations presented in this work, the assumption of neutrally stable disturbances at the freestream boundaries did not prove detrimental. Equation (4.25) has the solution

$$\hat{u}(y) = Ae^{yr_2} \sqrt{\alpha_r^2 + \frac{1}{r_3^2}} + Be^{-yr_2} \sqrt{\alpha_r^2 + \frac{1}{r_3^2}} . \quad (4.26)$$

Assuming that  $\hat{u}(y)$  is finite for all  $y$ , then for  $y \rightarrow -\infty$ ,  $B = 0$  and  $\hat{u}(y)$  satisfies the differential equation

$$\frac{d\hat{u}(y)}{dy} = r_2 \sqrt{\alpha_r^2 + \frac{1}{r_3^2}} \hat{u}(y) . \quad (4.27)$$

Combining equation (4.27) with equation (4.23) results in the following boundary condition for the streamwise perturbation velocity  $u'(x, y, z, t)$  at  $y = y_0$ :

$$\frac{\partial u'}{\partial y}(x, y_0, z, t) = r_2 \sqrt{\alpha_r^2 + \frac{1}{r_3^2}} u'(x, y_0, z, t) . \quad (4.28)$$

Similarly, the boundary condition at  $y = y_M$  is

$$\frac{\partial u'}{\partial y}(x, y_M, z, t) = -r_2 \sqrt{\alpha_r^2 + \frac{1}{r_3^2}} u'(x, y_M, z, t) . \quad (4.29)$$

In a similar manner, the following boundary conditions for the spanwise velocity  $w$  are obtained:

$$\frac{\partial w}{\partial y}(x, y_0, z, t) = r_2 \sqrt{\alpha_r^2 + \frac{1}{r_3^2}} w(x, y_0, z, t) \quad (4.30a)$$

and

$$\frac{\partial w}{\partial y}(x, y_M, z, t) = -r_2 \sqrt{\alpha_r^2 + \frac{1}{r_3^2}} w(x, y_M, z, t) . \quad (4.30b)$$

Boundary conditions for the transverse velocity  $v$  are obtained from the continuity equation. These boundary conditions are

$$\frac{\partial v}{\partial y}(x, y_0, z, t) = -\frac{\partial u}{\partial x}(x, y_0, z, t) - \frac{\partial w}{\partial z}(x, y_0, z, t) \quad (4.31a)$$

and

$$\frac{\partial v}{\partial y}(x, y_M, z, t) = -\frac{\partial u}{\partial x}(x, y_M, z, t) - \frac{\partial w}{\partial z}(x, y_M, z, t) . \quad (4.31b)$$

The vorticity at both freestream boundaries is assumed to be zero. At the lower boundary ( $y = y_0$ )

$$\omega_x(x, y_0, z, t) = 0 , \quad (4.32a)$$

$$\omega_y(x, y_0, z, t) = 0 , \quad (4.32b)$$

$$\omega_z(x, y_0, z, t) = 0 \quad (4.32c)$$

and at the upper boundary ( $y = y_M$ )

$$\omega_x(x, y_M, z, t) = 0 , \quad (4.33a)$$

$$\omega_y(x, y_M, z, t) = 0 , \quad (4.33b)$$

$$\omega_z(x, y_M, z, t) = 0 . \quad (4.33c)$$

One further consideration is the form of the coefficient  $r_2 \sqrt{\alpha_r^2 + \frac{1}{r_3^2}}$  in equations (4.28), (4.29), and (4.30). These boundary conditions were derived based on the assumption of three-dimensional disturbances for which  $\alpha_r = \alpha_r^{3d}$  and for which the coefficient  $r_2 \sqrt{\alpha_r^2 + \frac{1}{r_3^2}}$  becomes  $r_2 \sqrt{\alpha_r^{3d2} + \frac{1}{r_3^2}}$ . For two-dimensional disturbances, the coefficient  $r_2 \sqrt{\alpha_r^2 + \frac{1}{r_3^2}}$  becomes simply  $\alpha_r^{2d} r_2$ . When both two-dimensional and three-dimensional disturbances are present in the wake it is not

obvious whether  $r_2 \sqrt{\alpha_r^2 + \frac{1}{r_3^2}}$  should be set equal to  $\alpha_r^{2d} r_2$  or  $r_2 \sqrt{\alpha_r^{3d^2} + \frac{1}{r_3^2}}$ . This difficulty is resolved by decomposing the boundary conditions (4.28), (4.29), and (4.30) into two-dimensional and three-dimensional components. Then, for the two-dimensional component of equations (4.28), (4.29), and (4.30),  $r_2 \sqrt{\alpha_r^2 + \frac{1}{r_3^2}}$  is set equal to  $\alpha_r^{2d} r_2$ . For the three-dimensional component of equations (4.28), (4.29), and (4.30),  $r_2 \sqrt{\alpha_r^2 + \frac{1}{r_3^2}}$  is set equal to  $r_2 \sqrt{\alpha_r^{3d^2} + \frac{1}{r_3^2}}$ . This decomposition will be discussed further in the next chapter.

#### Lateral Boundaries ( $z = 0$ ) and ( $z = 2\pi$ )

As discussed in section 4.1, the spanwise width of the spatial domain is equal to one spanwise wavelength  $\lambda_z = 2\pi$ . Therefore, periodic lateral boundary conditions are employed. These boundary conditions for the  $u$  component are

$$u(x, y, 0, t) = u(x, y, 2\pi, t) , \quad (4.34)$$

with analogous conditions for all other variables.

#### Initial Conditions ( $t = 0$ )

This calculation starts at time  $t = 0$ . At this time an undisturbed flow is assumed and therefore the flow variables are set equal to the values of the previously computed base flow. Thus

$$u(x, y, z, 0) = u_{SS}(x, y) , \quad (4.35a)$$

$$v(x, y, z, 0) = v_{SS}(x, y) , \quad (4.35b)$$

$$w(x, y, z, 0) = 0 , \quad (4.35c)$$

$$\omega_x(x, y, z, 0) = 0 , \quad (4.35d)$$

$$\omega_y(x, y, z, 0) = 0 , \quad (4.35e)$$

$$\text{and } \omega_z(x, y, z, 0) = \omega_{zSS}(x, y) . \quad (4.35f)$$

## CHAPTER 5

### NUMERICAL METHOD

The governing equations (3.11) together with the boundary and initial conditions described in the previous chapter are solved using a combination of spectral and finite-difference methods. Fourier series are used to represent the spanwise variation of the dependent variables. Spatial derivatives in the streamwise and transverse direction are approximated using second-order finite-differences. The vorticity equation (3.11a) is numerically integrated in time using a combination of an Alternating-Direction-Implicit (ADI) method, the Crank-Nicolson method, and the second-order Adams-Basforth method. The nonlinear terms are computed spectrally at each time step. The discretized Helmholtz equations are solved using fast Helmholtz Solvers. The numerical method discussed here is based on the work of Pruett (1986).

#### 5.1 Spanwise Spectral Approximation

As discussed in Chapter 4, the disturbance flow is assumed to be periodic in the spanwise direction with wavelength  $\lambda_z = 2\pi$ . Because of this spanwise periodicity, the streamwise velocity can be represented by a truncated Fourier series of the form

$$u(x, y, z, t) \approx \sum_{k=-\frac{N}{2}}^{\frac{N}{2}} U^k(x, y, t) e^{ikz} \quad (5.1)$$

with analogous Fourier representations for the other flow variables. The Fourier coefficients  $U^k$ ,  $V^k$ ,  $W^k$ ,  $\Omega_x^k$ ,  $\Omega_y^k$ , and  $\Omega_z^k$  are functions of the two spatial variables  $x$  and  $y$  and the time variable  $t$ . The Fourier coefficients can be rewritten as the vectors

$$\mathbf{U}^k = (U^k, V^k, W^k) \quad (5.2a)$$

$$\text{and } \Omega^k = (\Omega_x^k, \Omega_y^k, \Omega_z^k) \quad (5.2a)$$

which are the Fourier representations of the velocity vector  $\mathbf{u} = (u, v, w)$  and the vorticity vector  $\boldsymbol{\omega} = (\omega_x, \omega_y, \omega_z)$ . Furthermore, because the physical variables  $\mathbf{u} = (u, v, w)$  and  $\boldsymbol{\omega} = (\omega_x, \omega_y, \omega_z)$  are real numbers, the Fourier coefficients satisfy the relations

$$\mathbf{U}^k(x, y, t) = \tilde{\mathbf{U}}^{-k}(x, y, t) \quad (5.3a)$$

$$\text{and } \boldsymbol{\Omega}^k(x, y, t) = \tilde{\boldsymbol{\Omega}}^{-k}(x, y, t) \quad (5.3b)$$

where  $\sim$  denotes the conjugate of a complex number. Equations (5.3) are valid for all values of  $k$ .

In the governing equations (3.11), the physical variables are replaced by their Fourier representations given by equation (5.1). Orthogonality of the exponential functions  $e^{ikz}$  in the spanwise interval  $0 \leq z \leq 2\pi$  decouples the three-dimensional governing equations into  $\frac{K}{2} + 1$  sets of two-dimensional equations of the form

$$\frac{\partial \Omega_x^k}{\partial t} - \frac{1}{Re} \left( \frac{\partial^2 \Omega_x^k}{\partial x^2} + \frac{1}{r_2^2} \frac{\partial^2 \Omega_x^k}{\partial y^2} - \left( \frac{k}{r_3} \right)^2 \Omega_x^k \right) = F_x^k \quad , \quad (5.4a)$$

$$\frac{\partial \Omega_y^k}{\partial t} - \frac{1}{Re} \left( \frac{\partial^2 \Omega_y^k}{\partial x^2} + \frac{1}{r_2^2} \frac{\partial^2 \Omega_y^k}{\partial y^2} - \left( \frac{k}{r_3} \right)^2 \Omega_y^k \right) = F_y^k \quad , \quad (5.4b)$$

$$\frac{\partial \Omega_z^k}{\partial t} - \frac{1}{Re} \left( \frac{\partial^2 \Omega_z^k}{\partial x^2} + \frac{1}{r_2^2} \frac{\partial^2 \Omega_z^k}{\partial y^2} - \left( \frac{k}{r_3} \right)^2 \Omega_z^k \right) = F_z^k \quad , \quad (5.4c)$$

$$\frac{\partial^2 U^k}{\partial x^2} + \frac{1}{r_2^2} \frac{\partial^2 U^k}{\partial y^2} - \left( \frac{k}{r_3} \right)^2 U^k = G_x^k \quad , \quad (5.4d)$$

$$\frac{\partial^2 V^k}{\partial x^2} + \frac{1}{r_2^2} \frac{\partial^2 V^k}{\partial y^2} - \left( \frac{k}{r_3} \right)^2 V^k = G_y^k \quad , \quad (5.4e)$$

$$\frac{\partial^2 W^k}{\partial x^2} + \frac{1}{r_2^2} \frac{\partial^2 W^k}{\partial y^2} - \left( \frac{k}{r_3} \right)^2 W^k = G_z^k \quad . \quad (5.4f)$$

Equations (5.4) are solved for  $0 \leq k \leq \frac{K}{2}$  to obtain the complete set of Fourier coefficients. The Fourier coefficients for which  $k < 0$  are obtained from equations

(5.3). Once the Fourier coefficients are obtained from equations (5.4), the physical variables  $u$  and  $\omega$  can be reconstructed using equations (5.1).

The functions  $F_x^k$ ,  $F_y^k$ , and  $F_z^k$  are Fourier representations of the nonlinear terms  $f_x$ ,  $f_y$ , and  $f_z$ . These functions are related by the expressions

$$f_x(x, y, z, t) \simeq \sum_{k=-\frac{K}{2}}^{\frac{K}{2}} F_x^k(x, y, t) e^{ikz} , \quad (5.5a)$$

$$f_y(x, y, z, t) \simeq \sum_{k=-\frac{K}{2}}^{\frac{K}{2}} F_y^k(x, y, t) e^{ikz} , \quad (5.5b)$$

$$\text{and } f_z(x, y, z, t) \simeq \sum_{k=-\frac{K}{2}}^{\frac{K}{2}} F_z^k(x, y, t) e^{ikz} . \quad (5.5c)$$

The functions  $f_x$ ,  $f_y$ , and  $f_z$  are defined by equations (3.12).

The functions  $G_x^k$ ,  $G_y^k$ , and  $G_z^k$  are Fourier representations of  $g_x$ ,  $g_y$ , and  $g_z$ . These functions are related by the expressions

$$g_x(x, y, z, t) \simeq \sum_{k=-\frac{K}{2}}^{\frac{K}{2}} G_x^k(x, y, t) e^{ikz} , \quad (5.6a)$$

$$g_y(x, y, z, t) \simeq \sum_{k=-\frac{K}{2}}^{\frac{K}{2}} G_y^k(x, y, t) e^{ikz} , \quad (5.6b)$$

$$\text{and } g_z(x, y, z, t) \simeq \sum_{k=-\frac{K}{2}}^{\frac{K}{2}} G_z^k(x, y, t) e^{ikz} . \quad (5.6c)$$

The functions  $g_x$ ,  $g_y$ , and  $g_z$  are defined by equations (3.13). The functions  $G_x^k$ ,  $G_y^k$ , and  $G_z^k$  have the simple form

$$G_x^k = \frac{r_3}{r_2^2} \frac{\partial \Omega_z^k}{\partial y} - \frac{ik}{r_3} \Omega_y^k , \quad (5.7a)$$

$$G_y^k = \frac{ik}{r_3 r_2^2} \Omega_z^k - \frac{r_3}{r_2^2} \frac{\partial \Omega_z^k}{\partial x} , \quad (5.7b)$$

$$\text{and } G_z^k = \frac{1}{r_3} \frac{\partial \Omega_y^k}{\partial x} - \frac{1}{r_3 r_2^2} \frac{\partial \Omega_z^k}{\partial y} . \quad (5.7c)$$

Equations (5.4) are solved for the Fourier coefficients, subject to the Fourier representations of the boundary and initial conditions from Chapter 4. For the undisturbed flow calculation, Fourier representations of the boundary and initial conditions from Section 4.3 are employed. For the disturbed flow calculation, Fourier representations of the boundary and initial conditions from Section 4.4 are employed.

### 5.1.1 Fourier Representation of the Boundary and Initial Conditions for the Undisturbed Flow

The Fourier representation of the boundary and initial conditions for the undisturbed flow are discussed in this section. The undisturbed flow is two-dimensional, so that

$$U^k = V^k = W^k = \Omega_x^k = \Omega_y^k = \Omega_z^k = 0 \quad \text{for } k > 0 . \quad (5.8)$$

Furthermore, for  $k = 0$

$$\Omega_z^0(x, y, t) = \Omega_y^0(x, y, t) = W^0(x, y, t) = 0 . \quad (5.9)$$

The remaining Fourier coefficients  $U^0(x, y, t)$ ,  $V^0(x, y, t)$ , and  $\Omega_z^0(x, y, t)$  satisfy the equations

$$\frac{\partial \Omega_z^0}{\partial t} - \frac{1}{Re} \left( \frac{\partial^2 \Omega_z^0}{\partial x^2} + \frac{1}{r_2^2} \frac{\partial^2 \Omega_z^0}{\partial y^2} \right) = F_z^0 , \quad (5.10a)$$

$$\frac{\partial^2 U^0}{\partial x^2} + \frac{1}{r_2^2} \frac{\partial^2 U^0}{\partial y^2} = \frac{r_3}{r_2^2} \frac{\partial \Omega_z^0}{\partial y} , \quad (5.10b)$$

$$\text{and } \frac{\partial^2 V^0}{\partial x^2} + \frac{1}{r_2^2} \frac{\partial^2 V^0}{\partial y^2} = -\frac{r_3}{r_2^2} \frac{\partial \Omega_z^0}{\partial x} \quad (5.10c)$$

which are the Fourier analogs of equations (4.3) in Chapter 4. The nonlinear term  $F_z^0(x, y, t)$  in equation (5.10a) is

$$F_z^0(x, y, t) = - \left( U^0 \frac{\partial \Omega_z^0}{\partial x} + V^0 \frac{\partial \Omega_z^0}{\partial y} \right) . \quad (5.11)$$

Solution of equations (5.10) requires the Fourier representation of the boundary and initial conditions from Section 4.3.

#### Inflow Boundary ( $x = x_0$ )

The Fourier representation of the inflow boundary conditions (4.4) are

$$U^0(x_0, y, t) = u^I(y) , \quad (5.12a)$$

$$V^0(x_0, y, t) = 0 , \quad (5.12b)$$

$$\text{and } \Omega_z^0(x_0, y, t) = \omega_z^I(y) . \quad (5.12c)$$

#### Outflow Boundary ( $x = x_N$ )

The Fourier representation of the outflow boundary conditions (4.10) are

$$\frac{\partial^2 U^0}{\partial x^2}(x_N, y, t) = 0 , \quad (5.13a)$$

$$\frac{\partial^2 V^0}{\partial x^2}(x_N, y, t) = 0 , \quad (5.13b)$$

$$\text{and } \frac{\partial^2 \Omega_z^0}{\partial x^2}(x_N, y, t) = 0 . \quad (5.13c)$$

#### Freestream Boundaries ( $y = y_0$ ) and ( $y = y_M$ )

The Fourier representation of the lower freestream boundary conditions are

$$U^0(x, y_0, t) = 1 , \quad (5.14a)$$

$$\frac{\partial V^0}{\partial y}(x, y_0, t) = 0 , \quad (5.14b)$$

$$\text{and } \Omega_z^0(x, y_0, t) = 0 . \quad (5.14c)$$

Similarly, the Fourier representation of the upper freestream boundary conditions are

$$U^0(x, y_M, t) = 1 , \quad (5.15a)$$

$$\frac{\partial V^0}{\partial y}(x, y_M, t) = 0 , \quad (5.15b)$$

$$\text{and } \Omega_z^0(x, y_M, t) = 0 . \quad (5.15c)$$

### Auxiliary Condition ( $y = 0$ )

The auxiliary condition is

$$V^0(x, 0, t) = 0 \quad . \quad (5.16)$$

### Initial Conditions ( $t = t_{L_1}$ )

The initial conditions for the base flow calculation are

$$U^0(x, y, t_{L_1}) = u^I(y) \quad , \quad (5.17a)$$

$$V^0(x, y, t_{L_1}) = 0 \quad , \quad (5.17b)$$

$$\text{and } \Omega_z^0(x, y, t_{L_1}) = \omega_z^I(y) \quad . \quad (5.17c)$$

### 5.1.2 Fourier Representation of the Boundary and Initial Conditions for the Disturbed Flow

The Fourier representation of the boundary and initial conditions that are used for the calculation of the disturbed wake are discussed in this section. In general, the disturbed wake is three-dimensional. This requires solving the governing equations for the three velocity components and the three vorticity components. Boundary and initial conditions are required for all of these components.

#### Inflow Boundary ( $x = x_0$ )

The Fourier representation of the inflow boundary conditions are shown below. For  $k = 0$ , the boundary conditions are

$$U^0(x_0, y, t) = u_{SS}(x_0, y) + P_u^{2d}(x_0, y, t) \quad , \quad (5.18a)$$

$$V^0(x_0, y, t) = 0 + P_v^{2d}(x_0, y, t) \quad , \quad (5.18b)$$

$$W^0(x_0, y, t) = 0 \quad , \quad (5.18c)$$

$$\Omega_x^0(x_0, y, t) = 0 \quad , \quad (5.18d)$$

$$\Omega_y^0(x_0, y, t) = 0 \quad , \quad (5.18e)$$

$$\text{and } \Omega_z^0(x_0, y, t) = \omega_{SS}(x_0, y) + P_{\omega_z}^{2d}(x_0, y, t) \quad . \quad (5.18f)$$

For  $k = 1$ , the inflow boundary conditions are

$$U^1(x_0, y, t) = \frac{1}{2} P_u^{3d}(x_0, y, t) \quad (5.19)$$

with similar conditions for the other flow variables. For  $k > 1$ , the Fourier components of the velocity and vorticity at the inflow boundary are

$$U^k(x_0, y, t) = 0 \quad \text{etc.} \quad (5.20)$$

#### Outflow Boundary ( $x = x_N$ )

At the outflow boundary, the wake is assumed to be undisturbed. For  $k = 0$ , the boundary conditions (4.21) become

$$U^0(x_N, y, t) = u_{SS}(x_N, y) , \quad (5.21a)$$

$$V^0(x_N, y, t) = v_{SS}(x_N, y) , \quad (5.21b)$$

$$W^0(x_N, y, t) = 0 , \quad (5.21c)$$

$$\Omega_x^0(x_N, y, t) = 0 , \quad (5.21d)$$

$$\Omega_y^0(x_N, y, t) = 0 , \quad (5.21e)$$

$$\Omega_z^0(x_N, y, t) = \omega_{zSS}(x_N, y) \quad (5.21f)$$

and for  $k > 0$ , become

$$U^k(x_N, y, t) = 0 \quad \text{etc.} \quad (5.22)$$

#### Freestream Boundaries ( $y = y_0$ ) and ( $y = y_M$ )

In Chapter 4, it was shown that a disturbance described by linear stability theory behaves like

$$\frac{\partial u'}{\partial y}(x, y, z, t) = \pm r_2 \sqrt{\alpha_r^2 + \frac{1}{r_3^2}} u'(x, y, z, t) \quad (5.23)$$

as  $y \rightarrow \pm\infty$ . For two-dimensional disturbances, equation (5.23) simplifies to

$$\frac{\partial u'}{\partial y}(x, y, z, t) = \pm r_2 \alpha_r u'(x, y, z, t) . \quad (5.24)$$

However, as noted in Chapter 4, equations (5.23) and (5.24) are not easily employed in their present form. The freestream boundary conditions are dealt with more easily in terms of the Fourier transformed variables.

If equation (4.28) is Fourier decomposed with respect to the spanwise direction  $z$ , then  $U^1$  satisfies boundary conditions similar to equation (5.23) and  $U^0$  satisfies boundary conditions similar to equation (5.24). One other question concerns the value of  $\alpha_r$  in these equations. For  $k = 0$ ,  $\alpha_r$  is set equal to  $\alpha_r^{2d}$  which is associated with the two-dimensional excitation at the inflow boundary (see equations 4.17). For  $k = 1$ ,  $\alpha_r$  is set equal to  $\alpha_r^{3d}$  which is associated with the three-dimensional excitation at the inflow boundary (see equations 4.18). For  $k > 1$ , the wake is assumed to be undisturbed at the freestream boundaries.

The Fourier representation of the lower freestream boundary conditions (4.28), (4.30a), (4.31a), and (4.32) are shown below. For  $k = 0$ , the boundary conditions are

$$\frac{\partial U'^0}{\partial y}(x, y_0, t) = r_2 \alpha_r^{2d} U'^0(x, y_0, t) , \quad (5.25a)$$

$$\frac{\partial V^0}{\partial y}(x, y_0, t) = -\frac{\partial U^0}{\partial x}(x, y_0, t) , \quad (5.25b)$$

$$W^0 = 0 , \quad (5.25c)$$

$$\Omega_z^0(x, y_0, t) = 0 , \quad (5.25d)$$

$$\Omega_y^0(x, y_0, t) = 0 , \quad (5.25e)$$

$$\text{and } \Omega_x^0(x, y_0, t) = 0 . \quad (5.25f)$$

As mentioned previously, primes denote the perturbation component of a variable.

For  $k = 1$ , the boundary conditions are

$$\frac{\partial U^1}{\partial y}(x, y_0, t) = r_2 \sqrt{\alpha_r^{3d^2} + \frac{1}{r_3^2}} U^1(x, y_0, t) , \quad (5.26a)$$

$$\frac{\partial V^1}{\partial y}(x, y_0, t) = -\frac{\partial U^1}{\partial x}(x, y_0, t) - iW^1(x, y_0, t) , \quad (5.26b)$$

$$\frac{\partial W^1}{\partial y}(x, y_0, t) = r_2 \sqrt{\alpha_r^{3d^2} + \frac{1}{r_3^2}} W^1(x, y_0, t) , \quad (5.26c)$$

$$\Omega_z^1(x, y_0, t) = 0 , \quad (5.26d)$$

$$\Omega_y^1(x, y_0, t) = 0 , \quad (5.26e)$$

$$\text{and } \Omega_z^1(x, y_0, t) = 0 . \quad (5.26f)$$

For  $k > 1$ , the boundary conditions are

$$U^k(x, y_0, t) = 0 \text{ etc.} \quad (5.27)$$

The upper freestream boundary conditions are similar to those at the lower freestream boundary. For  $k = 0$ , these conditions are

$$\frac{\partial U'^0}{\partial y}(x, y_M, t) = -r_2 \alpha_r^{2d} U'^0(x, y_M, t) , \quad (5.28a)$$

$$\frac{\partial V^0}{\partial y}(x, y_M, t) = -\frac{\partial U^0}{\partial x}(x, y_M, t) , \quad (5.28b)$$

$$W^0 = 0 , \quad (5.28c)$$

$$\Omega_x^0(x, y_M, t) = 0 , \quad (5.28d)$$

$$\Omega_y^0(x, y_M, t) = 0 , \quad (5.28e)$$

$$\text{and } \Omega_z^0(x, y_M, t) = 0 . \quad (5.28f)$$

For  $k = 1$ , the boundary conditions are

$$\frac{\partial U^1}{\partial y}(x, y_M, t) = -r_2 \sqrt{\alpha_r^{3d^2} + \frac{1}{r_3^2}} U^1(x, y_M, t) , \quad (5.29a)$$

$$\frac{\partial V^1}{\partial y}(x, y_M, t) = -\frac{\partial U^1}{\partial x}(x, y_M, t) - iW^1(x, y_M, t) , \quad (5.29b)$$

$$\frac{\partial W^1}{\partial y}(x, y_M, t) = -r_2 \sqrt{\alpha_r^{3d^2} + \frac{1}{r_s^2}} W^1(x, y_M, t) , \quad (5.29c)$$

$$\Omega_x^0(x, y_M, t) = 0 , \quad (5.29d)$$

$$\Omega_y^0(x, y_M, t) = 0 , \quad (5.29e)$$

$$\text{and } \Omega_z^0(x, y_M, t) = 0 . \quad (5.29f)$$

For  $k > 1$ , the upper freestream boundary conditions are

$$U^k(x, y_M, t) = 0 \text{ etc.} \quad (5.30)$$

Equations (5.25a) and (5.28a) enforce transverse exponential decay of the two-dimensional velocity disturbances. Equations (5.26a), (5.26c), (5.29a), and (5.29c) enforce transverse exponential decay of the three-dimensional velocity disturbances that correspond to the first spanwise mode  $k = 1$ .

#### Initial Conditions ( $t = 0$ )

As initial conditions for the calculation of the disturbed wake, the velocity and vorticity distributions of the two-dimensional base flow are prescribed in the entire integration domain. Thus, for  $k = 0$  the initial conditions are

$$U^0(x, y, 0) = u_{ss}(x, y) , \quad (5.31a)$$

$$V^0(x, y, 0) = v_{ss}(x, y) , \quad (5.31b)$$

$$W^0(x, y, 0) = 0 , \quad (5.31c)$$

$$\Omega_x^0(x, y, 0) = 0 , \quad (5.31d)$$

$$\Omega_y^0(x, y, 0) = 0 , \quad (5.31e)$$

$$\Omega_z^0(x, y, 0) = \omega_{zss}(x, y) \quad (5.31f)$$

and for  $k > 0$ , the initial conditions are

$$U^k(x, y, 0) = 0 \quad \text{etc.} \quad (5.32)$$

### 5.2 Computational Domain

As a result of the Fourier decomposition of the dependent variables, the spatial domain reduces to a two-dimensional plane in space  $(x, y)$  that is perpendicular to the  $z$ -axis. This domain is discretized into a finite number of uniformly spaced grid points. These grid points have coordinates  $(x_n, y_m)$  given by the relations

$$x_n = x_0 + n\Delta x \quad \text{for } n = 0, \dots, N \quad (5.33a)$$

$$\text{and } y_m = y_0 + m\Delta y \quad \text{for } m = 0, \dots, M \quad . \quad (5.33b)$$

The number of grid increments in the streamwise and transverse directions are denoted by  $N$  and  $M$  respectively. The constants  $\Delta x$  and  $\Delta y$  are the grid sizes in the streamwise and transverse directions respectively. The discretized spatial domain is shown in Figure 5.1.

The temporal domain is divided into discrete uniformly spaced time levels  $t_l$ , such that

$$t_l = l\Delta t \quad \text{for } l = L_1, \dots, 0, \dots, L_2 \quad (5.34)$$

where  $\Delta t$  is the time step between each time level. The base flow calculation is performed in the time interval

$$t_{L_1} \leq t_l \leq 0 \quad (5.35)$$

which corresponds to

$$L_1 \leq l \leq 0 \quad . \quad (5.36)$$

The disturbed flow is calculated in the time interval

$$0 < t_l \leq t_{L_2} \quad (5.37)$$

which corresponds to

$$0 < l \leq L_2 \quad . \quad (5.38)$$

Approximate numerical solutions of the governing equations (5.4) are obtained at the spatial and temporal locations  $(x_n, y_m, t_l)$ . The approximate solutions and their correspondence to the spatial and temporal grid points are denoted by

$$U_{n,m,l}^k = U^k(x_n, y_m, t_l) \quad \text{etc.} \quad (5.39)$$

### 5.3 Discretization of Spatial Derivatives

All spatial derivatives in equations (5.4) are approximated using the second-order finite-difference formulas shown below. Consider a complex function  $\phi(\xi, \eta)$  with known values at the equally spaced points,  $(\xi_0, \eta_0), (\xi_1, \eta_0), \dots, (\xi_{I-1}, \eta_J), (\xi_I, \eta_J)$ . Then the first partial derivative  $\frac{\partial \phi(\xi_i, \eta_j)}{\partial \xi}$  can be approximated by

$$\frac{\partial \phi(\xi_i, \eta_j)}{\partial \xi} = \frac{\phi_{i+1,j} - \phi_{i-1,j}}{2\Delta\xi} + O(\Delta\xi^2) \quad (5.40)$$

and the second partial derivative  $\frac{\partial^2 \phi(\xi_i, \eta_j)}{\partial \xi^2}$  can be approximated by

$$\frac{\partial^2 \phi(\xi_i, \eta_j)}{\partial \xi^2} = \frac{\phi_{i+1,j} - 2\phi_{i,j} + \phi_{i-1,j}}{\Delta\xi^2} + O(\Delta\xi^2) \quad (5.41)$$

where  $\Delta\xi$  is the grid increment in the  $\xi$  direction.

### 5.4 Discretized Vorticity Equations

A combination of different methods are used to solve the vorticity equations (5.4a) through (5.4c). The methods have been chosen because of their numerical

stability, their accuracy, and their computational efficiency. The Alternating-Direction-Implicit (ADI) method is used to discretize the streamwise and transverse diffusion terms. This method was selected because it is second-order time-accurate and is unconditionally stable when used for solving linear diffusion equations. Use of the Crank-Nicolson method for the spanwise diffusion term retains both second-order time-accuracy and good stability characteristics. Finally, the second-order Adams-Basforth method is used for the nonlinear terms. This method possesses favorable stability characteristics and is second-order time-accurate. The spatial derivatives are discretized using equations (5.40) and (5.41). The resulting discretized vorticity equations can be solved using noniterative methods.

This choice of numerical techniques results in a two-step method for integrating the vorticity equations. In the first integration step, the streamwise diffusion term is explicit and the transverse diffusion term is implicit. In this step, the vorticity, which is known at  $t_l = l\Delta t$ , is obtained at the intermediate time  $t_{l+\frac{1}{2}} = (l + \frac{1}{2})\Delta t$ . For the first integration step, the discretized streamwise vorticity equation is

$$\begin{aligned}
 & \frac{\Omega_{z,n,m,l+\frac{1}{2}}^k - \Omega_{z,n,m,l}^k}{\Delta t/2} - \frac{1}{Re} \left( \overbrace{\frac{\Omega_{z,n+1,m,l}^k - 2\Omega_{z,n,m,l}^k + \Omega_{z,n-1,m,l}^k}{\Delta x^2}}^{\text{ADI-Explicit}} \right. \\
 & \quad \left. + \overbrace{\frac{\Omega_{z,n,m+1,l+\frac{1}{2}}^k - 2\Omega_{z,n,m,l+\frac{1}{2}}^k + \Omega_{z,n,m-1,l+\frac{1}{2}}^k}{r_2^2 \Delta y^2}}^{\text{ADI-Implicit}} - \frac{k^2}{r_3^2} \left( \overbrace{\frac{\Omega_{z,n,m,l+\frac{1}{2}}^k + \Omega_{z,n,m,l}^k}{2}}^{\text{Crank-Nicolson}} \right) \right) \\
 & \quad = \left( \overbrace{\frac{3F_{z,n,m,l}^k - F_{z,n,m,l-\frac{1}{2}}^k}{2}}^{\text{Adams-Basforth}} \right) , \tag{5.42a}
 \end{aligned}$$

the discretized transverse vorticity equation is

$$\begin{aligned}
 & \frac{\Omega_{y,n,m,l+\frac{1}{2}}^k - \Omega_{y,n,m,l}^k}{\Delta t/2} - \frac{1}{Re} \left( \overbrace{\frac{\Omega_{y,n+1,m,l}^k - 2\Omega_{y,n,m,l}^k + \Omega_{y,n-1,m,l}^k}{\Delta x^2}}^{\text{ADI-Explicit}} \right. \\
 & + \overbrace{\frac{\Omega_{y,n,m+1,l+\frac{1}{2}}^k - 2\Omega_{y,n,m,l+\frac{1}{2}}^k + \Omega_{y,n,m-1,l+\frac{1}{2}}^k}{r_2^2 \Delta y^2}}^{\text{ADI-Implicit}} \left. - \frac{k^2}{r_3^2} \left( \frac{\Omega_{y,n,m,l+\frac{1}{2}}^k + \Omega_{y,n,m,l}^k}{2} \right) \right) \\
 & = \left( \overbrace{\frac{3F_{y,n,m,l}^k - F_{y,n,m,l-\frac{1}{2}}^k}{2}}^{\text{Adams-Basforth}} \right), \tag{5.42b}
 \end{aligned}$$

and the discretized spanwise vorticity equation is

$$\begin{aligned}
 & \frac{\Omega_{z,n,m,l+\frac{1}{2}}^k - \Omega_{z,n,m,l}^k}{\Delta t/2} - \frac{1}{Re} \left( \overbrace{\frac{\Omega_{z,n+1,m,l}^k - 2\Omega_{z,n,m,l}^k + \Omega_{z,n-1,m,l}^k}{\Delta x^2}}^{\text{ADI-Explicit}} \right. \\
 & + \overbrace{\frac{\Omega_{z,n,m+1,l+\frac{1}{2}}^k - 2\Omega_{z,n,m,l+\frac{1}{2}}^k + \Omega_{z,n,m-1,l+\frac{1}{2}}^k}{r_2^2 \Delta y^2}}^{\text{ADI-Implicit}} \left. - \frac{k^2}{r_3^2} \left( \frac{\Omega_{z,n,m,l+\frac{1}{2}}^k + \Omega_{z,n,m,l}^k}{2} \right) \right) \\
 & = \left( \overbrace{\frac{3F_{z,n,m,l}^k - F_{z,n,m,l-\frac{1}{2}}^k}{2}}^{\text{Adams-Basforth}} \right). \tag{5.42c}
 \end{aligned}$$

In the second integration step, the streamwise diffusion term is implicit and the transverse diffusion term is explicit. In this step, the vorticity is obtained at  $t = (l + 1)\Delta t$ . For this step, the discretized streamwise vorticity equation is

$$\begin{aligned}
 & \frac{\Omega_{z,n,m,l+1}^k - \Omega_{z,n,m,l+\frac{1}{2}}^k}{\Delta t/2} - \frac{1}{Re} \left( \overbrace{\frac{\Omega_{z,n+1,m,l+1}^k - 2\Omega_{z,n,m,l+1}^k + \Omega_{z,n-1,m,l+1}^k}{\Delta x^2}}^{\text{ADI-Implicit}} \right. \\
 & + \overbrace{\frac{\Omega_{z,n,m+1,l+\frac{1}{2}}^k - 2\Omega_{z,n,m,l+\frac{1}{2}}^k + \Omega_{z,n,m-1,l+\frac{1}{2}}^k}{r_2^2 \Delta y^2}}^{\text{ADI-Explicit}} \left. - \frac{k^2}{r_3^2} \left( \frac{\Omega_{z,n,m,l+1}^k + \Omega_{z,n,m,l+\frac{1}{2}}^k}{2} \right) \right) \\
 & = \left( \overbrace{\frac{3F_{z,n,m,l+\frac{1}{2}}^k - F_{z,n,m,l}^k}{2}}^{\text{Crank-Nicolson}} \right), \tag{5.43a}
 \end{aligned}$$

the discretized transverse vorticity equation is

$$\begin{aligned}
 & \frac{\Omega_{y,n,m,l+1}^k - \Omega_{y,n,m,l+\frac{1}{2}}^k}{\Delta t/2} - \frac{1}{Re} \left( \overbrace{\frac{\Omega_{y,n+1,m,l+1}^k - 2\Omega_{y,n,m,l+1}^k + \Omega_{y,n-1,m,l+1}^k}{\Delta x^2}}^{\text{ADI-Implicit}} \right. \\
 & \quad \left. + \overbrace{\frac{\Omega_{y,n,m+1,l+\frac{1}{2}}^k - 2\Omega_{y,n,m,l+\frac{1}{2}}^k + \Omega_{y,n,m-1,l+\frac{1}{2}}^k}{r_2^2 \Delta y^2}}^{\text{ADI-Explicit}} - \frac{k^2}{r_3^2} \left( \frac{\Omega_{y,n,m,l+1}^k + \Omega_{y,n,m,l+\frac{1}{2}}^k}{2} \right) \right) \\
 & = \left( \overbrace{\frac{3F_{y,n,m,l+\frac{1}{2}}^k - F_{y,n,m,l}^k}{2}}^{\text{Adams-Basforth}} \right) , \tag{5.43b}
 \end{aligned}$$

and the discretized spanwise vorticity equation is

$$\begin{aligned}
 & \frac{\Omega_{z,n,m,l+1}^k - \Omega_{z,n,m,l+\frac{1}{2}}^k}{\Delta t/2} - \frac{1}{Re} \left( \overbrace{\frac{\Omega_{z,n+1,m,l+1}^k - 2\Omega_{z,n,m,l+1}^k + \Omega_{z,n-1,m,l+1}^k}{\Delta x^2}}^{\text{ADI-Implicit}} \right. \\
 & \quad \left. + \overbrace{\frac{\Omega_{z,n,m+1,l+\frac{1}{2}}^k - 2\Omega_{z,n,m,l+\frac{1}{2}}^k + \Omega_{z,n,m-1,l+\frac{1}{2}}^k}{r_2^2 \Delta y^2}}^{\text{ADI-Explicit}} - \frac{k^2}{r_3^2} \left( \frac{\Omega_{z,n,m,l+1}^k + \Omega_{z,n,m,l+\frac{1}{2}}^k}{2} \right) \right) \\
 & = \left( \overbrace{\frac{3F_{z,n,m,l+\frac{1}{2}}^k - F_{z,n,m,l}^k}{2}}^{\text{Adams-Basforth}} \right) . \tag{5.43c}
 \end{aligned}$$

Equations (5.42) and (5.43) are valid in the interior of the spatial domain at the points  $(x_n, y_m)$  where

$$1 \leq n \leq N - 1 \tag{5.44a}$$

$$\text{and } 1 \leq m \leq M - 1 . \tag{5.44b}$$

Equations (5.42) and (5.43) are also valid for times  $t_l$  where

$$l = L_1, \dots, 0, \dots, L_2 . \tag{5.45}$$

At the domain boundary, the boundary conditions from Sections 5.1.1 and 5.1.2 are used to obtain the vorticity components.

#### 5.4.1 Discretized Boundary and Initial Conditions for the Undisturbed Vorticity

For the base flow calculation, the vorticity boundary and initial conditions from Section 5.1.1 are discretized. These boundary conditions are discussed here.

At the inflow boundary, the spanwise vorticity is

$$\Omega_{z,0,m,l}^k = \omega_z^I(y_m) . \quad (5.46)$$

At the outflow boundary, equation (5.13c) combined with equation (5.42c) results in

$$\begin{aligned} \frac{\Omega_{z,N,m,l+\frac{1}{2}}^0 - \Omega_{z,N,m,l}^0}{\Delta t/2} - \frac{1}{Re} \left( \frac{\Omega_{z,N,m+1,l+\frac{1}{2}}^0 - 2\Omega_{z,N,m,l+\frac{1}{2}}^0 + \Omega_{z,N,m-1,l+\frac{1}{2}}^0}{r_2^2 \Delta y^2} \right) \\ = \left( \frac{3F_{z,N,m,l}^0 - F_{z,N,m,l-\frac{1}{2}}^0}{2} \right) . \end{aligned} \quad (5.47)$$

Equation (5.13c) combined with equation (5.43c) results in

$$\begin{aligned} \frac{\Omega_{z,N,m,l+1}^0 - \Omega_{z,N,m,l+\frac{1}{2}}^0}{\Delta t/2} - \frac{1}{Re} \left( \frac{\Omega_{z,N,m+1,l+\frac{1}{2}}^0 - 2\Omega_{z,N,m,l+\frac{1}{2}}^0 + \Omega_{z,N,m-1,l+\frac{1}{2}}^0}{r_2^2 \Delta y^2} \right) \\ = \left( \frac{3F_{z,N,m,l+\frac{1}{2}}^0 - F_{z,N,m,l}^0}{2} \right) . \end{aligned} \quad (5.48)$$

At the freestream boundaries, the spanwise vorticity is

$$\Omega_{z,n,0,l}^0 = 0 \quad (5.49a)$$

$$\text{and } \Omega_{z,n,M,l}^0 = 0 . \quad (5.49b)$$

The initial condition for the base flow vorticity is

$$\Omega_{z,n,m,L_1}^0 = \omega_z^I(y_m) . \quad (5.50)$$

### 5.4.2 Discretized Boundary and Initial Conditions for the Disturbed Vorticity

The boundary and initial conditions from Section 5.1.2 are used for the calculation of the disturbed vorticity. The discretized versions of these boundary conditions are discussed here.

At the inflow boundary, the vorticity boundary conditions for which  $k = 0$  are

$$\Omega_{x,0,m,l}^0 = 0 \quad , \quad (5.51a)$$

$$\Omega_{y,0,m,l}^0 = 0 \quad , \quad (5.51b)$$

$$\text{and } \Omega_{z,0,m,l}^0 = \omega_{zSS}(x_0, y_m) + P_{\omega_z}^{2d}(x_0, y_m, t_l) \quad . \quad (5.51c)$$

For  $k = 1$ , the boundary conditions are

$$\Omega_{x,0,m,l}^1 = \frac{1}{2} P_{\omega_x}^{3d}(x_0, y_m, t_l) \quad , \quad (5.52a)$$

$$\Omega_{y,0,m,l}^1 = \frac{1}{2} P_{\omega_y}^{3d}(x_0, y_m, t_l) \quad , \quad (5.52b)$$

$$\text{and } \Omega_{z,0,m,l}^1 = \frac{1}{2} P_{\omega_z}^{3d}(x_0, y_m, t_l) \quad . \quad (5.52c)$$

For  $k > 1$ , the vorticity components at the inflow boundary are

$$\Omega_{x,0,m,l}^k = 0 \quad \text{etc.} \quad (5.53)$$

At the outflow boundary, the vorticity boundary conditions for which  $k = 0$  are

$$\Omega_{x,N,m,l}^0 = 0 \quad , \quad (5.54a)$$

$$\Omega_{y,N,m,l}^0 = 0 \quad , \quad (5.54b)$$

$$\Omega_{z,N,m,l}^0 = \omega_{zSS}(x_N, y_m) \quad (5.54c)$$

and for  $k > 0$ , are

$$\Omega_{z,N,m,l}^k = 0 \quad \text{etc.} \quad (5.55)$$

At the freestream boundaries, the wake is assumed to be irrotational. For  $k \geq 0$ , the lower freestream boundary conditions are

$$\Omega_{z,n,0,l}^k = 0 \quad \text{etc.} \quad (5.56)$$

For  $k \geq 0$ , the upper freestream boundary conditions are

$$\Omega_{z,n,M,l}^k = 0 \quad \text{etc.} \quad (5.57)$$

Finally, the discretized initial conditions for the disturbed vorticity calculation are presented. For  $k = 0$ , the initial conditions are

$$\Omega_{z,n,m,0}^0 = 0 \quad , \quad (5.58a)$$

$$\Omega_{y,n,m,0}^0 = 0 \quad , \quad (5.58b)$$

$$\Omega_{z,n,m,0}^0 = \omega_{zSS}(x_n, y_m) \quad (5.58c)$$

and for  $k > 0$ , are

$$\Omega_{z,n,m,0}^k = 0 \quad \text{etc.} \quad (5.59)$$

#### 5.4.3 Equation Systems for the Calculation of the Vorticity

The discretized vorticity equations, (5.42) and (5.43), combined with the discretized vorticity boundary conditions form systems of linear algebraic equations that are solved for the unknown vorticity. To obtain the vorticity at the interme-

diate time  $t_{l+\frac{1}{2}}$ , the tridiagonal system

is solved. For the base flow calculation, equation (5.60) is solved for

$$k=0 \quad , \quad 1 \leq n \leq N \quad , \quad \text{and} \quad L_1 \leq l < 0 \quad . \quad (5.61)$$

For the disturbed flow calculation, equation (5.60) is solved for

$$0 \leq k \leq \frac{K}{2} \quad , \quad 1 \leq n \leq N-1 \quad , \quad \text{and} \quad 0 \leq l < L_2 \quad . \quad (5.62)$$

The constants in equation (5.60) are

$$a_1 = -\frac{\Delta t}{2Re(r_2 \Delta y)^2} \quad ; \quad (5.63a)$$

$$b_1 = 1 + \frac{\Delta t}{Re(r_2 \Delta y)^2} + \frac{\Delta t}{4Re} \left( \frac{k}{r_3} \right)^2 ; \quad (5.63b)$$

$$c_1 = \begin{cases} 1 - \frac{\Delta t}{4Re} \left( \frac{k}{r_3} \right)^2 \frac{\Delta t}{Re \Delta x^2}, & \text{if } n \neq N; \\ 1 - \frac{\Delta t}{4Re} \left( \frac{k}{r_3} \right)^2, & \text{if } n = N; \end{cases} \quad (5.63c)$$

$$\text{and } d_n = \begin{cases} \frac{\Delta t}{2Re\Delta x^2}, & \text{if } n \neq N; \\ 0, & \text{if } n = N. \end{cases} \quad (5.63d)$$

The function  $H_{n,m,l}^k$  is

$$H_{n,m,l}^k = \frac{\Delta t}{4}(3F_{z,n,m,l}^k - F_{z,n,m,l-\frac{1}{2}}^k) \quad (5.64)$$

and  $\delta_{N,n}$ , the Kronecker delta, is

$$\delta_{N,n} = \begin{cases} 1, & n = N; \\ 0, & n \neq N. \end{cases} \quad (5.65)$$

To obtain the unknown vorticity at time  $t_{l+1}$ , the tridiagonal system

$$\left( \begin{array}{ccc|c} b_2 & a_2 & & \Omega_{z,1,m,l+1}^k \\ a_2 & b_2 & a_2 & \vdots \\ \ddots & \ddots & \ddots & \vdots \\ a_2 & b_2 & a_2 & \Omega_{z,N',m,l+1}^k \\ a'_2 & b'_2 & & \vdots \end{array} \right) \left( \begin{array}{c} c_2 \Omega_{z,1,m,l+\frac{1}{2}}^k + d_2(\Omega_{z,1,m+1,l+\frac{1}{2}}^k + \Omega_{z,1,m-1,l+\frac{1}{2}}^k) + H_{1,m,l+\frac{1}{2}}^k - a_2 \Omega_{z,0,m,l+1}^k \\ c_2 \Omega_{z,2,m,l+\frac{1}{2}}^k + d_2(\Omega_{z,2,m+1,l+\frac{1}{2}}^k + \Omega_{z,2,m-1,l+\frac{1}{2}}^k) + H_{2,m,l+\frac{1}{2}}^k \\ \vdots \\ \vdots \\ \vdots \\ c_2 \Omega_{z,N'-1,m,l+\frac{1}{2}}^k + d_2(\Omega_{z,N'-1,m+1,l+\frac{1}{2}}^k + \Omega_{z,N'-1,m-1,l+\frac{1}{2}}^k) + H_{N'-1,m,l+\frac{1}{2}}^k \\ c_2 \Omega_{z,N',m,l+\frac{1}{2}}^k + d_2(\Omega_{z,N',m+1,l+\frac{1}{2}}^k + \Omega_{z,N',m-1,l+\frac{1}{2}}^k) + H_{N',m,l+\frac{1}{2}}^k - a'_2 \Omega_{z,N,m,l+1}^k \end{array} \right) = \quad (5.66)$$

is solved. For the base flow calculation, equation (5.66) is solved for

$$N' = N \quad , \quad k = 0 \quad , \quad 1 \leq m \leq M-1 \quad , \quad \text{and} \quad L_1 \leq l < 0 \quad . \quad (5.67)$$

For the disturbed flow calculation, equation (5.66) is solved for

$$N' = N-1 \quad , \quad 0 \leq k \leq \frac{K}{2} \quad , \quad 1 \leq m \leq M-1 \quad , \quad \text{and} \quad 0 \leq l < L_2 \quad . \quad (5.68)$$

The function  $H_{n,m,l}^k$  is

$$H_{n,m,l}^k = \frac{\Delta t}{4} (3F_{z,n,m,l+\frac{1}{2}}^k - F_{z,n,m,l}^k) . \quad (5.69)$$

The constants in equation (5.66) are

$$a_2 = -\frac{\Delta t}{2Re\Delta x^2} , \quad (5.70a)$$

$$b_2 = 1 + \frac{\Delta t}{Re\Delta x^2} + \frac{\Delta t}{4Re} \left( \frac{k}{r_3} \right)^2 , \quad (5.70b)$$

$$c_2 = 1 - \frac{\Delta t}{4Re} \left( \frac{k}{r_3} \right)^2 - \frac{\Delta t}{Re(r_2\Delta y)^2} : \quad (5.70c)$$

$$\text{and } d_2 = \frac{\Delta t}{2Re(r_2\Delta y)^2} . \quad (5.70d)$$

The constant  $a'_2$  is

$$a'_2 = \begin{cases} 0, & \text{for the base flow calculation;} \\ a_2, & \text{otherwise.} \end{cases} \quad (5.71)$$

The constant  $b'_2$  is

$$b'_2 = \begin{cases} 1 + \frac{\Delta t}{4Re} \left( \frac{k\gamma}{r_3} \right)^2, & \text{for the base flow calculation;} \\ b_2, & \text{otherwise.} \end{cases} \quad (5.72)$$

Equations (5.60) and (5.66) are solved for the spanwise vorticity. Equation systems for the streamwise and transverse vorticity components are identical to equations (5.60) and (5.66) and are not shown.

For the base flow calculation, equations (5.60) and (5.66) are solved beginning with the initial data at time  $t = t_{L_1}$ . For the disturbed flow calculation, equations (5.60) and (5.66) are solved beginning with the initial data at time  $t = 0$ . For the initial integration step of both the base flow and the disturbed flow calculations, the nonlinear terms are evaluated using the first-order Euler method instead of the second-order Adams-Basforth method.

### 5.5 Discretized Velocity Equations

The Helmholtz equations, (5.4d) through (5.4f), are discretized using the second-order finite-difference formulas derived in Section 5.3. The discretized Helmholtz equations are, for the streamwise velocity component

$$\frac{U_{n+1,m,l}^k - 2U_{n,m,l}^k + U_{n-1,m,l}^k}{\Delta x^2} + \frac{U_{n,m+1,l}^k - 2U_{n,m,l}^k + U_{n,m-1,l}^k}{r_2^2 \Delta y^2} - \left(\frac{k}{r_3}\right)^2 U_{n,m,l}^k = G_{x,n,m,l}^k ; \quad (5.73a)$$

for the transverse velocity component

$$\frac{V_{n+1,m,l}^k - 2V_{n,m,l}^k + V_{n-1,m,l}^k}{\Delta x^2} + \frac{V_{n,m+1,l}^k - 2V_{n,m,l}^k + V_{n,m-1,l}^k}{r_2^2 \Delta y^2} - \left(\frac{k}{r_3}\right)^2 V_{n,m,l}^k = G_{y,n,m,l}^k ; \quad (5.73b)$$

and for the spanwise velocity component

$$\frac{W_{n+1,m,l}^k - 2W_{n,m,l}^k + W_{n-1,m,l}^k}{\Delta x^2} + \frac{W_{n,m+1,l}^k - 2W_{n,m,l}^k + W_{n,m-1,l}^k}{r_2^2 \Delta y^2} - \left(\frac{k}{r_3}\right)^2 W_{n,m,l}^k = G_{z,n,m,l}^k . \quad (5.73c)$$

The right hand sides of equations (5.73) are

$$G_{x,n,m,l}^k = \frac{r_3}{r_2^2} \left( \frac{\Omega_{z,n,m+1,l}^k - \Omega_{z,n,m-1,l}^k}{2\Delta y} \right) - \frac{ik}{r_3} \Omega_{y,n,m,l}^k , \quad (5.74a)$$

$$G_{y,n,m,l}^k = \frac{ik}{r_3 r_2^2} \Omega_{z,n,m,l}^k - \frac{r_3}{r_2^2} \left( \frac{\Omega_{z,n+1,m,l}^k - \Omega_{z,n-1,m,l}^k}{2\Delta x} \right) , \quad (5.74b)$$

$$\text{and } G_{z,n,m,l}^k = \frac{1}{r_3} \left( \frac{\Omega_{y,n+1,m,l}^k - \Omega_{y,n-1,m,l}^k}{2\Delta x} \right) - \frac{1}{r_3 r_2^2} \left( \frac{\Omega_{z,n,m+1,l}^k - \Omega_{z,n,m-1,l}^k}{2\Delta y} \right). \quad (5.74c)$$

The Helmholtz equations are solved for each integration step, subject to the appropriate boundary conditions from Sections 5.1.1 and 5.1.2.

Equations (5.73) are valid in the interior of the spatial domain. At the domain boundary, equations (5.73) combined with the discretized boundary conditions are used to obtain the velocity components.

### 5.5.1 Discretized Boundary and Initial Conditions for the Undisturbed Velocity

For the base flow calculation, the velocity boundary and initial conditions from Section 5.1.1 are discretized as discussed below.

At the inflow boundary, the streamwise and transverse velocity components are

$$U_{0,m,l}^0 = u^I(y_m) \quad (5.75a)$$

$$\text{and } V_{0,m,l}^0 = 0. \quad (5.75b)$$

The discretized version of the outflow boundary conditions, (5.13a) and (5.13b), combined with equations (5.73a) and (5.73b) result in

$$\frac{U_{N,m+1,l}^0 - 2U_{N,m,l}^0 + U_{N,m-1,l}^0}{(r_2 \Delta y)^2} = G_{z,N,m,l}^0 \quad (5.76)$$

for the streamwise velocity and

$$\frac{V_{N,m+1,l}^0 - 2V_{N,m,l}^0 + V_{N,m-1,l}^0}{(r_2 \Delta y)^2} = G_{y,N,m,l}^0 \quad (5.77)$$

for the transverse velocity.

At the freestream boundaries, the streamwise velocity is

$$U_{n,0,l}^k = 1 \quad (5.78a)$$

$$\text{and } U_{n,M,l}^k = 1 . \quad (5.78b)$$

Equations (5.14b) and (5.15b) combined with equation (5.73b) result in

$$\frac{V_{n+1,0,l}^0 - 2V_{n,0,l}^0 + V_{n-1,0,l}^0}{\Delta x^2} + \frac{2V_{n,1,l}^0 - 2V_{n,0,l}^0}{r_2^2 \Delta y^2} = 0 \quad (5.79)$$

at the lower freestream boundary and

$$\frac{V_{n+1,M,l}^0 - 2V_{n,M,l}^0 + V_{n-1,M,l}^0}{\Delta x^2} + \frac{2V_{n,M-1,l}^0 - 2V_{n,M,l}^0}{r_2^2 \Delta y^2} = 0 \quad (5.80)$$

at the upper freestream boundary.

The auxiliary condition

$$V_{n,\frac{M}{2},l}^0 = 0 \quad (5.81)$$

imposes antisymmetry on the transverse velocity field. Because of this antisymmetry, the transverse velocity  $V_{n,m,l}^0$  is solved only in the lower half of the spatial domain for which

$$1 \leq n \leq N \quad (5.82a)$$

$$\text{and } 0 \leq m \leq \frac{M}{2} - 1 . \quad (5.82b)$$

The transverse velocity in the upper half of the spatial domain is found from the relation

$$V_{n,\frac{M}{2}+m,l}^0 = -V_{n,\frac{M}{2}-m,l}^0 \quad \text{for } 1 \leq m \leq \frac{M}{2} \quad \text{and } 1 \leq n \leq N . \quad (5.83)$$

Finally, the initial conditions for the streamwise and transverse velocities are

$$U_{n,m,L_1}^0 = u^I(y_m) \quad (5.84a)$$

$$\text{and } V_{n,m,L_1}^0 = 0 . \quad (5.84b)$$

### 5.5.2 Discretized Boundary and Initial Conditions for the Disturbed Velocity

Boundary and initial conditions from Section 5.1.2 are used for the calculation of the disturbed velocity. The discretized versions of these boundary and initial conditions are discussed in this section.

At the inflow boundary, the velocity components for  $k = 0$  are

$$U_{0,m,l}^0 = u_{ss}(x_0, y_m) + P_u^{2d}(x_0, y_m, t_l) , \quad (5.85a)$$

$$V_{0,m,l}^0 = 0 + P_v^{2d}(x_0, y_m, t_l) , \quad (5.85b)$$

$$\text{and } W_{0,m,l}^0 = 0 . \quad (5.85c)$$

For  $k = 1$ , the velocity components are

$$U_{0,m,l}^1 = \frac{1}{2} P_u^{3d}(x_0, y_m, t_l) , \quad (5.86a)$$

$$V_{0,m,l}^1 = \frac{1}{2} P_v^{3d}(x_0, y_m, t_l) , \quad (5.86b)$$

$$\text{and } W_{0,m,l}^1 = \frac{1}{2} P_w^{3d}(x_0, y_m, t_l) . \quad (5.86c)$$

For  $k > 1$ , the velocity components are

$$U_{0,m,l}^k = 0 \text{ etc.} \quad (5.87)$$

At the outflow boundary, the velocity components for  $k = 0$  are

$$U_{N,m,l}^0 = u_{ss}(x_N, y_m) , \quad (5.88a)$$

$$V_{N,m,l}^0 = v_{ss}(x_N, y_m) , \quad (5.88b)$$

$$W_{N,m,l}^0 = 0 \quad (5.88c)$$

and for  $k > 0$ , are

$$U_{N,m,l}^k = 0 \text{ etc.} \quad (5.89)$$

At the lower freestream boundary, equation (5.25a) combined with equation (5.73a) results in the following equation for the  $k = 0$  streamwise velocity:

$$\begin{aligned} \frac{U_{n+1,0,l}^0 - 2U_{n,0,l}^0 + U_{n-1,0,l}^0}{\Delta x^2} + \frac{2U_{n,1,l}^0 - (2 + 2C_\alpha^{2d})U_{n,0,l}^0}{r_2^2 \Delta y^2} \\ = \frac{1}{(r_2 \Delta y)^2} (2u_{ss}(x_n, y_1) - (2 + 2C_\alpha^{2d})u_{ss}(x_n, y_0)) \quad (5.90) \end{aligned}$$

where  $C_\alpha^{2d} = \alpha_r^{2d} r_2 \Delta y$ . Equation (5.25b) combined with equation (5.73b) results in

$$\begin{aligned} \frac{V_{n+1,0,l}^0 - 2V_{n,0,l}^0 + V_{n-1,0,l}^0}{\Delta x^2} + \frac{2V_{n,1,l}^0 - 2V_{n,0,l}^0}{r_2^2 \Delta y^2} \\ = -\frac{1}{\Delta x \Delta y r_2^2} (U_{n+1,0,l}^0 - U_{n-1,0,l}^0) \quad (5.91) \end{aligned}$$

for the  $k = 0$  transverse velocity. For  $k = 0$ , the spanwise velocity is

$$W_{n,0,l}^0 = 0 \quad (5.92)$$

at the lower boundary.

For  $k = 1$ , equation (5.26a) combined with (5.73a) results in the following equation for the streamwise velocity:

$$\begin{aligned} \frac{U_{n+1,0,l}^1 - 2U_{n,0,l}^1 + U_{n-1,0,l}^1}{\Delta x^2} \\ + \frac{2U_{n,1,l}^1 - (2 + 2C_\alpha^{3d})U_{n,0,l}^1}{r_2^2 \Delta y^2} - \left(\frac{1}{r_3}\right)^2 U_{n,0,l}^1 = 0 \quad (5.93) \end{aligned}$$

where  $C_\alpha^{3d} = \Delta y r_2 \sqrt{\alpha_r^{3d}^2 + (\frac{1}{r_3})^2}$ . Similarly, equation (5.26c) combined with (5.73c) results in

$$\begin{aligned} \frac{W_{n+1,0,l}^1 - 2W_{n,0,l}^1 + W_{n-1,0,l}^1}{\Delta x^2} \\ + \frac{2W_{n,1,l}^1 - (2 + 2C_\alpha^{3d})W_{n,0,l}^1}{r_2^2 \Delta y^2} - \left(\frac{1}{r_3}\right)^2 W_{n,0,l}^1 = 0 \quad (5.94) \end{aligned}$$

for the  $k = 1$  spanwise velocity. Equation (5.26b) combined with equation (5.73b) results in

$$\frac{V_{n+1,0,l}^1 - 2V_{n,0,l}^1 + V_{n-1,0,l}^1}{\Delta x^2} + \frac{2V_{n,1,l}^1 - 2V_{n,0,l}^1}{r_2^2 \Delta y^2} - \left(\frac{1}{r_3}\right)^2 V_{n,0,l}^1 = -\frac{1}{(r_2 \Delta y)^2} \left( \frac{\Delta y}{\Delta x} (U_{n+1,0,l}^1 - U_{n-1,0,l}^0) + i \Delta y W_{n,0,l}^1 \right) \quad (5.95)$$

which is valid for the  $k = 1$  transverse velocity. For  $k > 1$ , the velocity components at the lower freestream boundary are

$$U_{n,0,l}^k = 0 \quad \text{etc.} \quad (5.96)$$

At the upper freestream boundary, the following equations are valid. For  $k = 0$ , the velocity boundary conditions are

$$\frac{U_{n+1,M,l}^0 - 2U_{n,M,l}^0 + U_{n-1,M,l}^0}{\Delta x^2} + \frac{2U_{n,M-1,l}^0 - (2 + 2C_\alpha^{2d})U_{n,M,l}^0}{r_2^2 \Delta y^2} = \frac{1}{(r_2 \Delta y)^2} (2u_{SS}(x_n, y_{M-1}) - (2 + 2C_\alpha^{2d})u_{SS}(x_n, y_M)) , \quad (5.97a)$$

$$\frac{V_{n+1,M,l}^0 - 2V_{n,M,l}^0 + V_{n-1,M,l}^0}{\Delta x^2} + \frac{2V_{n,M-1,l}^0 - 2V_{n,M,l}^0}{r_2^2 \Delta y^2} = \frac{1}{\Delta x \Delta y r_2^2} (U_{n+1,M,l}^0 - U_{n-1,M,l}^0) , \quad (5.97b)$$

and

$$W_{n,M,l}^0 = 0 . \quad (5.97c)$$

For  $k = 1$ , the velocity boundary conditions are

$$\frac{U_{n+1,M,l}^1 - 2U_{n,M,l}^1 + U_{n-1,M,l}^1}{\Delta x^2} + \frac{2U_{n,M-1,l}^1 - (2 + 2C_\alpha^{3d})U_{n,M,l}^1}{r_2^2 \Delta y^2} - \left(\frac{1}{r_3}\right)^2 U_{n,M,l}^1 = 0 , \quad (5.98a)$$

$$\frac{W_{n+1,M,l}^1 - 2W_{n,M,l}^1 + W_{n-1,M,l}^1}{\Delta x^2} + \frac{2W_{n,M-1,l}^1 - (2 + 2C_\alpha^{3d})W_{n,M,l}^1}{r_2^2 \Delta y^2} - \left(\frac{1}{r_3}\right)^2 W_{n,M,l}^1 = 0 \quad , \quad (5.98b)$$

and

$$\frac{V_{n+1,M,l}^1 - 2V_{n,0,l}^1 + V_{n-1,M,l}^1}{\Delta x^2} + \frac{2V_{n,M-1,l}^1 - 2V_{n,M,l}^1}{r_2^2 \Delta y^2} - \left(\frac{1}{r_3}\right)^2 V_{n,M,l}^1 = \frac{1}{(r_2 \Delta y)^2} \left( \frac{\Delta y}{\Delta x} (U_{n+1,M,l}^1 + U_{n-1,M,l}^0) + i \Delta y W_{n,M,l}^1 \right) . \quad (5.98c)$$

For  $k > 1$ , the velocity components at the upper freestream boundary are

$$U_{n,M,l}^k = 0 \quad \text{etc.} \quad (5.99)$$

Finally, initial conditions must be specified for the velocity components. For  $k = 0$ , the initial conditions are

$$U_{n,m,0}^0 = u_{SS}(x_n, y_m) \quad , \quad (5.100a)$$

$$V_{n,m,0}^0 = v_{SS}(x_n, y_m) \quad , \quad (5.100b)$$

$$W_{n,m,0}^0 = 0 \quad (5.100c)$$

and for  $k > 0$ , the initial conditions are

$$U_{n,m,0}^0 = 0 \quad \text{etc.} \quad (5.101)$$

### 5.5.3 Equation Systems for the Calculation of the Velocity

The discretized velocity equations (5.73) combined with the discretized velocity boundary conditions form systems of linear algebraic equations that are solved to obtain the velocity components.

### Base flow Streamwise Velocity

Equation (5.73a) combined with boundary conditions (5.75a), (5.76), and (5.78) form a system of linear algebraic equations that is solved for the base flow streamwise velocity. To derive this system of equations, let

$$\phi_n = \begin{pmatrix} U_{n,1,l}^0 \\ \vdots \\ \vdots \\ \vdots \\ U_{n,M-1,l}^0 \end{pmatrix}_{(M-1) \times 1}, \quad g_n = \begin{pmatrix} G_{z,n,1,l}^0 \\ \vdots \\ \vdots \\ \vdots \\ G_{z,n,M-1,l}^0 \end{pmatrix}_{(M-1) \times 1}, \quad (5.102a)$$

$$A = \begin{pmatrix} -2 & 1 & & & & \\ 1 & -2 & 1 & & & \\ & \ddots & \ddots & \ddots & & \\ & & \ddots & \ddots & \ddots & \\ & & & \ddots & \ddots & \ddots \\ & & & & 1 & -2 & 1 \\ & & & & 1 & -2 & \end{pmatrix}_{(M-1) \times (M-1)}, \quad (5.102b)$$

$$\text{and } h_n = \begin{pmatrix} U_{n,0,l}^0 \\ 0 \\ \vdots \\ \vdots \\ \vdots \\ 0 \\ U_{n,M,l}^0 \end{pmatrix}_{(M-1) \times 1}. \quad (5.102c)$$

Then, the resulting system of equations

$$\left( \begin{array}{cccc} A' & I & & \\ I & A' & I & \\ \ddots & \ddots & \ddots & \\ & \ddots & \ddots & \\ & & \ddots & \\ & & & I & A' & I \\ & & & 0 & \Lambda A \end{array} \right)_{N \times N} \left( \begin{array}{c} \phi_1 \\ \vdots \\ \phi_N \end{array} \right)_{N \times 1} = \left( \begin{array}{c} \Delta x^2 g_1 - h_1 \Lambda - \phi_0 \\ \Delta x^2 g_2 - h_2 \Lambda \\ \vdots \\ \vdots \\ \vdots \\ \Delta x^2 g_N - h_N \Lambda \end{array} \right)_{N \times 1} \quad (5.103)$$

is solved for the base flow streamwise velocity. The constant  $\Lambda$  is

$$\Lambda = \left( \frac{\Delta x}{r_2 \Delta y} \right)^2 , \quad (5.104)$$

the matrix  $A'$  is

$$A' = \Lambda A - 2I , \quad (5.105)$$

and  $I$  is the identity matrix.

#### Base flow Transverse Velocity

Equation (5.73b) combined with boundary conditions (5.75b), (5.77), (5.79), and (5.80) form a system of linear algebraic equations that is solved for the base

flow transverse velocity. To derive this system of equations, let

$$\phi_n = \begin{pmatrix} V_{n,\frac{M}{2}-1,l}^0 \\ \vdots \\ \vdots \\ \vdots \\ V_{n,0,l}^0 \end{pmatrix}_{\frac{M}{2} \times 1}, \quad g_n = \begin{pmatrix} G_{y,n,\frac{M}{2}-1,l}^0 \\ \vdots \\ \vdots \\ \vdots \\ G_{y,n,0,l}^0 \end{pmatrix}_{\frac{M}{2} \times 1}, \quad (5.106a)$$

$$\text{and } A = \begin{pmatrix} -2 & 1 & & & & \\ 1 & -2 & 1 & & & \\ & \ddots & \ddots & \ddots & & \\ & & \ddots & \ddots & \ddots & \\ & & & \ddots & \ddots & \ddots \\ & & & & 1 & -2 & 1 \\ & & & & 2 & -2 & -2 \end{pmatrix}_{\frac{M}{2} \times \frac{M}{2}}. \quad (5.106b)$$

Then, the system of equations

$$\begin{pmatrix} A' & I & & & & \\ I & A' & I & & & \\ & \ddots & \ddots & \ddots & & \\ & & \ddots & \ddots & \ddots & \\ & & & \ddots & \ddots & \ddots \\ & & & & I & A' & I \\ & & & & 0 & \Lambda A \end{pmatrix}_{N \times N} \begin{pmatrix} \phi_1 \\ \vdots \\ \vdots \\ \vdots \\ \phi_N \end{pmatrix}_{N \times 1} = \begin{pmatrix} \Delta x^2 g_1 \\ \vdots \\ \vdots \\ \vdots \\ \Delta x^2 g_N \end{pmatrix}_{N \times 1} \quad (5.107)$$

is solved for the base flow transverse velocity in the lower half of the spatial domain, for which

$$1 \leq n \leq N, \quad (5.108a)$$

$$\text{and } 0 \leq m \leq \frac{M}{2} - 1. \quad (5.108b)$$

The base flow transverse velocity in the upper half of the spatial domain is obtained from the relation

$$V_{n, \frac{M}{2}+m,l}^0 = -V_{n, \frac{M}{2}-m,l}^0 \quad \text{for } 1 \leq m \leq \frac{M}{2} \quad \text{and } 1 \leq n \leq N . \quad (5.109)$$

As previously ,

$$\Lambda = \left( \frac{\Delta x}{r_2 \Delta y} \right)^2 \quad (5.110a)$$

and

$$A' = \Lambda A - 2I . \quad (5.110b)$$

#### Disturbed Velocity Components for $k \leq 1$

Equation (5.73a) combined with the boundary conditions (5.85a), (5.88a), (5.90), and (5.97a) form a system of equations that is solved for the zeroth spanwise mode of the disturbed streamwise velocity  $U^0$ . To derive this system of equations, let

$$\phi_m = \begin{pmatrix} U_{1,m,l}^0 \\ \vdots \\ \vdots \\ \vdots \\ \vdots \\ U_{N-1,m,l}^0 \end{pmatrix}_{(N-1) \times 1}, g_m = \begin{pmatrix} G_{z,1,m,l}^0 \\ \vdots \\ \vdots \\ \vdots \\ \vdots \\ G_{z,N-1,m,l}^0 \end{pmatrix}_{(N-1) \times 1}, \quad (5.111a)$$

$$A = \begin{pmatrix} -2 & 1 & & & & & \\ 1 & -2 & 1 & & & & \\ & \ddots & \ddots & \ddots & & & \\ & & \ddots & \ddots & \ddots & & \\ & & & \ddots & \ddots & \ddots & \\ & & & & \ddots & \ddots & \ddots \\ & & & & & 1 & -2 & 1 \\ & & & & & 1 & -2 & \\ & & & & & & 1 & -2 \end{pmatrix}_{(N-1) \times (N-1)} \quad (5.111b)$$

$$\text{and } h_m = \begin{pmatrix} U_{0,m,l}^0 \\ 0 \\ \vdots \\ \vdots \\ 0 \\ U_{N,m,l}^0 \end{pmatrix}_{(N-1)} . \quad (5.111c)$$

Then, the system of equations

$$\begin{pmatrix} A' - B' & 2\Lambda I & & & \\ \Lambda I & A' & \Lambda I & & \\ \ddots & \ddots & \ddots & & \\ \ddots & \ddots & \ddots & & \\ \ddots & \ddots & \ddots & & \\ & \ddots & \ddots & & \\ & \Lambda I & A' & \Lambda I & \\ & 2\Lambda I & A' + B'' & & \end{pmatrix}_{(M+1) \times (M+1)} \begin{pmatrix} \phi_0 \\ \vdots \\ \vdots \\ \vdots \\ \vdots \\ \vdots \\ \phi_M \end{pmatrix}_{(M+1) \times 1} =$$

$$\begin{pmatrix} \Delta x^2 g_0 - h_0 + 2\Delta y \Lambda f' \\ \Delta x^2 g_1 - h_1 \\ \vdots \\ \vdots \\ \vdots \\ \Delta x^2 g_{M-1} - h_{M-1} \\ \Delta x^2 g_M - h_M - 2\Delta y \Lambda f'' \end{pmatrix}_{(M+1) \times 1} \quad (5.112)$$

is solved for the zeroth spanwise mode ( $k = 0$ ) of the disturbed streamwise velocity.

In equation (5.112),  $\Lambda'$  is

$$\Lambda' = \left( \frac{k\gamma\Delta x}{r_3} \right)^2 \quad (5.113a)$$

and  $\Lambda$  is

$$\Lambda = \left( \frac{\Delta x}{r_2 \Delta y} \right)^2 . \quad (5.113b)$$

The matrix  $A'$  is

$$A' = A - (2\Lambda + \Lambda')I , \quad (5.114)$$

the matrix  $B'$  is

$$B' = 2\Lambda\Delta y c' I , \quad (5.115)$$

and the matrix  $B''$  is

$$B'' = 2\Lambda\Delta y c'' I . \quad (5.116)$$

The vectors  $\mathbf{f}' = [f'_n]$  and  $\mathbf{f}'' = [f''_n]$  and the scalars  $c'$  and  $c''$  result from the freestream boundary conditions. For the zeroth spanwise mode ( $k = 0$ ) of the streamwise velocity  $U^0$ ,

$$f'_n = -\alpha_r^{2d} r_2 u_{SS}(x_n, y_0) + \frac{u_{SS}(x_n, y_1) - u_{SS}(x_n, y_0)}{\Delta y} , \quad (5.117a)$$

$$f''_n = \alpha_r^{2d} r_2 u_{SS}(x_n, y_M) + \frac{u_{SS}(x_n, y_M) - u_{SS}(x_n, y_{M-1})}{\Delta y} \quad (5.117b)$$

and

$$c' = \alpha_r^{2d} r_2 , \quad (5.117c)$$

$$c'' = -\alpha_r^{2d} r_2 . \quad (5.117d)$$

Equation systems for the velocity components  $V^0$ ,  $U^1$ ,  $V^1$ , and  $W^1$  are almost identical to equation (5.112). The only difference between equation (5.112) and systems of equations for the other velocity components  $V^0$ ,  $U^1$ ,  $V^1$ , and  $W^1$  are the vectors  $\mathbf{f}' = [f'_n]$  and  $\mathbf{f}'' = [f''_n]$  and the constants  $c'$  and  $c''$ . Therefore, for these other velocity components, only  $f'_n$ ,  $f''_n$ ,  $c'$  and  $c''$  will be shown.

For the zeroth spanwise mode ( $k = 0$ ) of the transverse velocity  $V^0$ ,

$$f'_n = -\frac{U_{n+1,0,l}^0 - U_{n-1,0,l}^0}{2\Delta x} , \quad (5.118a)$$

$$f''_n = -\frac{U_{n+1,M,l}^0 - U_{n-1,M,l}^0}{2\Delta x} \quad (5.118b)$$

and

$$c' = 0 \quad , \quad c'' = 0 \quad . \quad (5.118c)$$

For the first spanwise mode ( $k = 1$ ) of both the streamwise and spanwise velocities,  $U^1$  and  $W^1$ ,

$$f'_n = 0 \quad , \quad (5.119a)$$

$$f''_n = 0 \quad (5.119b)$$

and

$$c' = r_2 \sqrt{\alpha_r^{3d^2} + \left(\frac{1}{r_3}\right)^2} \quad , \quad (5.119c)$$

$$c'' = r_2 \sqrt{\alpha_r^{3d^2} + \left(\frac{1}{r_3}\right)^2} \quad . \quad (5.119d)$$

Finally, for the first spanwise mode ( $k = 1$ ) of the transverse velocity  $V^1$ ,

$$f'_n = -\frac{U_{n+1,0,l}^1 - U_{n-1,0,l}^1}{2\Delta x} - iW_{n,0,l}^1 \quad , \quad (5.120a)$$

$$f''_n = -\frac{U_{n+1,M,l}^1 - U_{n-1,M,l}^1}{2\Delta x} - iW_{n,M,l}^1 \quad (5.120b)$$

and

$$c' = 0 \quad , \quad c'' = 0 \quad . \quad (5.120c)$$

### Disturbed Velocity Components for $k > 1$

Equation (5.73a) combined with the boundary conditions (5.87), (5.89), (5.96), and (5.99) form a system of equations that is solved for the disturbed streamwise

velocity  $U^k$  for  $k > 1$ . To derive this system of equations, let

$$\phi_m = \begin{pmatrix} U_{1,m,l}^k \\ \vdots \\ \vdots \\ \vdots \\ \vdots \\ U_{N-1,m,l}^k \end{pmatrix}_{(N-1) \times 1}, \quad g_m = \begin{pmatrix} G_{z,1,m,l}^k \\ \vdots \\ \vdots \\ \vdots \\ \vdots \\ G_{z,N-1,m,l}^k \end{pmatrix}_{(N-1) \times 1}, \quad (5.121a)$$

$$\text{and } A = \begin{pmatrix} -2 & 1 & & & & \\ 1 & -2 & 1 & & & \\ \ddots & \ddots & \ddots & \ddots & & \\ & \ddots & \ddots & \ddots & \ddots & \\ & & \ddots & \ddots & \ddots & \\ & & & 1 & -2 & 1 \\ & & & 1 & -2 & \end{pmatrix}_{(N-1) \times (N-1)}. \quad (5.121b)$$

Then, the system of equations

$$\left( \begin{array}{ccc|c} A' & \Lambda I & & \phi_1 \\ \Lambda I & A' & \Lambda I & \\ \ddots & \ddots & \ddots & \\ & \Lambda I & A' & \Lambda I \\ & \Lambda I & A' & \end{array} \right)_{(M-1) \times (M-1)} \left( \begin{array}{c} \phi_1 \\ \vdots \\ \vdots \\ \vdots \\ \vdots \\ \vdots \\ \phi_{M-1} \end{array} \right)_{(M-1) \times 1} =$$

$$\left( \begin{array}{c} \Delta x^2 g_1 \\ \vdots \\ \vdots \\ \vdots \\ \vdots \\ \vdots \\ \Delta x^2 g_{M-1} \end{array} \right)_{(M-1) \times 1} \quad (5.122)$$

is solved for the streamwise velocity component  $U^k$ . As before,

$$\Lambda' = \left( \frac{\Delta x}{r_3} \right)^2 \quad (5.123a)$$

$$\text{and } \Lambda = \left( \frac{\Delta x}{r_2 \Delta y} \right)^2 . \quad (5.123b)$$

The matrix  $A'$  is

$$A' = A - (2\Lambda + \Lambda')I . \quad (5.124)$$

Equation systems for  $W^0$  and for  $V^k$  and  $W^k$  with  $k > 1$ , are identical to equation (5.122) and will not be shown.

Equations (5.103), (5.107), (5.112), and (5.122) are systems of linear algebraic equations that are solved for the velocity components. For each system, the coefficient matrix is large and sparse. However, because of the structure of

these matrices, fast Helmholtz solvers can be used to solve these equation systems. Details of these techniques are given by Swarztrauber (1977).

### 5.6 Evaluation of the Nonlinear Terms

Up to this point in the development of the numerical method, the evaluation of the nonlinear terms  $F_{x,n,m,l}^k$ ,  $F_{y,n,m,l}^k$ , and  $F_{z,n,m,l}^k$  at each time step has been ignored. However, in order to calculate  $\Omega_{x,n,m,l}^k$ ,  $\Omega_{y,n,m,l}^k$ , and  $\Omega_{z,n,m,l}^k$  from equations (5.42) and (5.43), the nonlinear terms must be computed at times  $t_{l-\frac{1}{2}}$ ,  $t_l$ , and  $t_{l+\frac{1}{2}}$ . Generally, computing the nonlinear terms is the most time consuming aspect of using spectral methods to solve the Navier-Stokes equations. The difficulties arise from the fact that the nonlinear terms do not have a simple Fourier representation.

The nonlinear terms can be computed either pseudo-spectrally or spectrally. The pseudo-spectral method works in the following manner. The physical representation of the velocity and vorticity are obtained from the Fourier coefficients using equations (5.1). Then, the nonlinear terms  $f_{x,n,m,l}^k$ ,  $f_{y,n,m,l}^k$ , and  $f_{z,n,m,l}^k$  are computed from the formulae

$$\begin{aligned} f_{x,n,m,l}^k &= \omega_{x,n,m,l}^k \frac{u_{n+1,m,l}^k - u_{n-1,m,l}^k}{2\Delta x} + \omega_{y,n,m,l}^k \frac{u_{n,m+1,l}^k - u_{n,m-1,l}^k}{2\Delta y} \\ &\quad + \omega_{z,n,m,l}^k \frac{\partial u}{\partial z}|_{n,m,l}^k - u_{n,m,l}^k \frac{\omega_{z,n+1,m,l}^k - \omega_{z,n-1,m,l}^k}{2\Delta x} \\ &\quad - v_{n,m,l}^k \frac{\omega_{z,n,m+1,l}^k - \omega_{z,n,m-1,l}^k}{2\Delta y} - w_{n,m,l}^k \frac{\partial \omega_z}{\partial z}|_{n,m,l}^k , \end{aligned} \quad (5.125a)$$

$$\begin{aligned} f_{y,n,m,l}^k &= \omega_{x,n,m,l}^k \frac{v_{n+1,m,l}^k - v_{n-1,m,l}^k}{2\Delta x} + \omega_{y,n,m,l}^k \frac{v_{n,m+1,l}^k - v_{n,m-1,l}^k}{2\Delta y} \\ &\quad + \omega_{z,n,m,l}^k \frac{\partial v}{\partial z}|_{n,m,l}^k - u_{n,m,l}^k \frac{\omega_{y,n+1,m,l}^k - \omega_{y,n-1,m,l}^k}{2\Delta x} \\ &\quad - v_{n,m,l}^k \frac{\omega_{y,n,m+1,l}^k - \omega_{y,n,m-1,l}^k}{2\Delta y} - w_{n,m,l}^k \frac{\partial \omega_y}{\partial z}|_{n,m,l}^k , \end{aligned} \quad (5.125b)$$

$$\text{and } f_{z,n,m,l}^k = \omega_{x,n,m,l}^k \frac{w_{n+1,m,l}^k - w_{n-1,m,l}^k}{2\Delta x} + \omega_{y,n,m,l}^k \frac{w_{n,m+1,l}^k - w_{n,m-1,l}^k}{2\Delta y} \\ + \omega_{z,n,m,l}^k \frac{\partial w}{\partial z}|_{n,m,l}^k - u_{n,m,l}^k \frac{\omega_{z,n+1,m,l}^k - \omega_{z,n-1,m,l}^k}{2\Delta x} \\ - v_{n,m,l}^k \frac{\omega_{z,n,m+1,l}^k - \omega_{z,n,m-1,l}^k}{2\Delta y} - w_{n,m,l}^k \frac{\partial \omega_z}{\partial z}|_{n,m,l}^k , \quad (5.125c)$$

which are the finite-difference versions of equations (3.12).

The  $z$  derivatives in equations (5.125) are computed using the formula

$$\frac{\partial h}{\partial z}(z) = \sum_{k=-\frac{K}{2}}^{\frac{K}{2}} ik H^k e^{ikz} \quad (5.126)$$

where

$$h(z) = \sum_{k=-\frac{K}{2}}^{\frac{K}{2}} H^k e^{ikz} . \quad (5.127)$$

The nonlinear terms  $f_{x,n,m,l}^k$ ,  $f_{y,n,m,l}^k$ , and  $f_{z,n,m,l}^k$  are transformed back to Fourier space using equations (5.5). This results in the nonlinear terms  $F_{x,n,m,l}^k$ ,  $F_{y,n,m,l}^k$ , and  $F_{z,n,m,l}^k$  for all  $n, m, l$ , and  $k$ . The pseudo-spectral method, together with the use of fast Fourier transforms, has an asymptotic operation count of

$$O(NMK \log_2 K) . \quad (5.128)$$

An alternative to the pseudo-spectral method is the spectral method. For the representative nonlinear term

$$\omega_z \frac{\partial u}{\partial x} , \quad (5.129)$$

the spectral method proceeds as follows: The Fourier series representation of the dependent variables  $u(x_n, y_m, z_k, t_l)$  and  $\omega_z(x_n, y_m, z_k, t_l)$  are substituted into

equation (5.129) to get

$$\omega_z \frac{\partial u}{\partial x} |_{n,m,l}^k = \left( \sum_{k=-\frac{K}{2}}^{\frac{K}{2}} \Omega_z^k(x_n, y_m, t_l) e^{ikz} \right) \left( \sum_{k=-\frac{K}{2}}^{\frac{K}{2}} \frac{\partial U^k}{\partial x}(x_n, y_m, t_l) e^{ikz} \right) . \quad (5.130)$$

The multiplication of the two series in equation (5.130) is performed in order to obtain the Fourier series representation of equation (5.129). This procedure is repeated for the other terms that make up the nonlinear part of the governing equations. In this way, the Fourier representation of the nonlinear terms is obtained. The asymptotic operation count for the spectral method is

$$O(NMK^2) . \quad (5.131)$$

For large values of  $K$ , the pseudo-spectral method requires fewer operations than does the spectral method. However, for small values of  $K$  the spectral method is faster. In this work, which is limited to small values of  $K$ , the spectral method is used.

### 5.7 Consistency, Stability, and Convergence of the Numerical Method

Finally, consistency, numerical stability, and convergence of the numerical method are discussed. A consistent numerical method is one whose truncation error approaches zero as the spatial and temporal grid increments approach zero. A numerical method is stable if the round-off error contained in the numerical solution does not grow with time. A convergent numerical method is one in which the numerical solution of the discretized partial differential equation approaches the exact solution of the partial differential equation as the grid sizes approach zero.

The relationship between consistency, stability, and convergence of a discretization scheme is given by the Lax Equivalence Theorem (Smith, 1985):

Given a properly posed linear initial-value problem and a linear finite-difference approximation to it that satisfies the consistency condition, stability is the necessary and sufficient condition for convergence.

In this work, the governing equations are not linear. However, it is still useful to examine the consistency and stability of the numerical method.

The truncation error of the numerical method described in this chapter is now discussed. Let

$$L_{\Delta x, \Delta y, \Delta t}(\hat{\Omega}) = 0 \quad (5.132)$$

represent the difference equations (5.42) and (5.43) and let  $\hat{\Omega}$  be the solution of those difference equations. Furthermore, let  $\Omega$  be the exact solution of the partial differential equations (5.4). Then, the truncation error  $E_{T, \Delta x, \Delta y, \Delta t}$  associated with the discrete operator  $L_{\Delta x, \Delta y, \Delta t}$  is

$$E_{T, \Delta x, \Delta y, \Delta t} = L_{\Delta x, \Delta y, \Delta t}(\Omega) \quad . \quad (5.133)$$

It can be shown that the hybrid ADI, Crank-Nicolson, Adams-Bashforth discretization scheme, coupled with second-order finite-difference approximations of the spatial derivatives, has the local truncation error

$$E_{T, \Delta x, \Delta y, \Delta t} = O(\Delta x^2, \Delta y^2, \Delta t^2) \quad . \quad (5.134)$$

This truncation error approaches zero as  $\Delta x$ ,  $\Delta y$ , and  $\Delta t$  approach zero and therefore the scheme is consistent. Similarly, the discretization scheme used to solve the Helmholtz equations is consistent and exhibits second-order spatial accuracy. The numerical method has spectral accuracy in the spanwise direction.

Evaluating the numerical stability of the discretization scheme used in this work is very difficult due to the nonlinearity of the governing equations. However, Pruett (1986), who used the same discretization scheme as discussed here, found that for simulations of instability waves in free shear layers, the condition

$$|u|_{max} \frac{\Delta t}{\Delta x} + |v|_{max} \frac{\Delta t}{\Delta y} + |w|_{max} \frac{\Delta t}{\Delta z} \leq 1 \quad (5.135)$$

was sufficient to ensure the numerical stability of the hybrid ADI, Crank-Nicolson, Adams-Bashforth discretization scheme.

For the simulation of instability waves in high-deficit wakes, it is noted that, because of numerical stability considerations, simulations of three-dimensional disturbances required a smaller time step  $\Delta t$  than did simulations of two-dimensional disturbances. Furthermore, although a stability criterion has not been derived, for these simulations the numerical method was stable for the spatial and temporal resolution that was employed.

## CHAPTER 6

### RESULTS

As discussed in Chapter 3, the laminar-turbulent transition of wakes is influenced by many nondimensional parameters. A thorough study of wake transition would require investigating the role of many of these parameters. However, due to the large amount of computer time and memory that is required to solve the Navier-Stokes equations, a detailed study of the effect of each parameter on wake transition is not possible.

In this work, investigations are limited to two areas. First, the influence of different levels of excitation on the behavior of two-dimensional disturbances is investigated. The results of these investigations are discussed in Section 6.1. Secondly, the interaction of two- and three-dimensional disturbances is investigated. This latter topic will be discussed in Section 6.2.

Before proceeding, the techniques used to analyze the data that result from the numerical simulations are discussed. The harmonic content of the flow variables is obtained by Fourier time series analysis. With  $\psi^k(x, y, t)$  representing any one of the flow quantities, the Fourier analyzed variables are obtained from

$$\hat{\psi}^k(x, y, F) = \frac{1}{L'_2 - L'_1 + 1} \sum_{l=L'_1}^{L'_2} c\psi^k(x, y, t_l) e^{-iI_{per}Ft_l}$$

with  $F = 0, \frac{1}{I_{per}}, \frac{2}{I_{per}}, \dots, \frac{L'_2 - L'_1}{I_{per}}$  .

(6.1)

The parameters  $L'_1$  and  $L'_2$  are the first and last time steps respectively of the time interval in which the data is Fourier analyzed. The parameter  $I_{per}$  denotes the number of oscillation periods that are analyzed. If one period of oscillation is

analyzed then  $I_{per} = 1$ , and if two periods of oscillation are analyzed then  $I_{per} = 2$ . The parameter  $c$  assumes different values depending on the flow variable that is analyzed. If  $\psi^k$  represents  $U^k$  or  $\Omega_x^k$  then  $c = 1$ . If  $\psi^k$  represents  $V^k$  or  $\Omega_y^k$  then  $c = r_2$ . Finally, if  $\psi^k$  represents  $W^k$  or  $\Omega_z^k$  then  $c = r_3$ . The parameter  $i$  is the imaginary number  $\sqrt{-1}$ .

The transformed variable  $\hat{\psi}^k(x, y, F)$  is the  $F^{\text{th}}$  time harmonic component of the flow variable  $\psi^k(x, y, t)$ . The  $F^{\text{th}}$  harmonic oscillates in time with the frequency  $F\beta$ , where  $\beta$  is the frequency of the wake excitation.

The amplitude of the  $F^{\text{th}}$  harmonic  $\hat{\psi}^k(x, y, F)$ , for  $k = 0$ , is

$$\psi_A^0(x, y, F) = \begin{cases} |\hat{\psi}^k(x, y, F)|, & \text{if } F = 0; \\ 2|\hat{\psi}^k(x, y, F)|, & \text{if } F > 0 \end{cases} \quad (6.2a)$$

and for  $k > 0$  is

$$\psi_A^k(x, y, F) = \begin{cases} 2|\hat{\psi}^k(x, y, F)|, & \text{if } F = 0; \\ 4|\hat{\psi}^k(x, y, F)|, & \text{if } F > 0. \end{cases} \quad (6.2b)$$

The phase of the  $F^{\text{th}}$  harmonic  $\hat{\psi}^k(x, y, F)$  is

$$\phi_\psi^k(x, y, F) = \arctan \left( \frac{-\text{Im}(\hat{\psi}^k(x, y, F))}{\text{Re}(\hat{\psi}^k(x, y, F))} \right) \quad (6.3a)$$

if  $\psi^k$  represents  $U^k$ ,  $V^k$ , or  $\Omega_x^k$ . The phase of the  $F^{\text{th}}$  harmonic  $\hat{\psi}^k(x, y, F)$  is

$$\phi_\psi^k(x, y, F) = \arctan \left( \frac{\text{Re}(\hat{\psi}^k(x, y, F))}{\text{Im}(\hat{\psi}^k(x, y, F))} \right) \quad (6.3b)$$

if  $\psi^k$  represents  $W^k$ ,  $\Omega_x^k$ , or  $\Omega_y^k$ .  $\text{Im}(\ )$  and  $\text{Re}(\ )$  denote the real and imaginary parts of  $\hat{\psi}^k(x, y, F)$  respectively.

Additional quantities that are calculated are the wavenumber  $\alpha_r^k$ , the amplification rate  $\alpha_i^k$ , and the phase velocity  $c_p^k$  of the various harmonic components. For

linear stability theory, in which the base flow is assumed to be parallel, these quantities are uniquely defined for a given disturbance frequency, spanwise wavenumber, and flow Reynolds number. Furthermore, for a disturbance that is governed by linear stability theory,  $\alpha_r^k$ ,  $\alpha_i^k$ , and  $c_p^k$  can be computed from

$$\alpha_{r,LST}^k = \frac{\partial \phi_\psi^k}{\partial x}(x, y) , \quad (6.4a)$$

$$\alpha_{i,LST}^k = -\frac{\partial}{\partial x} (\ln(\psi_A^k(x, y))) , \quad (6.4b)$$

$$\text{and } c_{p,LST}^k = \frac{\beta}{\alpha_{i,LST}^k} . \quad (6.4c)$$

The values of  $\alpha_{r,LST}$ ,  $\alpha_{i,LST}$ , and  $c_{p,LST}$  are independent of  $x$  and  $y$  and are independent of which flow variable is represented by  $\psi^k$ . However, if expressions analogous to equations (6.4) are used to obtain similar quantities for a nonparallel flow, then the coordinates  $x$  and  $y$  as well as the flow variable that is represented by  $\psi^k$  have considerable influence on the values of  $\alpha_r^k$ ,  $\alpha_i^k$ , and  $c_p^k$ . Gaster (1974) discusses some of the various ways to calculate  $\alpha_r^k$ ,  $\alpha_i^k$ , and  $c_p^k$  for nonparallel flows.

For this work, the disturbance quantities  $\alpha_r^k$ ,  $\alpha_i^k$ , and  $c_p^k$  are calculated in the following manner. The streamwise wavenumber  $\alpha_r^k$  of the  $F^{\text{th}}$  harmonic  $\hat{\psi}^k(x, y, F)$  is calculated from

$$\alpha_r^k(x, F) = \frac{\partial \phi_\psi^k}{\partial x}(x, y, F) \quad (6.5a)$$

where the transverse coordinate  $y$  is taken to be constant in equation (6.5a). The amplification rate  $\alpha_i^k$  of the  $F^{\text{th}}$  harmonic  $\hat{\psi}^k(x, y, F)$  is calculated from

$$\alpha_i^k(x, F) = -\frac{\partial}{\partial x} (\ln(\psi_A^k(x, y_{max}(x), F))) . \quad (6.5b)$$

In formula (6.5b),  $y_{max}(x)$  is the transverse coordinate, as a function of  $x$ , at which the amplitude  $\psi_A^k(x, y, F)$  attains its maximum value. The phase velocity of the  $F^{\text{th}}$  harmonic  $\hat{\psi}^k(x, y, F)$  is computed from

$$c_p^k(x, F) = \frac{\beta F}{\alpha_r^k(x, F)} . \quad (6.5c)$$

Finally, the disturbance kinetic energy is calculated from

$$\hat{E}^k(x, F) = \frac{1}{2} \int_{y_0}^{y_M} (u_A^k(x, y, F)^2 + v_A^k(x, y, F)^2 + w_A^k(x, y, F)^2) dy . \quad (6.6)$$

The kinetic energy  $\hat{E}^k(x, F)$  is a measure of the disturbance amplitude. Also, because the kinetic energy is an integral quantity, it does not depend on the transverse coordinate  $y$ . Amplification rates of the harmonic components can be calculated from the kinetic energy using

$$\alpha_i^k(x, F) = -\frac{1}{2} \frac{\partial}{\partial x} (\ln(\hat{E}^k(x, F))) . \quad (6.7)$$

Use of equation (6.7) to calculate  $\alpha_i^k$  is advantageous because, unlike equation (6.5b), it does not depend on the transverse coordinate  $y$ .

### 6.1 Investigations of Two-Dimensional Disturbance Development

In this section, investigations of two-dimensional disturbance development in a high-deficit flat plate wake are discussed. Several different calculations are undertaken. With the first two calculations, termed Case-1 and Case-2, the suitability of the numerical method for the calculation of wake disturbances is tested. In Case-1, the method is tested by comparing the results for small amplitude disturbances to linear stability theory. In Case-2, the results of the calculation are compared to the experimental measurements of Sato (1970). In Case-2, the numerical method is tested for larger amplitude disturbances than in Case-1. In Case-3 and Case-4, the large amplitude behavior of wake disturbances is investigated. Case-4 is identical to Case-3 except that the amplitude level of the excitation, denoted by  $A_2$ , is larger than in Case-3. By calculating disturbances for different excitation levels, the influence of the initial amplitude on the disturbance development is observed. Finally, in Case-5 the effect of the outflow boundary conditions on the results is

investigated. This is done by repeating Case-3 in a longer spatial domain. In all of these calculations, the wake is excited with a two-dimensional sinuous mode disturbance of frequency  $\beta$ . Finally, because the calculated disturbances are two-dimensional, only  $U^0$ ,  $V^0$ , and  $\Omega_z^0$  are calculated.

#### Case-1

In this case, the behavior of a small amplitude disturbance in a nonparallel flat plate wake is investigated. Because the base flow is nonparallel, there is no proper way to compare these results to linear stability theory. In fact, Gaster (1974) states that the agreement between linear stability theory, for which the flow is assumed to be parallel, and experiments (numerical or physical), for which the flow is nonparallel, can never be better than  $O(Re^{-\frac{1}{2}})$ . Therefore, comparisons of the numerical results to linear stability theory are qualitative in nature and can not be used to test the accuracy of the numerical method. However, this calculation can be used to obtain some measure of the suitability of the numerical method for calculations of small amplitude disturbances.

This calculation was performed in a spatial domain bounded by

$$x_0 = .3 , \quad x_N = .7 , \quad y_0 = -10 , \quad \text{and} \quad y_M = 10 . \quad (6.8)$$

The transverse extent of the spatial domain was specified so that the vorticity disturbances would be approximately zero at the freestream boundaries. For the streamwise extent of the domain, it was required that the domain be long enough to contain several wavelengths of the fundamental disturbance. The domain is shown in Figures 2.1 and 5.1.

The base flow was calculated subject to the inflow streamwise velocity distribution  $u^I(y)$  given by equation (4.6a). At the inflow boundary, the wake centerline

velocity  $U_c$  and the wake half-width  $b$  were

$$U_c = .5 \quad \text{and} \quad b = 1.3 \quad . \quad (6.9)$$

The streamwise velocity component of the computed base flow is shown in Figure 6.1.

As discussed in Section 4.4, the wake is excited using the time-dependent boundary conditions (4.16). For this calculation, the disturbance amplitude was  $A_2 = .001$ . In terms of the streamwise velocity disturbance  $u'(x_0, y)$  at the inflow boundary,  $A_2$  is given by the relation  $A_2 = \max(|u'(x_0, y)|)$  where the function  $\max(|u'(x_0, y)|)$  denotes the maximum value of  $|u'(x_0, y)|$  with respect to the  $y$  direction. The disturbance frequency was  $\beta = .317$ . For this frequency, the amplification rate is less than the maximum amplification rate that is predicted by linear stability theory. Furthermore, the disturbance that corresponds to this frequency experiences amplification throughout the spatial domain. The Orr-Sommerfeld eigenfunctions that correspond to this frequency are shown in Figures 6.2.

The influence of  $\Delta x$  and  $\Delta y$  on the numerical results was investigated to determine the spatial discretization that results in solutions that are reasonable independent of the grid sizes. A detailed discussion of these investigations is given in Appendix B. For this calculation, the grid

$$N = 128 \quad \text{and} \quad M = 64 \quad (6.10)$$

was sufficient for this purpose. For the time step  $\Delta t$ , numerical stability rather than temporal accuracy was the most severe constraint. Therefore, the influence of

the time step on the numerical results was not investigated. To maintain numerical stability, the time step was specified to be

$$\Delta t = \frac{T_F}{L_{max}} \quad \text{with} \quad L_{max} = 64 \quad . \quad (6.11)$$

The parameter  $L_{max}$  denotes the number of time steps per fundamental disturbance period. The response of the wake to the excitation at the inflow boundary was calculated for five periods  $T_F$  of the fundamental disturbance ( $L_2 = 320$ ) where  $T_F = \frac{2\pi}{\beta}$ .

For this calculation, the spatial domain contained approximately eight wavelengths of the fundamental disturbance. Each disturbance wavelength was discretized by approximately sixteen grid points. In the transverse direction, the spatial domain contained approximately twenty momentum thicknesses (based on the inflow velocity distribution) with approximately 3.2 grid points per momentum thickness. As mentioned previously, investigations of the influence of the grid sizes on the results of the numerical calculation (see Appendix B) have established the suitability of the spatial discretization.

The relevant parameters in this calculation are summarized below:

Case-1:

the streamwise location of the inflow boundary,	$x_0$	=	.3;
the streamwise location of the outflow boundary,	$x_N$	=	.7;
the transverse location of the lower freestream boundary, $y_0$		=	-10;
the transverse location of the upper freestream boundary, $y_M$		=	10;
the Reynolds number $Re = \frac{U_\infty l}{\nu}$ ,		$Re$	= 200000;
the amplitude level of the wake excitation,		$A_2$	= .001;
the frequency of the wake excitation,		$\beta$	= .317;
the number of streamwise grid increments,		$N$	= 128;
the number of transverse grid increments,		$M$	= 64;
the number of time steps calculated,		$L_2$	= 320;
and the time steps per fundamental disturbance period, $L_{max}$		$L_{max}$	= 64.

Results of this calculation are shown in Figures 6.3, 6.4, 6.5, and 6.6. Amplification curves based on the disturbance kinetic energy  $\hat{E}^0(x, F)$  are shown in Figure 6.3. These amplification curves are compared with analogous curves from linear stability theory that are based on the amplification rate  $\alpha_i$ . However, the amplification of the kinetic energy that results from the Navier-Stokes calculation arises from two different sources. First, the kinetic energy amplifies due to the linear instability. Secondly, the kinetic energy changes due to the slow divergence of the base flow. However, despite the differences between linear stability theory and the calculation, the kinetic energy of the fundamental disturbance ( $F = 1$ ) still compares closely to the linear stability theory prediction of the fundamental disturbance kinetic energy. The mean disturbance component ( $F = 0$ ) and the second harmonic ( $F = 2$ ) are also present, but are much smaller than the fundamental disturbance.

For the streamwise location  $x = .35$ , the amplitude and phase distributions of the fundamental disturbance component ( $F = 1$ ) are compared to the amplitude and phase distributions of the Orr-Sommerfeld eigenfunctions. These comparisons are shown in Figures 6.4 and 6.5. The amplitudes of the Orr-Sommerfeld eigenfunctions are multiplied by the constant

$$c_{LST} = \frac{\psi_A^0(x = .35, y_{max}, 1)}{\psi_{ALST}(y_{max})} \quad (6.12)$$

so that at  $y = y_{max}$ , they will be exactly equal to the amplitude distribution  $\psi_A^0$  of the calculated fundamental disturbance. The phase distributions of the Orr-Sommerfeld eigenfunctions are shifted by the constant

$$d_{LST} = \phi_\psi^0(x = .35, y_{max}, 1) - \phi_{\psi LST}(y_{max}) \quad (6.13)$$

so that at  $y = y_{max}$ , they will be equal to the phase distributions of the calculated fundamental disturbance. The constant  $y_{max}$  was defined previously. The function  $\psi_{ALST}(y)$  is the amplitude of the Orr-Sommerfeld eigenfunction and  $\phi_{\psi LST}(y)$  is the phase of the Orr-Sommerfeld eigenfunction. As before,  $\psi^k$  can represent any one of the flow variables.

As can be observed in Figures 6.4, the amplitude distributions of the fundamental disturbance are very similar to the amplitude distributions of the Orr-Sommerfeld eigenfunctions. In Figure 6.4c, the vorticity disturbances are observed to be quite small ( $O(10^{-8})$ ) at the freestream boundaries. This confirms that the transverse domain was wide enough for this calculation.

The comparison of the phase distributions of the fundamental disturbance to those of the Orr-Sommerfeld eigenfunctions is shown in Figures 6.5. In these figures, reasonably good agreement between the numerical and theoretical phase

distributions is observed. The differences between the numerical and theoretical phase distributions that are observed at the transverse locations  $y = \pm 10$  are due to the freestream boundary conditions. For the streamwise and transverse velocity components, the observed differences are due to the exponential decay boundary conditions, (5.25a) and (5.28a). For the spanwise vorticity, the differences arise because the theoretical spanwise vorticity satisfies exponential decay freestream boundary conditions while the calculated spanwise vorticity is set to zero at the freestream boundaries.

Finally, in Figures 6.6 the streamwise wavenumber  $\alpha_r^0$ , the amplification rate  $\alpha_i^0$ , and the phase velocity  $c_p^0$  of the fundamental disturbance are compared to the analogous quantities from linear stability theory. As mentioned previously, the agreement between linear stability theory and the numerical experiments can not be better than  $O(Re^{-\frac{1}{2}})$  Gaster (1974). Furthermore, the values of  $\alpha_r^0$ ,  $\alpha_i^0$ , and  $c_p^0$  depend on the flow variable and transverse location that are used for calculation of these quantities. The streamwise wavenumber  $\alpha_r^0$  and the phase velocity  $c_p^0$  are computed from the flow variables  $U^0$ ,  $V^0$ , and  $\Omega_z^0$  for the transverse location  $y = 5$ . The amplification rate  $\alpha_i^0$  is computed from all three flow variables as well as from the kinetic energy  $\hat{E}^0(x, 1)$ . Equations (6.5) and (6.7) are used to calculate these values. In Figures 6.6, the observed differences between the theoretical and calculated values are approximately of the order  $O(Re^{-\frac{1}{2}})$ . Therefore, based on the results of Figures 6.6, the agreement between the calculation and linear stability theory is reasonable. Additionally, comparable results were obtained when other transverse locations were used to calculate  $\alpha_r$  and  $c_p$ .

The agreement between the calculated results and linear stability theory is within the limitations imposed by comparisons of parallel linear stability theory to nonparallel numerical simulations. The disturbance amplification rate and

wavenumber,  $\alpha_z$ ; and  $\alpha_r$ , as well as the disturbance amplitude and phase distributions, all exhibit reasonable agreement with linear stability theory. It is concluded that the numerical method, with the spatial and temporal discretization that was employed, is suitable for the calculation of small amplitude disturbances in flat plate wakes.

### Case-2

As a further test of the numerical method, the results of this calculation are compared to the experiments of Sato (1970). In contrast to Case-1, in this calculation the disturbances attain large amplitude levels. To facilitate the comparison of the numerical results to the experimental data, the parameters for this calculation are selected so that the calculated wake models the wake from the experiments of Sato.

This calculation was performed in a spatial domain with boundaries at

$$x_0 = .03 , \quad x_N = .75 , \quad y_0 = -16 , \quad \text{and} \quad y_M = 16 . \quad (6.14)$$

As in Case-1, the transverse extent of the domain was designed so that the vorticity disturbances would be approximately zero at the freestream boundaries. In the discussion of Case-5, it will be shown that the streamwise extent of the domain is sufficiently long for the present case.

The base flow was computed subject to the Gaussian inflow streamwise velocity distribution given by equation (4.5a). This distribution was employed because, as shown in Figure 6.7, it compares well to experimentally obtained streamwise velocity distributions of high-deficit flat plate wakes (Sato and Kuriki, 1961). At the inflow boundary, the wake centerline velocity  $U_c$  and the wake half-width  $b$  were

$$U_c = .234826 \quad \text{and} \quad b = 1.15 . \quad (6.15)$$

The values of  $U_c$ ,  $b$ , and  $x_0$  were chosen so that the computed base flow would closely model the wake in the experiments of Sato (1970).

The streamwise velocity  $U^0$  of the computed base flow is shown in Figure 6.8. As observed in Figure 6.9, the streamwise variation of the centerline ( $y = 0$ ) velocity of the calculated base flow compares closely to the similarity solution of Goldstein (1929). The similarity solution was calculated using the series representation for the inner wake given by Goldstein (1929). The large variation of the centerline velocity indicates that nonparallel effects may play an important role in the initial development of disturbances in high-deficit wakes.

In his experimental work, Sato (1970) found that the frequency of the predominant small amplitude disturbance in flat plate wakes corresponded almost exactly to the frequency of maximum amplification as predicted by linear stability theory. Therefore, in this calculation the undisturbed wake was excited at its most unstable frequency. This frequency was determined from a linear stability analysis of the inflow streamwise velocity distribution. The eigenvalues (streamwise wavenumber and amplification rate) of the Orr-Sommerfeld equation were obtained for a range of frequencies in order to determine the frequency of greatest instability. The streamwise wavenumber  $\alpha_r$ , amplification rate  $\alpha_i$ , and phase velocity  $c_p$  obtained from this analysis are shown in Figures 6.10. As seen in Figure 6.10b, the amplification rate  $-\alpha_i$  of the sinuous mode (mode-1) achieves its maximum value at the frequency  $\beta = .51$ . The eigenfunctions of the Orr-Sommerfeld equation, corresponding to the frequency  $\beta = .51$ , are shown in Figures 6.11.

When this calculation was undertaken, it was thought that Sato (1970) had not indicated the initial disturbance levels in his experiments. Therefore, it was necessary to estimate the amplitude level for the disturbance excitation in the calculation. The amplitude of the wake excitation was chosen to be  $A_2 = .000667$

as this was thought to be a good estimate of the disturbance level in Sato's (1970) experiments. However, after these calculations were completed, it was learned that the forcing level in Sato's experiments corresponded to  $A_2 \approx .001$ .

As in Case-1, the influence of the grid sizes  $\Delta x$  and  $\Delta y$  on the numerical results was investigated in order to determine the spatial discretization that resulted in solutions that were reasonable independent of the grid sizes. A discussion of these investigations is given in Appendix B. For this calculation, the grid

$$N = 1024 \quad \text{and} \quad M = 256 \quad (6.16)$$

was sufficient for this purpose. Again, the time step was determined by stability considerations rather than considerations of temporal accuracy. Therefore, the influence of the time step on the numerical results was not investigated. For this calculation, the time step

$$\Delta t = \frac{T_F}{L_{max}} , \quad \text{with} \quad L_{max} = 128 \quad (6.17)$$

was sufficiently small to ensure numerical stability. The response of the wake to the excitation at the inflow boundary was calculated for seventeen oscillation periods  $T_F$  of the fundamental disturbance ( $L_2 = 2176$ ).

For this calculation, greater spatial resolution than in Case-1 was required because of the presence of large amplitude harmonics of the fundamental disturbance. The spatial domain contained approximately thirty wavelengths of the fundamental disturbance (based on the wavelength at the inflow boundary), with approximately 34 grid points per wavelength. In the transverse direction, the spatial domain contained approximately 32 momentum thicknesses (based on the inflow boundary velocity distribution) with approximately eight grid points per

momentum thickness. As mentioned, investigations of the influence of the grid sizes on the results of the numerical calculation (see Appendix B) have established the suitability of the spatial discretization.

The relevant parameters in this calculation are summarized below:

**Case-2:**

the streamwise location of the inflow boundary,	$x_0$	=	.03;
the streamwise location of the outflow boundary,	$x_N$	=	.75;
the transverse location of the lower freestream boundary, $y_0$		=	-16;
the transverse location of the upper freestream boundary, $y_M$		=	16;
the Reynolds number $Re = \frac{\bar{U}_\infty \bar{\ell}}{\nu}$ ,	$Re$	=	200000;
the amplitude level of the wake excitation,	$A_2$	=	.000667;
the frequency of the wake excitation,	$\beta$	=	.51;
the number of streamwise grid increments,	$N$	=	1024;
the number of transverse grid increments,	$M$	=	256;
the number of time steps calculated,	$L_2$	=	2176;
and the time steps per fundamental disturbance period, $L_{max}$		=	128.

Amplitude distributions of the fundamental disturbance component of the streamwise velocity were obtained by Fourier time series analysis in the time interval  $15T_F < t \leq 17T_F$ . Comparisons of these amplitude distributions to those from the experiments of Sato (1970) are shown in Figures 6.12. The experimental results are plotted on an arbitrary scale, but the relative amplitude level at each streamwise location is accurately represented in the figure. The streamwise locations  $x$  for which the amplitudes in Figure 6.12a are plotted relate to the streamwise locations  $X$  in Figure 6.12b according to

$$x = \frac{X}{\bar{\ell}} . \quad (6.18)$$

The flat plate length  $\bar{l}$  was defined in Chapter 3 and was equal to 300mm in Sato's experiments. There is good qualitative agreement between the numerical and experimental amplitude distributions at the streamwise locations  $z = .067$  ( $X = 20\text{mm}$ ),  $z = .1$  ( $X = 30\text{mm}$ ), and  $z = .133$  ( $X = 40\text{mm}$ ). At  $z = .200$  ( $X = 60\text{mm}$ ), the shapes of the amplitude distributions for both the numerical simulation and the experiment are similar, but the amplitude level relative to the level at the previous location ( $z = .133$ ) is smaller for the numerical calculation than for the experiment. This is due to differences between the excitation amplitude in the calculation and in the experiment. Additionally, it is noted that in Figure 6.12b, the experimentally obtained amplitude distribution for  $X = 20\text{mm}$  is larger than the amplitude distribution for  $X = 30\text{mm}$ . As this is somewhat inconsistent with expected behavior, it is possible that the curves are mislabeled so that the curve labeled  $X = 30\text{mm}$  actually corresponds to  $X = 20\text{mm}$  and vice-versa. The comparison of the numerical results to the experimental results that was discussed in this paragraph was based on the assumption that the curves were mislabeled.

The streamwise variation of the mean centerline velocity and the mean wake half-width for both the calculation and the experiments of Sato (1970) are shown in Figures 6.13. The horizontal scale  $0 \leq z \leq 2.67$  in Figure 6.13a corresponds to the horizontal scale  $0 \leq X \leq 800\text{mm}$  in Figure 6.13b. The mean flow is the zero frequency ( $F = 0$ ) component of the disturbed wake and it therefore contains any nonlinearly generated 0<sup>th</sup> harmonic of the fundamental disturbance.

In Figures 6.13, the calculated mean centerline velocity compares reasonably well to the experimentally obtained mean centerline velocity (open circles in Figure 6.13b). Both the numerical and experimental centerline velocities increase rapidly.

This rapid rise is due to nonlinear interactions. As observed in Figures 6.13, the wake half-width for the calculation is similar to the half-width for the experiment.

The results of this calculation exhibit good qualitative comparison with the experimental results of Sato (1970). Good agreement between the numerical and experimental results was obtained for large amplitude levels where nonlinear interactions were important. Therefore, it is concluded that the numerical method is suitable for the calculation of large amplitude disturbances in high-deficit wakes.

### Case-3

The purpose of this calculation was to investigate the effect of larger amplitudes on the disturbance development. Therefore, for this calculation all parameters except for the excitation amplitude were kept the same as in Case-2. For this calculation (Case-3), the excitation amplitude was  $A_2 = .001$ . The base flow that was used as the initial condition was identical to the base flow from Case-2 (see Figures 6.8 and 6.9).

Figures 6.14 display the flow variables  $U^0$ ,  $V^0$ , and  $\Omega_z^0$  at the final time of the calculation,  $t = 2176\Delta t$ . Due to the rapid growth of the disturbances, the wake changes significantly from its undisturbed state. Very near the inflow boundary, the wake appears undisturbed because the disturbances are still quite small in this region of the spatial domain. Beyond  $x/\Delta x \approx 128$  ( $x \approx .12$ ), the disturbances become large enough so that they are the dominant feature in the wake. Observing the spanwise vorticity  $\Omega_z^0$  in Figure 6.14c, a pattern develops that resembles that of a Kármán vortex street. This pattern develops as the disturbances reach large amplitude levels. As mentioned in Chapter 3, the vorticity is defined as  $\omega = -\nabla \times u$ .

As seen in Figures 6.14, at this time the disturbances are still quite far upstream of the outflow boundary. Based on the wavelength of the vortex street

observed in Figure 6.14c, the leading edge of the disturbance wave is approximately seven wavelengths upstream of the outflow boundary. Therefore, at this time the assumption that the wake is undisturbed near the outflow boundary is clearly satisfied. Furthermore, the vorticity disturbances are confined to a region near the wake centerline and appear to be quite small at the freestream boundaries.

In order to see more details of the vorticity field, vorticity plots that correspond to smaller regions of the spatial domain are shown in Figures 6.15 and 6.16. Figure 6.15a shows the spanwise vorticity  $\Omega_z^0$  in the upstream half of the spatial domain ( $.03 \leq z \leq .39$ ,  $0 \leq z/\Delta z \leq 512$ ) and Figure 6.15b shows the spanwise vorticity  $\Omega_z^0$  for the streamwise interval  $.03 \leq z \leq .27$  ( $0 \leq z/\Delta z \leq 340$ ). In both of these figures, rapid disturbance development is observed. In Figures 6.16, the spanwise vorticity  $\Omega_z^0$  is shown for the streamwise intervals  $.03 \leq z \leq .12$  ( $0 \leq z/\Delta z \leq 128$ ),  $.12 \leq z \leq .21$  ( $128 \leq z/\Delta z \leq 256$ ),  $.21 \leq z \leq .30$  ( $256 \leq z/\Delta z \leq 384$ ), and  $.30 \leq z \leq .39$  ( $384 \leq z/\Delta z \leq 512$ ). These figures show in great detail the disturbances development that results from the wake excitation. In Figure 6.16d, a very distinct vortex street pattern is visible.

Amplification curves based on the kinetic energy  $\hat{E}^0(z, F)$  are shown in Figure 6.17. The kinetic energy is calculated using equation (6.6). The harmonic content of the flow variables was obtained by Fourier time series analysis of the velocity components in the time interval  $13T_F < t \leq 15T_F$ . For  $z < .11$ , the streamwise variation of the kinetic energy of the fundamental disturbance ( $F = 1$ ) agrees closely with that obtained from linear stability theory calculations. In the linear stability theory calculations, the streamwise variation of the base flow was accounted for by the use of a quasi-uniform assumption. The mean disturbance component ( $F = 0$ ), the second harmonic ( $F = 2$ ), and the third harmonic ( $F = 3$ ) also grow rapidly in the region  $z < .11$ . In particular, the second and

third harmonics grow more rapidly than the fundamental disturbance. Sato and Kuriki (1961) and Sato (1970) have also observed large mean and second harmonic components in flat plate wakes.

The saturation of the fundamental disturbance occurs at  $x \approx .11$ . There, the amplitude of the streamwise velocity component of the fundamental disturbance is approximately twenty percent of the freestream streamwise velocity. Beyond  $x \approx .11$ , the fundamental disturbance varies little in the streamwise direction. The mean disturbance component and the second harmonic also saturate and reach a state in which they vary little in the streamwise direction.

The saturation of the fundamental disturbance, which does not occur for the small amplitude, linear development of disturbances, may nevertheless be indirectly explained by the changing stability characteristics of the mean flow. As a simple way of determining the stability of the mean flow, the spatial amplification rate  $-\alpha_i(x)$  of the fundamental disturbance is computed from a linear stability theory analysis of the mean flow. Then, the streamwise variation of the kinetic energy of the fundamental disturbance is computed from

$$\hat{E}^0(x, 1) = \hat{E}^0(x_0, 1) e^{-\int_{x_0}^x 2\alpha_i dx} \quad (6.19)$$

using the amplification rates of linear stability theory. The streamwise variation of the kinetic energy of the fundamental disturbance, as predicted by a linear stability analysis of the mean flow, is denoted in Figure 6.17 by the label 'LST MEAN FLOW'. This simplified model also exhibits saturation of the fundamental disturbance. However, the amplitude of the fundamental disturbance after saturation is over-predicted. These results indicate that the saturation of the fundamental disturbance is at least partly due to the changing stability characteristics of the

nonlinearly generated mean flow. Alternatively, the variation of the mean flow can be thought of as being due to the growth and eventual saturation of the fundamental disturbance.

The presence of the harmonic components  $F = 0.5$ ,  $F = 1.5$ , and  $F = 2.5$  in Figure 6.17 is due to the fact that the wake has not yet achieved a truly time periodic state in the time interval  $13T_F < t \leq 15T_F$ . Evidence of the nonperiodic nature of the wake is given in Figure 6.18 which shows the temporal variation of the transverse velocity  $V^0$  in the time interval  $13T_F < t \leq 15T_F$ . It is apparent from Figure 6.18 that, in the time interval shown, the transverse velocity  $V^0$  is not temporally periodic at  $x = .27$ . Instead, the amplitude of  $V^0$  that corresponds to the streamwise location  $x = .27$  appears to be increasing with time. Fourier analysis of this data results in the  $F = 0.5$ ,  $F = 1.5$ , and  $F = 2.5$  harmonics that appear in Figure 6.17. Later, in the discussion of Case-5 in which a larger streamwise domain was employed, it will be shown that for the same streamwise locations the flow variables eventually become temporally periodic after more time has elapsed. When periodicity is reached, the harmonic components  $F = 0.5$ ,  $F = 1.5$ , and  $F = 2.5$  decrease to negligible levels. However, as will also be shown in Case-5, the  $F = 0.5$ ,  $F = 1.5$ , and  $F = 2.5$  harmonics do not influence the other harmonic components.

The streamwise variation of the mean centerline velocity and the mean wake half-width are shown in Figures 6.19 and 6.20 respectively. From these figures, it is apparent that the mean flow is quite different from the base flow and may have very different stability characteristics.

The streamwise wavenumber  $\alpha$ , and the phase velocity  $c_p$  of the fundamental disturbance are shown in Figures 6.21. They are compared with the corresponding quantities that are obtained from a linear stability analysis of the calculated mean

flow. The wavenumber and phase velocity that are obtained from this analysis compare well to the wavenumber and phase velocity of the calculated fundamental disturbance.

#### Case-4

The results of Case-3 have shown that a larger excitation amplitude has significant effects on the disturbance development. For this calculation, the amplitude was increased by a factor of ten over that in Case-3, resulting in  $A_2 = .01$ . The base flow was identical to that of Case-2 and Case-3 (see Figures 6.8 and 6.9). The response of the wake to the excitation at the inflow boundary, was calculated for fifteen fundamental disturbance periods ( $L_2 = 1920$ ). All other parameters were identical to Case-3.

Amplification curves based on the disturbance kinetic energy of the mean component  $F = 0$ , the fundamental disturbance  $F = 1$ , and the second harmonic  $F = 2$  are shown in Figures 6.22. For comparison, the analogous curves of Case-3 for which  $A_2 = .001$  are also displayed in these figures. The amplification curves for the larger excitation level,  $A_2 = .01$ , saturate further upstream and at higher amplitude levels than those for Case-3. However, qualitatively the amplification curves are quite similar for the two excitation levels.

The streamwise variation of the mean centerline velocity and the mean wake half-width are shown in Figures 6.23 and 6.24 and are compared with the corresponding curves from Case-3. For both excitation levels, the centerline velocity increases rapidly due to nonlinear interactions. However, for the higher excitation amplitude, the rapid increase in the centerline velocity begins further upstream. The wake half-width, shown in Figure 6.24, behaves in a manner similar to the centerline velocity. The increase in the wake half-width, which is also due to

nonlinear interactions, begins further upstream when the excitation amplitude is larger.

The qualitative behavior of the disturbed wake, as observed in Figures 6.22, 6.23, and 6.24, is similar regardless of the excitation amplitude. The main influence of the larger excitation amplitude is to accelerate the onset of nonlinear interactions and the saturation of the various disturbance components.

#### Case-5

With this calculation, the influence of the outflow boundary conditions on the numerical results is investigated. For this, the calculation of Case-3 is repeated with a streamwise domain that is 1.5 times longer than the one in Case-3. All other parameters for this calculation were identical to those of Case-3. Thus, the influence of the outflow boundary conditions can be assessed.

This calculation was performed in a spatial domain bounded by

$$x_0 = .03 \quad , \quad x_N = 1.11 \quad , \quad y_0 = -16 \quad , \quad \text{and} \quad y_M = 16 \quad . \quad (6.20)$$

The spatial domain was discretized into  $N$  streamwise grid increments and  $M$  transverse grid increments with

$$N = 1536 \quad \text{and} \quad M = 256 \quad . \quad (6.21)$$

The spatial resolution that resulted from this discretization was identical to that of Case-3. The response of the wake to the excitation at the inflow boundary was calculated for 25 periods  $T_F$  of the fundamental disturbance ( $L_2 = 3200$ ) using the same time step as in Case-3. The base flow was computed subject to the same inflow boundary conditions as discussed in Case-2.

The relevant parameters in this calculation are summarized below:

**Case-5:**

the streamwise location of the inflow boundary,	$x_0$	=	.03;
the streamwise location of the outflow boundary,	$x_N$	=	1.11;
the transverse location of the lower freestream boundary, $y_0$		=	-16;
the transverse location of the upper freestream boundary, $y_M$		=	16;
the Reynolds number $Re = \frac{U_{\infty} L}{\nu}$ ,	$Re$	=	200000;
the amplitude level of the wake excitation,	$A_2$	=	.001;
the frequency of the wake excitation,	$\beta$	=	.51;
the number of streamwise grid increments,	$N$	=	1536;
the number of transverse grid increments,	$M$	=	256;
the number of time steps calculated,	$L_2$	=	3200;
and the time steps per fundamental disturbance period, $L_{max}$		=	128.

The streamwise variation of the base flow centerline velocity for this calculation ( $N = 1536$ ) is shown in Figure 6.25 together with the corresponding curve of Case-3 ( $N = 1024$ ). It is obvious that the centerline velocity is practically identical for both cases. This is an indication that the outflow boundary had negligible effect on the base flow for Case-3.

Contours of instantaneous spanwise vorticity for  $t = 2176\Delta t$  and  $t = 3200\Delta t$  are shown in Figures 6.26. For  $t = 2176\Delta t$ , the spanwise vorticity contours are similar to those in Figure 6.14c (Case-3). The disturbances experience rapid streamwise amplification downstream of the inflow boundary, attain relatively large amplitude levels, and eventually dominate the flow field. The wake develops a Kármán vortex street pattern similar to what was observed in Figure 6.14c. Figure 6.26b shows the spanwise vorticity at  $t = 3200\Delta t$ . A vortex street pattern is also visible

for this time. However, the vortex street has propagated much farther downstream than in Figure 6.26a.

In Figures 6.27, amplification curves for the disturbance kinetic energy  $\hat{E}^0(x, F)$  of the mean component  $F = 0$ , the fundamental disturbance  $F = 1$ , and the second harmonic  $F = 2$  are compared to the corresponding curves from Case-3. The disturbance kinetic energy for Case-3 ( $N = 1024$ ) is computed using equation (6.6) and the Fourier analyzed velocity components from the time interval  $13T_F < t \leq 15T_F$ . Similarly, the disturbance kinetic energy for Case-5 ( $N = 1536$ ) is computed using the Fourier analyzed velocity components from the time interval  $23T_F < t \leq 25T_F$ . From Figures 6.27, it is obvious that the amplification curves for the various harmonic components corresponding to Case-5 ( $N = 1536$ ) are almost identical to the corresponding curves from Case-3 ( $N = 1024$ ). The only differences are observed in the region  $x > .20$ . These differences are due to the different time intervals used to Fourier analyze the velocity components for each case. The otherwise good agreement between the results of Case-3 and Case-5 indicates that the influence of the outflow boundary conditions on Case-3 is minimal.

Figure 6.28 shows the amplification curves for the kinetic energy  $\hat{E}^0(x, F)$  that results from the Fourier time series analysis of the velocity components in the time interval  $23t_F < t \leq 25T_F$ . It is observed that the harmonic components  $F = 0.5$ ,  $F = 1.5$ , and  $F = 2.5$  are smaller by several decades when compared to the results of Case-3 as displayed in Figure 6.17. This reduction is due to the fact that the wake disturbances are periodic in the time interval  $23T_F < t \leq 25T_F$ . This periodic behavior is apparent from Figure 6.29 which shows the temporal behavior of the transverse velocity  $V^0$  in the time interval  $23T_F < t \leq 25T_F$ .

Clearly,  $V^0$  is approximately periodic for all the streamwise locations that are shown in Figure 6.29.

### 6.2 Investigations of Three-Dimensional Disturbance Development

In this section, investigations of three-dimensional disturbance development in a high-deficit flat plate are discussed. Several different calculations are undertaken. With the first calculation (Case-6), the ability of the numerical method to accurately simulate three-dimensional disturbances is demonstrated. This calculation is the three-dimensional analog of Case-1. In Case-7, the response of a wake when subject to a three-dimensional excitation is investigated. In contrast to Case-6, in this calculation the base flow exhibits considerable streamwise variation. In Case-8 and Case-9, the response of the wake to a combination of two-dimensional and three-dimensional excitations is investigated.

#### Case-6

For this case, the development of a small amplitude, three-dimensional disturbance in a flat plate wake is calculated. The results of this calculation are compared to linear stability theory in order to verify the ability of the numerical method to accurately simulate three-dimensional disturbances. For this calculation, the spatial and temporal domains, and the base flow were identical to Case-1.

The wake was excited with a three-dimensional sinuous mode disturbance of amplitude  $A_3 = .001$ , spanwise wave number  $\gamma = .5$ , and frequency  $\beta = .28$ . The two-dimensional component of the excitation was set to zero, so that  $A_2 = 0$ . In terms of the three-dimensional streamwise velocity disturbance  $u'_{3d}(x_0, y)$  at the inflow boundary,  $A_3$  is given by the relation  $A_3 = \max(|u'_{3d}(x_0, y)|)$ . The amplitude and phase of the Orr-Sommerfeld eigenfunctions that correspond to the frequency  $\beta = .28$  and spanwise wavenumber  $\gamma = .5$  are shown in Figures 6.30.

The spatial discretization was identical to that used in Case-1. Three spanwise modes ( $K = 6$ ) were calculated. Restrictions on the allowable time step, due to numerical stability considerations, are more severe for calculations of three-dimensional disturbances than for the calculation of two-dimensional disturbances. For this calculation, the time step

$$\Delta t = \frac{T_F}{L_{max}} \quad \text{with} \quad L_{max} = 256 \quad (6.22)$$

was sufficiently small to ensure numerical stability. Five periods  $T_F$  of the fundamental disturbance component were calculated ( $L_2 = 1280$ ).

The relevant parameters in this calculation are summarized below:

Case-6:

the streamwise location of the inflow boundary,	$x_0$	=	.3;
the streamwise location of the outflow boundary,	$x_N$	=	.7;
the transverse location of the lower freestream boundary, $y_0$		=	-10;
the transverse location of the upper freestream boundary, $y_M$		=	10;
the Reynolds number $Re = \frac{\bar{U}_\infty \bar{l}}{\nu}$ ,		$Re$	= 200000;
the amplitude level of the two-dimensional excitation,	$A_2$	=	0;
the amplitude level of the three-dimensional excitation,	$A_3$	=	.001;
the frequency of the wake excitation,	$\beta$	=	.28;
the spanwise wave number of the wake excitation,	$\gamma$	=	.5;
the number of streamwise grid increments,	$N$	=	128;
the number of transverse grid increments,	$M$	=	64;
the number of spanwise modes computed,	$K/2$	=	3;
the number of time steps calculated,	$L_2$	=	1280;
and the time steps per fundamental disturbance period, $L_{max}$		=	256.

The amplification curves for the disturbance kinetic energy  $\hat{E}^1(x, F)$  of the first spanwise mode ( $k = 1$ ) are shown in Figure 6.31 and are compared to the corresponding curves from linear stability theory. The amplification curve for the fundamental disturbance ( $F = 1$ ) compares well to the linear stability theory prediction of the kinetic energy. In the Navier-Stokes calculation, the second harmonic ( $F = 2$ ) is present but is much smaller than the fundamental disturbance.

For the streamwise location  $x = .35$ , the amplitude and phase distributions of the fundamental disturbance component ( $k = 1, F = 1$ ) are compared to the amplitude and phase distributions obtained from a spatial linear stability theory analysis of the base flow. This comparison is shown in Figures 6.32 and 6.33. The Orr-Sommerfeld amplitude and phase distributions are normalized in the same manner as discussed in connection with Case-1. The amplitude distributions of the fundamental disturbance are virtually identical to the Orr-Sommerfeld amplitude distributions. The phase distributions of the fundamental disturbance also exhibit good agreement with the Orr-Sommerfeld phase distributions.

The results of this calculation, as represented by the disturbance kinetic energy as well as the disturbance amplitude and phase distributions, compared reasonably well to linear stability theory. It is concluded that the numerical method is suitable for calculations of three-dimensional disturbances.

#### Case-7

With this calculation, the development of a three-dimensional disturbance in a high-deficit flat plate wake is investigated. In contrast to Case-6, the base flow changes significantly in the streamwise direction and was approximately the same as the base flow that was used for Case-2, Case-3, and Case-4. For this case, the frequency of the excitation was chosen to be identical to the forcing frequency for Case-2 through Case-5 so that the results of this calculation can be compared to

those earlier cases. The results of this calculation will serve as a reference for other calculations for which both two-dimensional and three-dimensional disturbances were introduced.

This calculation was performed in a spatial domain that is bounded by

$$x_0 = .03 , \quad x_N = .36 , \quad y_0 = -16 , \quad \text{and} \quad y_M = 16 . \quad (6.23)$$

As in Case-2, the undisturbed wake was computed subject to a Gaussian inflow streamwise velocity distribution. The resulting base flow modeled the wake from the experiments of Sato (1970).

The wake was excited with a three-dimensional sinuous mode disturbance of amplitude  $A_3 = .001$ , spanwise wavenumber  $\gamma = .5$ , and frequency  $\beta = .51$ . The amplitude of the two-dimensional component of the excitation was  $A_2 = 0$ . The amplitude and phase of the Orr-Sommerfeld eigenfunctions that correspond to the frequency  $\beta$  and spanwise wavenumber  $\gamma$  are shown in Figures 6.34.

The spatial domain was discretized into  $N$  streamwise grid intervals and  $M$  transverse grid intervals where

$$N = 256 \quad \text{and} \quad M = 128 . \quad (6.24)$$

Three spanwise modes ( $K = 6$ ) were computed. For this calculation, the time step

$$\Delta t = \frac{T_F}{L_{max}} \quad \text{with} \quad L_{max} = 512 \quad (6.25)$$

was sufficient to ensure numerical stability. The time-dependent response of the wake was calculated for eight fundamental disturbance periods  $T_F$  which is equivalent to  $t = 4096\Delta t$ .

For this calculation, the spatial domain contained approximately eight streamwise wavelengths of the fundamental disturbance (based on the wavelength at the

inflow boundary) with approximately sixteen grid points per streamwise wavelength. In the transverse direction, the domain contained approximately 32 momentum thicknesses (based on the inflow boundary velocity distribution) with approximately four grid points per momentum thickness. Based on the results of the two-dimensional calculations, it is felt that the spatial discretization discussed here results in solutions that are sufficiently independent of the grid sizes.

The relevant parameters in this calculation are summarized below:

Case-7:

the streamwise location of the inflow boundary,	$x_0$	=	.03;
the streamwise location of the outflow boundary,	$x_N$	=	.36;
the transverse location of the lower freestream boundary, $y_0$		=	-16;
the transverse location of the upper freestream boundary, $y_M$		=	16;
the Reynolds number $Re = \frac{\bar{U}_\infty \bar{l}}{\nu}$ ,	$Re$	=	200000;
the amplitude level of the two-dimensional excitation,	$A_2$	=	0;
the amplitude level of the three-dimensional excitation,	$A_3$	=	.001;
the frequency of the wake excitation,	$\beta$	=	.51;
the spanwise wave number of the wake excitation,	$\gamma$	=	.5;
the number of streamwise grid increments,	$N$	=	256;
the number of transverse grid increments,	$M$	=	128;
the number of spanwise modes computed,	$K/2$	=	3;
the number of time steps calculated,	$L_2$	=	4096;
and the time steps per fundamental disturbance period,	$L_{max}$	=	512.

Amplification curves of the kinetic energy  $\hat{E}^1(x, F)$  are shown in Figure 6.35a. The disturbance kinetic energy is calculated using the Fourier analyzed velocity components that correspond to the time interval  $6T_F < t \leq 8T_F$ . The variation of

the kinetic energy of the fundamental disturbance ( $F = 1$ ) agrees closely with that obtained from linear stability theory calculations. As was the case for calculations of two-dimensional disturbances, the large amplitude level of the  $F = 0.5$  and  $F = 1.5$  harmonics is due to the fact that the wake has not achieved a time periodic state in the time interval  $6T_F < t \leq 8T_F$ . At  $x \approx .12$ , the fundamental disturbance appears to saturate. However, this saturation may be due to the nonperiodic component of the wake disturbances.

For comparison purposes, amplification curves of the disturbance kinetic energy that correspond to the time interval  $8T_F < t \leq 10T_F$  are shown in Figure 6.35b. In this figure, the fundamental disturbance does not saturate. In addition, the other harmonic components, particularly the  $F = 0.5$  and  $F = 1.5$  harmonics, have decreased relative to their values in Figure 6.35a. This indicates that the disturbances are not periodic in the time interval  $6T_F < t \leq 8T_F$ . The saturation of the fundamental disturbance that was observed in Figure 6.35a is apparently due to this nonperiodicity.

Figures 6.36 show contours of streamwise vorticity  $\omega_x$  in the  $yz$ -plane for  $t = 4096\Delta t$ . The horizontal scale of the plots in Figures 6.36,  $0 \leq z/\Delta z \leq 32$ , is equivalent to two spanwise wavelengths of the fundamental disturbance. The vorticity shown in Figure 6.36a corresponds to the inflow boundary  $x = .03$  and is due solely to the three-dimensional excitation at this boundary. Figure 6.36b shows the streamwise vorticity corresponding to  $x = .146$ . For this location, the vorticity concentrations have rotated relative to the vorticity concentrations at the inflow boundary. The numerical results of Meiburg and Lasheras (1988), which are shown in Figure 6.37, display a similar behavior. Meiburg and Lasheras attributed the rotation of the vorticity concentrations to the velocity field induced by these

concentrations. In Figures 6.36, the solid contours denote positive streamwise vorticity. Because the vorticity is defined as

$$\omega = -\nabla \times \mathbf{u} , \quad (6.26)$$

positive vorticity induces a counterclockwise azimuthal velocity component and a counterclockwise rotation of the positive streamwise vorticity concentrations. For similar reasons, the negative streamwise vorticity concentrations rotate in the clockwise direction. The vorticity in Figures 6.36 is also distributed in a more complicated pattern than the vorticity observed in Figure 6.37 (Meiburg and Lasheras, 1988). It is believed that the simpler vorticity distribution in Figure 6.37, as compared to Figure 6.36b, is due to the simpler initial perturbation that was employed by Meiburg and Lasheras (they used inviscid vortex dynamics and disturbed the wake by perturbing the vortex filaments sinusoidally in the streamwise and spanwise directions).

#### Case-8 and Case-9

With these calculations, an attempt is made to investigate certain aspects of the secondary instability of wakes. These studies are undertaken by calculating the interaction of a large amplitude two-dimensional disturbance with a smaller amplitude three-dimensional disturbance. The results of these calculations are compared to the results of Case-7 and Case-4 in order to observe how the two-dimensional disturbance influences the development of the three-dimensional disturbance and vice-versa.

The base flow and most relevant parameters were identical to those in Case-7. For both Case-8 and Case-9, the amplitude, frequency, and spanwise wavenumber of the three-dimensional excitation had the same values as in Case-7, so that

$$A_3 = .001 , \quad \beta = .51 , \quad \text{and} \quad \gamma = .5 . \quad (6.27)$$

For Case-8, the amplitude of the two-dimensional excitation had the same value as in Case-4, so that

$$A_2 = .01 \quad . \quad (6.28)$$

For Case-9, the amplitude and frequency of the two-dimensional excitation was

$$A_2 = .05 \quad . \quad (6.29)$$

Amplification curves of the kinetic energy  $\hat{E}^k(x, F = 1)$  for Case-8 are shown in Figure 6.38. The curve corresponding to  $k = 0$  represents the kinetic energy of the two-dimensional disturbance. The curve corresponding to  $k = 1$  is for the kinetic energy of the three-dimensional disturbance. The curve labeled 'LST MEAN FLOW' is for the kinetic energy  $\hat{E}^1(x, F = 1)$  of the three-dimensional disturbance component, as predicted by a linear stability theory analysis of the mean flow. This last curve is computed in the same manner as discussed previously (Case-3). The two-dimensional disturbance ( $k = 0$ ) grows very rapidly at first and then saturates at an amplitude of  $\hat{E}^0(x, F = 1) \approx .20$ . This behavior is very similar to that observed for the two-dimensional disturbance development in Case-4 where three-dimensional disturbances were not present.

The three-dimensional disturbance ( $k = 1$ ) initially grows in a manner similar to the three-dimensional disturbance from Case-7. However, the saturation of the two-dimensional disturbance causes a temporary reduction in the amplification rate of the three-dimensional disturbance. After a brief period of lower amplification, the three-dimensional disturbance resumes stronger growth. However, the amplification rate is smaller than the amplification rate that was observed before the saturation of the two-dimensional disturbance. The reduction in the three-dimensional growth rate, that is probably caused by the saturation of the

two-dimensional disturbance, may be due to the changing stability characteristics of the mean flow. This proposition is supported by the close comparison in Figure 6.38 of the three-dimensional disturbance and the curve labeled 'LST MEAN FLOW'. The resumption of rapid three-dimensional disturbance growth, following the saturation of the two-dimensional disturbance, could be explained by a secondary instability mechanism.

Amplification curves of the kinetic energy  $\hat{E}^k(x, F = 1)$  for Case-9 are shown in Figure 6.39. Due to the now larger two-dimensional excitation amplitude, the two-dimensional disturbance saturates further upstream than in Case-8. As in the previous case, the saturation of the two-dimensional disturbance causes a strong reduction in the three-dimensional amplification rate. After a short period of reduced three-dimensional growth, the three-dimensional disturbance continues its amplification. Qualitatively, this behavior is the same as in Case-8. However, as a result of the larger two-dimensional excitation amplitude, the reduction in the three-dimensional amplification rate and the subsequent resumption of stronger growth occur further upstream than in Case-8.

In Figure 6.39, the resumption of strong three-dimensional growth is short-lived: the three-dimensional disturbance tends to saturate for a second time. However, this second saturation is in contrast to the observed behavior in Figure 6.38 (Case-8). To further check the validity of the results of Case-9, this calculation is repeated in a spatial domain that is twice as long ( $x_N = .69$ ,  $N = 512$ ) as the spatial domain of the original calculation but which in all other respects is identical to the original calculation. The amplification curves of the disturbance kinetic energy  $\hat{E}^1(x, F)$  for both the original calculation ( $x_N = .36$ ,  $N = 256$ ) and the long domain calculation ( $x_N = .69$ ,  $N = 512$ ) are shown in Figures 6.40. For the long domain calculation (Figure 6.40b), the three-dimensional fundamental

disturbance ( $F = 1$ ) initially grows more slowly after its initial saturation than was the case for the original calculation (Figure 6.40a). However, the fundamental disturbance does not saturate for a second time as it did in the original calculation. Therefore, it appears that the second saturation of the three-dimensional fundamental disturbance that is observed in Figures 6.39 and 6.40a is due to the influence of the outflow boundary.

The three-dimensional disturbance behavior observed in Figures 6.38 and 6.39 is similar to that observed by Metcalfe et al. (1987) in their investigations of secondary instability in free shear layers (see Figure 6.41). They numerically calculated the temporal development of a large amplitude two-dimensional disturbance as it interacted with a smaller amplitude three-dimensional disturbance. They found that the saturation of the two-dimensional disturbance temporarily inhibited the amplification of the three-dimensional disturbance. After a brief period of reduced growth, the three-dimensional disturbance continued growing and eventually surpassed the two-dimensional disturbance.

For Case-8 and Case-9, the presence of the two-dimensional disturbance appears to alter the distribution of vorticity as compared to Case-7. The streamwise vorticity in the  $yz$ -plane for  $t = 4096\Delta t$  is shown in Figures 6.42. Figure 6.42a shows the streamwise vorticity for Case-8 which corresponds to the streamwise location  $x = .146$ . Figure 6.42b shows the streamwise vorticity for Case-9 for the same streamwise location. Due to the presence of the two-dimensional disturbance, the streamwise vorticity is distributed quite differently than in Figure 6.36b (Case-7). In Figure 6.36b, the streamwise vorticity is distributed in a pattern of discrete streamwise vortices. For Case-8 and Case-9, in which both two-dimensional and three-dimensional disturbances are present, the streamwise vorticity is distributed

in a large number of small vortices. Furthermore, in contrast to Case-7, these vortices do not appear to rotate.

Additional displays of the interactions of the two- and three-dimensional disturbances are shown in Figures 6.43 through 6.45. In Figures 6.43, the spanwise vorticity  $\omega_z$  in the  $yz$ -plane for  $t = 4096\Delta t$  is shown for Case-7, Case-8, and Case-9. The interaction of the two- and three-dimensional disturbances (Case-8 and Case-9) significantly alters the vorticity distribution as compared to Case-7 for which only a three-dimensional disturbance was introduced.

In Figures 6.44, the streamwise vorticity  $\omega_x$  in the  $xy$ -plane for  $t = 4096\Delta t$  is shown for Case-7, Case-8, and Case-9. The two-dimensional disturbance, which is present in Case-8 and Case-9, causes a much broader transverse distribution of vorticity as compared to Case-7 for which the two-dimensional disturbance was absent. In Figures 6.45, similar plots of the spanwise vorticity  $\omega_z$  are shown. For Case-7 (Figure 6.45a) the spanwise vorticity disturbance is much smaller than for Case-8 and Case-9 (Figure 6.45b and 6.45c). For Case-8 and Case-9, the vorticity develops in a manner similar to Case-3 (see Figure 6.14c).

Figures 6.46, 6.47, 6.48, 6.49, and 6.50 (Case-8) give detailed views of the vorticity fields in the braid regions between the large concentrations of spanwise vorticity. It is in these regions that Meiburg and Lasheras (1988) observed the formation of lambda vortices. However, from the results of these calculations, no conclusive evidence of these vortices was observed. This might be due to the fact that the forcing amplitudes that were used for Case-8 were different from those used for the simulations of Meiburg and Lasheras (1988). For Case-8, the wake was forced with a large two-dimensional disturbance and a small three-dimensional disturbance while Meiburg and Lasheras employed a large three-dimensional disturbance and a smaller two-dimensional disturbance. Furthermore, there is a considerable

difference between the Reynolds number for this work,  $Re_\theta = \frac{\bar{U}_\infty \bar{\theta}_{lc}}{\nu} = 594$  and the Reynolds number for Meiburg and Lasheras's calculations,  $Re_\theta = 74$ . Finally, it was not possible to duplicate the amplitude levels used by Meiburg and Lasheras because a larger three-dimensional forcing amplitude would have required the use of more Fourier modes in these calculations. This was not feasible due to the limitations of the available computer resources.

In Figures 6.51 through 6.53, the amplitude distributions of the spanwise vorticity for ( $k = 0, F = 1$ ) and ( $k = 1, F = 1$ ) and the amplitude distributions of the streamwise vorticity for ( $k = 1, F = 1$ ) are shown. Case-7, Case-8, and Case-9 are represented in these figures. Due to the influence of the two-dimensional disturbance in Case-8 and Case-9, the amplitude distributions of the streamwise and spanwise vorticity are significantly different from those for Case-7 (Figures 6.51).

Additional consequences of the interaction of the two-dimensional and three-dimensional disturbances are obvious from observing the behavior of the wake half-width  $b$ . In Figure 6.54, the wake half-width  $b$  corresponding to three different calculations: Case-4 ( $A_2 = .01, A_3 = 0$ ), Case-7 ( $A_2 = 0, A_3 = .001$ ), and Case-8 ( $A_2 = .01, A_3 = .001$ ) is displayed. For reference the wake half-width of the base flow is also shown. When only two-dimensional disturbances are present ( $A_2 = .01, A_3 = 0$ ), the wake as characterized by its half-width  $b$  becomes much broader. However, when forced with only a three-dimensional disturbance ( $A_2 = 0, A_3 = .001$ ), the wake width does not differ significantly from the width of the base flow. The strongest effect of broadening is observed when the wake is excited with both two-dimensional and three-dimensional disturbances (Case-8). For Case-8 ( $A_2 = .01, A_3 = .001$ ), the wake half-width development is initially very similar to that of Case-4 ( $A_2 = .01, A_3 = 0$ ). However, while for Case-4 the

half-width stops increasing when the two-dimensional fundamental disturbance saturates, for Case-8 the half-width continues increasing beyond this point. This additional increase in the wake half-width is due to the presence of the three-dimensional disturbance.

In Figure 6.55, the wake half-width for both Case-8 and Case-9 is shown. For Case-9, in which the two-dimensional disturbance is larger than in Case-8, the initial increase of the half-width begins further upstream. However, the variation of the wake half-width is similar for both cases once the two-dimensional disturbance has saturated.

## CHAPTER 7

### CONCLUSIONS

A numerical method has been developed for studying the evolution of two- and three-dimensional disturbances in high-deficit wakes. Comparison of the results of this method were made to both linear stability theory and experiments. The numerical method was found to be capable of simulating both small and large amplitude disturbances.

Simulations of two-dimensional sinuous mode disturbances in a high-deficit flat plate wake were undertaken. At small amplitude levels, the disturbances grew exponentially at rates predicted by linear stability theory. At higher amplitude levels, nonlinear effects became important and the disturbances saturated. The saturation of the fundamental disturbance was found to be related to the stability characteristics of the mean flow. The main influence of a larger excitation amplitude on the resulting disturbances was to accelerate saturation. For large disturbance amplitudes, the wake developed a Kármán vortex street pattern. Furthermore, the influence of the outflow boundary conditions on the results of the numerical simulations was found to be negligible. The subharmonic component that appeared in the wake was found to be due to a nonperiodic wake disturbance. For a fixed spatial location, the subharmonic component decreased with time.

Investigations of three-dimensional disturbances were also undertaken. Associated with three-dimensional disturbances were pairs of counter-rotating streamwise vortices that appeared to rotate as a result of the velocity field induced by these vortices. When both two- and three-dimensional disturbances were present, the saturation of the two-dimensional disturbance caused the three-dimensional

disturbance to saturate. Shortly after saturation, the three-dimensional disturbance resumed stronger growth, possibly because of a secondary instability mechanism. Larger two-dimensional forcing amplitudes accelerated the saturation of the two-dimensional and three-dimensional disturbances and also accelerated the resumption of strong three-dimensional growth.

The interaction of two-dimensional and three-dimensional disturbances resulted in complicated distributions of vorticity. Instead of a small number of discrete streamwise vortices, as when the wake was excited with only three-dimensional disturbances, a larger number of vortices spread over a much wider transverse region were present. Furthermore, these interactions resulted in a much broader wake distribution than that observed when only two-dimensional or three-dimensional disturbances were excited.

Future simulations of three-dimensional disturbances in wakes will undoubtedly require larger computational grids in order to better resolve the flow field. For these simulations to be practical, the numerical method should be modified. It is felt that greater efficiency could be obtained by solving the Navier-Stokes equations in velocity-pressure formulation. This would result in both reduced memory requirements because a smaller number of variables would have to be stored, and in reduced computation times because of the smaller number of nonlinear terms.

Furthermore, for simulations of three-dimensional disturbances, the stability of the current numerical method was found to be quite restraining. This had an adverse effect on the computational efficiency. In the future, this inefficiency should be avoided by employing numerical methods with more favorable stability characteristics.

In this work, interactions of two-dimensional and three-dimensional disturbances appeared to be an important factor in the three-dimensional breakdown

of the wake. In these simulations, only the initial stage of these interactions was observed. In the future, more complete simulations of these interactions should be attempted as these interactions most likely play an important role in the development of the three-dimensionality in transitional wakes. Of particular interest is how these interactions lead to the formation of the dominant three-dimensional structures that are observed in experiments.

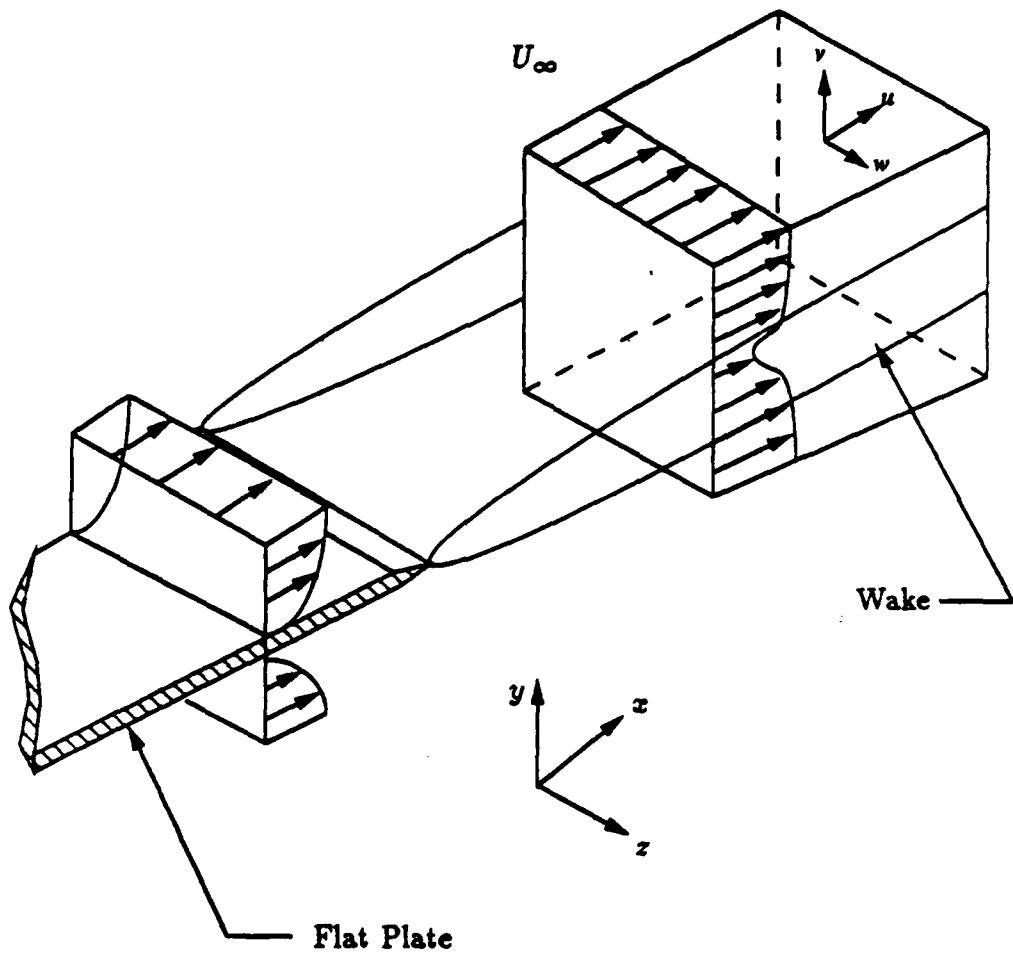
**FIGURES**

Figure 2.1 Spatial domain.

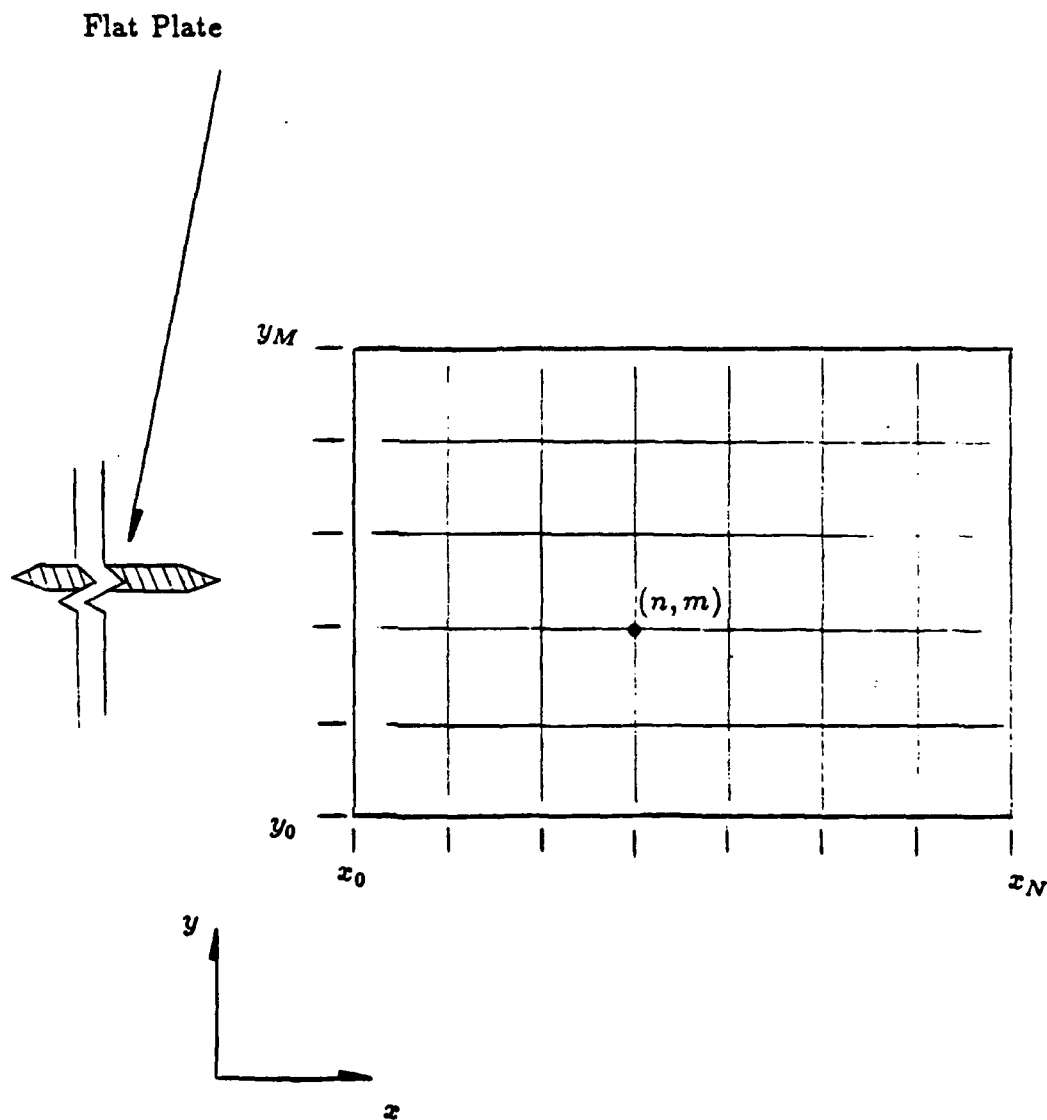


Figure 5.1 Discretization of the spatial computational domain.

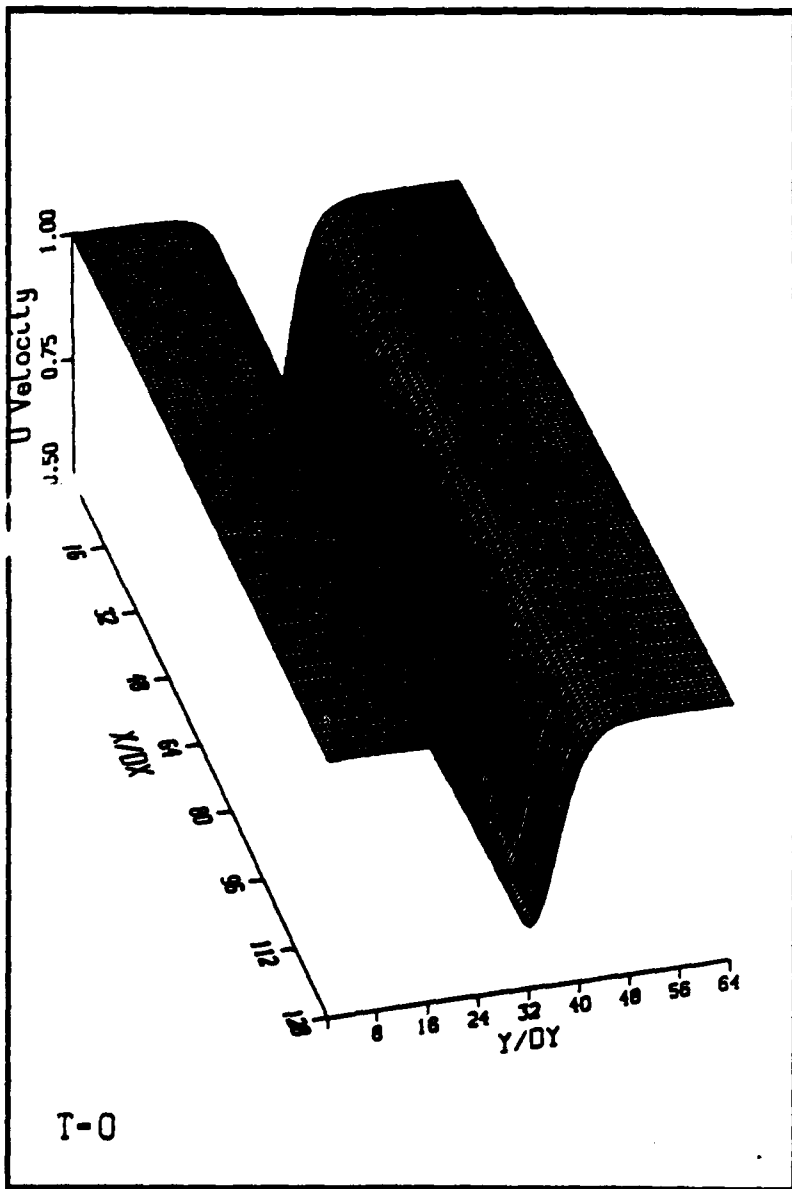


Figure 6.1 Base flow streamwise velocity  $U^0$  for Case-1.

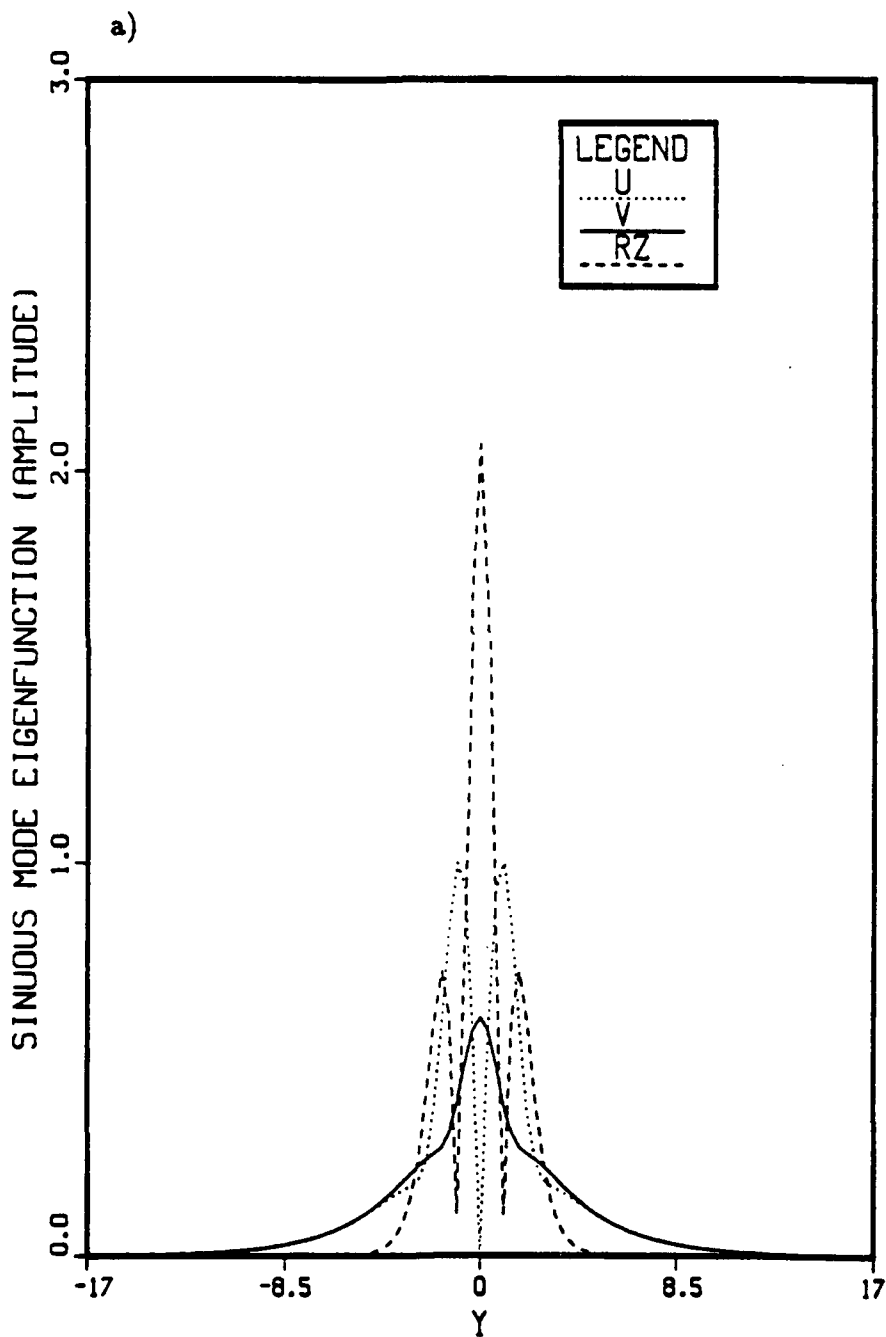


Figure 6.2 Sinuous mode eigenfunctions of the two-dimensional Orr-Sommerfeld equation corresponding to  $\beta = .317$  and  $Re_\theta = \frac{\bar{v}_{le} \bar{U}_\infty}{\nu} = 594$ .  
 a) amplitudes of  $U^0$ ,  $V^0$ , and  $\Omega_z^0$ ; b) phases of  $U^0$ ,  $V^0$ , and  $\Omega_z^0$ .

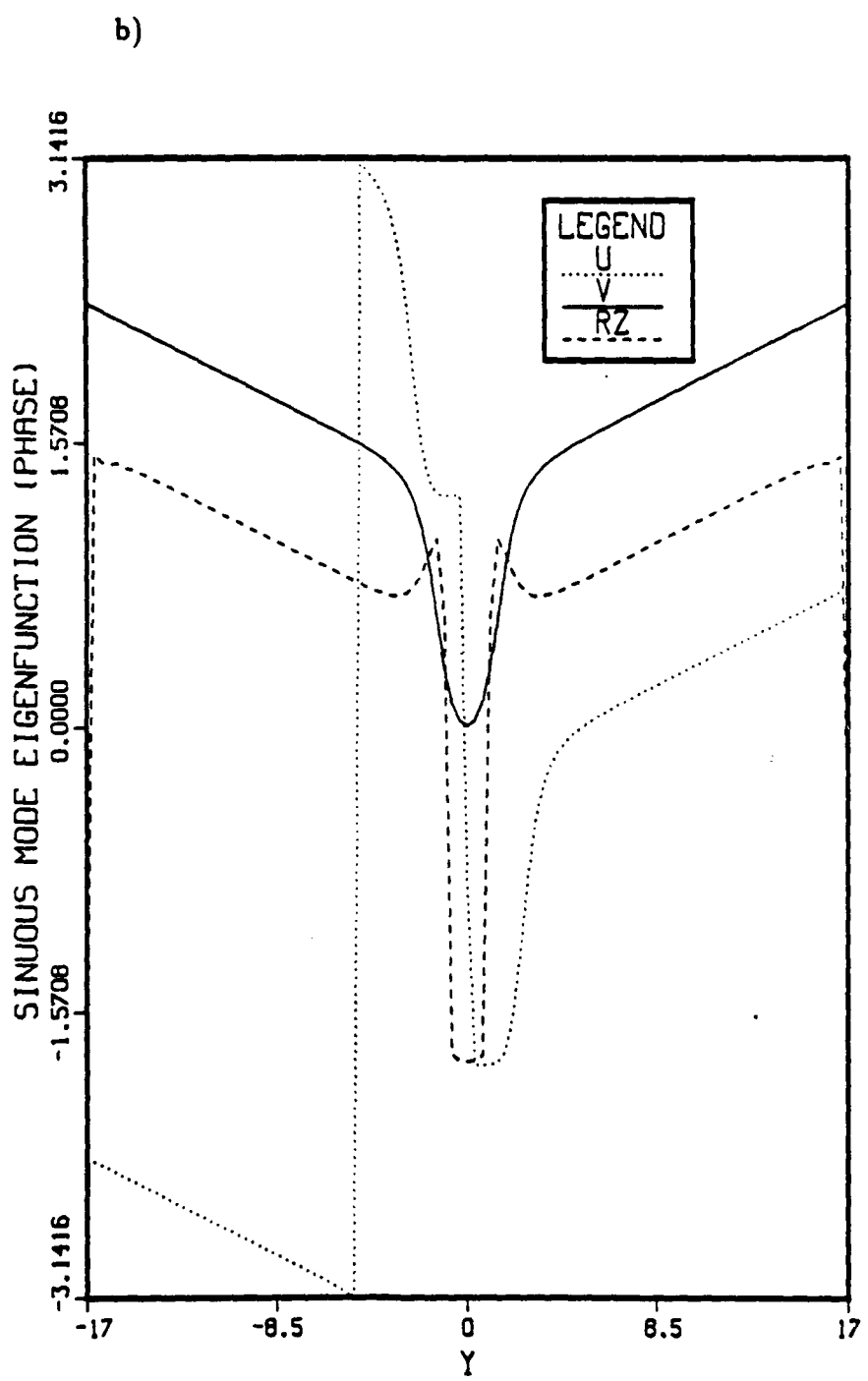


Figure 6.2 Continued.

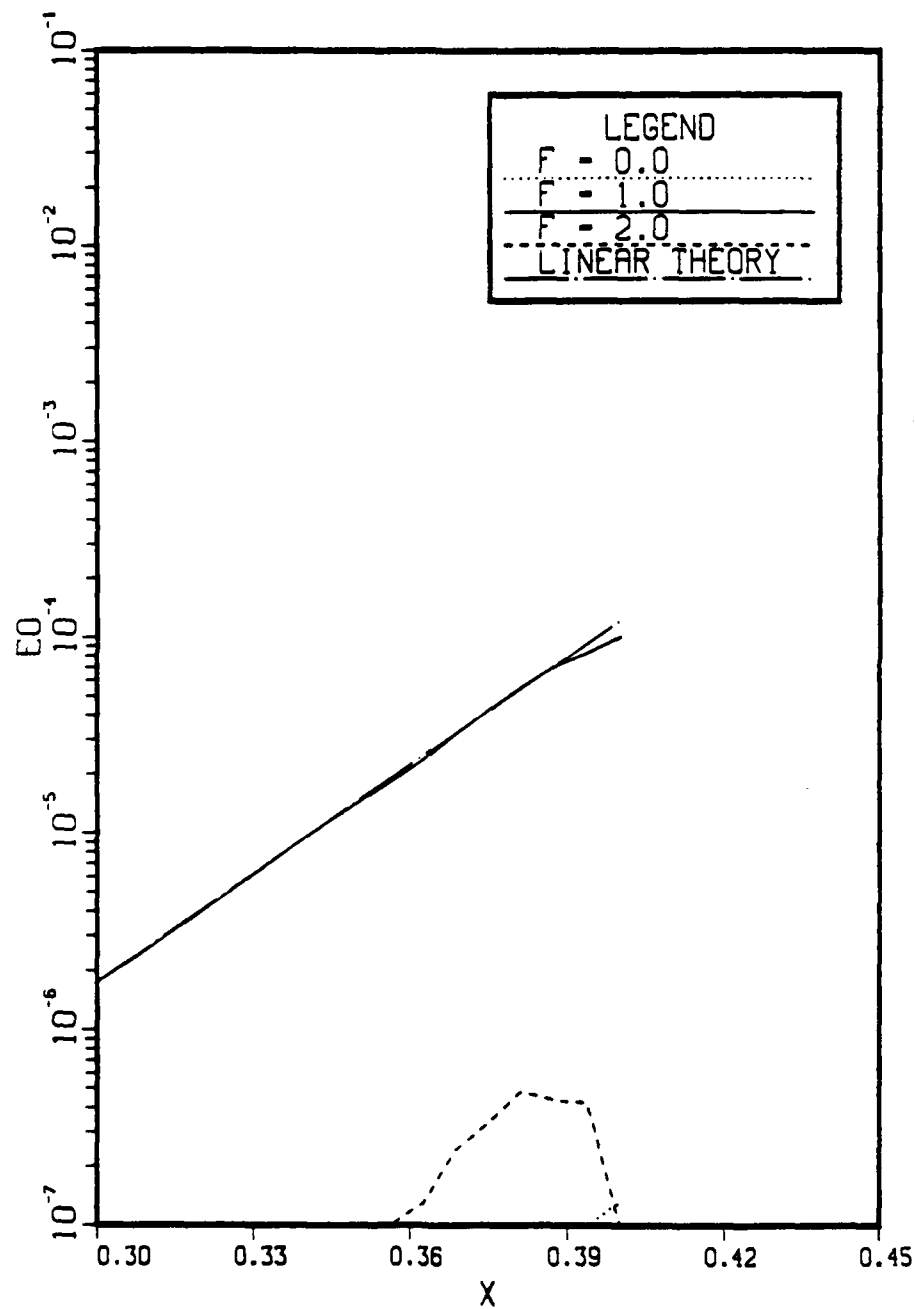


Figure 6.3 Comparison of amplification curves based on the kinetic energy  $\hat{E}^0(x, F)$  to linear stability theory. Case-1:  $A_2 = .001$ ,  $A_3 = 0$ , and  $\beta = .317$ .

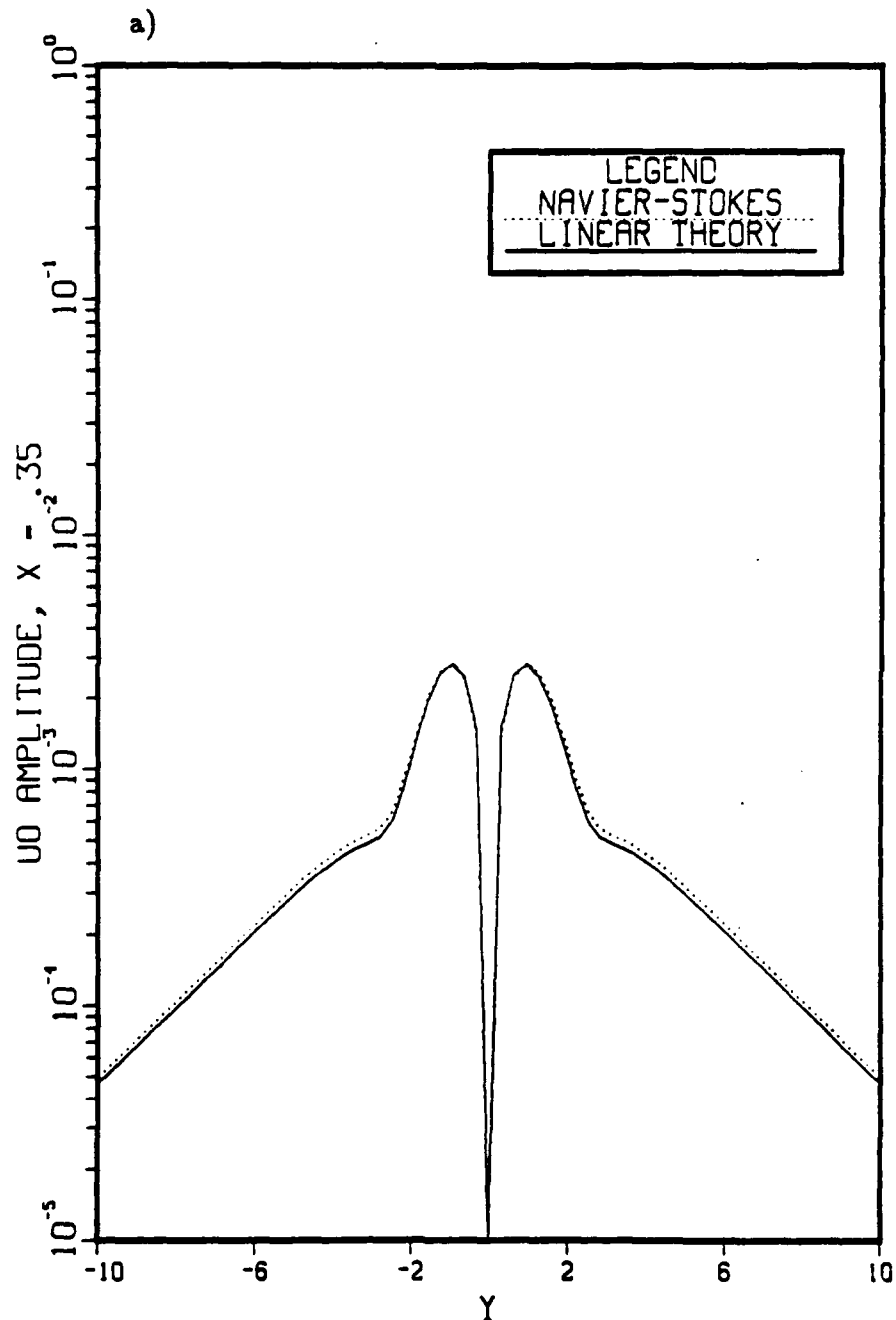


Figure 6.4 Comparison of the amplitude distributions of the fundamental disturbance ( $F = 1$ ) to linear stability theory. Case-1:  $A_2 = .001$ ,  $A_3 = 0$ , and  $\beta = .317$ . a) streamwise velocity,  $U^0$ ; b) transverse velocity,  $V^0$ ; c) spanwise vorticity,  $\Omega_z^0$ .

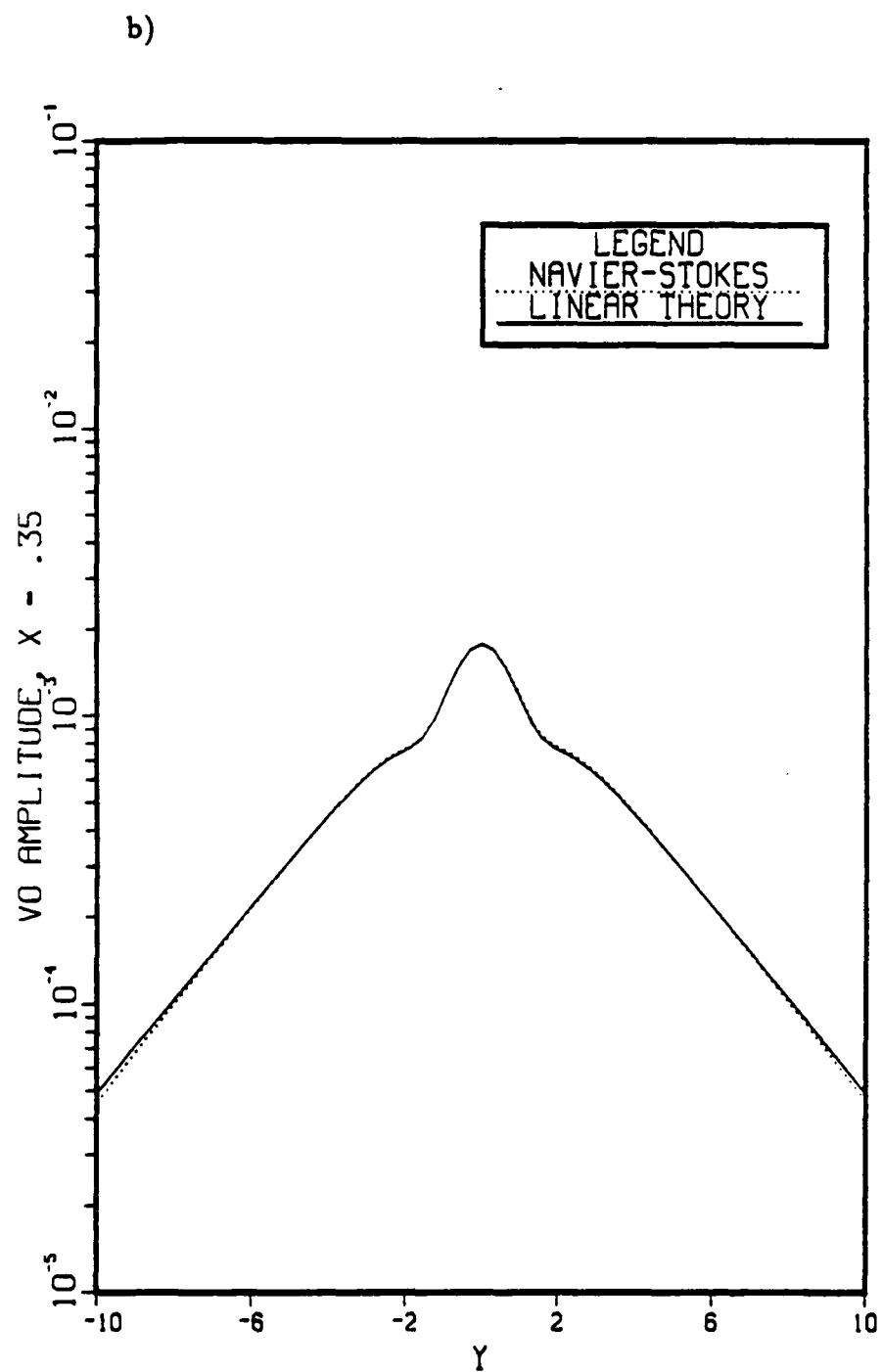


Figure 6.4 Continued.

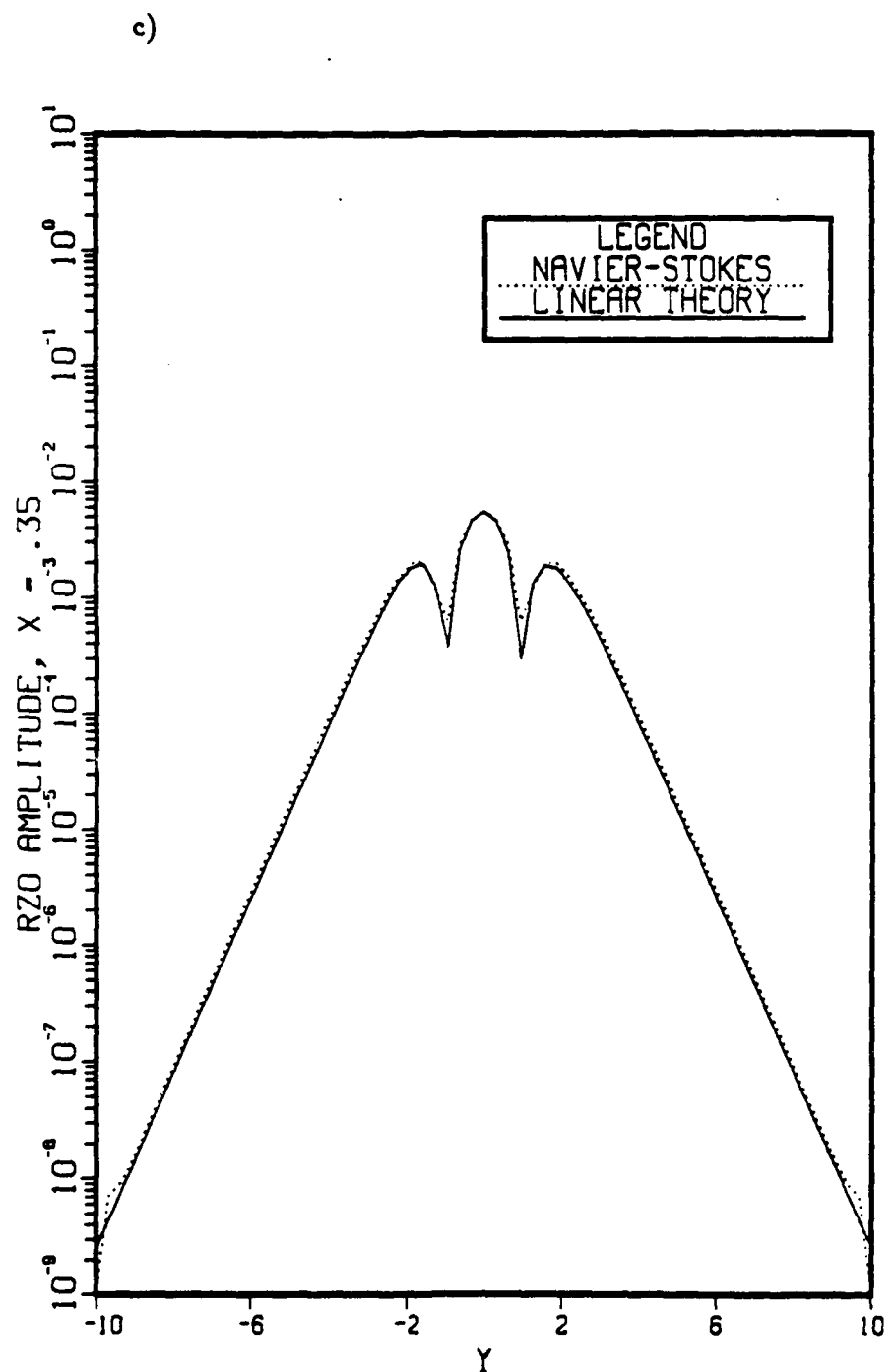


Figure 6.4 Continued.

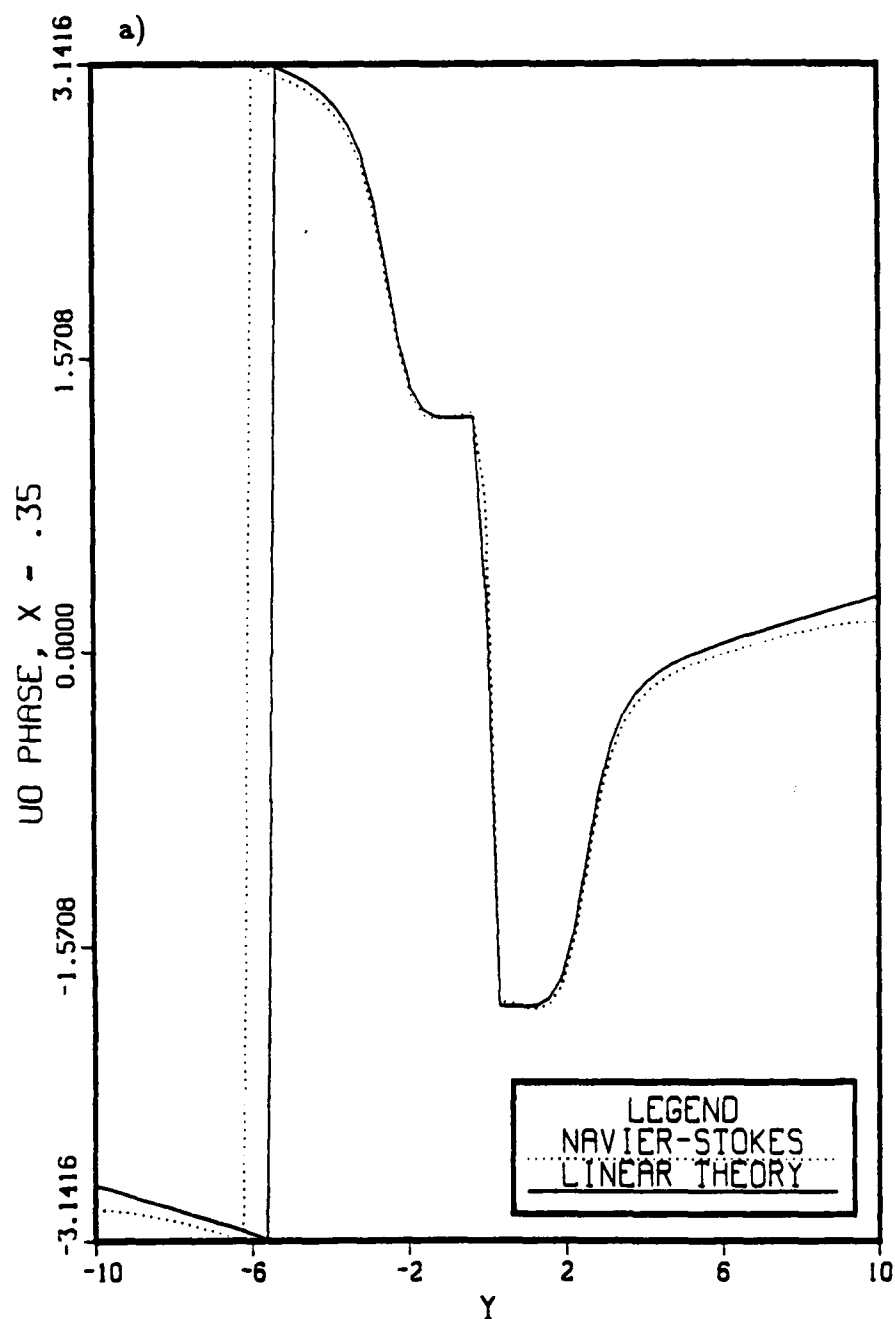


Figure 6.5 Comparison of the phase distributions of the fundamental disturbance ( $F = 1$ ) to linear stability theory. Case-1:  $A_2 = .001$ ,  $A_3 = 0$ , and  $\beta = .317$ . a) streamwise velocity,  $U^0$ ; b) transverse velocity,  $V^0$ ; c) spanwise vorticity,  $\Omega_z^0$ .

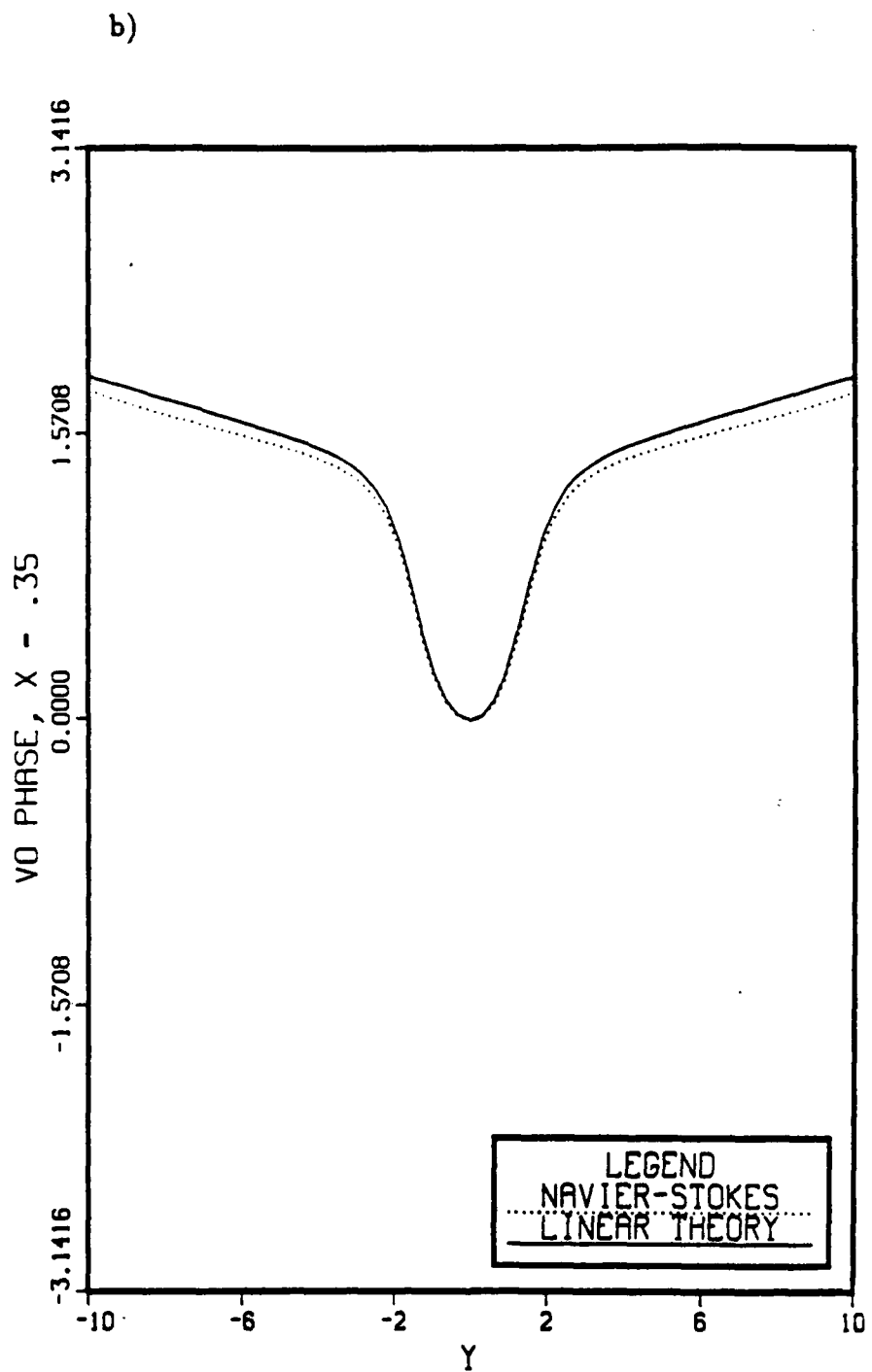


Figure 6.5 Continued.

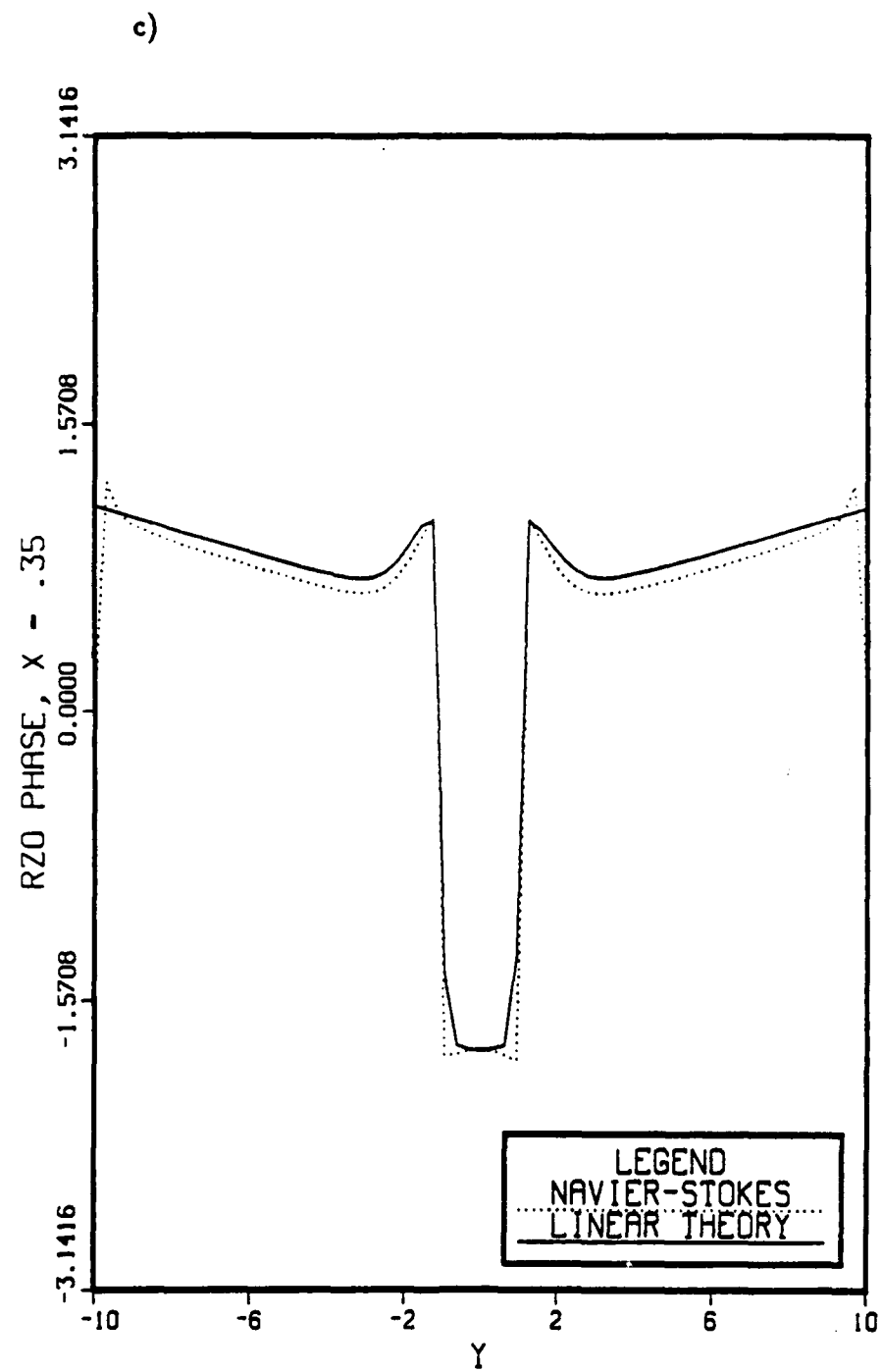


Figure 6.5 Continued.

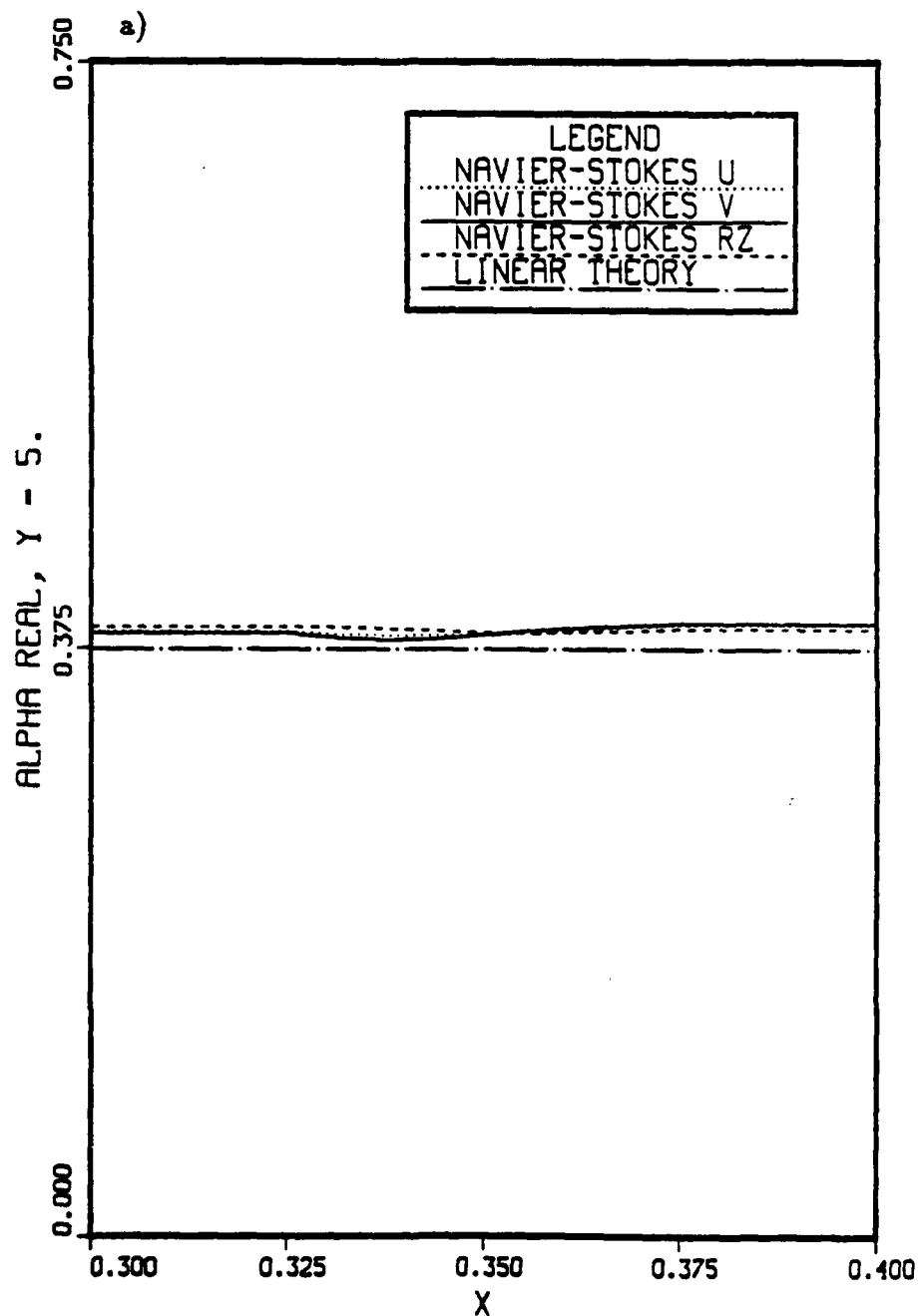


Figure 6.6 Comparison of the streamwise variation of  $\alpha_r$ ,  $\alpha_i$ , and  $c_p$  for the fundamental disturbance ( $F = 1$ ) to linear stability theory. Case 1:  $A_2 = .001$ ,  $A_3 = 0$ , and  $\beta = .317$ . a) streamwise wavenumber,  $\alpha_r$ ; b) amplification rate,  $\alpha_i$ ; c) phase velocity,  $c_p$ .

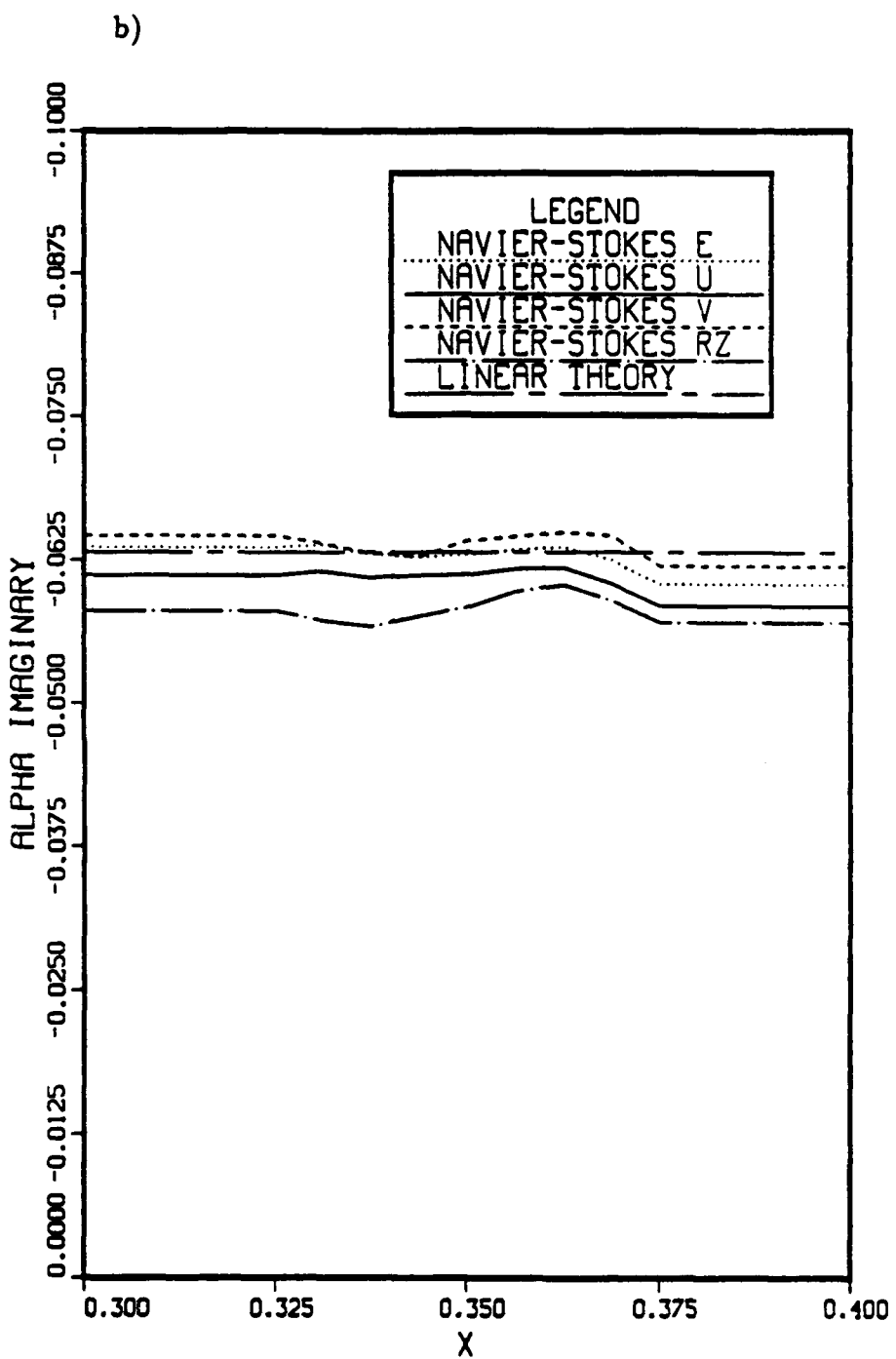


Figure 6.6 Continued.

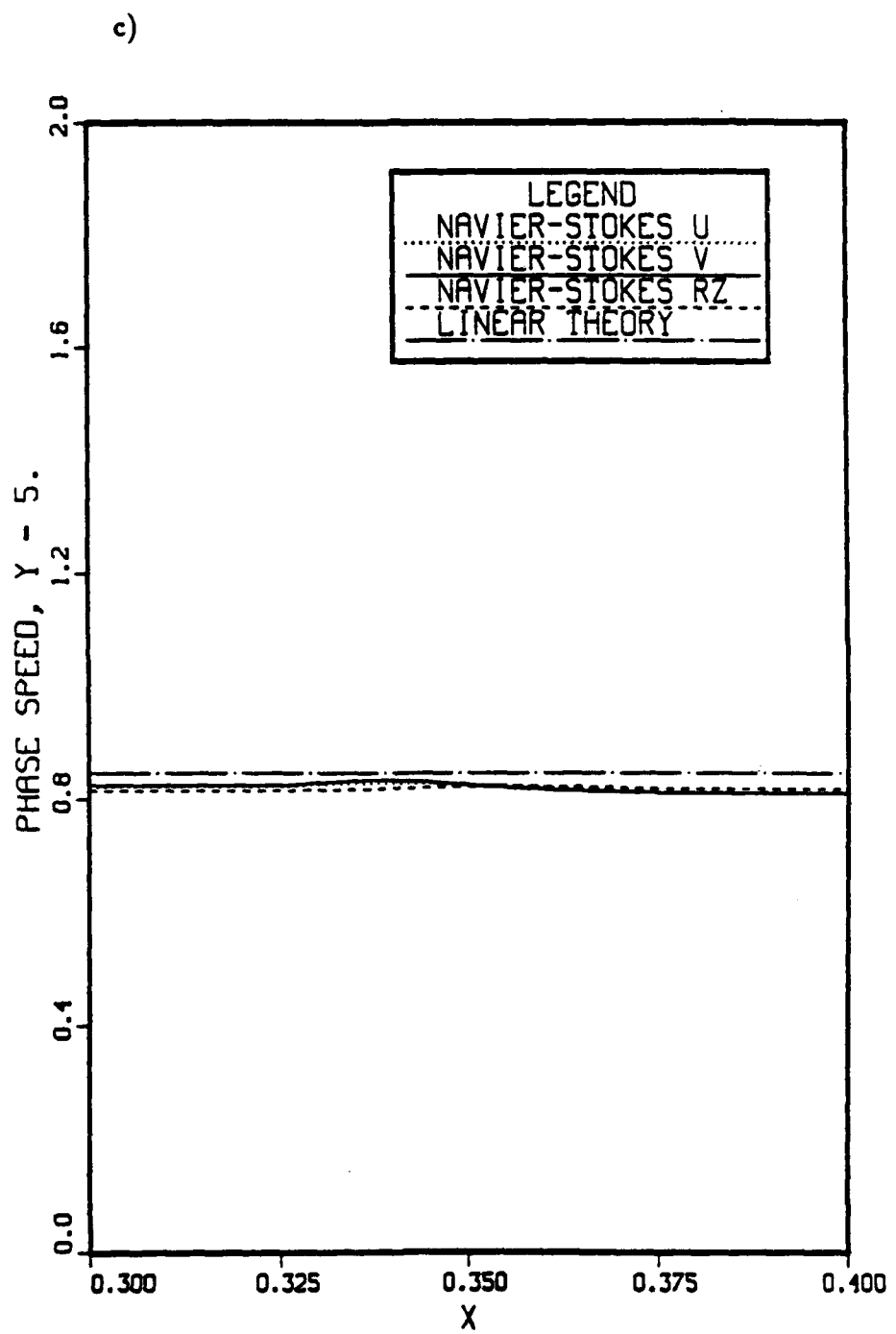


Figure 6.6 Continued.

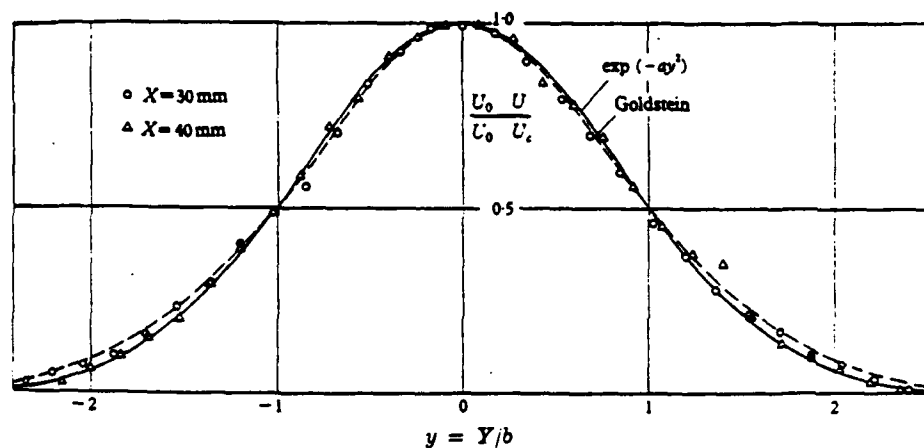


FIGURE 13. Non-dimensional mean-velocity distribution in linear region.

Figure 6.7 Comparison of a Gaussian streamwise velocity distribution to experimental data and to the similarity solution of Goldstein (1929), reproduced from Sato and Kuriki (1961).

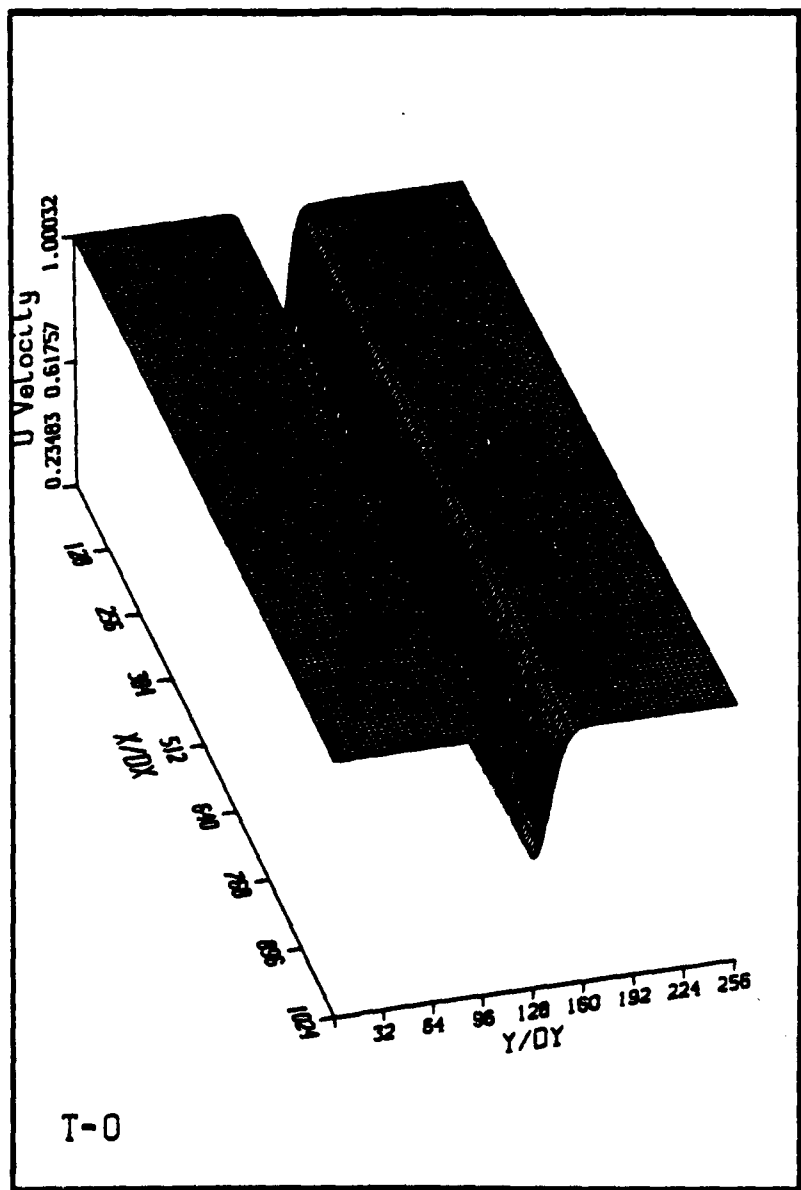


Figure 6.8 Base flow streamwise velocity  $U^0$  for Case-2.

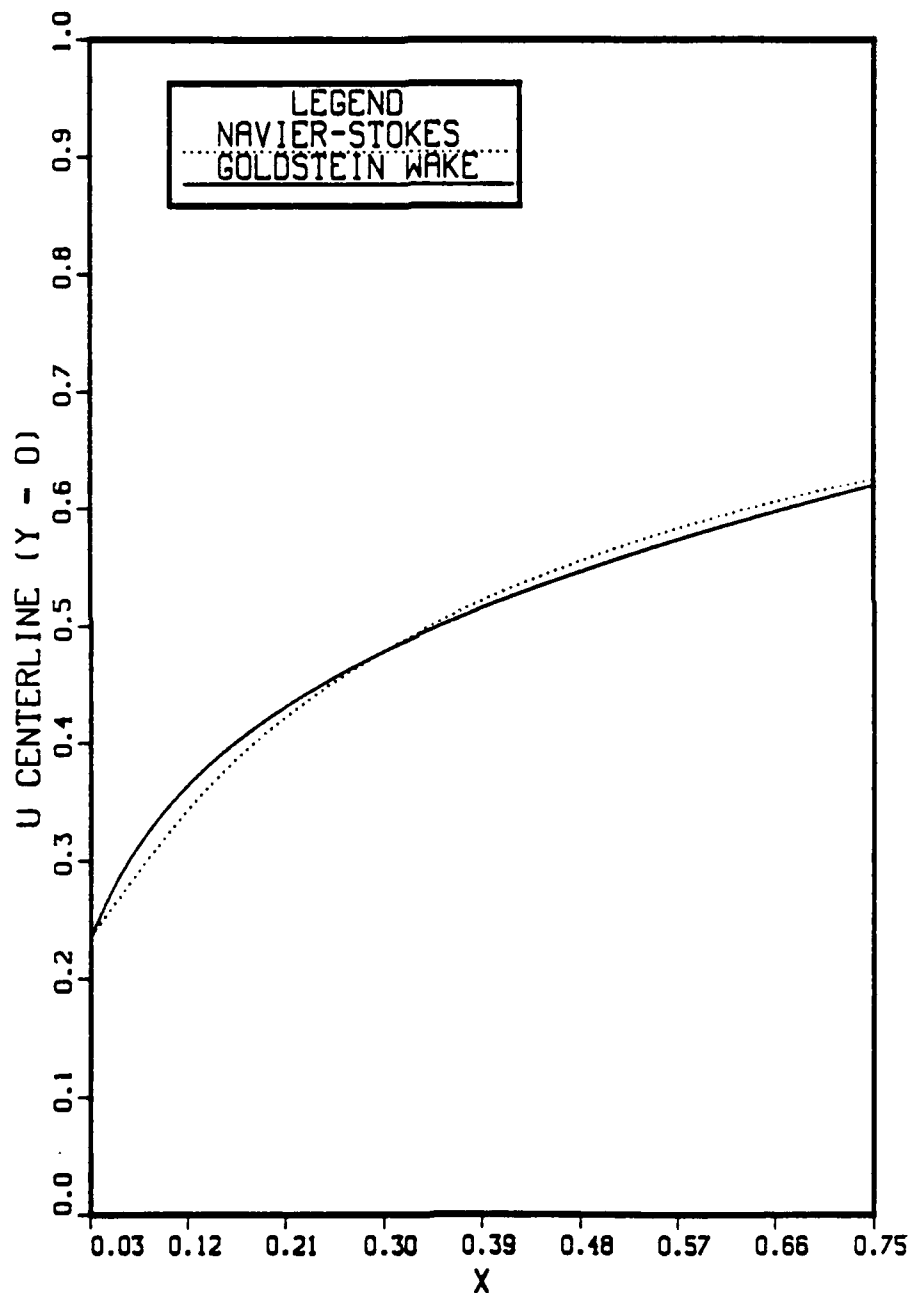


Figure 6.9 Comparison of the base flow centerline streamwise velocity  $U^0$  for Case-2 to the similarity solution of Goldstein (1929).

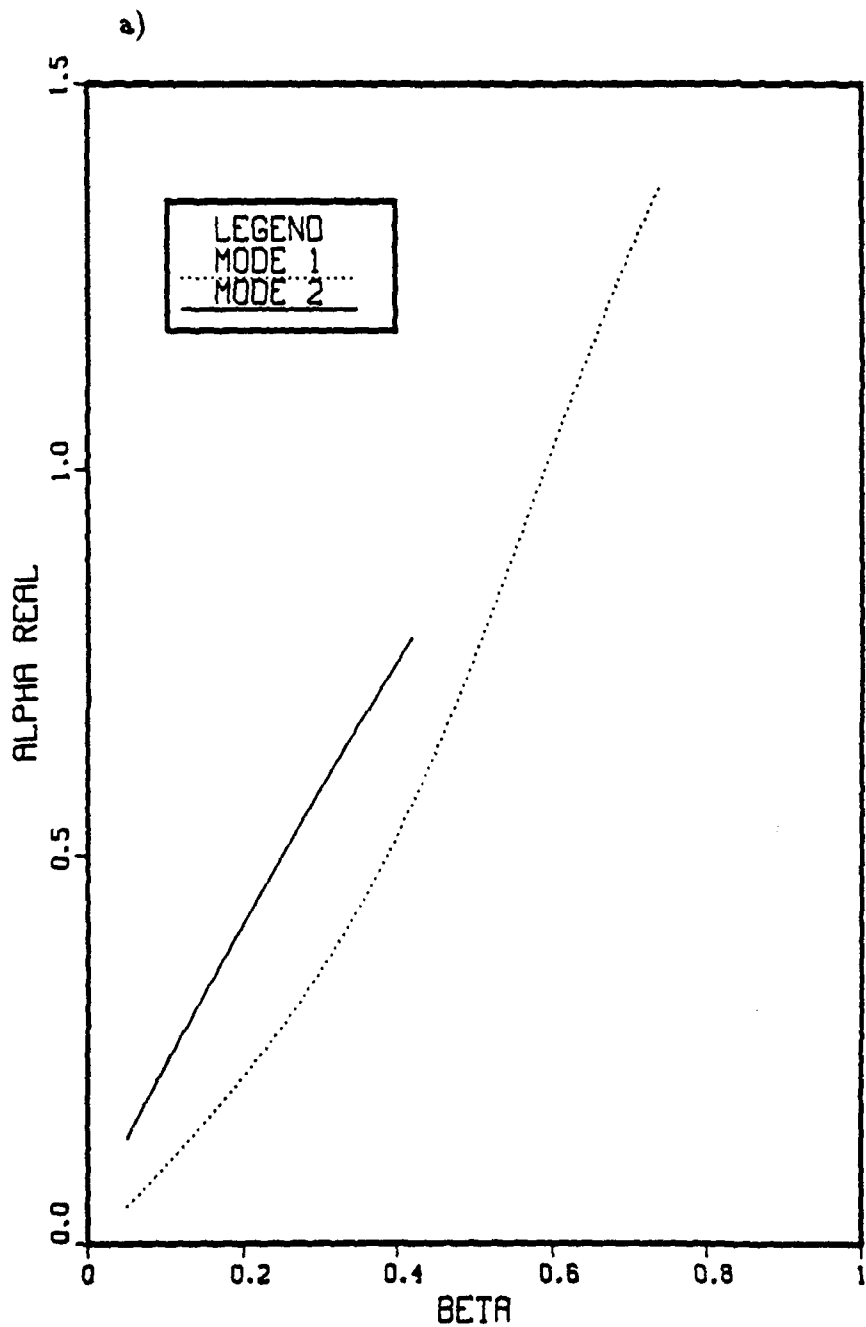


Figure 6.10 Orr-Sommerfeld eigenvalues for the sinuous mode (mode-1) and the varicose mode (mode-2), corresponding to the streamwise velocity distribution at the inflow boundary (Case-2) and  $Re_\theta = \frac{\theta_{in} U_\infty}{\nu} = 594$ . a) streamwise wavenumber,  $\alpha_r$ ; b) amplification rate,  $\alpha_i$ ; c) phase velocity,  $c_p$ .

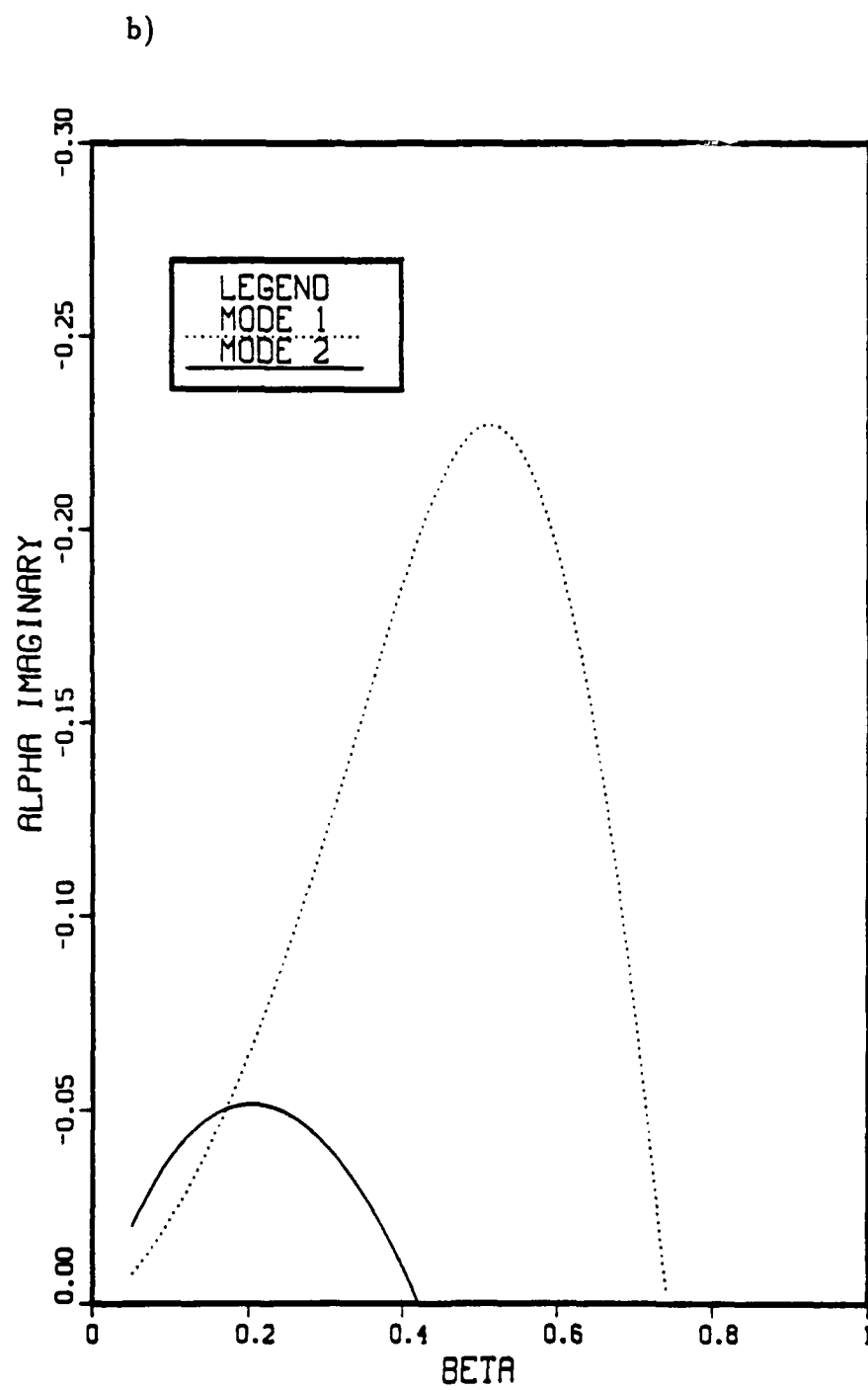


Figure 6.10 Continued.

c)

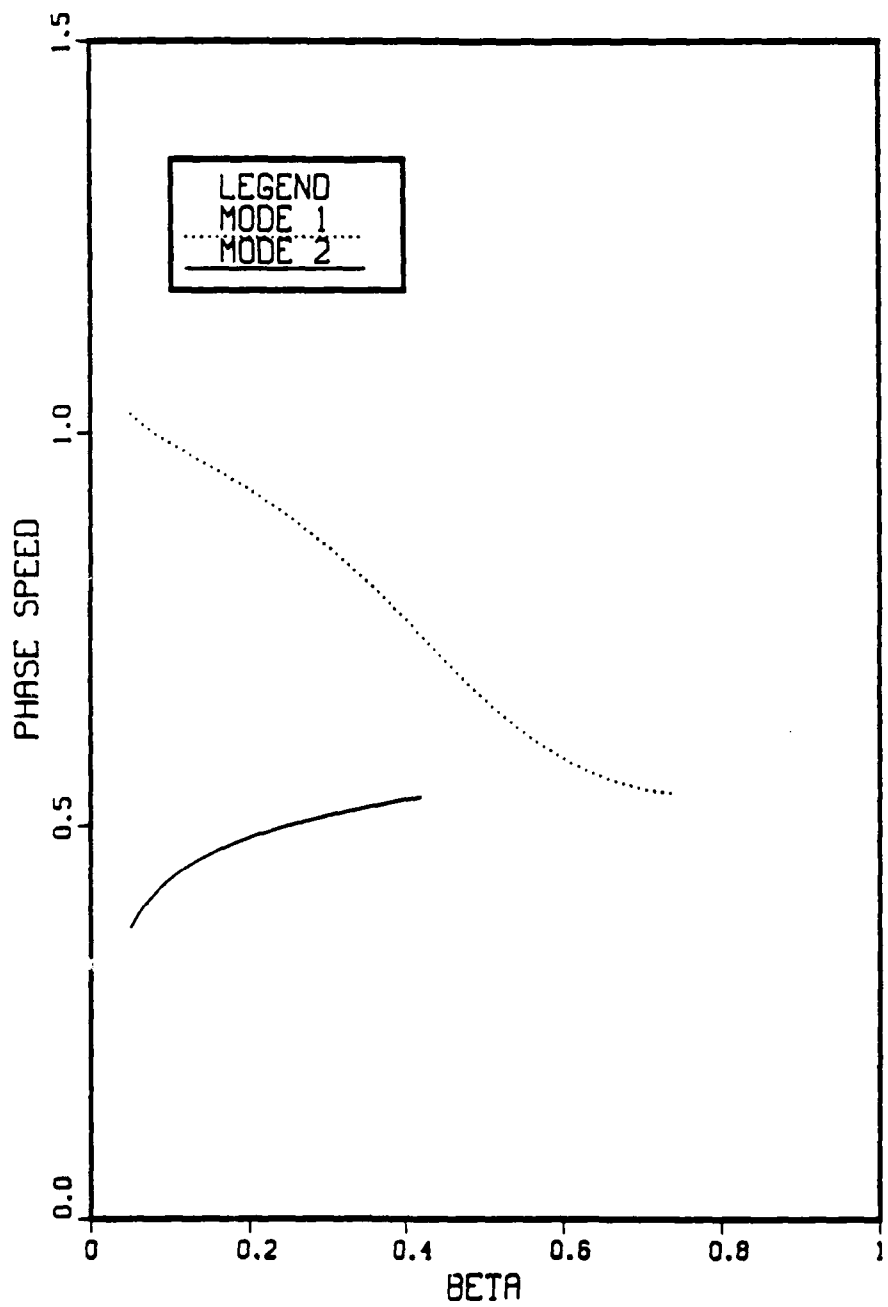


Figure 6.10 Continued.

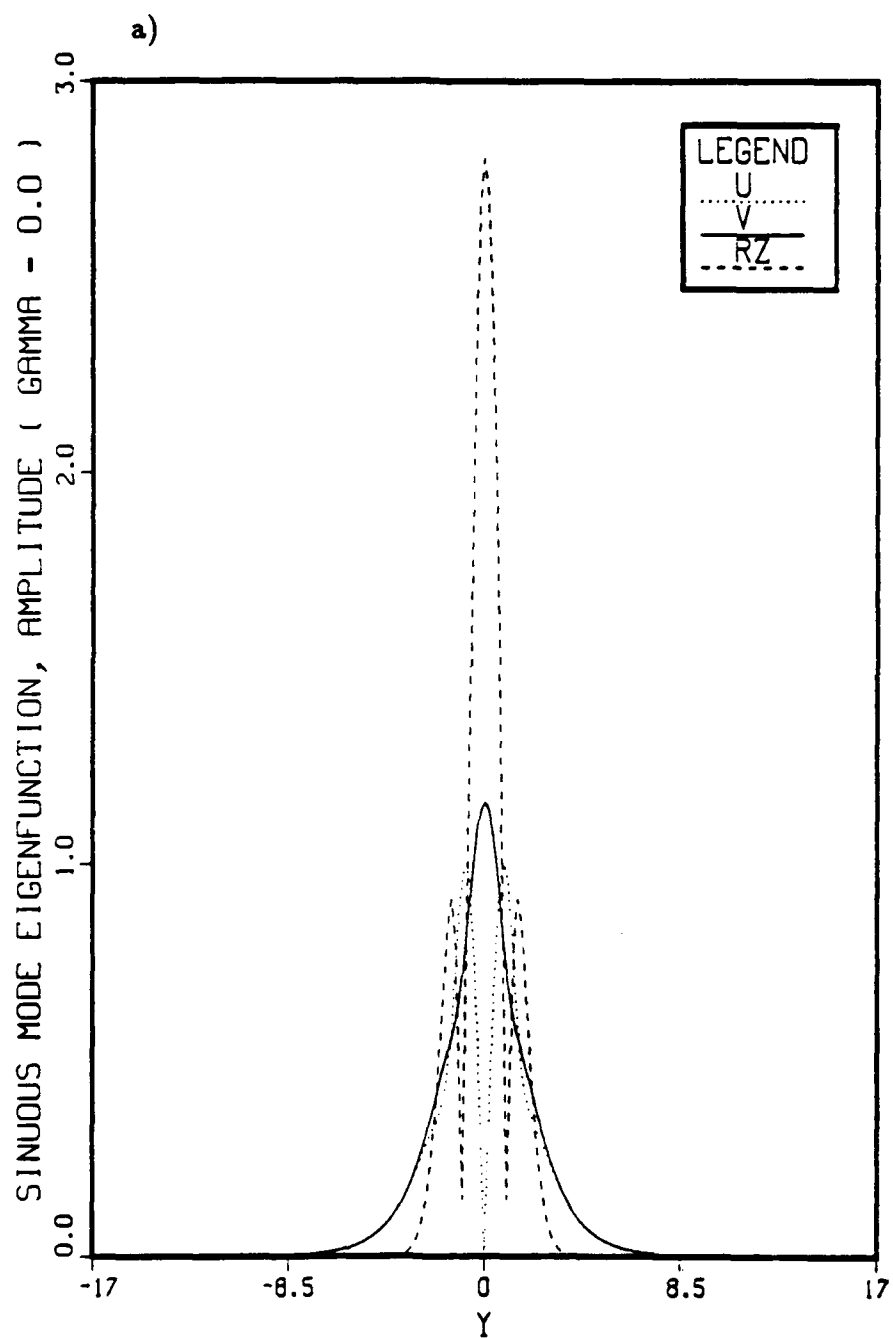


Figure 6.11 Sinuous mode eigenfunctions of the two-dimensional Orr-Sommerfeld equation corresponding to  $\beta = .51$  and  $Re_\theta = \frac{\theta_u \bar{U}_\infty}{\nu} = 594$ .  
 a) amplitudes of  $U^0$ ,  $V^0$ , and  $\Omega_z^0$ ; b) phases of  $U^0$ ,  $V^0$ , and  $\Omega_z^0$ .

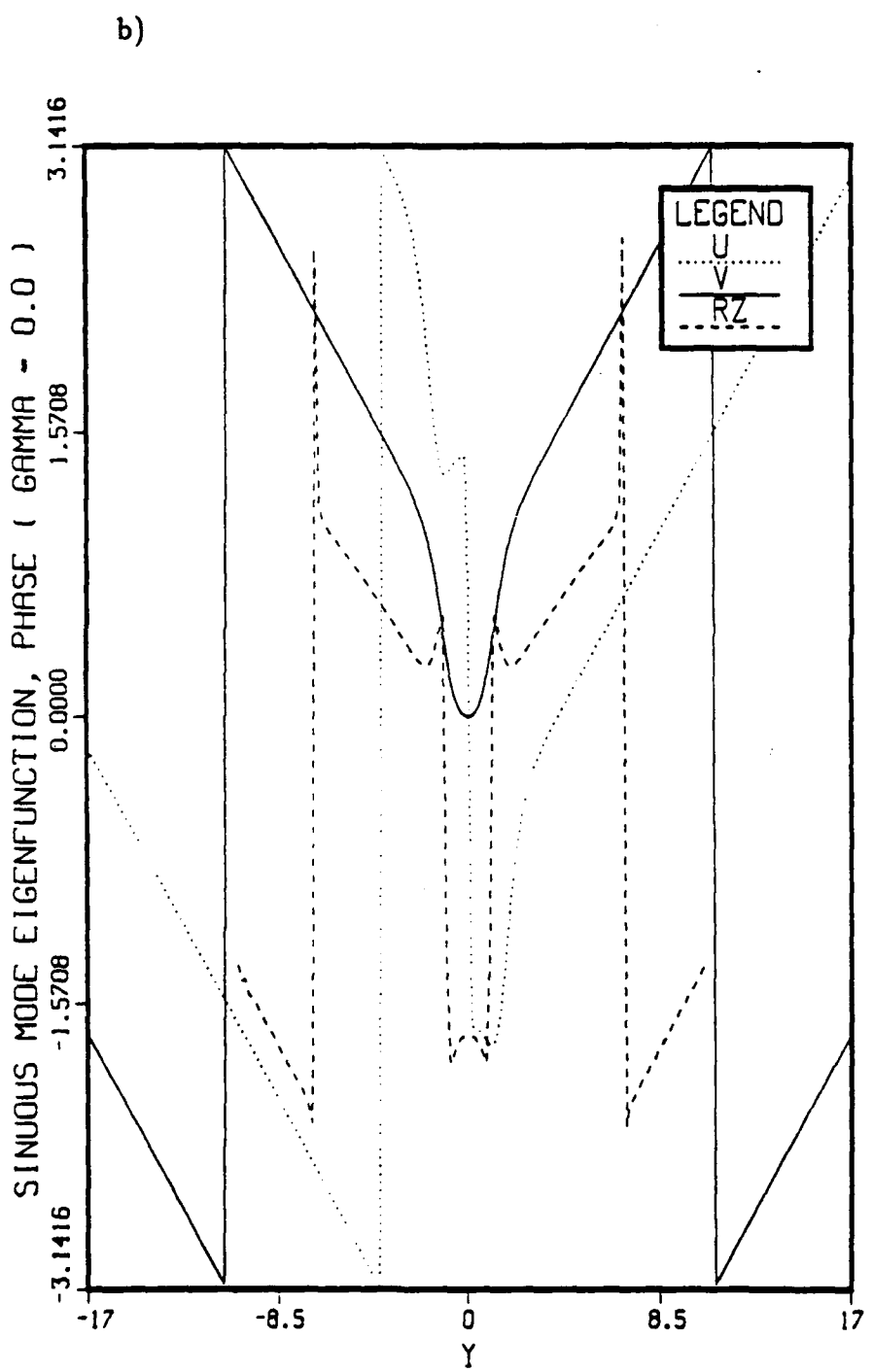


Figure 6.11 Continued.

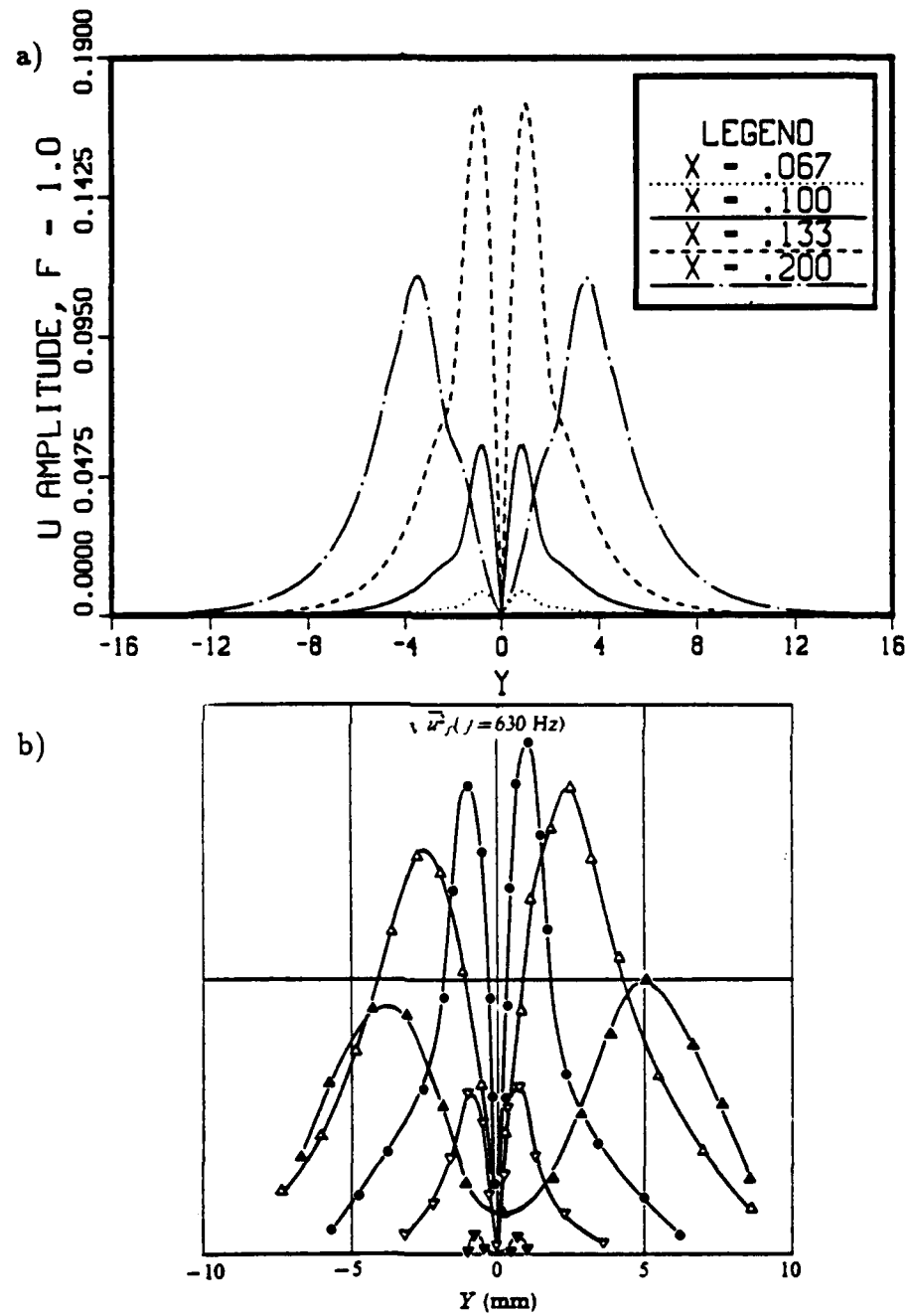


FIGURE 9. Distributions of fundamental (630 Hz) component. Natural transition. The ordinate scale is arbitrary.  $X$  (mm):  $\nabla$ , 20;  $\blacktriangledown$ , 30;  $\bullet$ , 40;  $\triangle$ , 60;  $\blacktriangle$ , 150.

Figure 6.12 Comparison of streamwise velocity amplitude distributions of the fundamental disturbance ( $F = 1$ ) to experimental data. a) Case-2:  $A_2 = .000667$ ,  $A_3 = 0$ , and  $\beta = .51$ ; b) experimental, reproduced from Sato (1970).

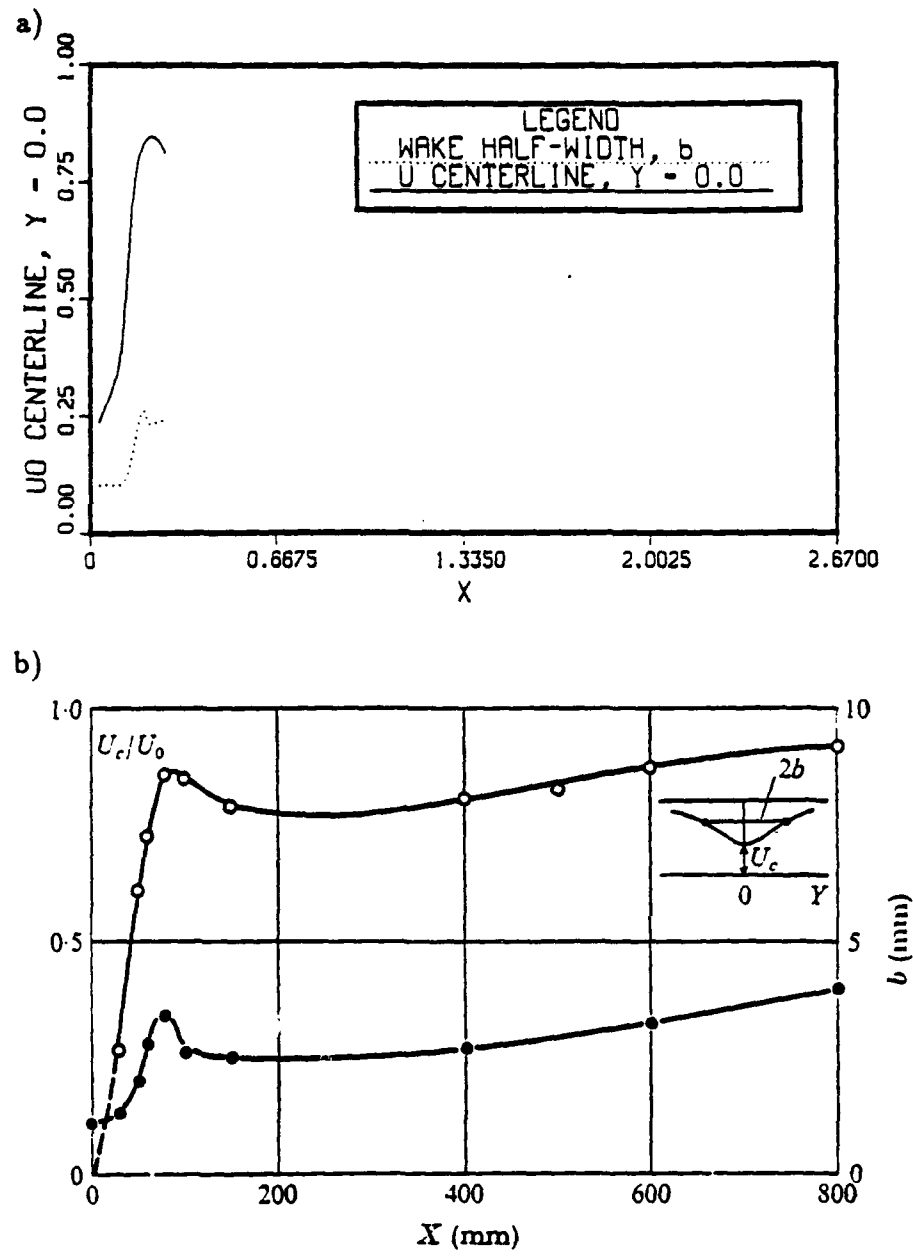


FIGURE 3. Streamwise variations of velocity on the centre-line  $U_c$ ,  $\circ$  and half-value-breadth  $b$ ,  $\bullet$ . Natural transition.

Figure 6.13 Comparison of the streamwise variation of the mean streamwise centerline velocity  $U^0$  and the mean wake half-width to experimental data. a) Case-2:  $A_2 = .000667$ ,  $A_3 = 0$ , and  $\beta = .51$ ; b) experimental, reproduced from Sato (1970).

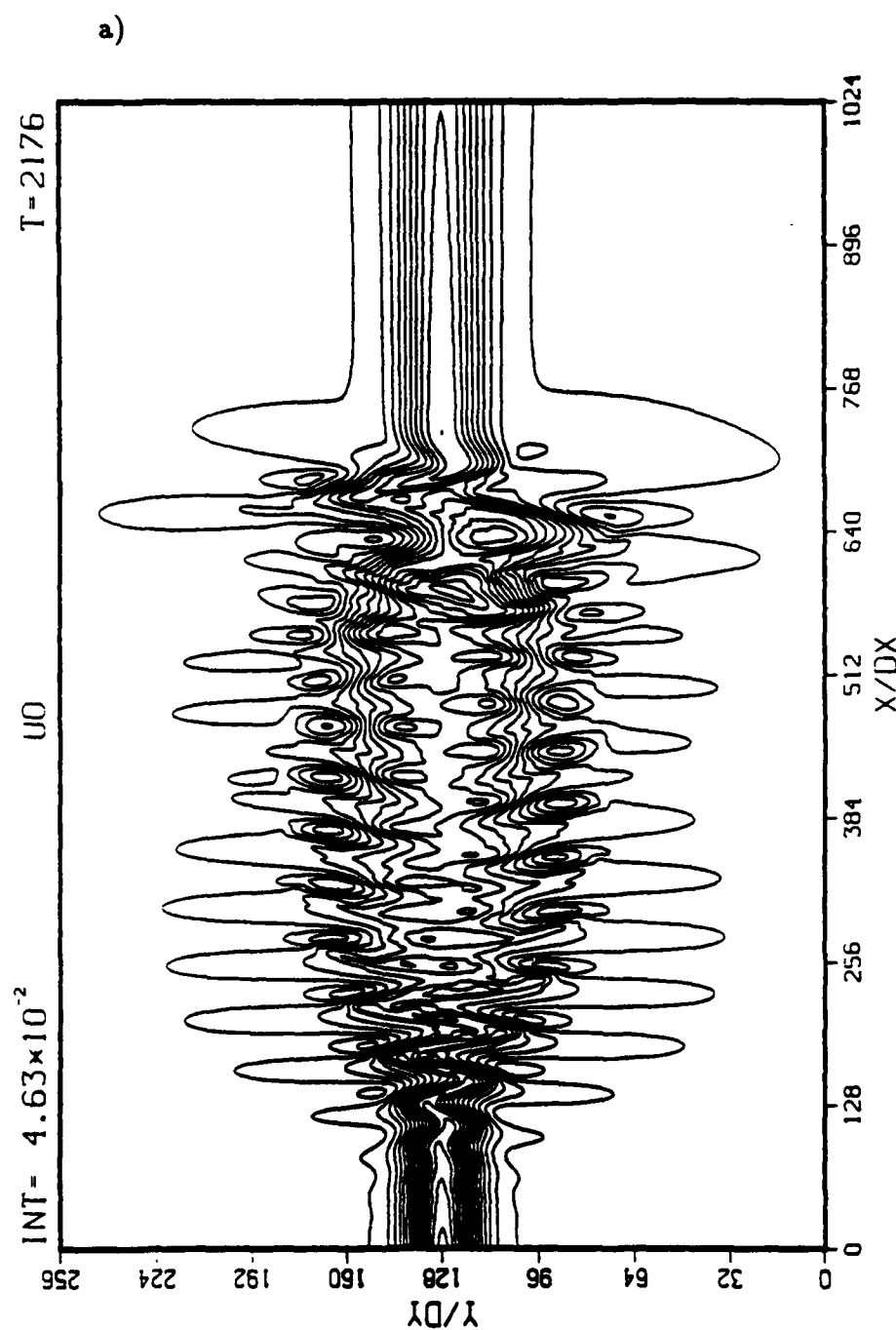


Figure 6.14 Contours of  $U^0$ ,  $V^0$ , and  $\Omega_z^0$  for  $t = 2176\Delta t$ . Case-3:  $A_2 = .001$ ,  $A_3 = 0$ , and  $\beta = .51$ . Twenty contour intervals between the minimum and maximum values. Solid lines denote positive vorticity and dashed lines denote negative vorticity. a) streamwise velocity,  $U^0$ ; b) transverse velocity,  $V^0$ ; c) spanwise vorticity,  $\Omega_z^0$ .

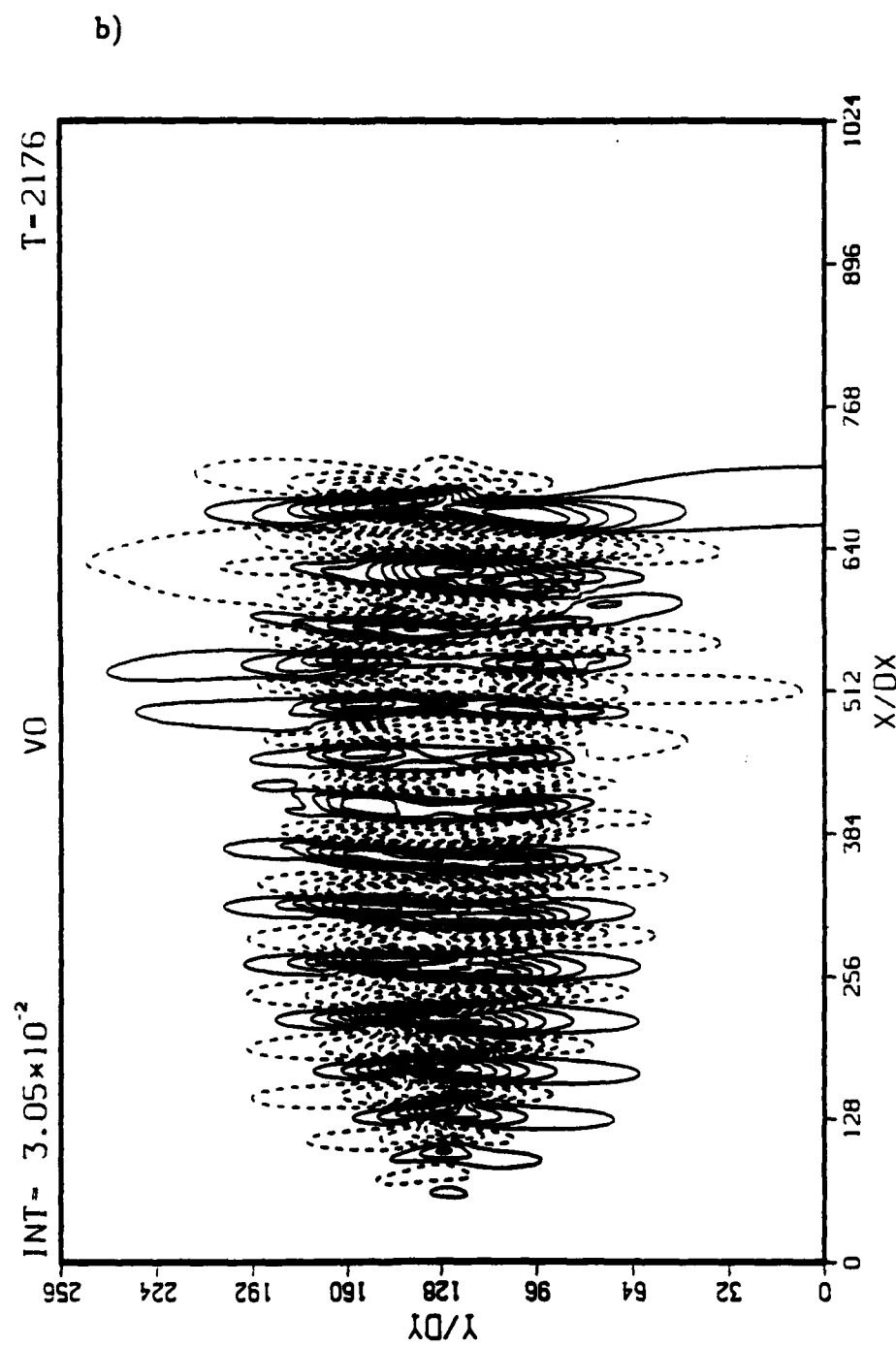


Figure 6.14 Continued.

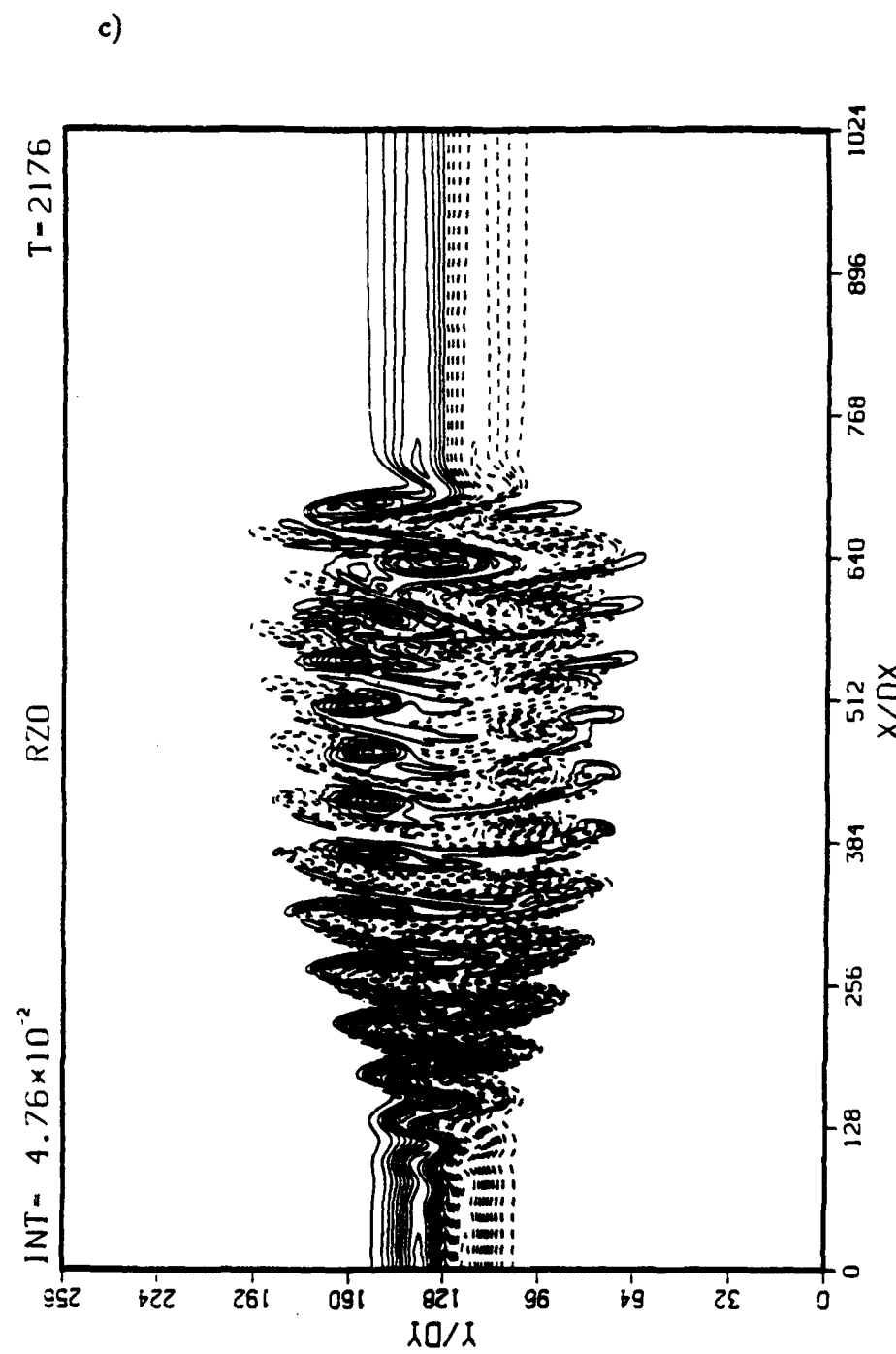


Figure 6.14 Continued.

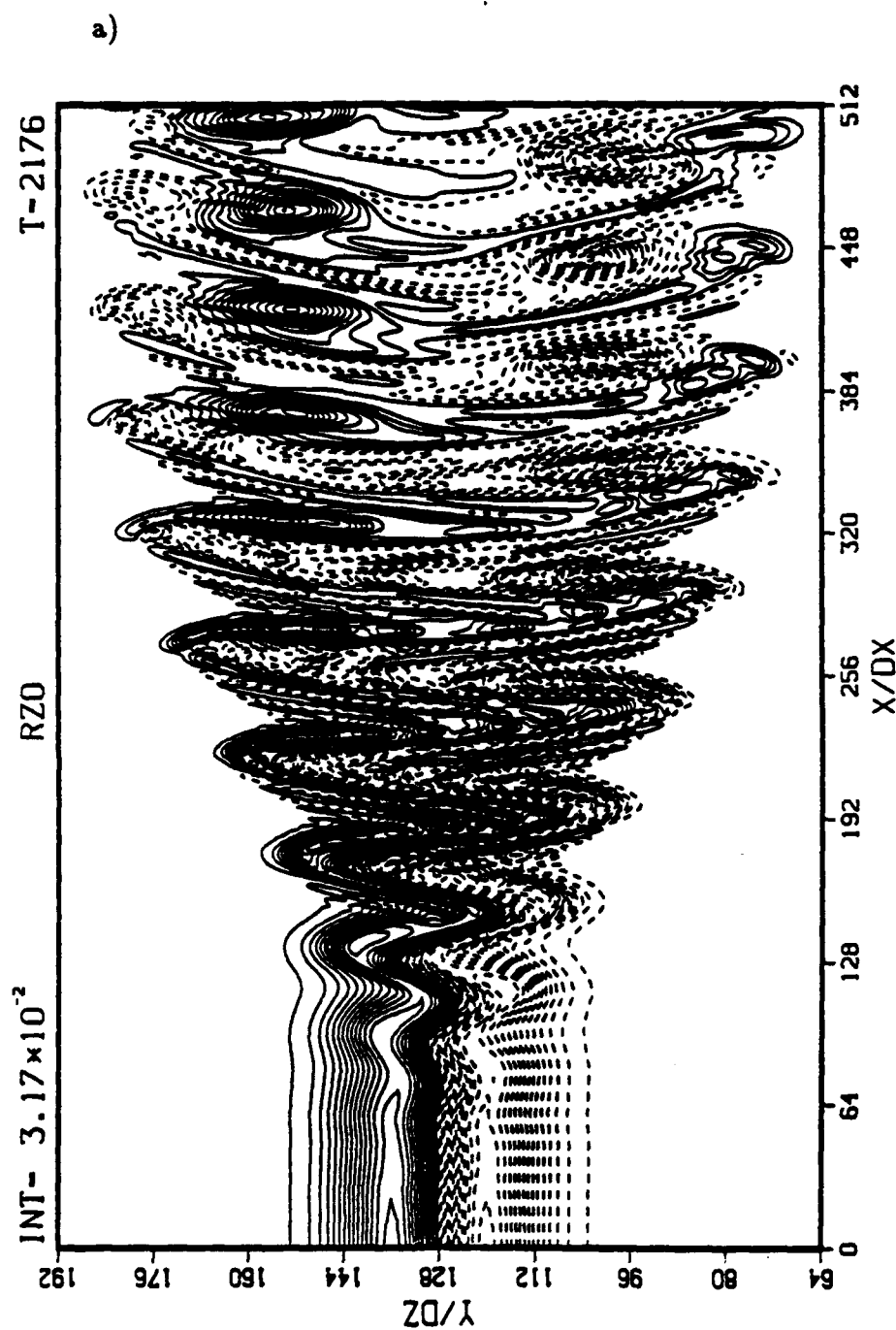


Figure 6.15 Contours of spanwise vorticity  $\Omega_z^0$  for  $t = 2176\Delta t$ . Case-3:  $A_2 = .001$ ,  $A_3 = 0$ , and  $\beta = .51$ . Thirty contour intervals between the minimum and maximum values. Solid lines denote positive vorticity and dashed lines denote negative vorticity. a)  $0 \leq z/\Delta z \leq 512$ , b)  $0 \leq z/\Delta z \leq 340$ .

160

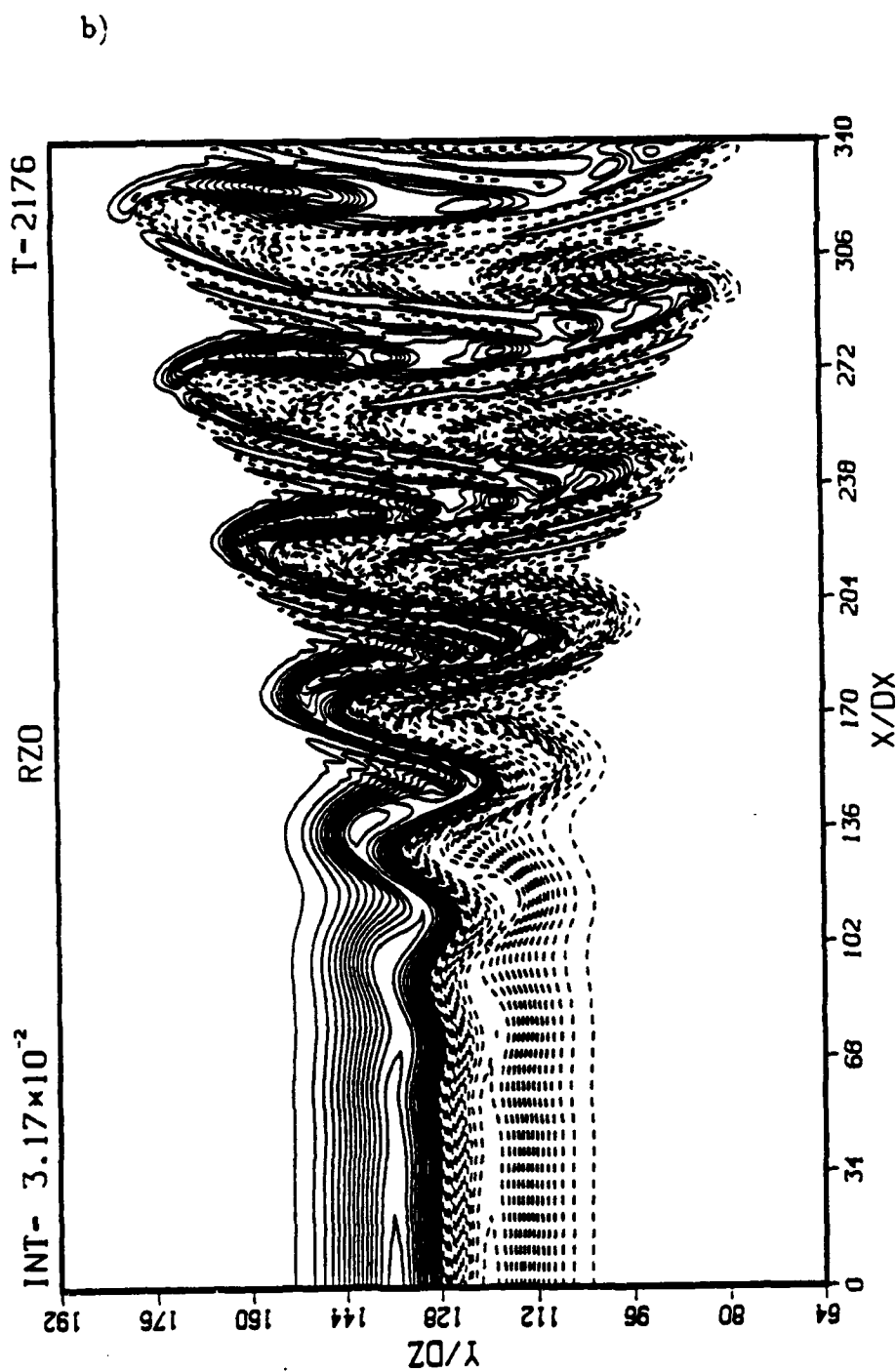


Figure 6.15 Continued.

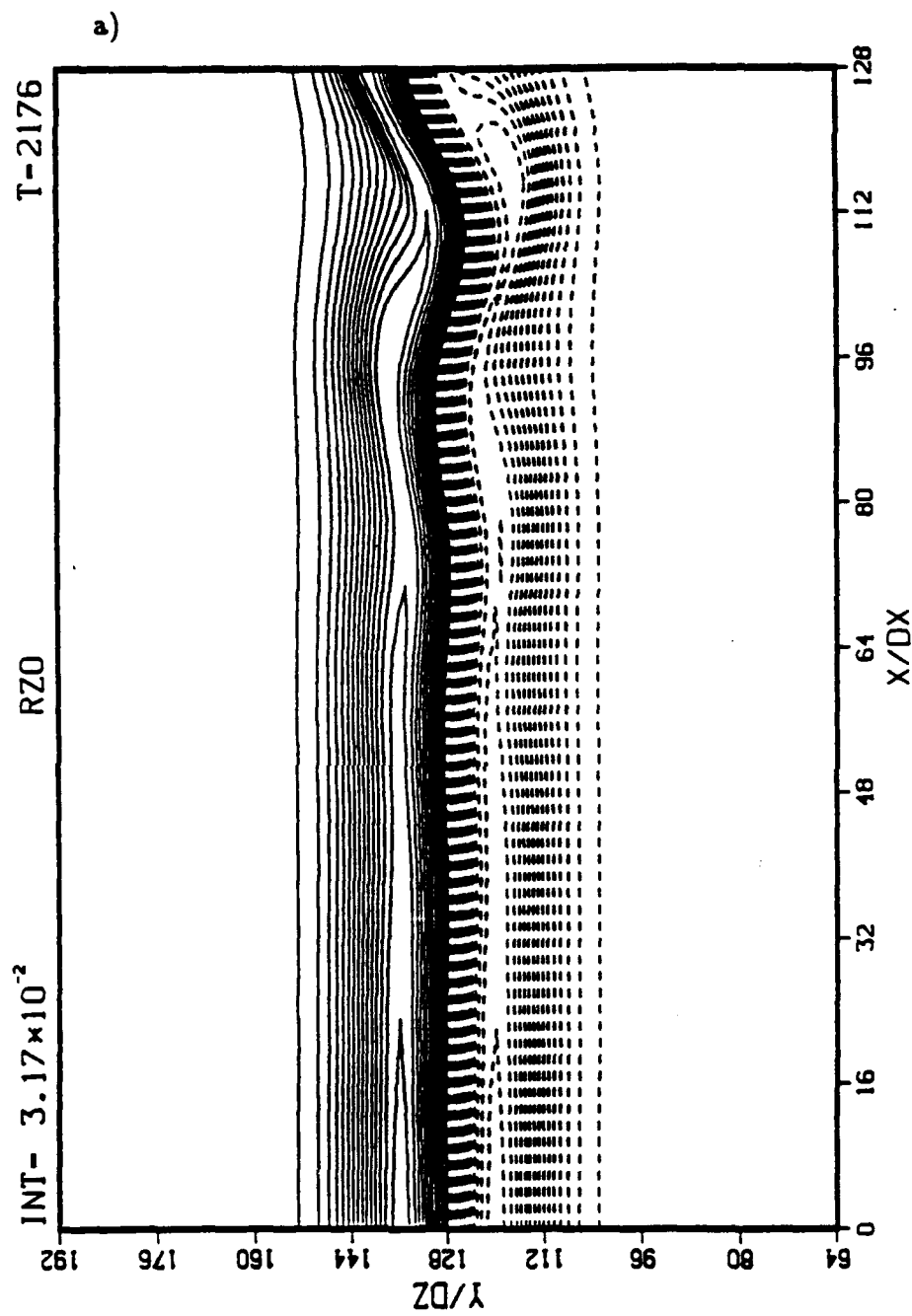


Figure 6.16 Contours of spanwise vorticity  $\Omega_z^0$  for  $t = 2176\Delta t$ . Case-3:  $A_2 = .001$ ,  $A_3 = 0$ , and  $\beta = .51$ . Thirty contour intervals between the minimum and maximum values. Solid lines denote positive vorticity and dashed lines denote negative vorticity. a)  $0 \leq z/\Delta z \leq 128$ , b)  $128 \leq z/\Delta z \leq 256$ , c)  $256 \leq z/\Delta z \leq 384$ , d)  $384 \leq z/\Delta z \leq 512$ .

b)

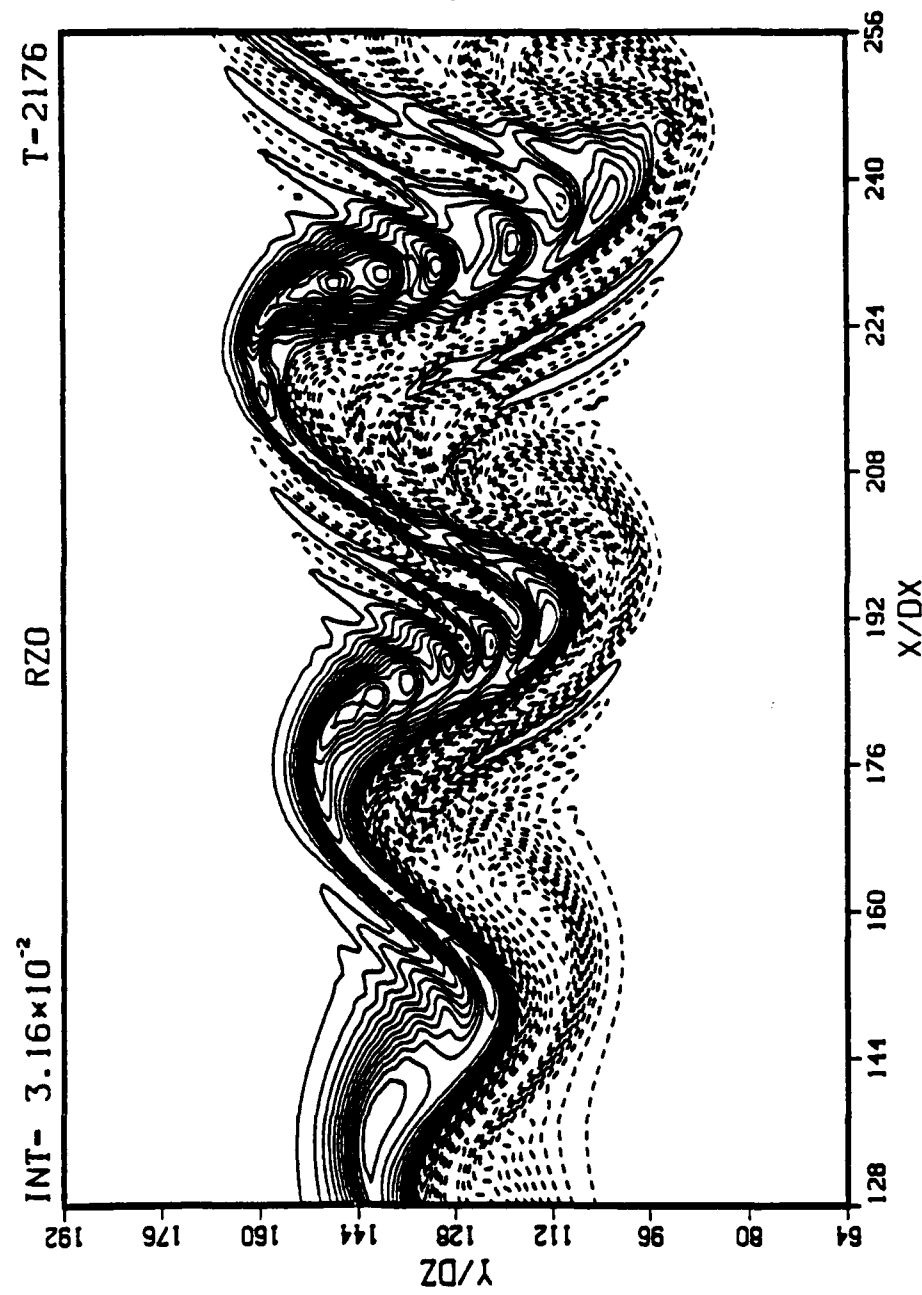


Figure 6.16 Continued.

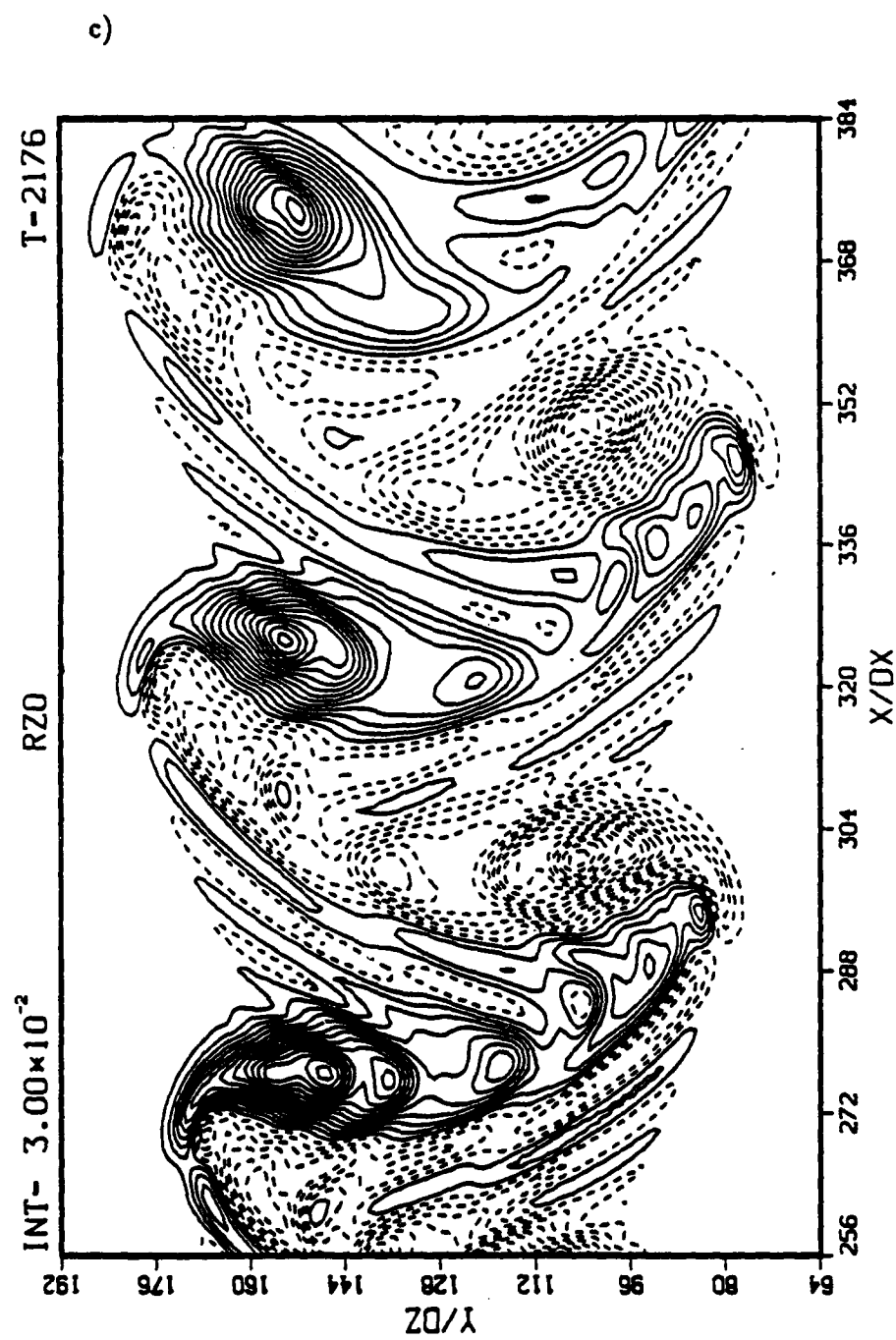


Figure 6.16 Continued.

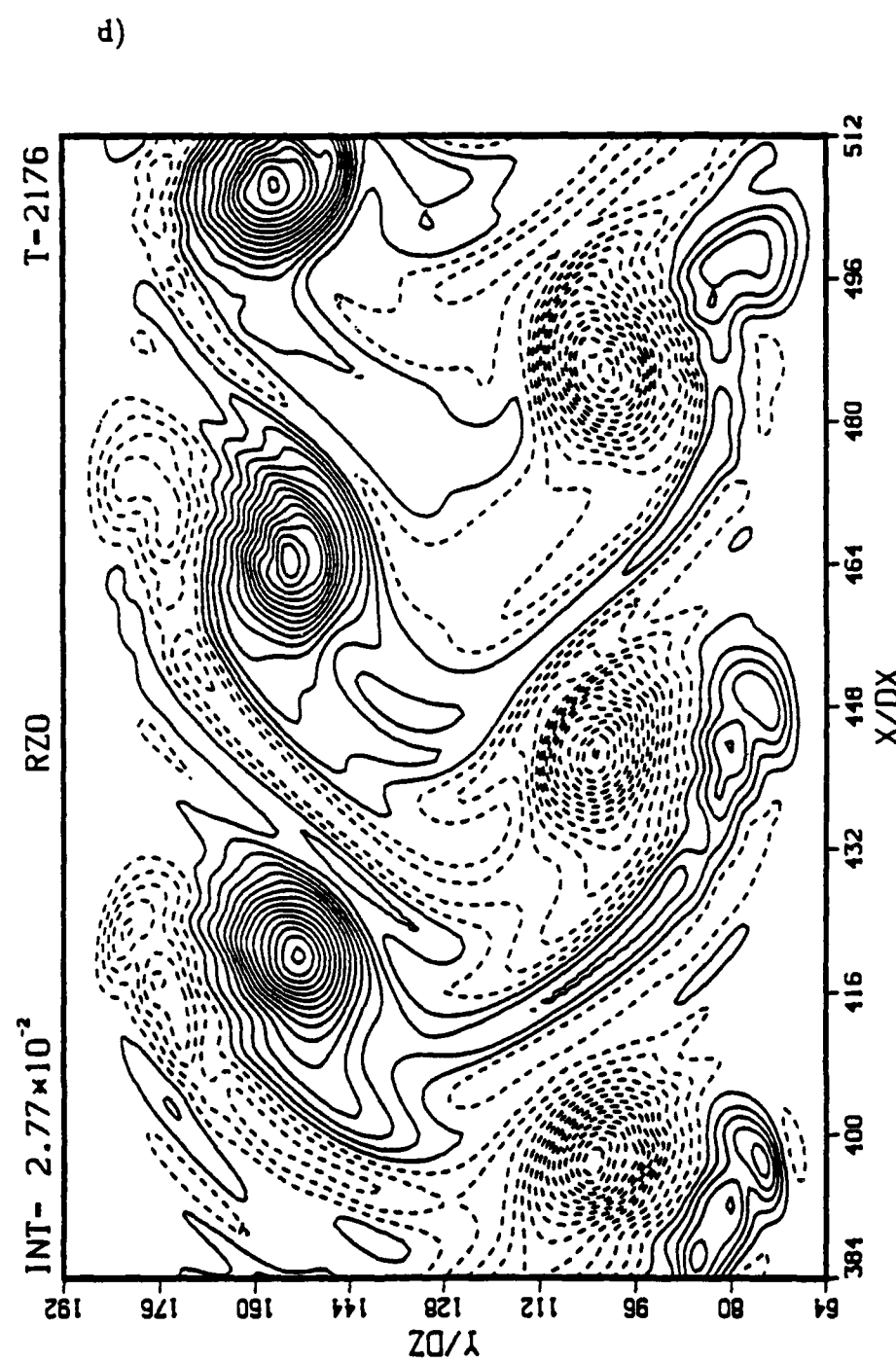


Figure 6.16 Continued.

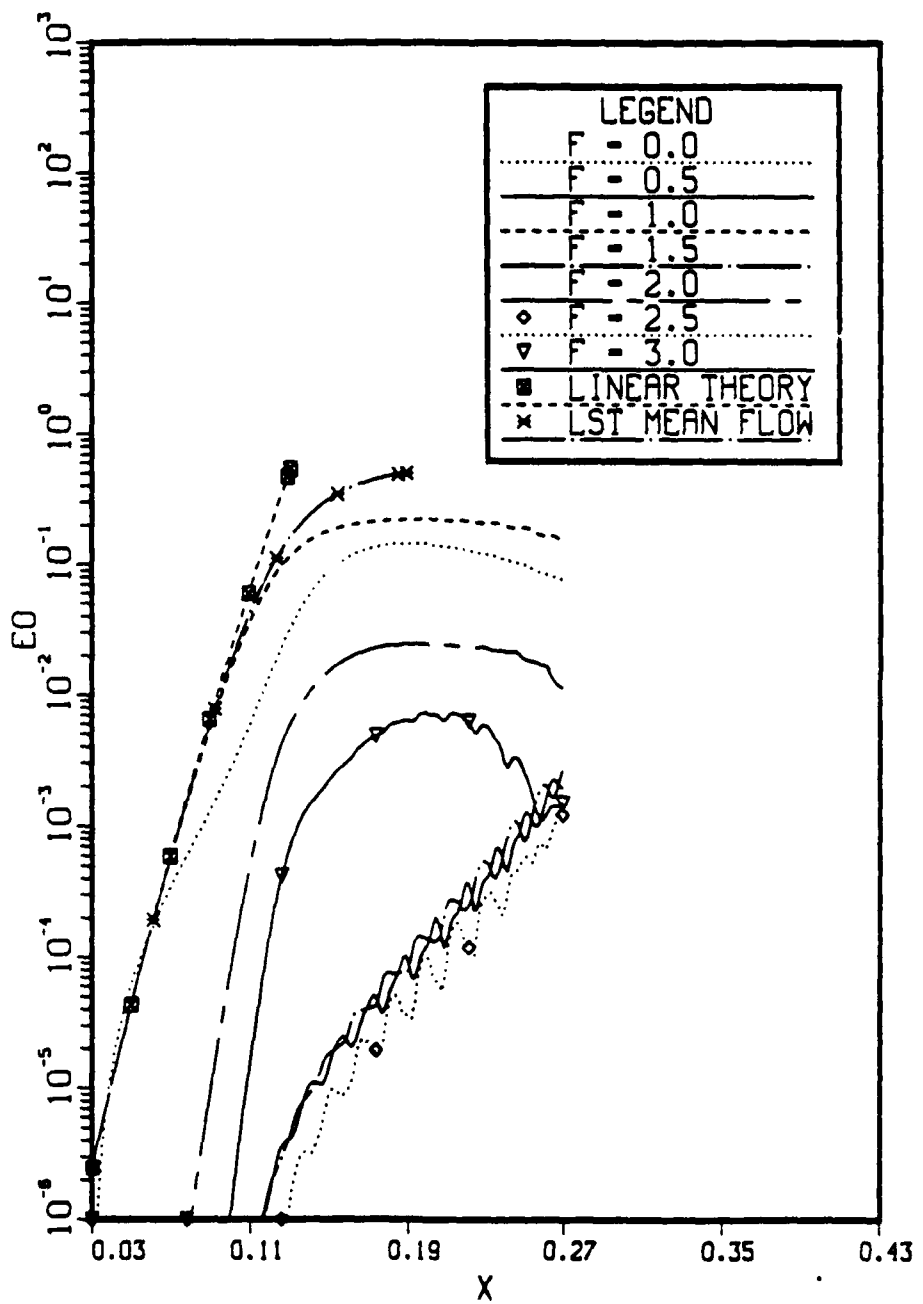


Figure 6.17 Amplification curves of the kinetic energy  $\hat{E}^0(x, F)$  obtained from the time interval  $13T_F < t \leq 15T_F$ . Case-3:  $A_2 = .001$ ,  $A_3 = 0$ , and  $\beta = .51$ .

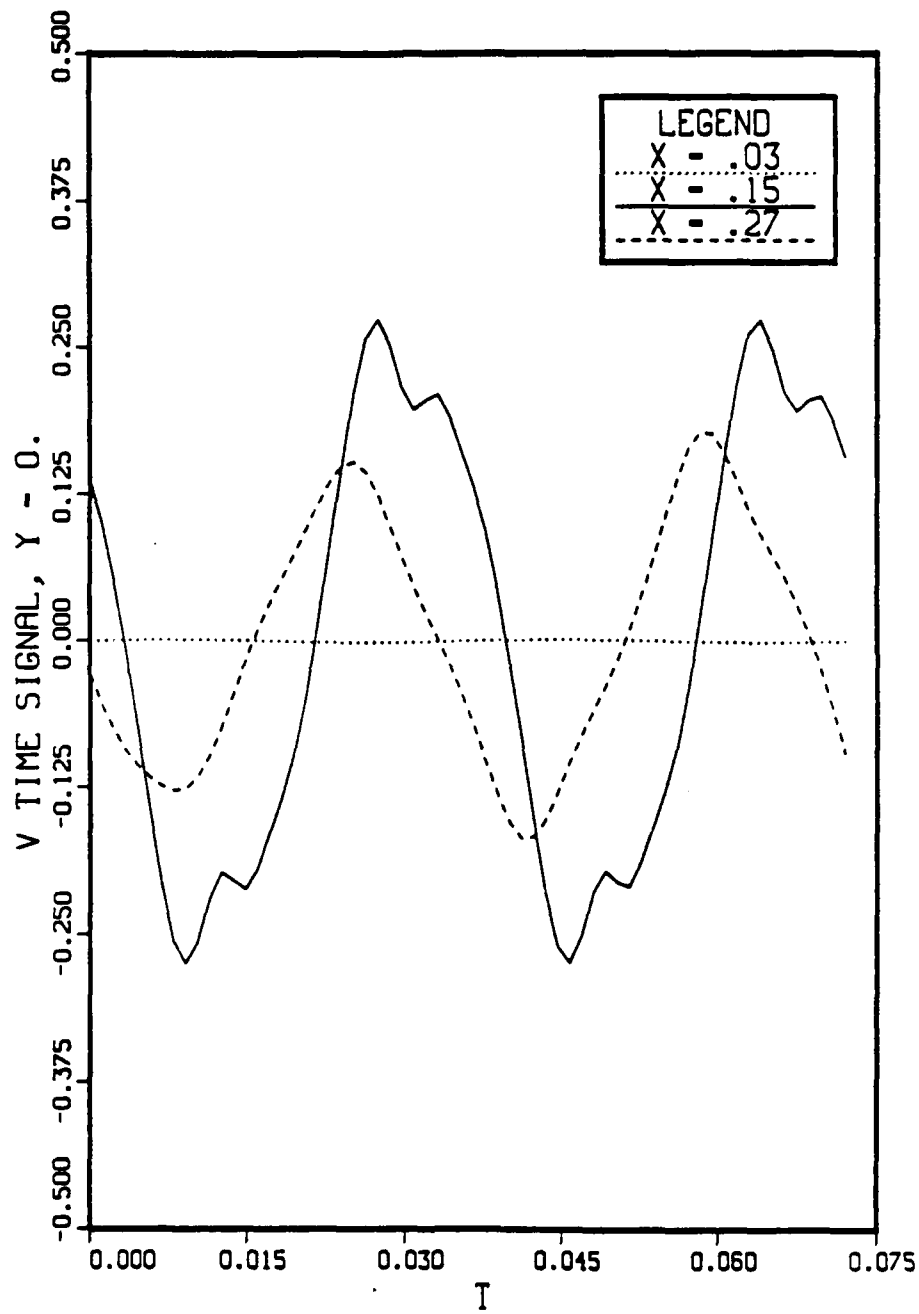


Figure 6.18 Temporal variation of the centerline transverse velocity  $V^0$  in the time interval  $13T_F < t \leq 15T_F$ . Case-3:  $A_2 = .001$ ,  $A_3 = 0$ , and  $\beta = .51$ .

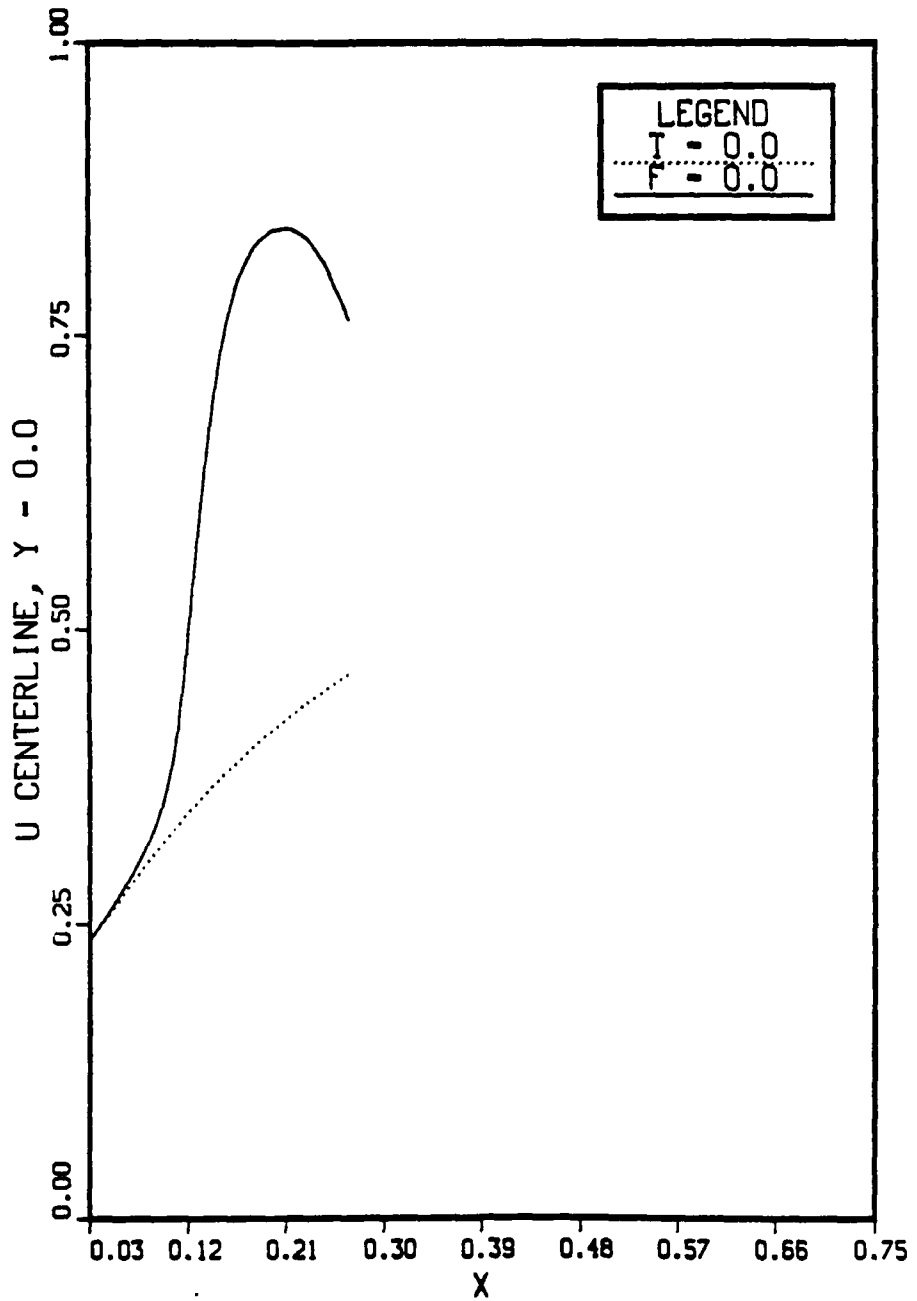


Figure 6.19 Streamwise variation of the centerline streamwise velocity  $U^0$  for the mean flow and the base flow. Case-3:  $A_2 = .001$ ,  $A_3 = 0$ , and  $\beta = .51$ .

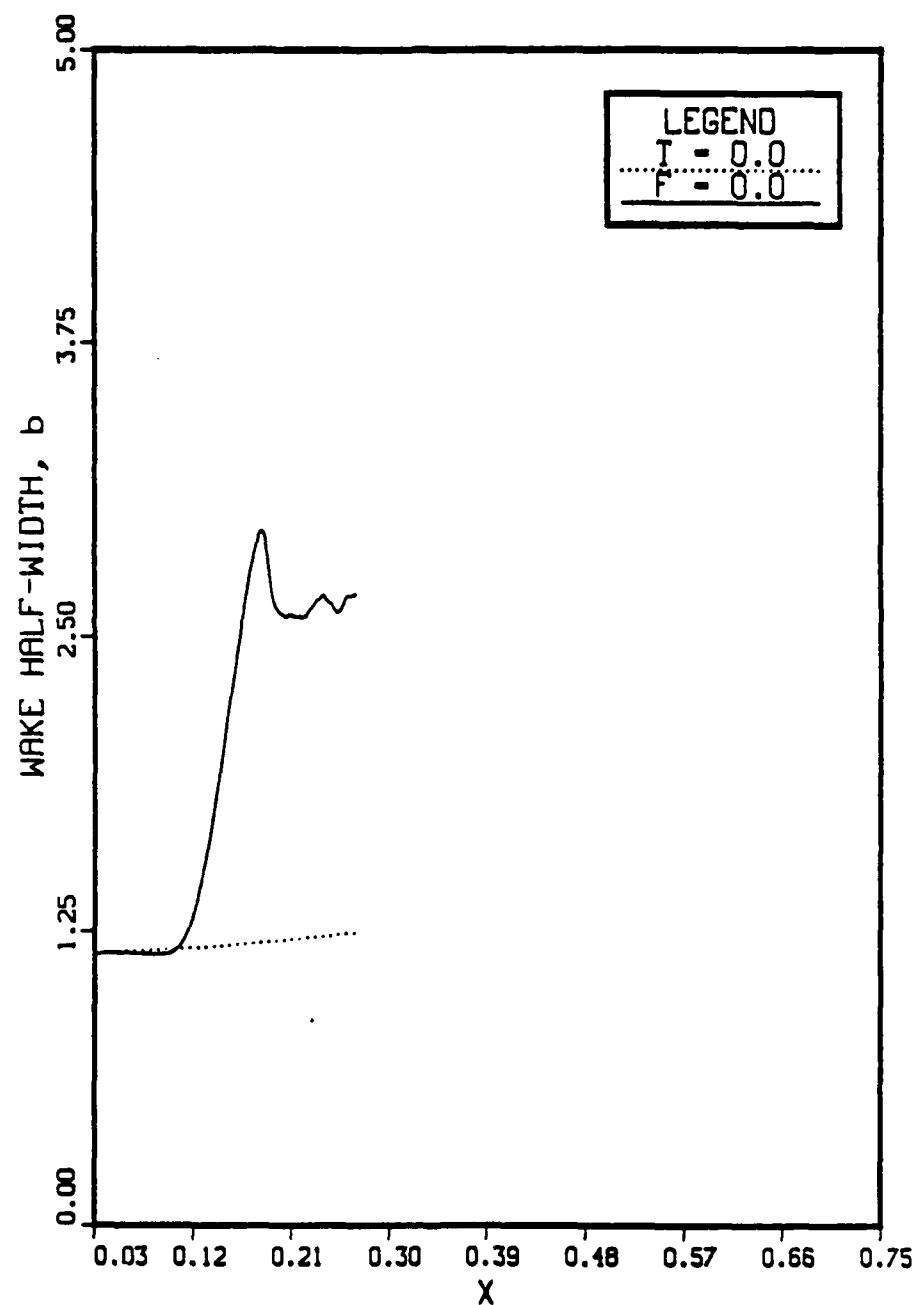


Figure 6.20 Streamwise variation of the wake half-width  $b$  for the mean flow and the base flow. Case-3:  $A_2 = .001$ ,  $A_3 = 0$ , and  $\beta = .51$ .

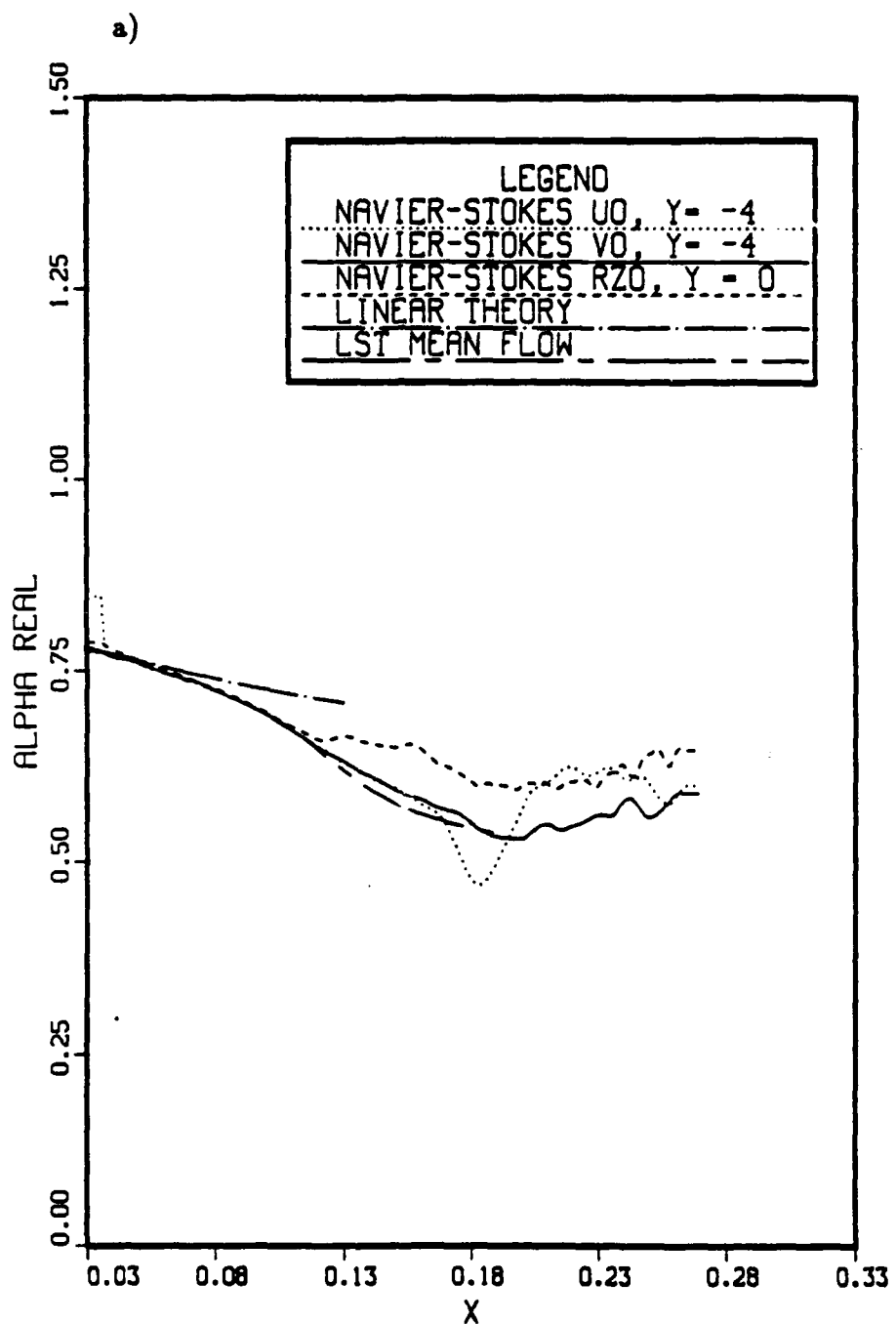


Figure 6.21 Streamwise variation of  $\alpha_r$  and  $c_p$  for the fundamental disturbance component ( $F = 1$ ). Case-3:  $A_2 = .001$ ,  $A_3 = 0$ , and  $\beta = .51$ . a) streamwise wavenumber,  $\alpha_r$ ; b) phase velocity,  $c_p$ .

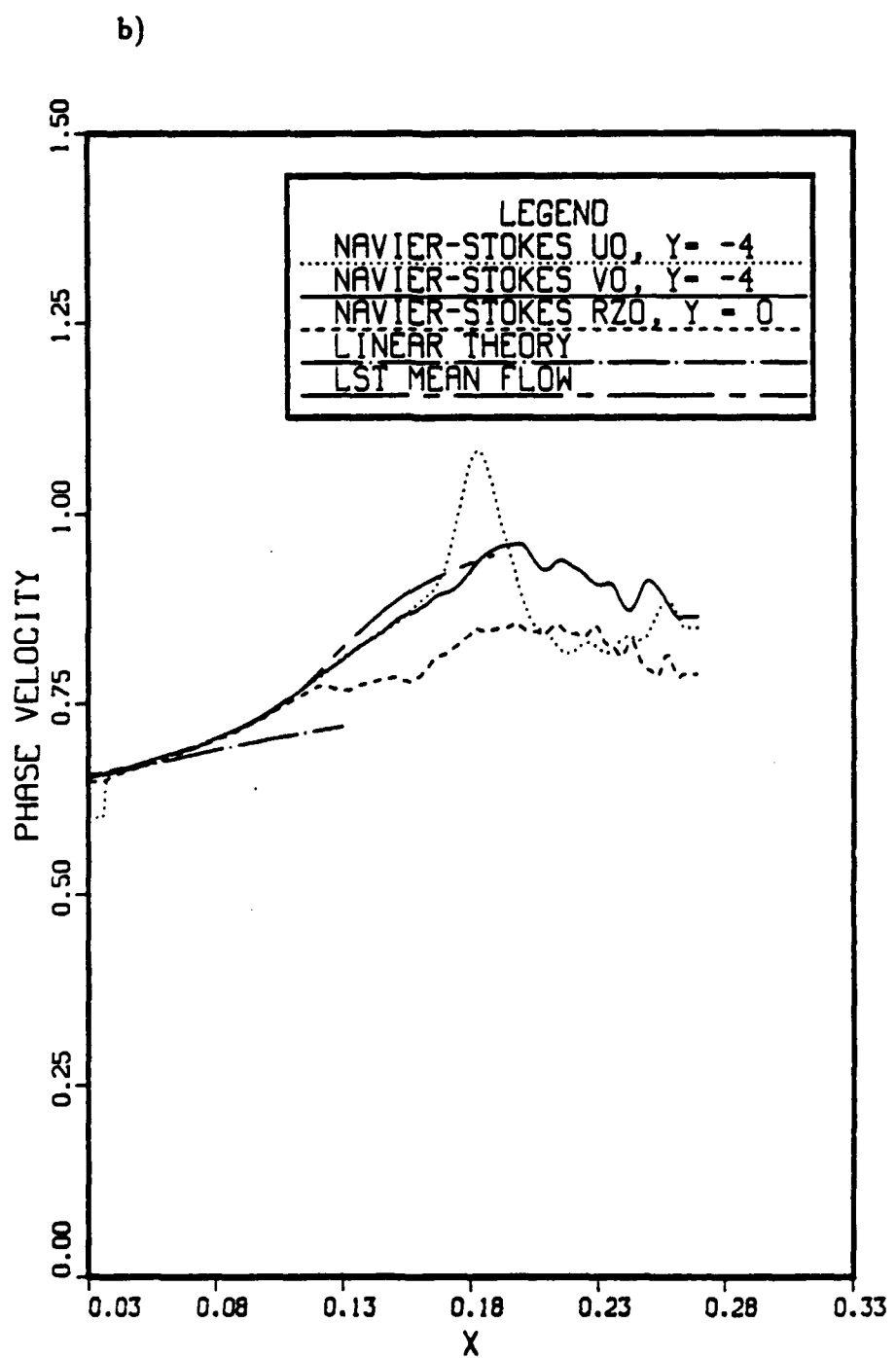


Figure 6.21 Continued.

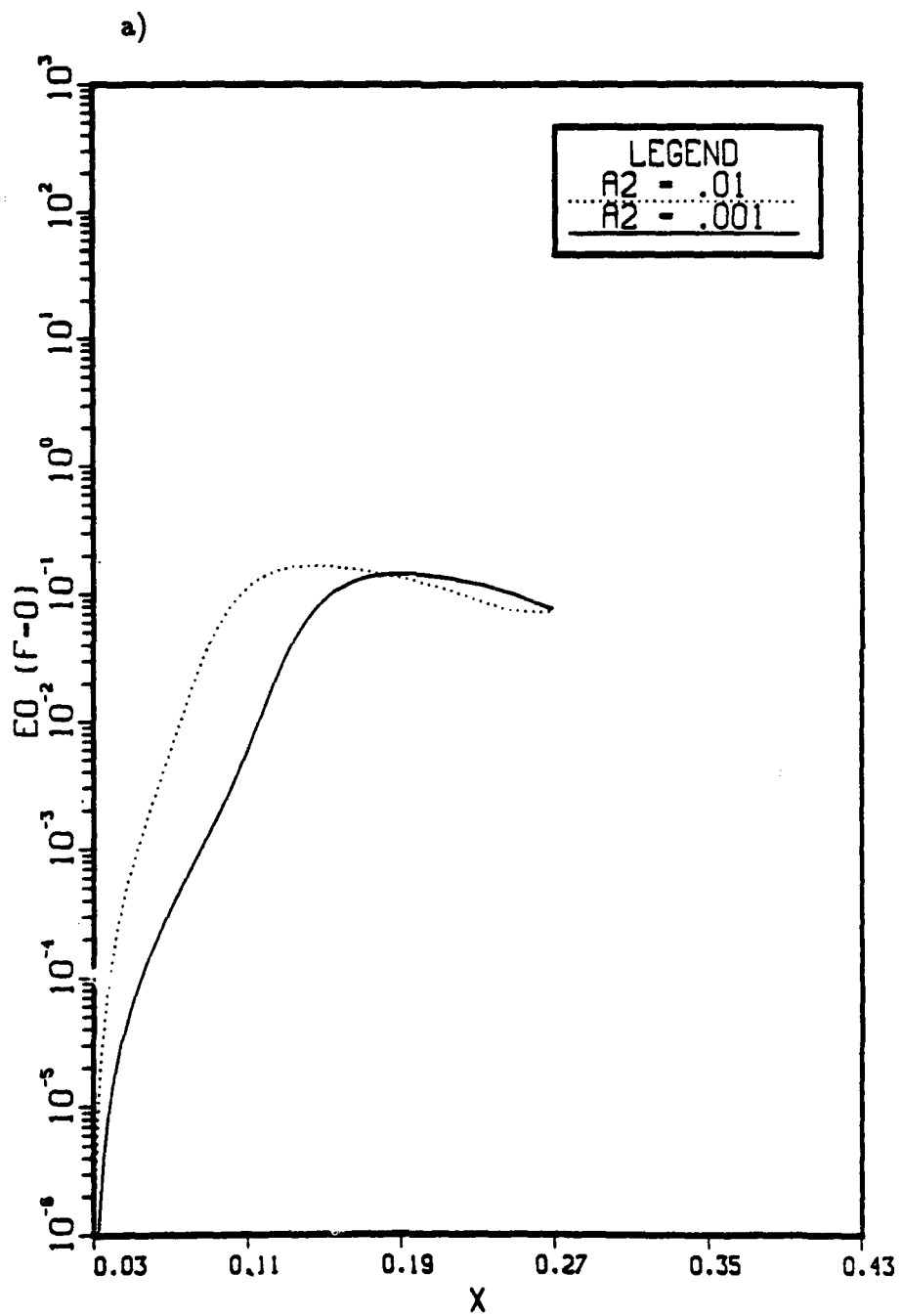


Figure 6.22 Amplification curves of the kinetic energy  $\hat{E}^0(x, F)$  for Case-3 ( $A_2 = .001$ ) and Case-4 ( $A_2 = .01$ ). a)  $F = 0$ , b)  $F = 1$ , c)  $F = 2$ .

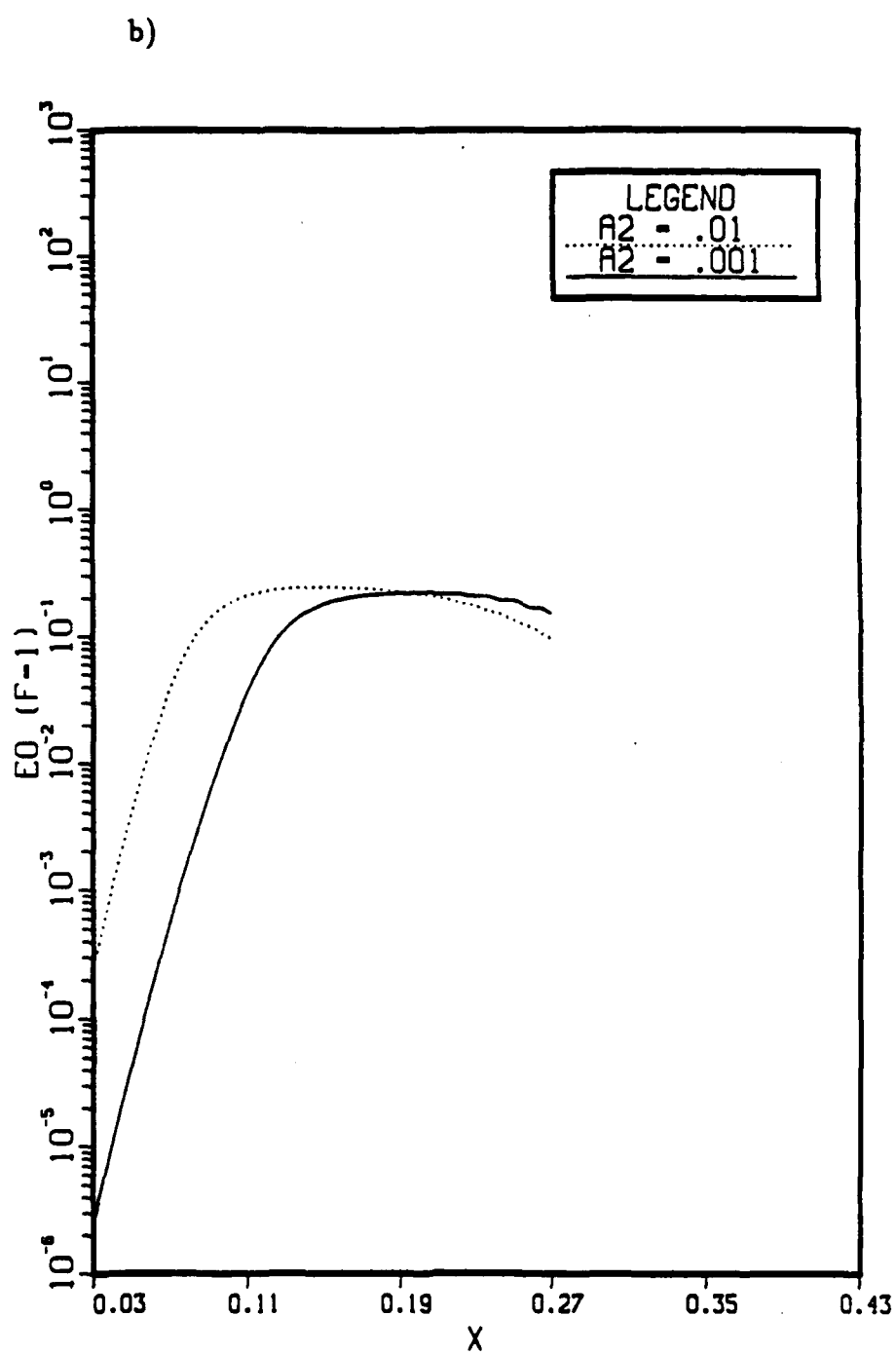


Figure 6.22 Continued.

c)

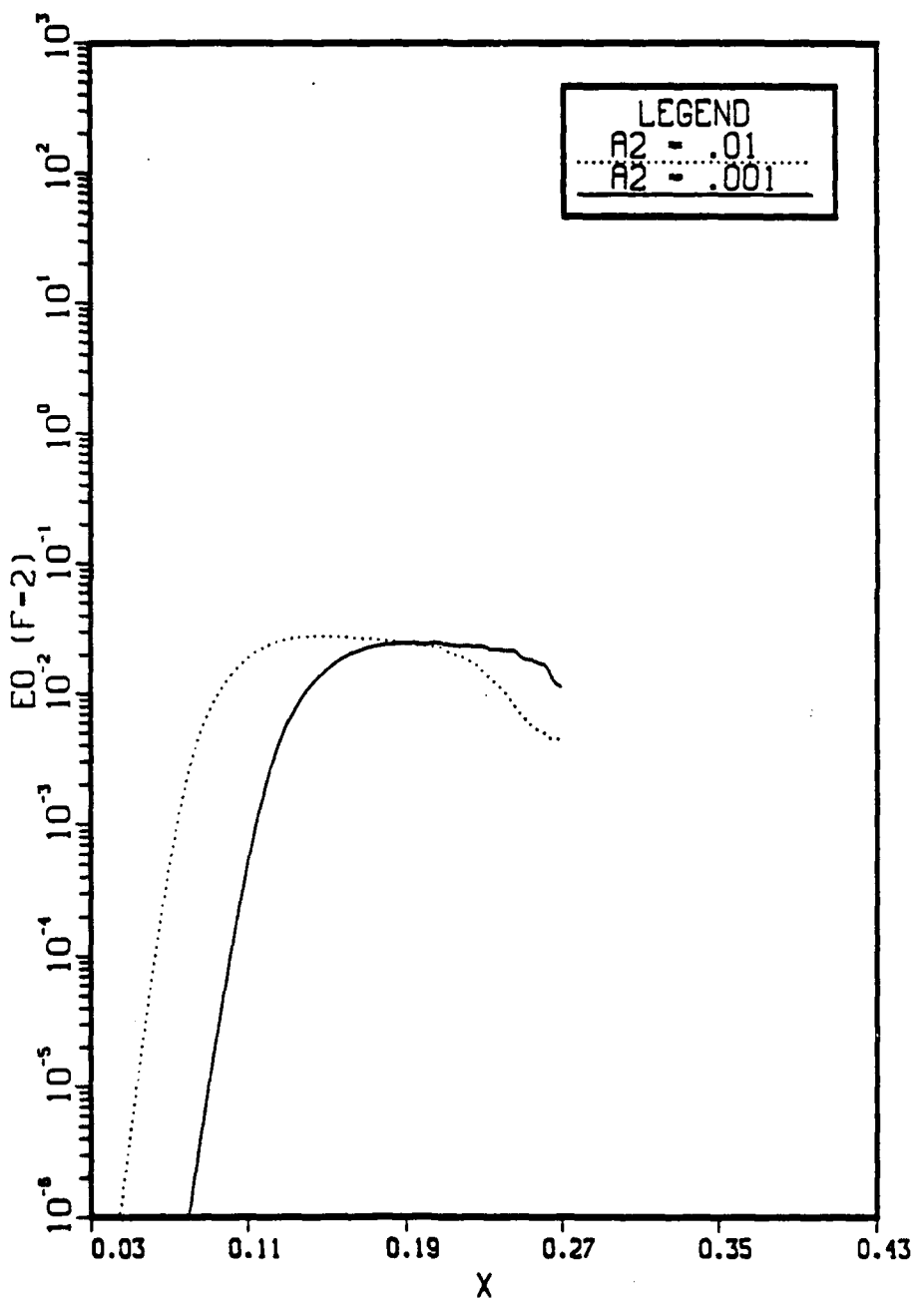


Figure 6.22 Continued.

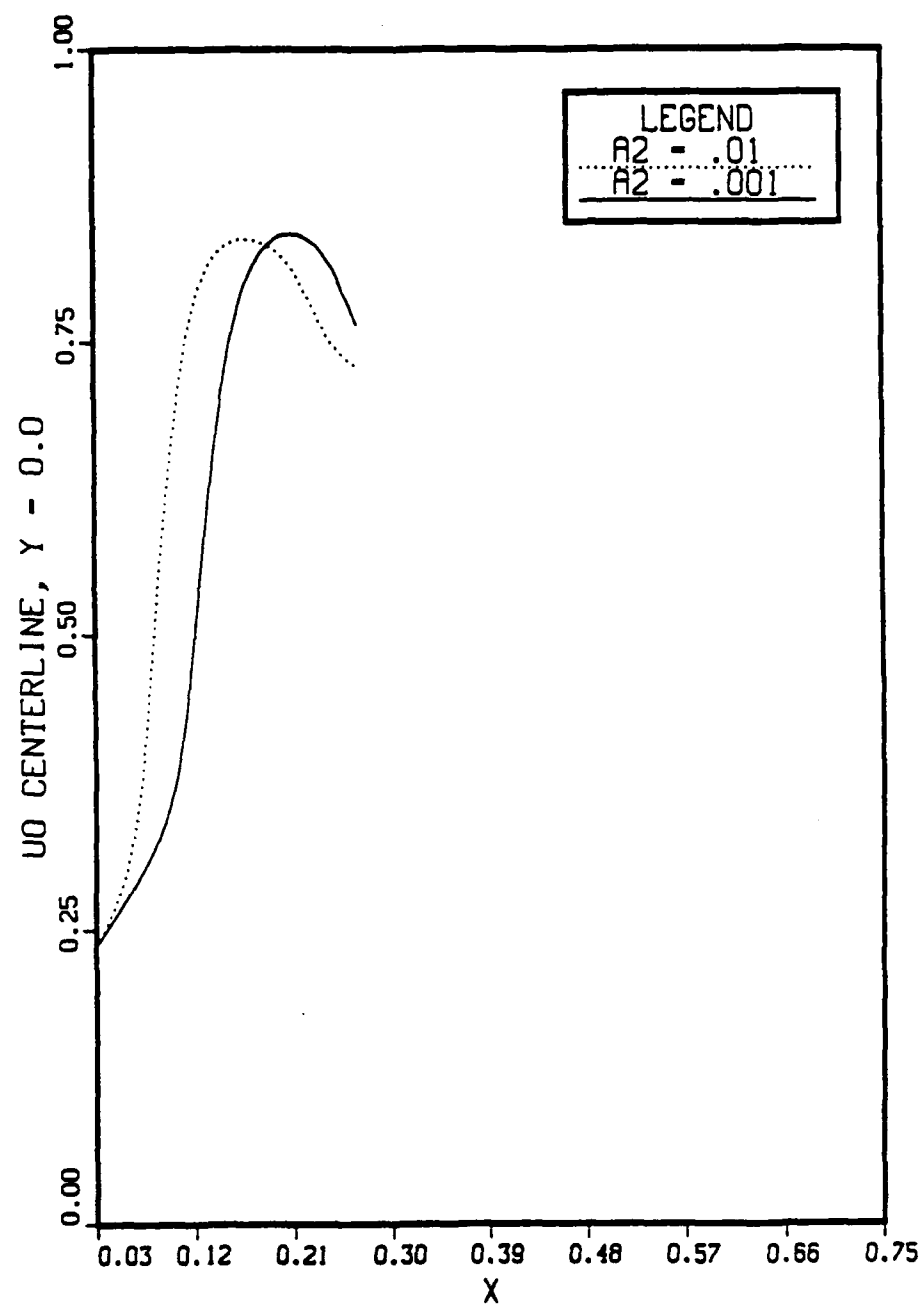


Figure 6.23 Comparison of the mean centerline streamwise velocity  $U^0$  for Case-3 ( $A_2 = .001$ ) and Case-4 ( $A_2 = .01$ ).

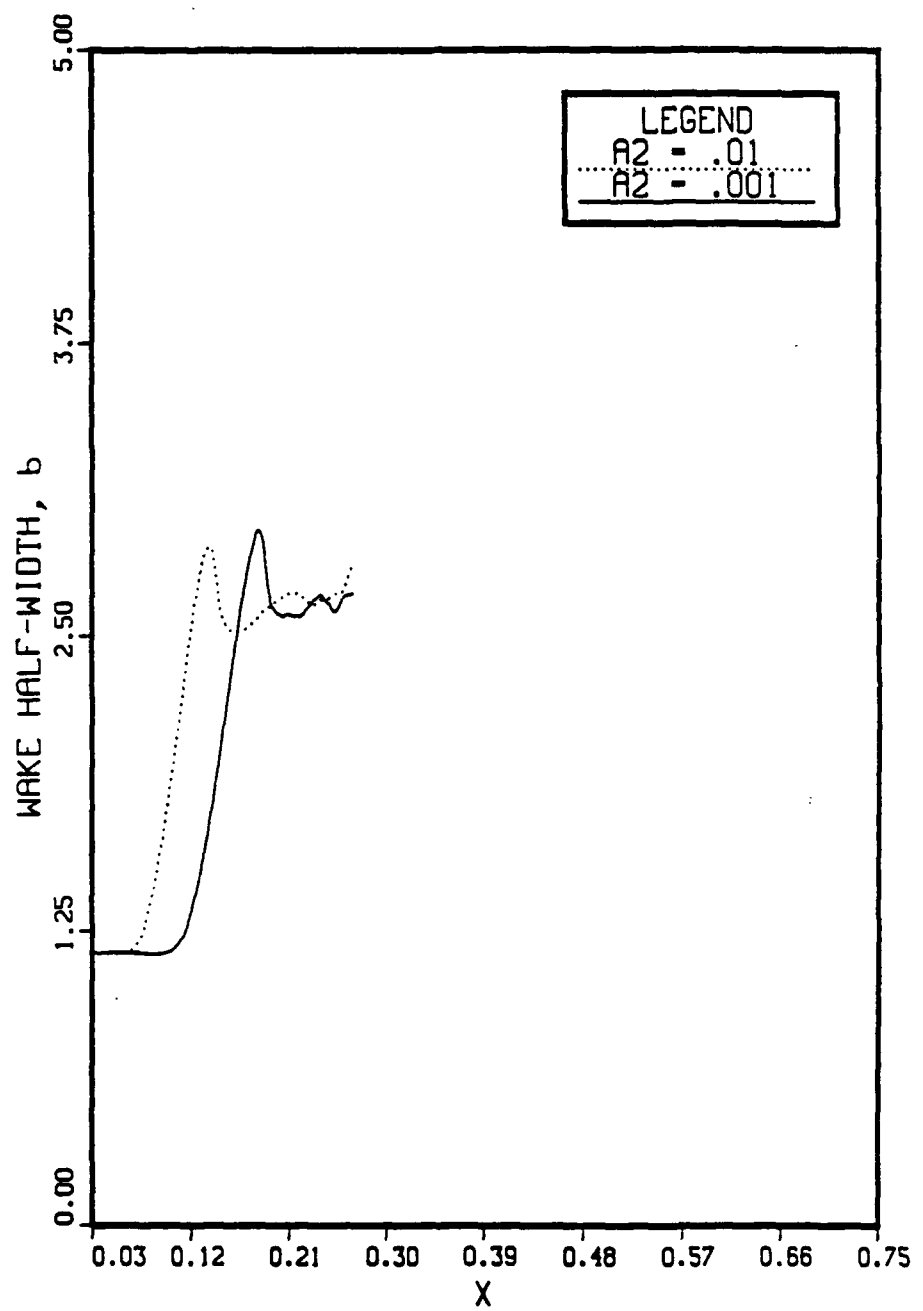


Figure 6.24 Comparison of the streamwise variation of the mean half-width  $b$  for Case-3 ( $A_2 = .001$ ) and Case-4 ( $A_2 = .01$ ).

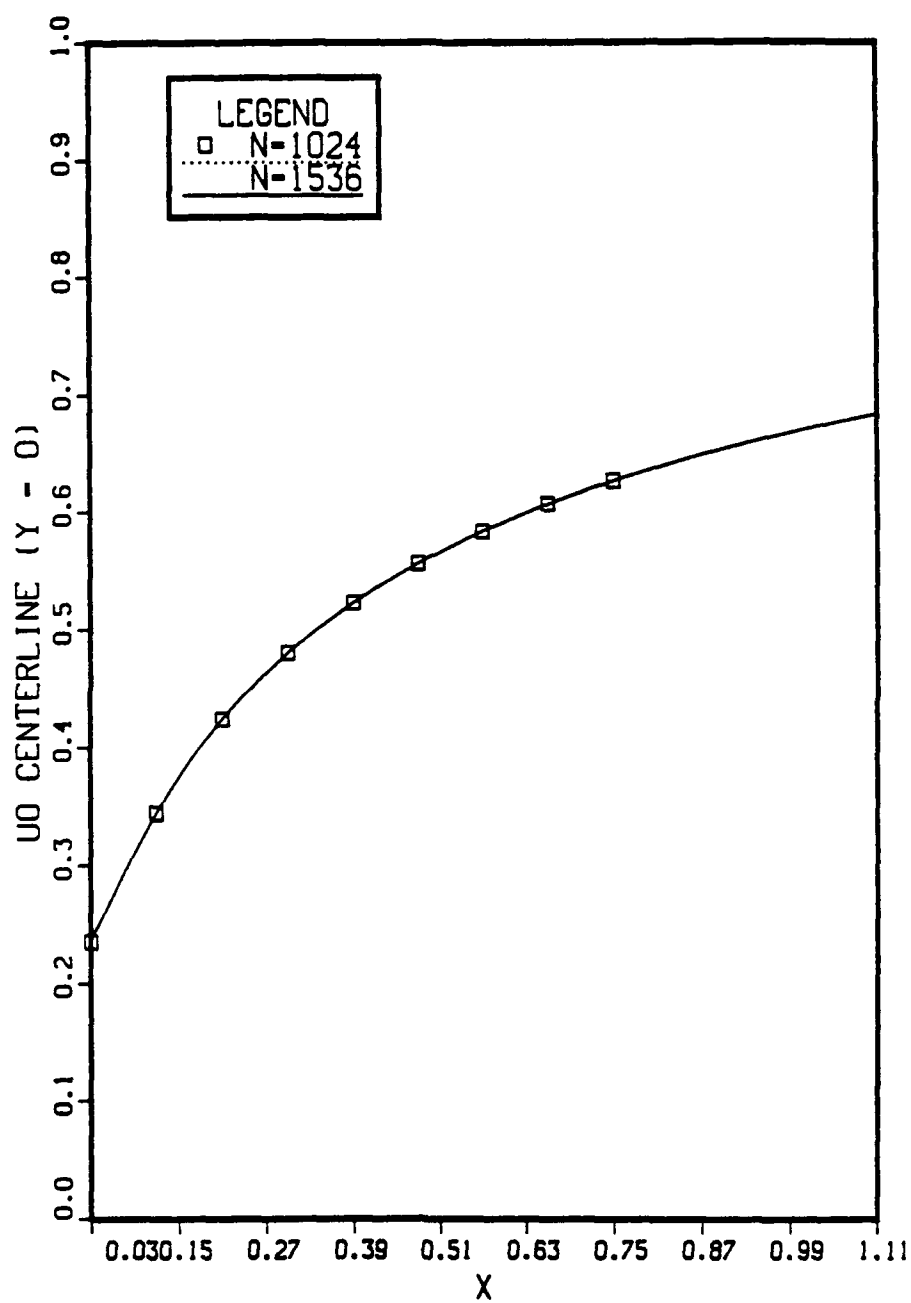


Figure 6.25 Comparison of the base flow centerline streamwise velocity  $U^0$  for Case-3 ( $N = 1024$ ) and Case-5 ( $N = 1536$ ).

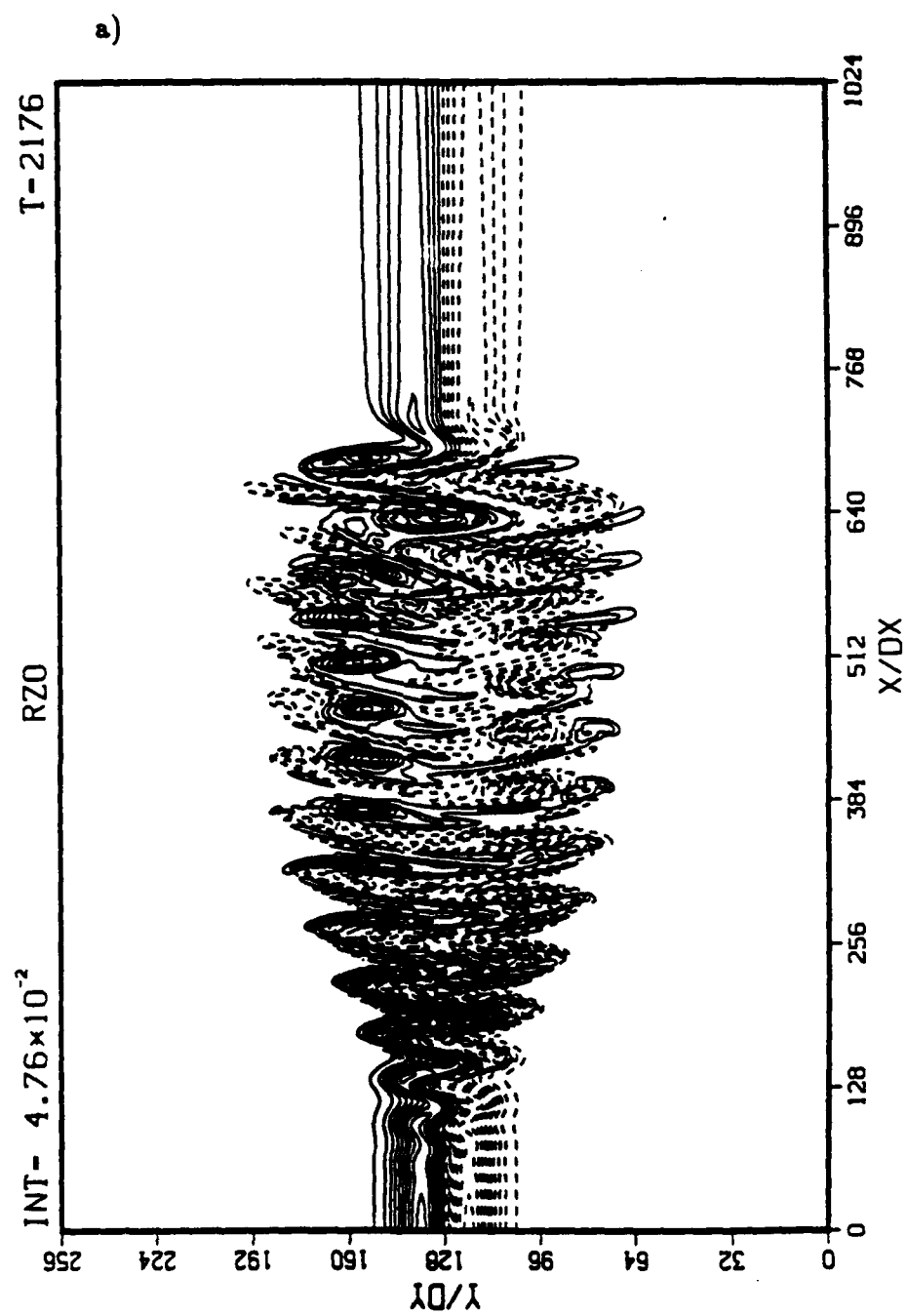


Figure 6.26 Contours of spanwise vorticity  $\Omega_z^0$  for Case-5.  $A_2 = .001$ ,  $A_3 = 0$ ,  $\beta = .51$ . Solid lines denote positive vorticity and dashed lines denote negative vorticity. a)  $t = 2176\Delta t$  and  $0 \leq z/\Delta z \leq 1024$ , twenty contour intervals; b)  $t = 3200\Delta t$  and  $0 \leq z/\Delta z \leq 1536$ , ten contour intervals.

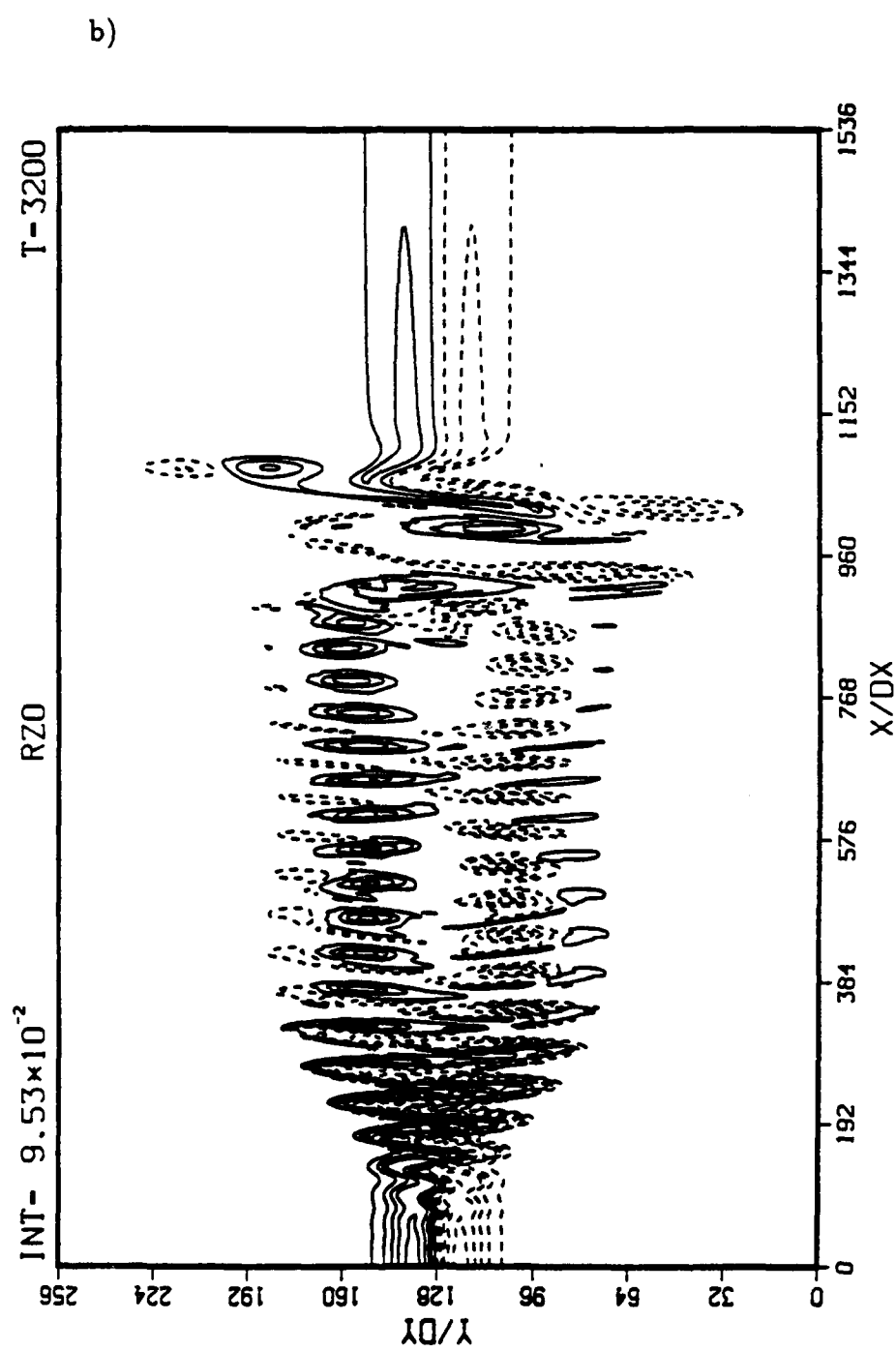


Figure 6.26 Continued.

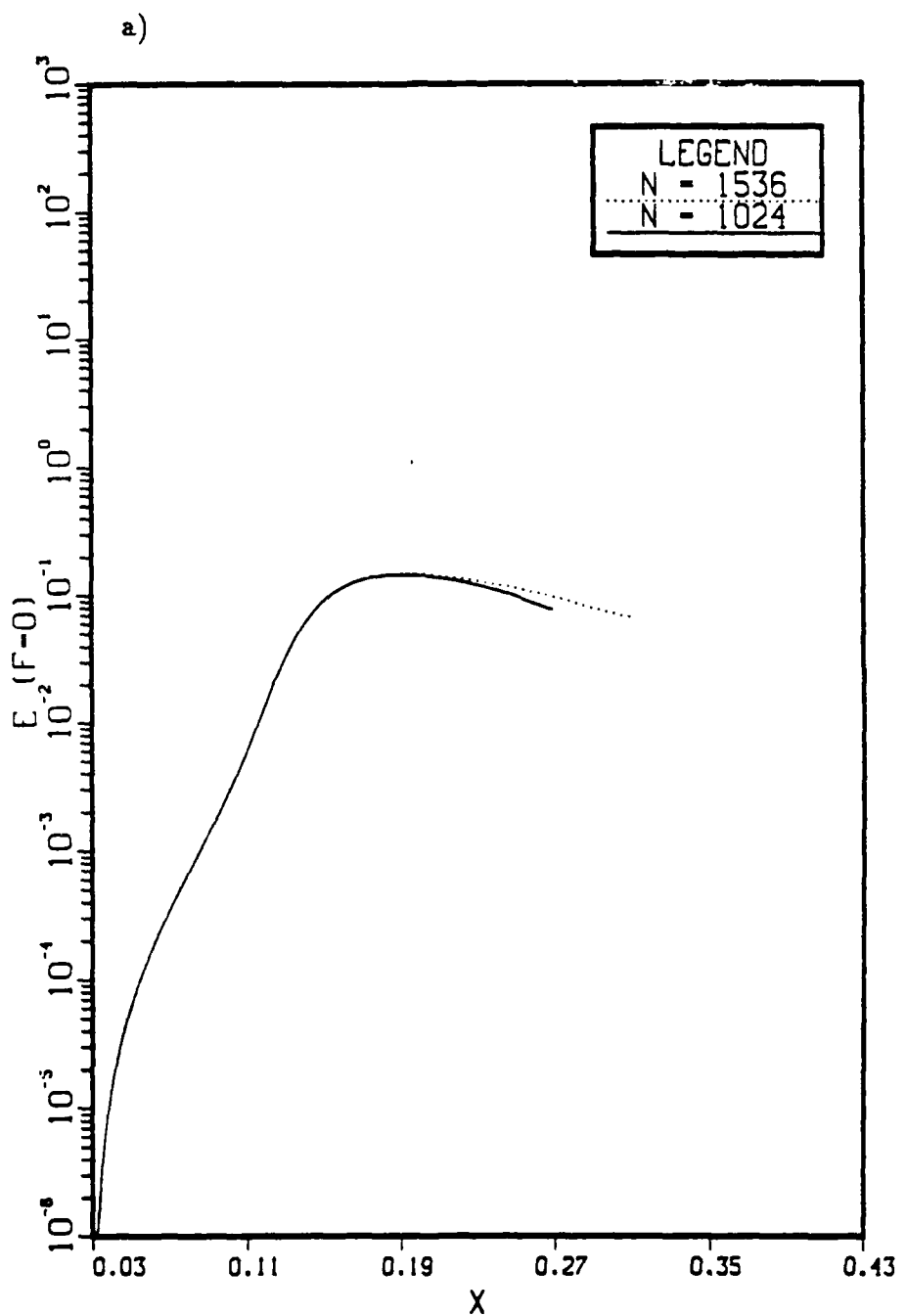


Figure 6.27 Comparison of amplification curves of the kinetic energy  $\hat{E}^0(x, F)$  for Case-3 ( $N = 1024$ ) and Case-5 ( $N = 1536$ ). a)  $F = 0$ , b)  $F = 1$ , c)  $F = 2$ .

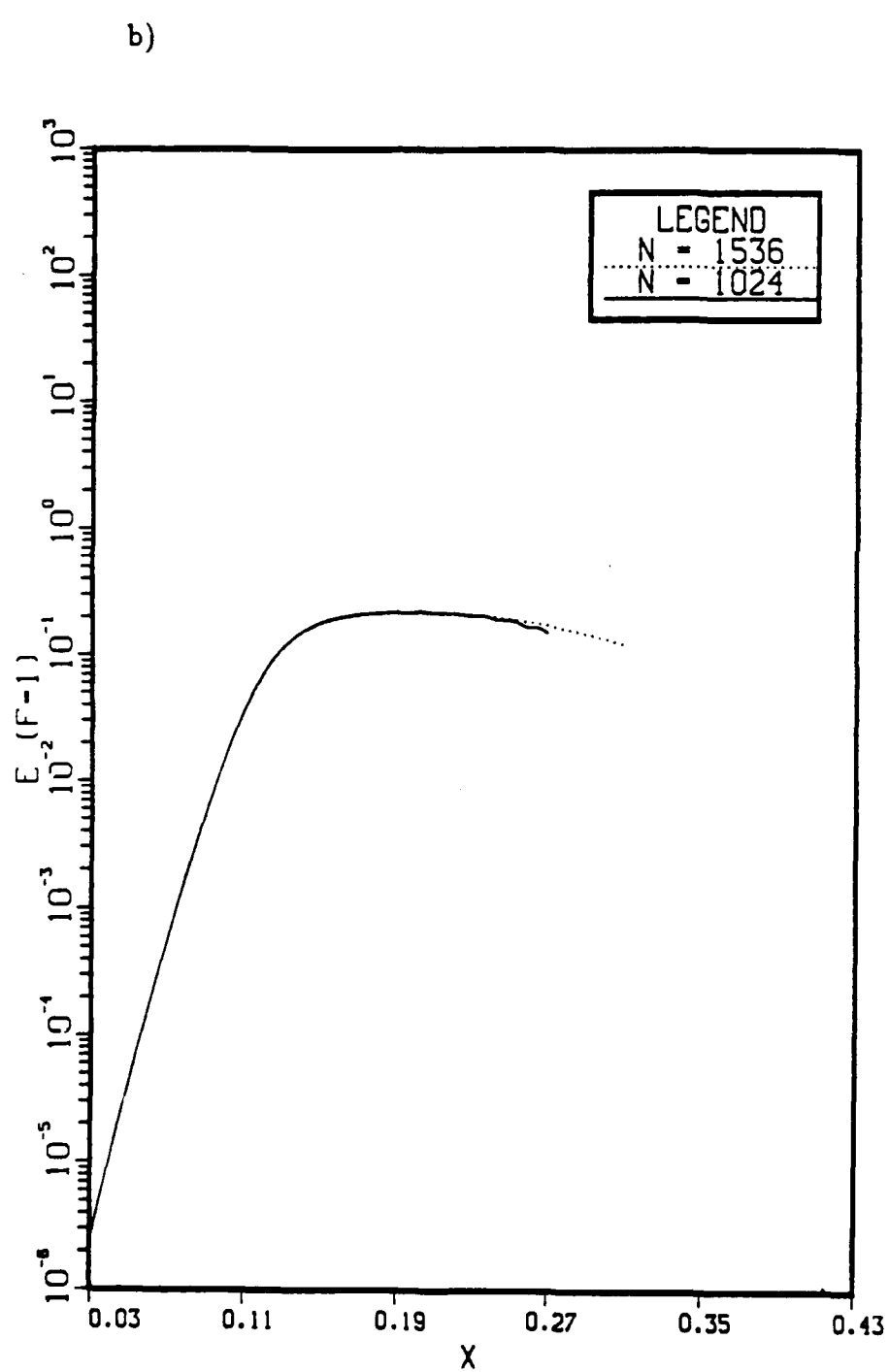


Figure 6.27 Continued.

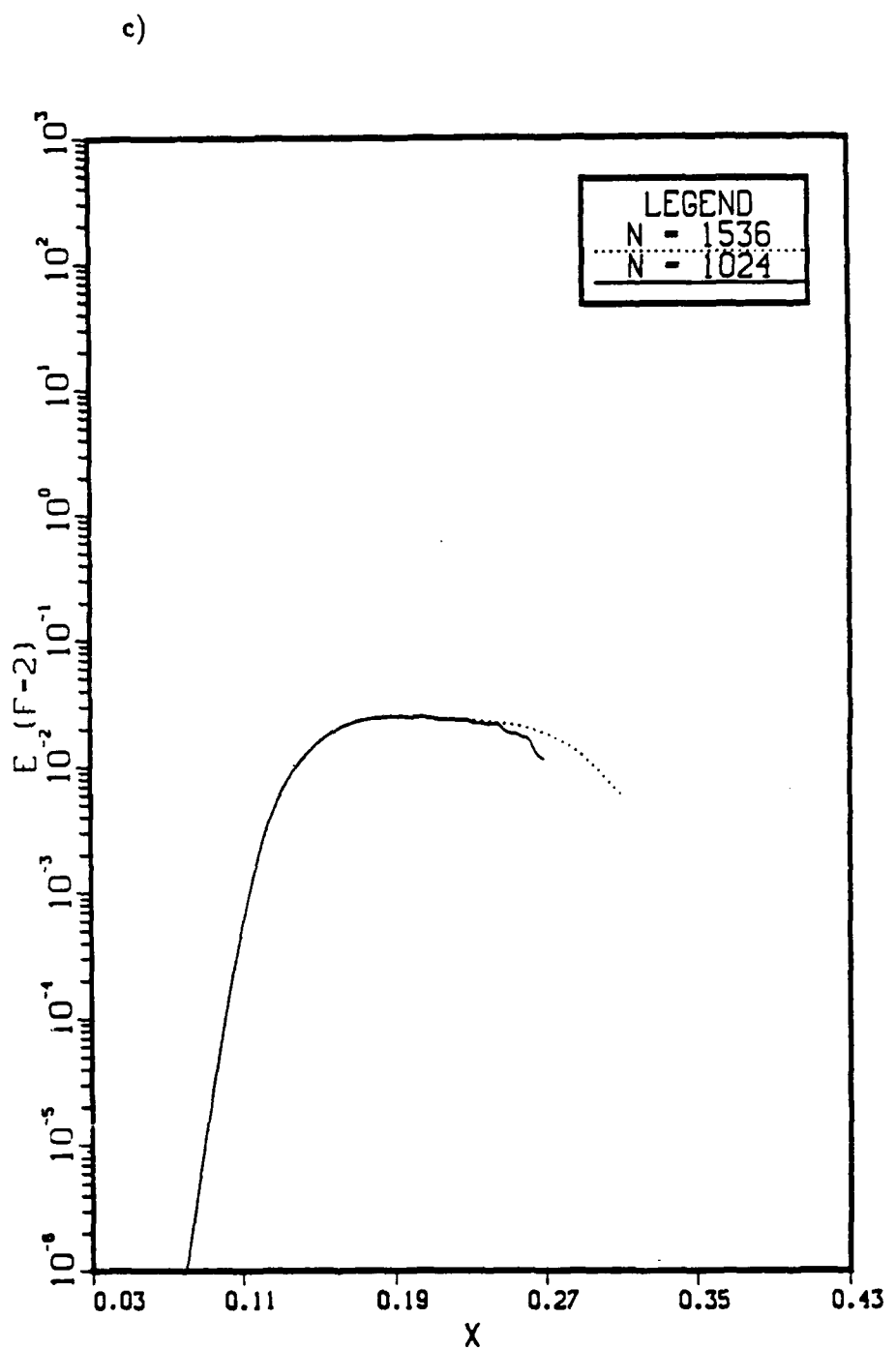


Figure 6.27 Continued.

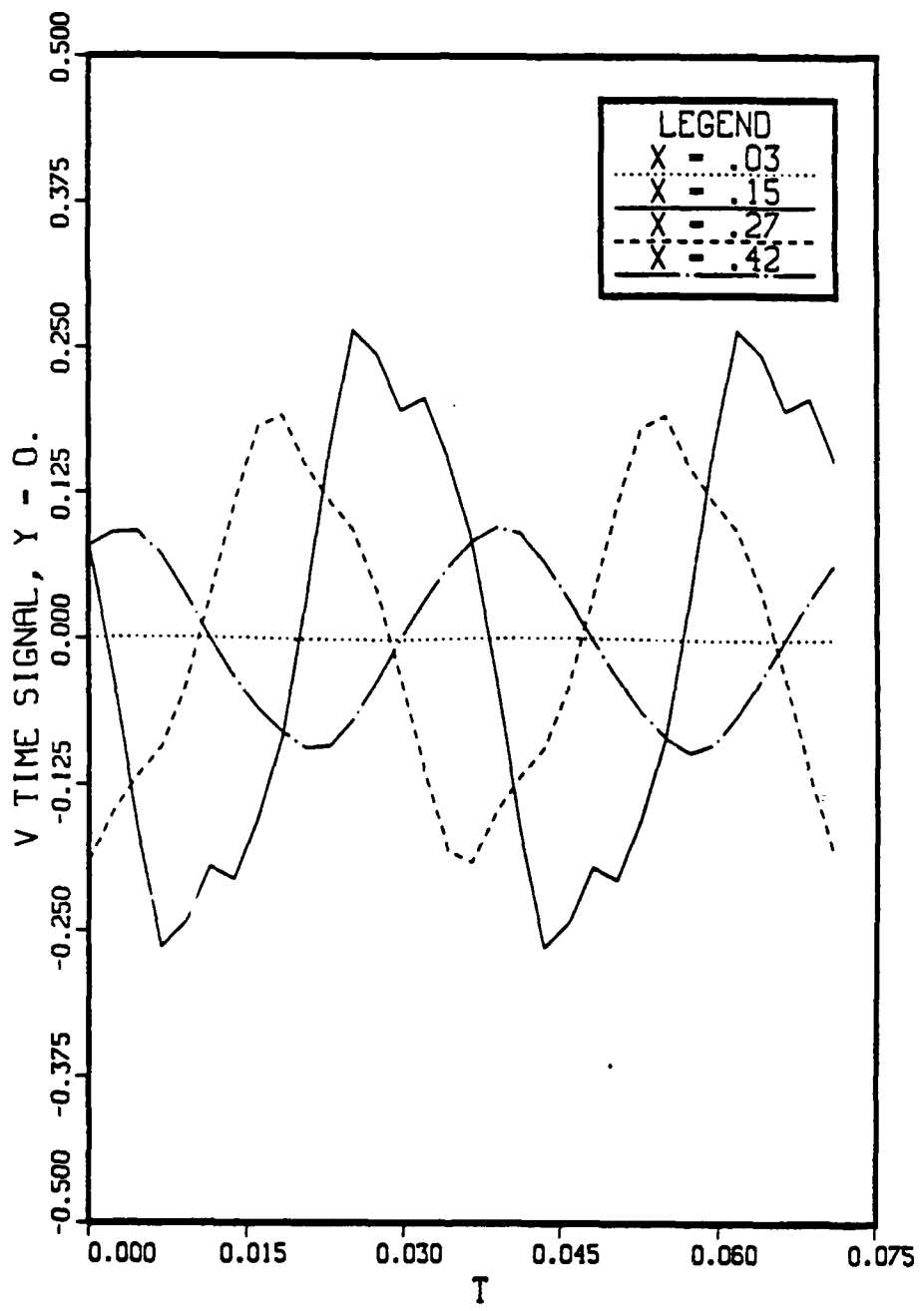


Figure 6.29 Temporal variation of the centerline transverse velocity  $V^0$  in the time interval  $23T_F < t \leq 25T_F$ . Case-5:  $A_2 = .001$ ,  $A_3 = 0$ , and  $\beta = .51$ .

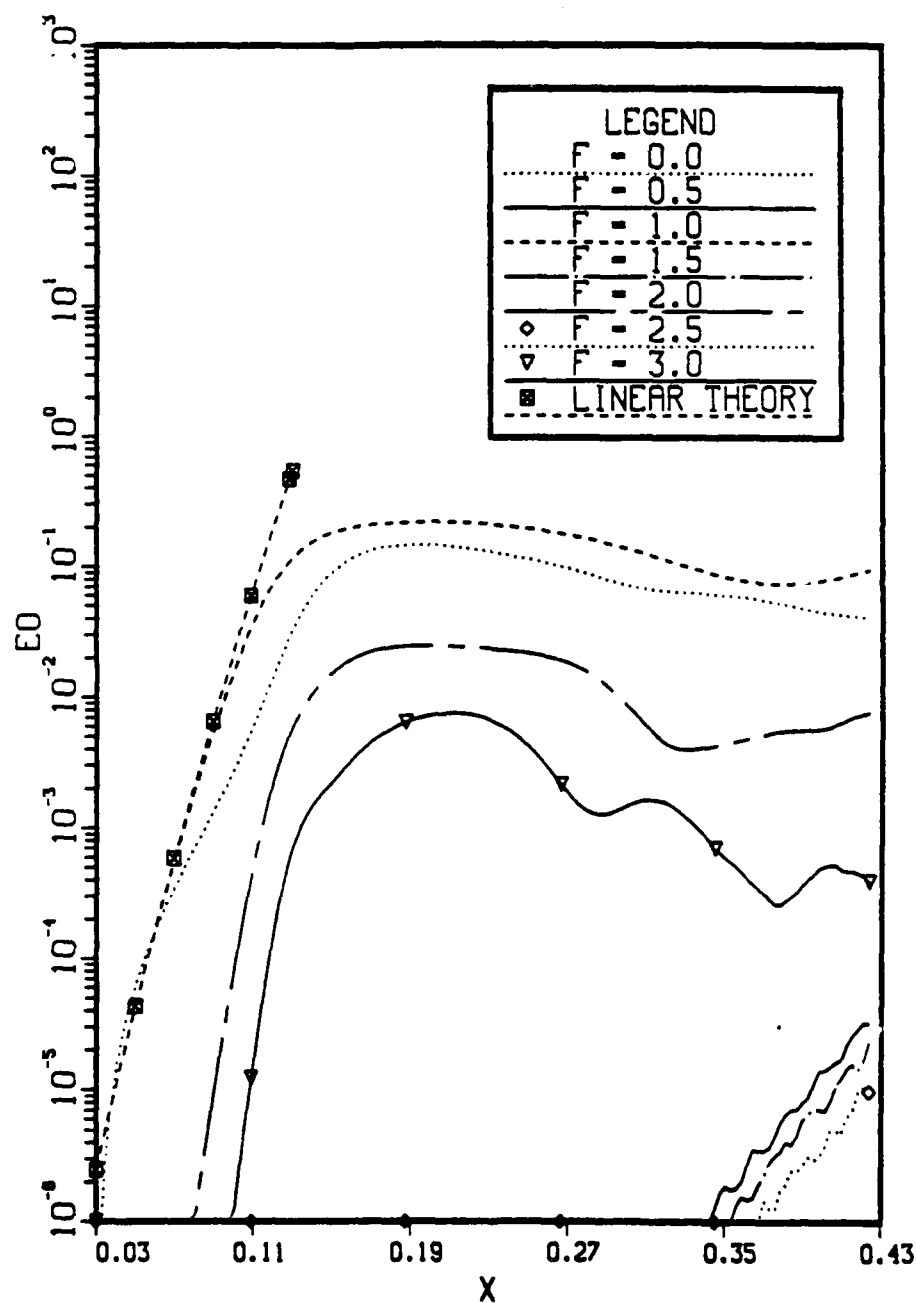


Figure 6.28 Amplification curves of the kinetic energy  $\hat{E}^0(x, F)$  obtained from the time interval  $23T_F < t \leq 25T_F$ . Case-5:  $A_2 = .001$ ,  $A_3 = 0$ , and  $\beta = .51$ .

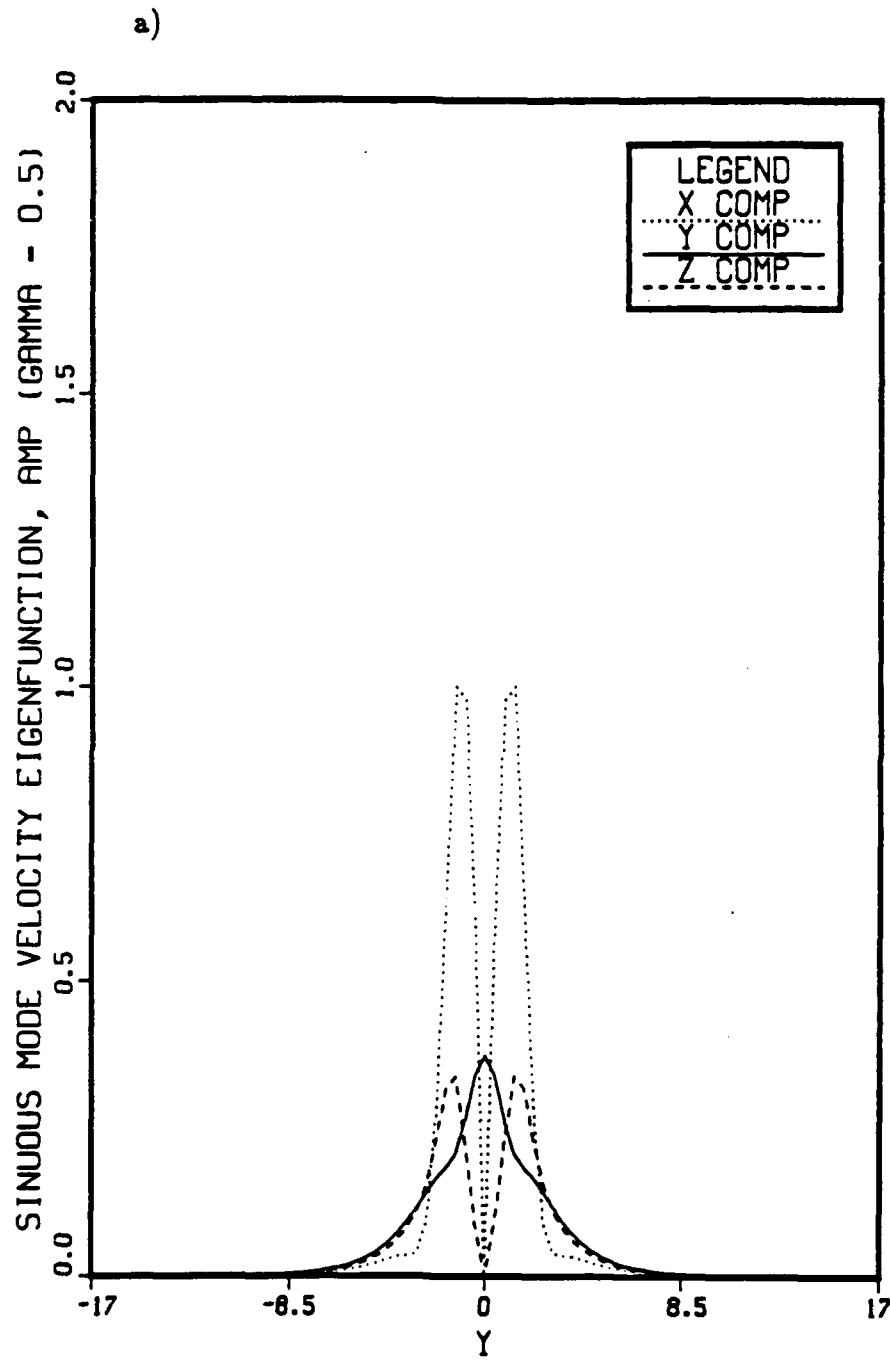


Figure 6.30 Sinuous mode eigenfunctions of the three-dimensional Orr-Sommerfeld equation corresponding to  $\beta = .28$ ,  $\gamma = .5$ , and  $Re_\theta = \frac{\bar{\theta}_1 \bar{U}_\infty}{\nu} = 594$ . a) amplitudes of  $U^1$ ,  $V^1$ , and  $W^1$ ; b) amplitudes of  $\Omega_x^1$ ,  $\Omega_y^1$ , and  $\Omega_z^1$ ; c) phases of  $U^1$ ,  $V^1$ , and  $W^1$ ; d) phases of  $\Omega_x^1$ ,  $\Omega_y^1$ , and  $\Omega_z^1$ .

b)

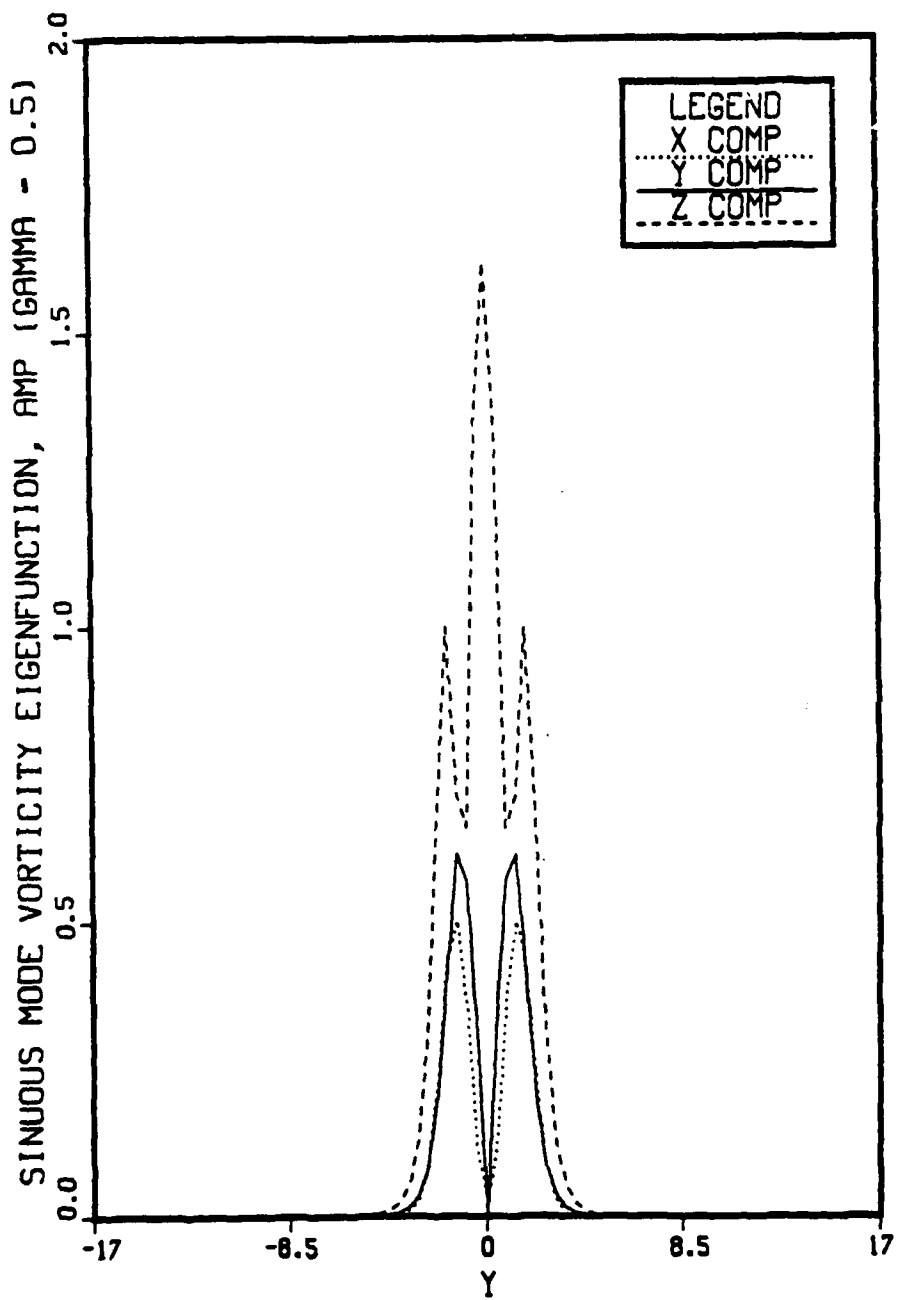


Figure 6.30 Continued.

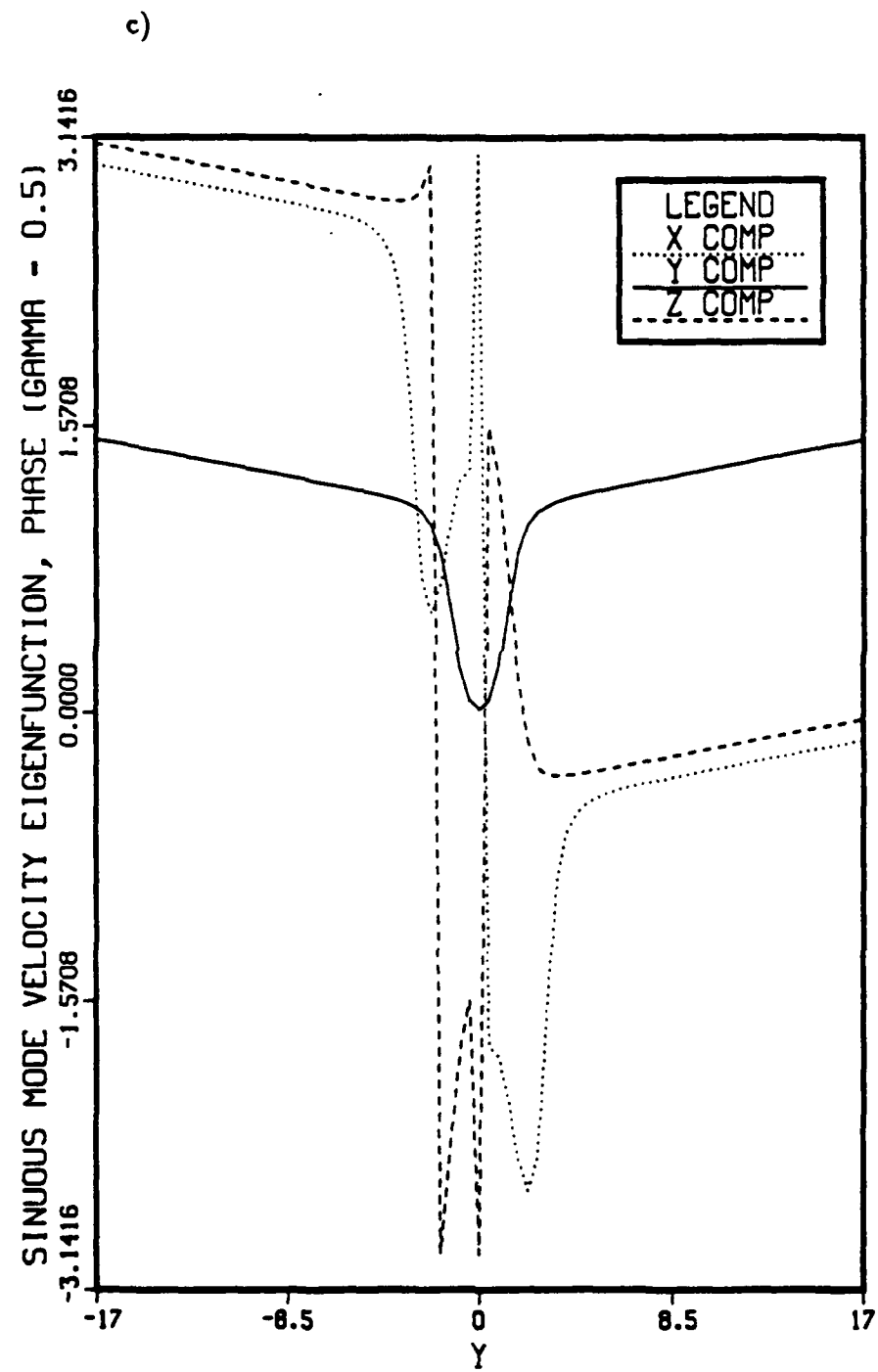


Figure 6.30 Continued.

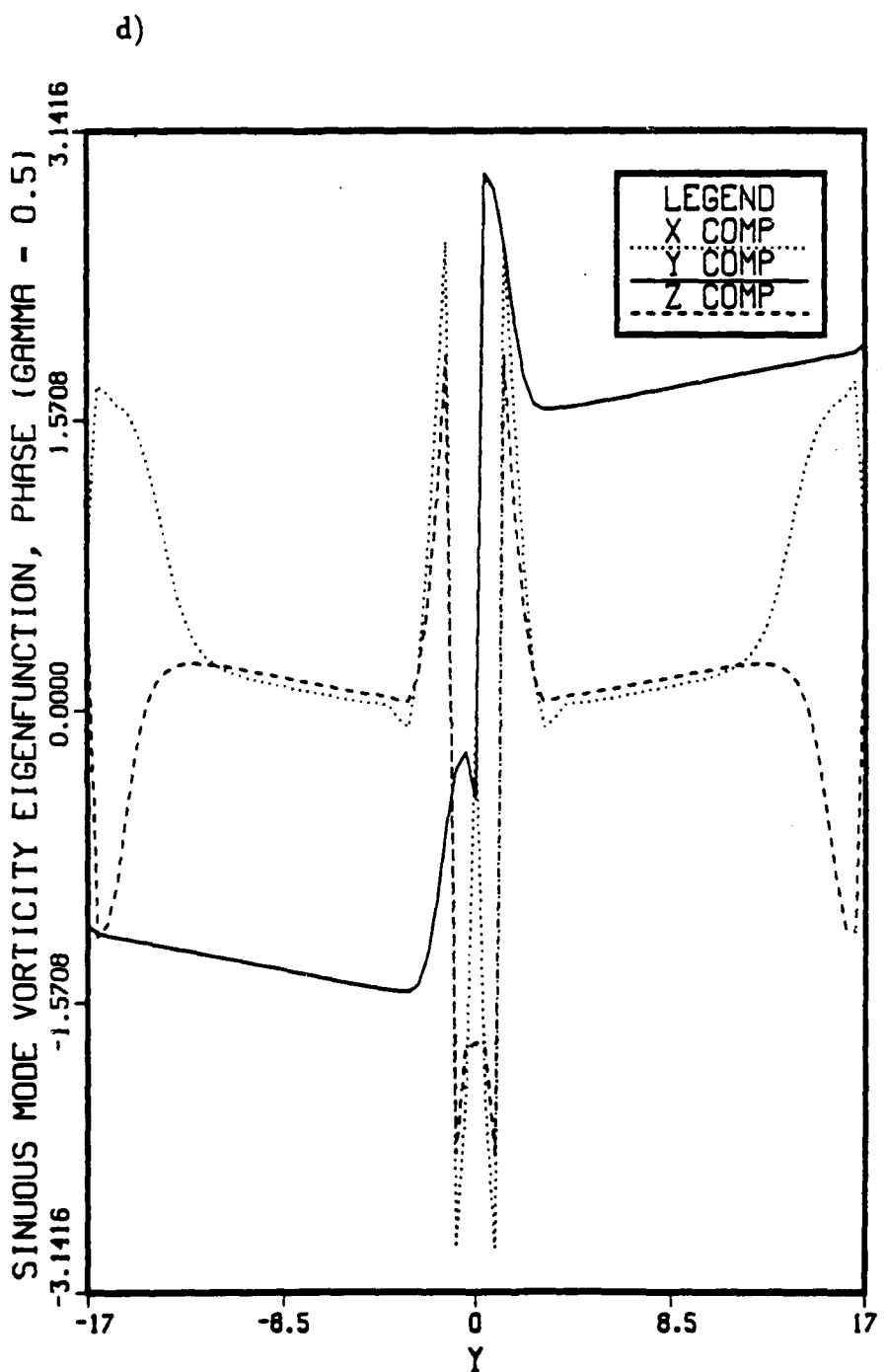


Figure 6.30 Continued.

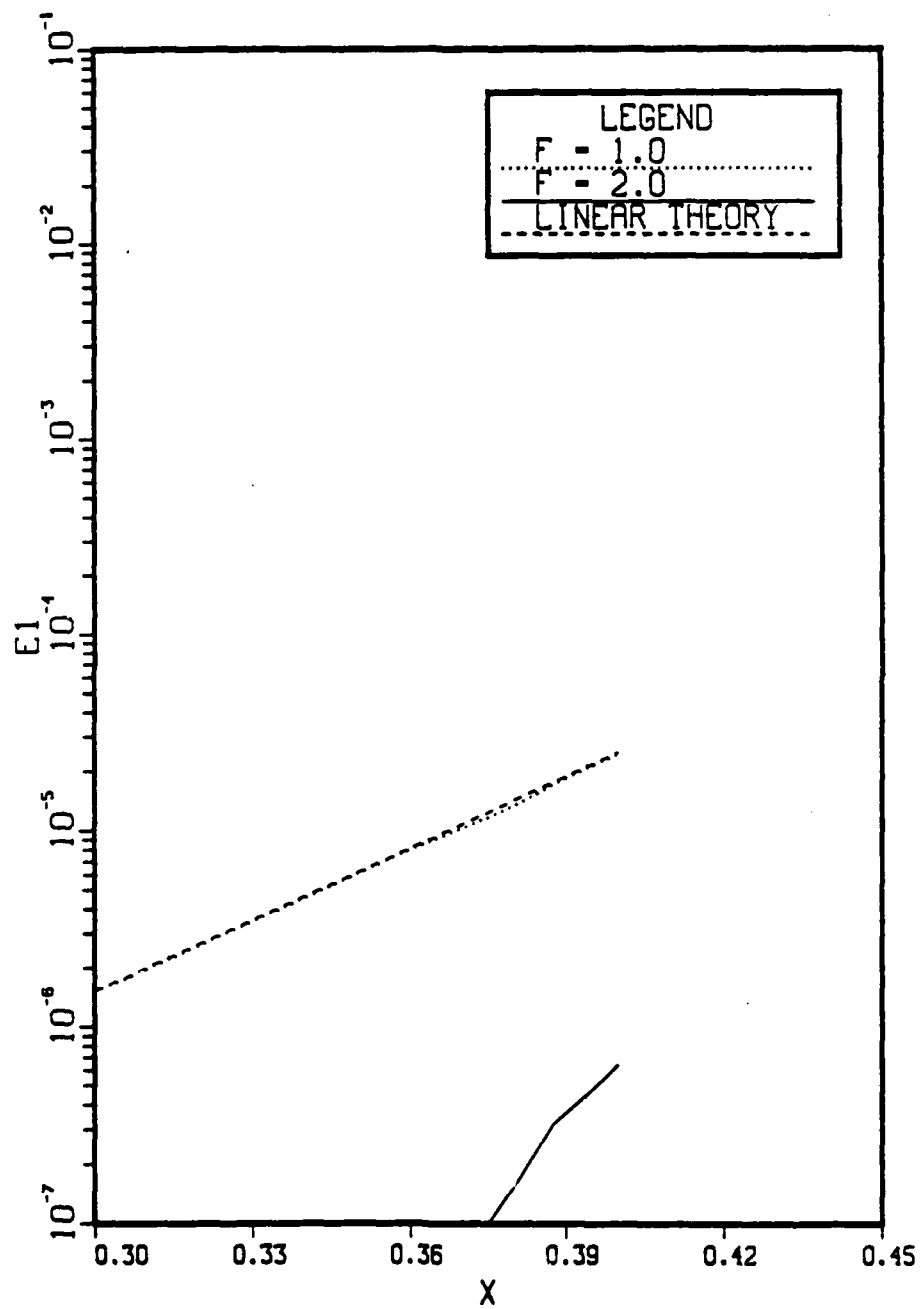


Figure 6.31 Comparison of amplification curves of the kinetic energy  $\hat{E}^1(x, F)$  to linear stability theory. Case-6:  $A_2 = 0$ ,  $A_3 = .001$ ,  $\beta = .28$ , and  $\gamma = .5$ .

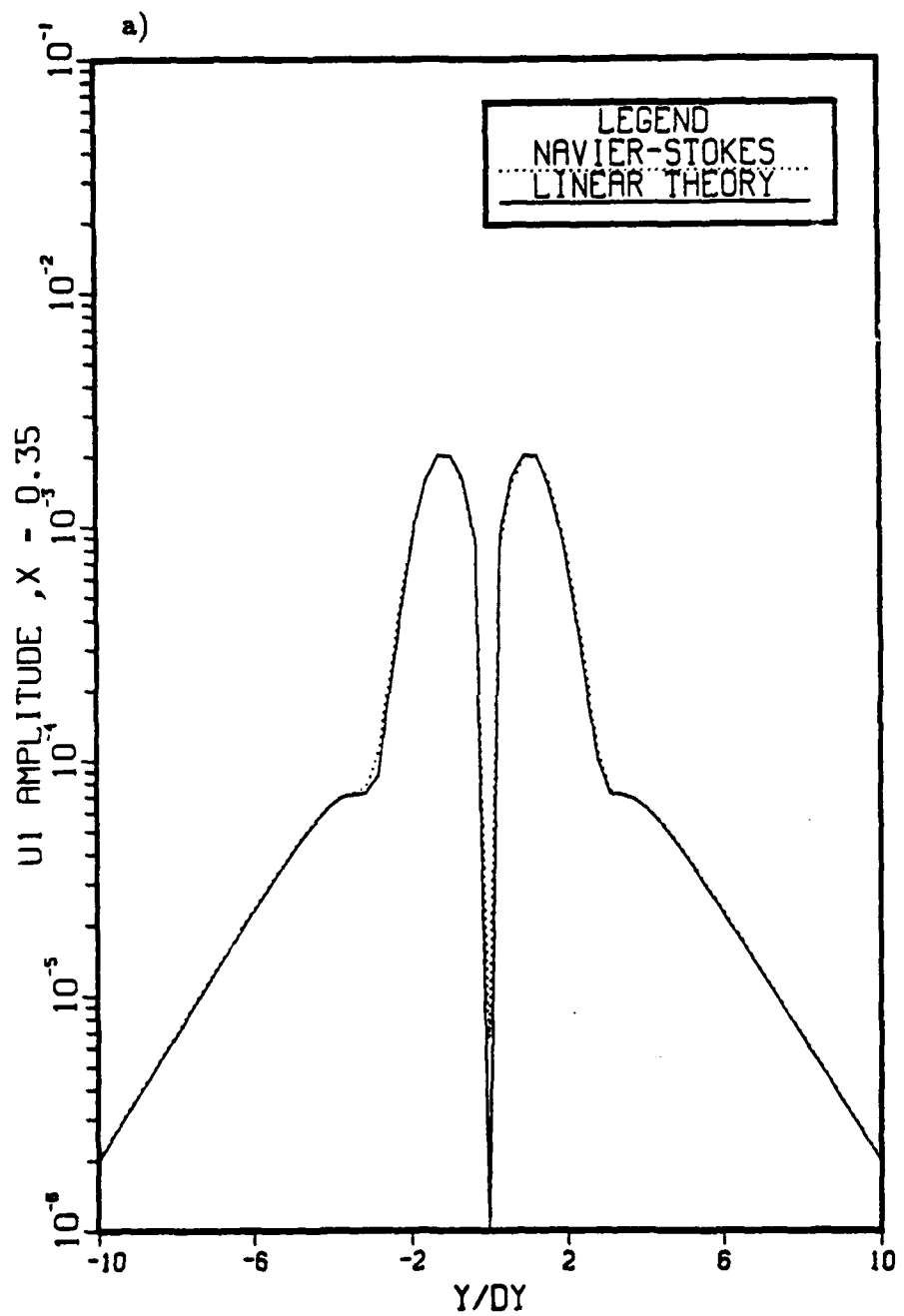


Figure 6.32 Comparison of the amplitude distributions of the fundamental disturbance ( $F = 1, k = 1$ ) to linear stability theory. Case-6:  $A_2 = 0$ ,  $A_3 = .001$ ,  $\beta = .28$ , and  $\gamma = .5$  a) streamwise velocity,  $U^1$ ; b) transverse velocity,  $V^1$ ; c) spanwise velocity,  $W^1$ .

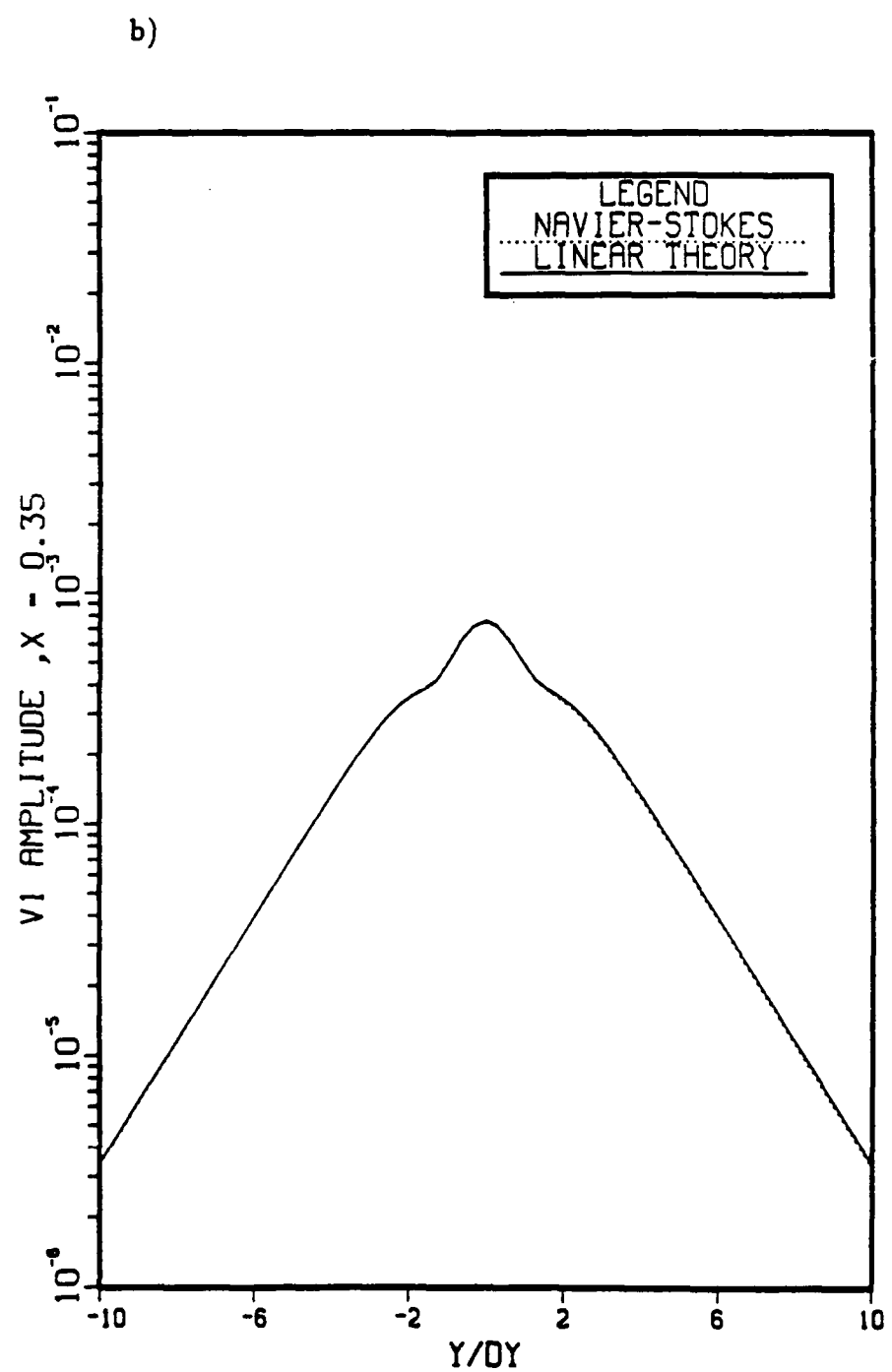


Figure 6.32 Continued.

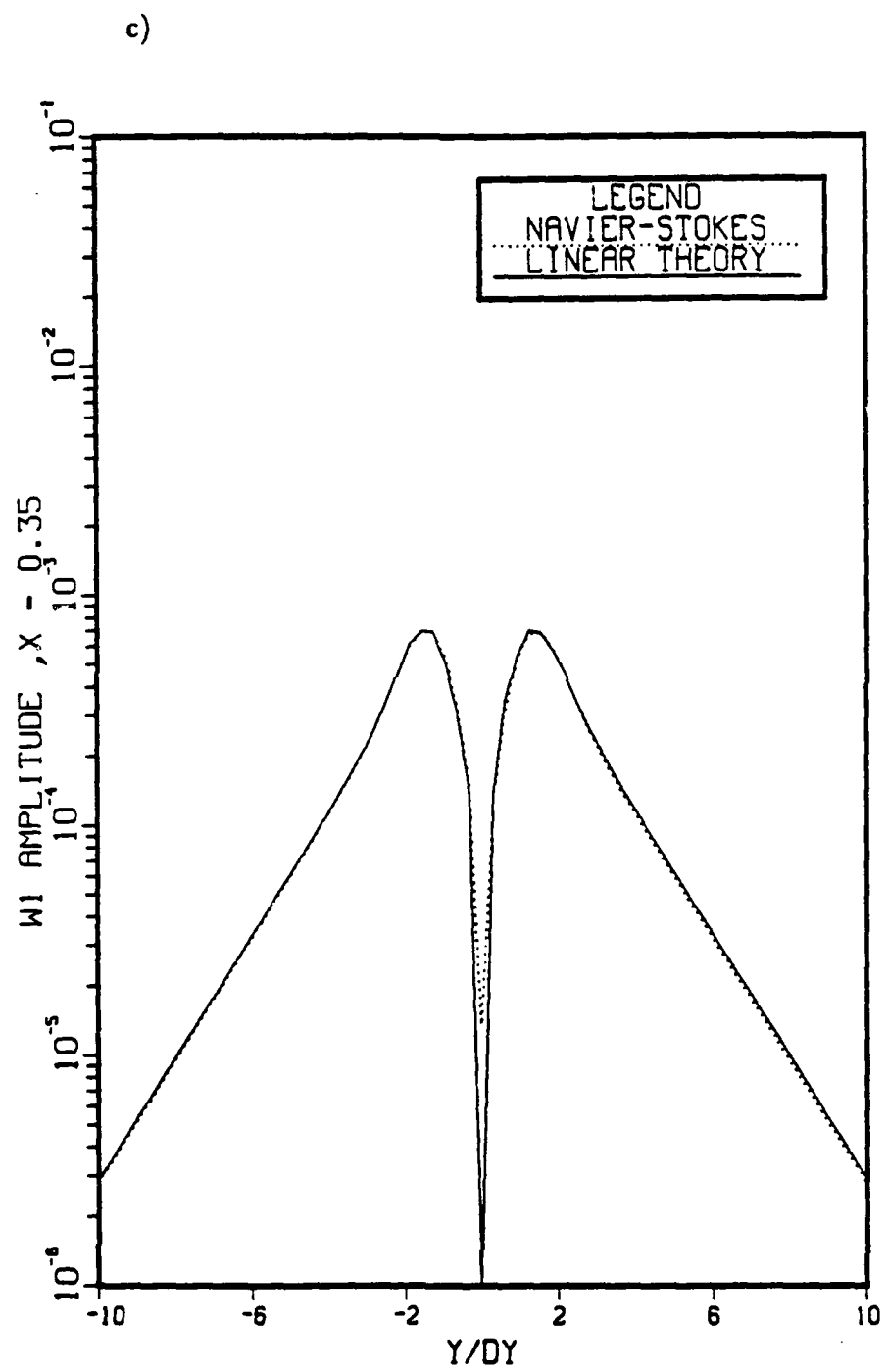


Figure 6.32 Continued.

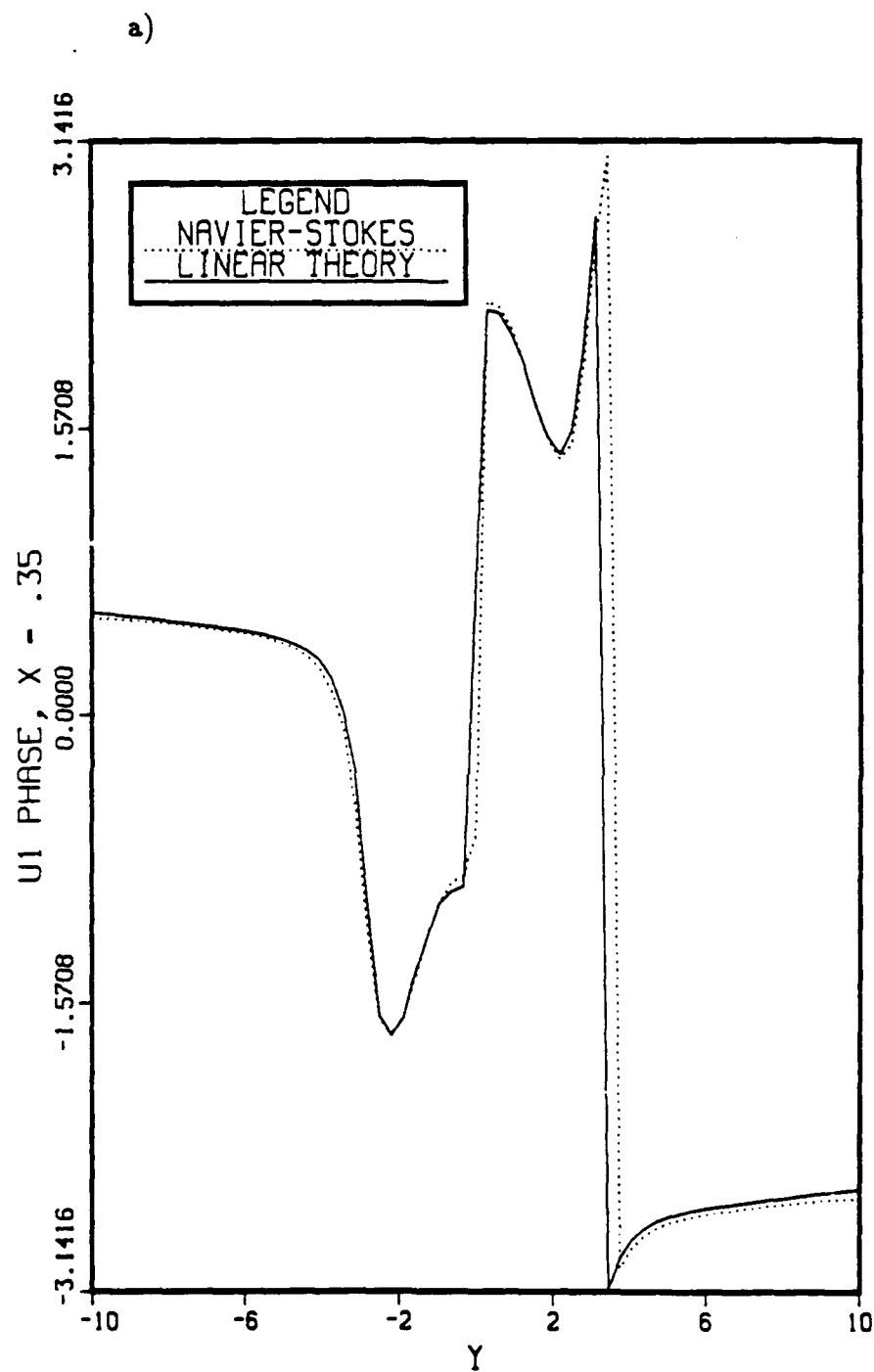


Figure 6.33 Comparison of the phase distributions of the fundamental disturbance ( $F = 1, k = 1$ ) to linear stability theory. Case-6:  $A_2 = 0$ ,  $A_3 = .001$ ,  $\beta = .28$ , and  $\gamma = .5$ . a) streamwise velocity,  $U^1$ ; b) transverse velocity,  $V^1$ ; c) spanwise velocity,  $W^1$ .

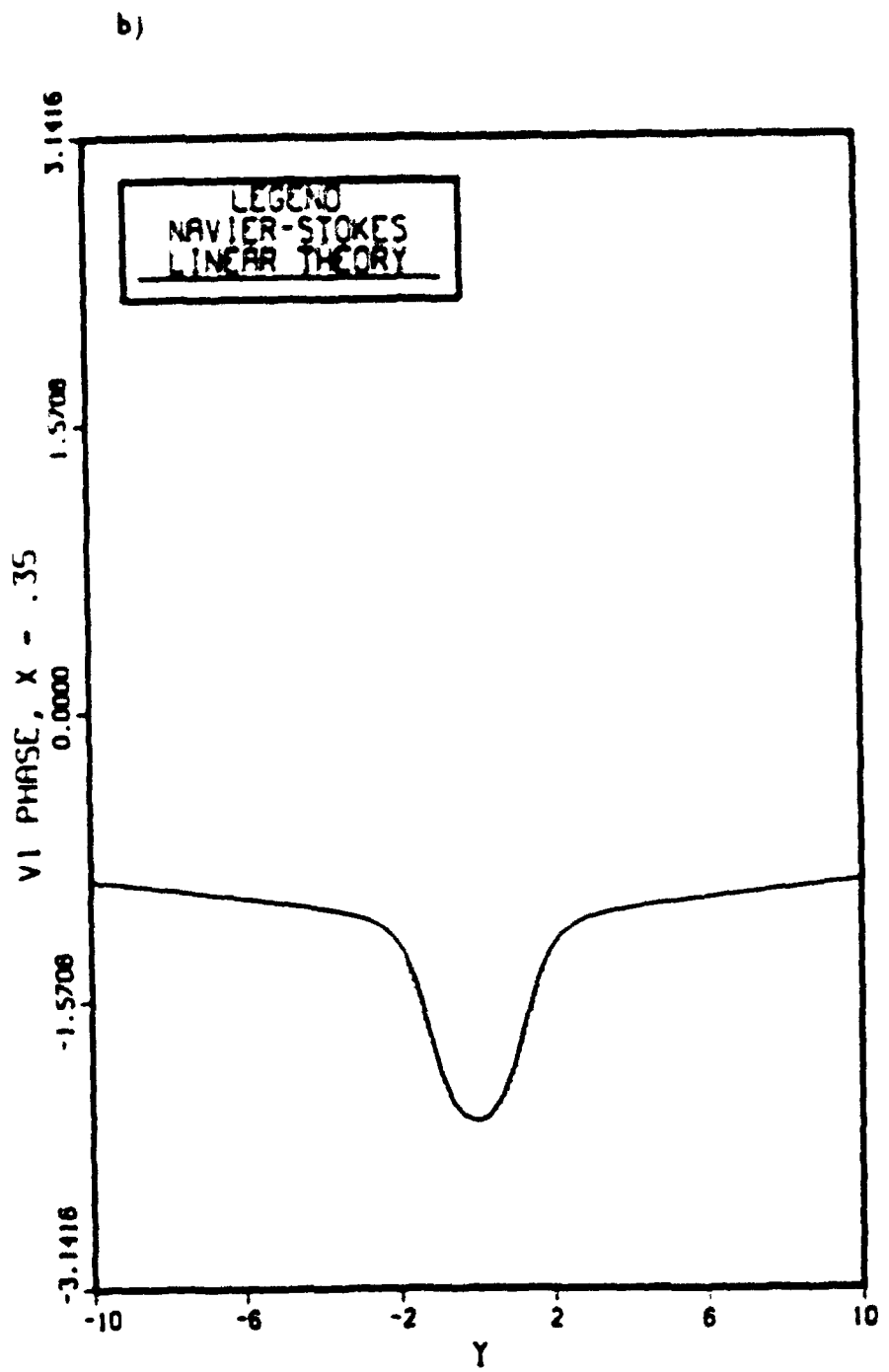


Figure 6.33 Continued.

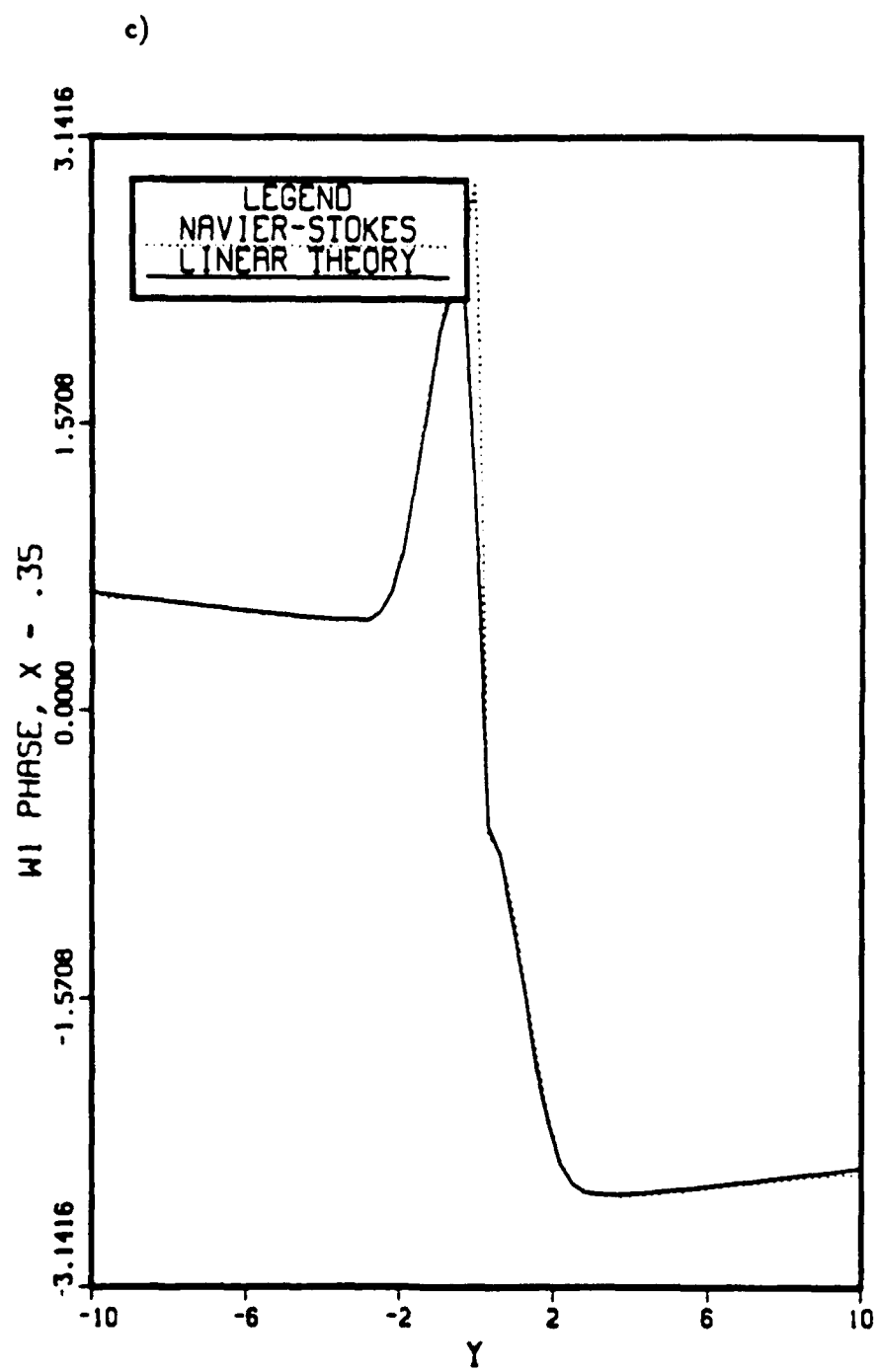


Figure 6.33 Continued.

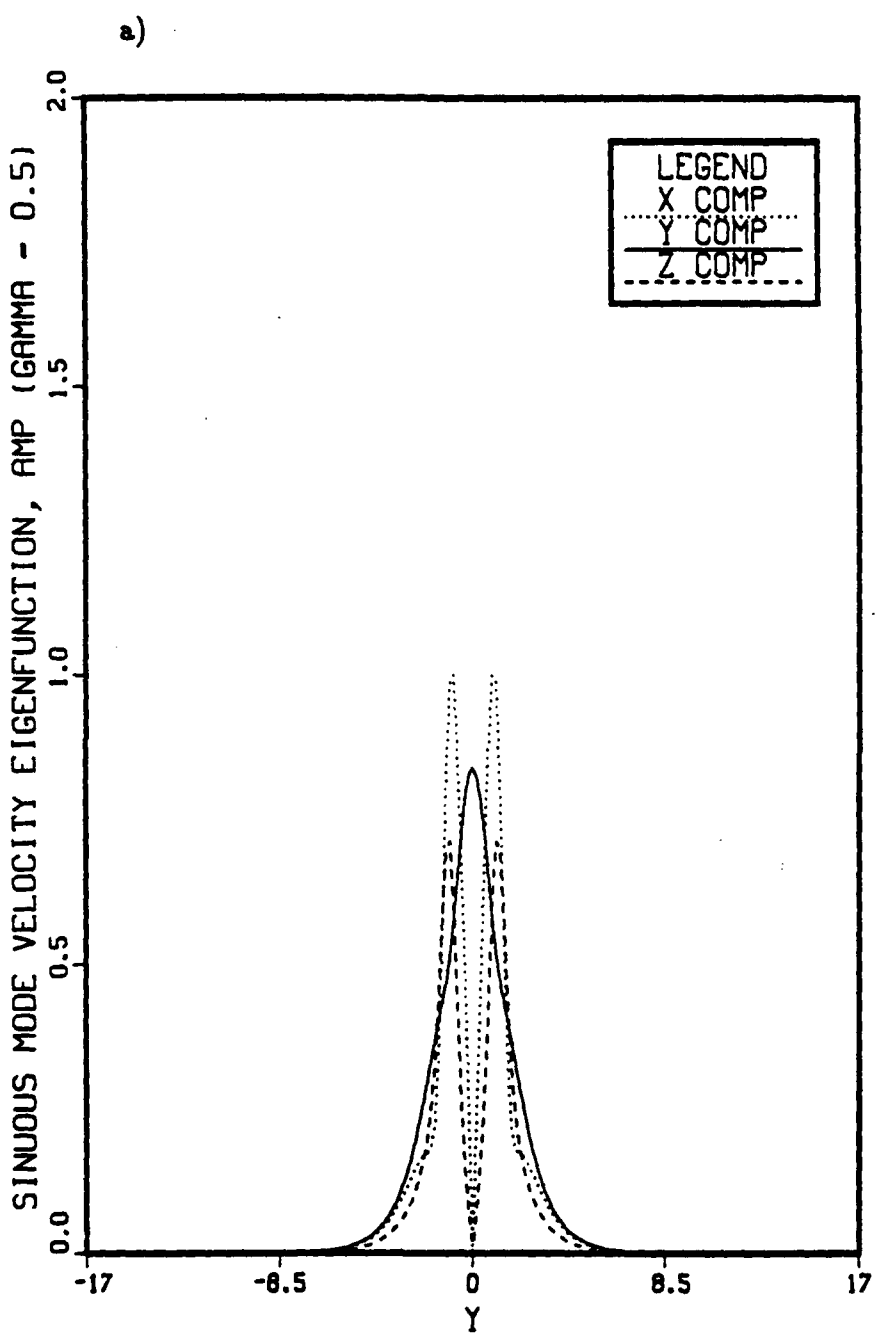


Figure 6.34 Sinuous mode eigenfunctions of the three-dimensional Orr-Sommerfeld equation corresponding to  $\beta = .51$ ,  $\gamma = .5$ , and  $Re_\theta = \frac{\theta_{1c} U_\infty}{\nu} = 594$ . a) amplitudes of  $U^1$ ,  $V^1$ , and  $W^1$ ; b) amplitudes of  $\Omega_x^1$ ,  $\Omega_y^1$ , and  $\Omega_z^1$ ; c) phases of  $U^1$ ,  $V^1$ , and  $W^1$ ; d) phases of  $\Omega_x^1$ ,  $\Omega_y^1$ , and  $\Omega_z^1$ .

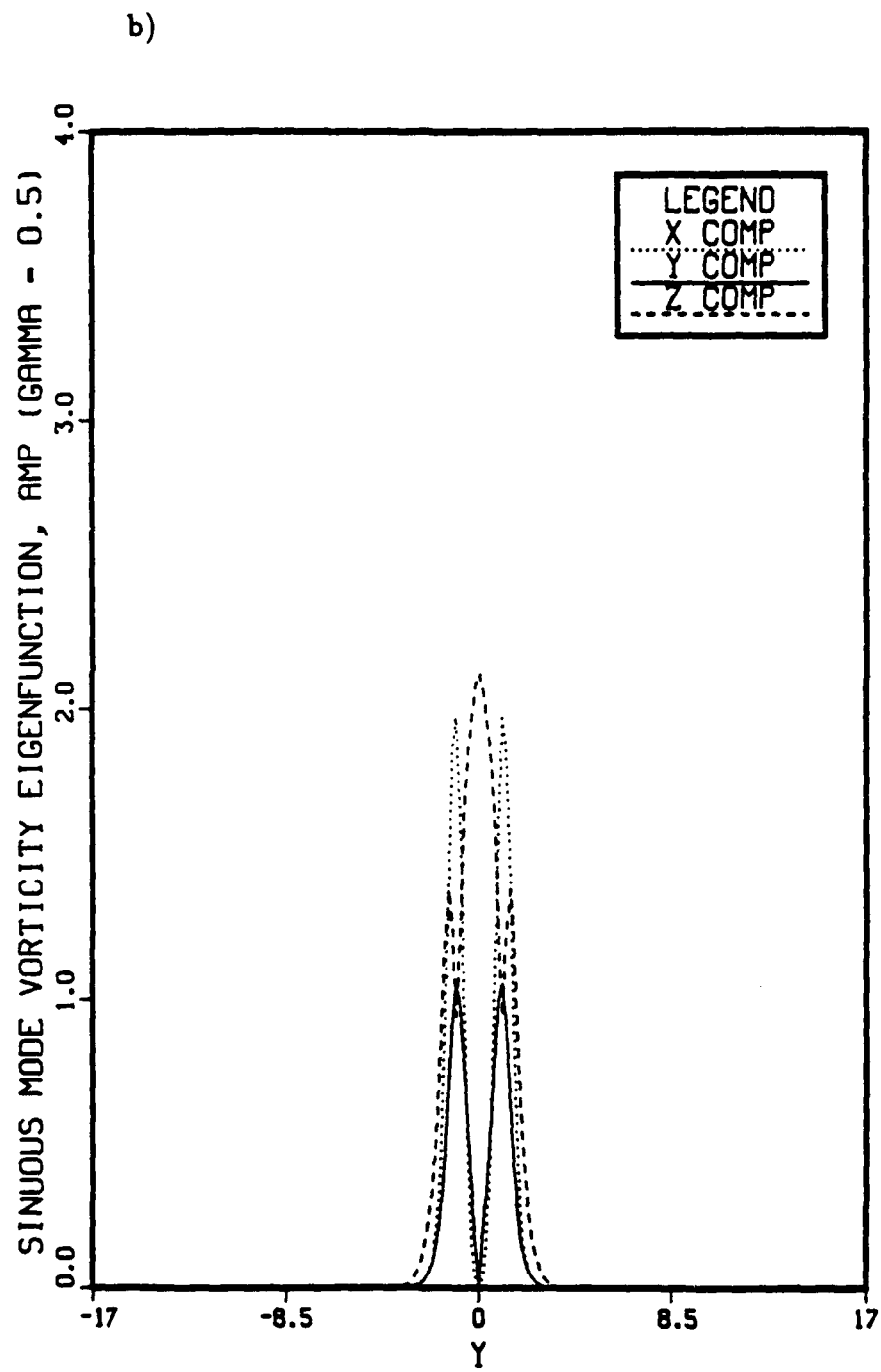


Figure 6.34 Continued.

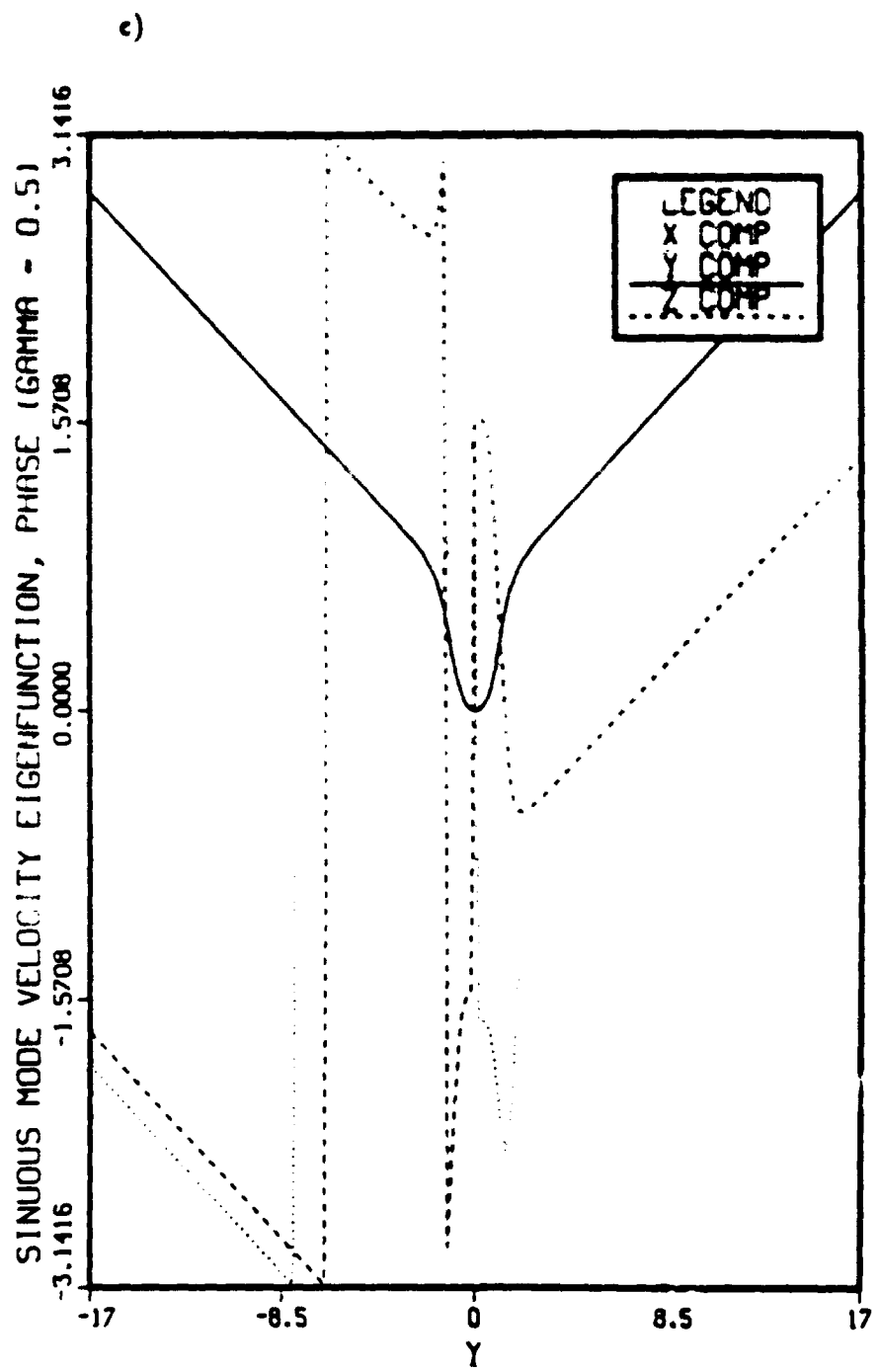


Figure 6.34 Continued.

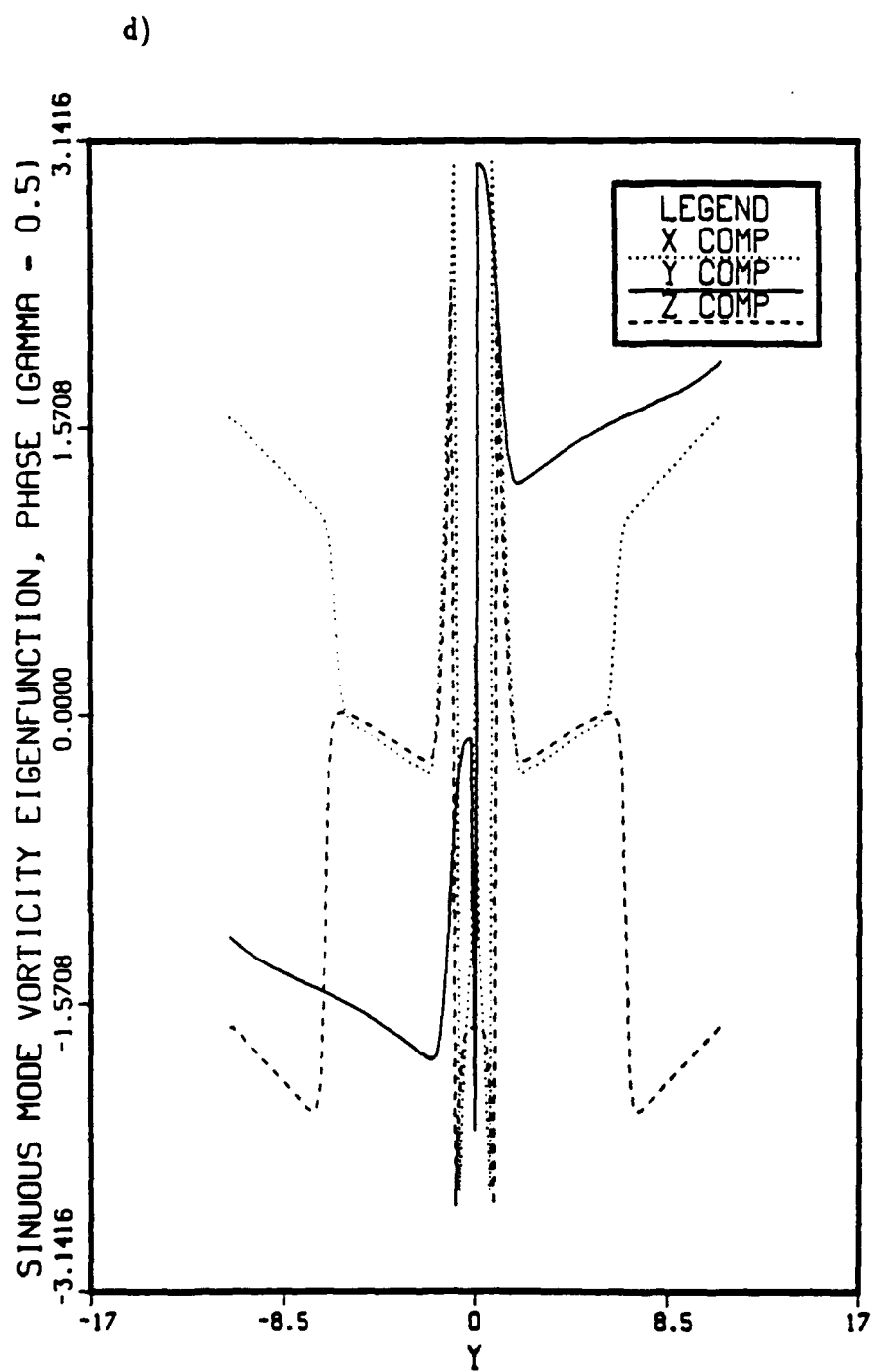


Figure 6.34 Continued.

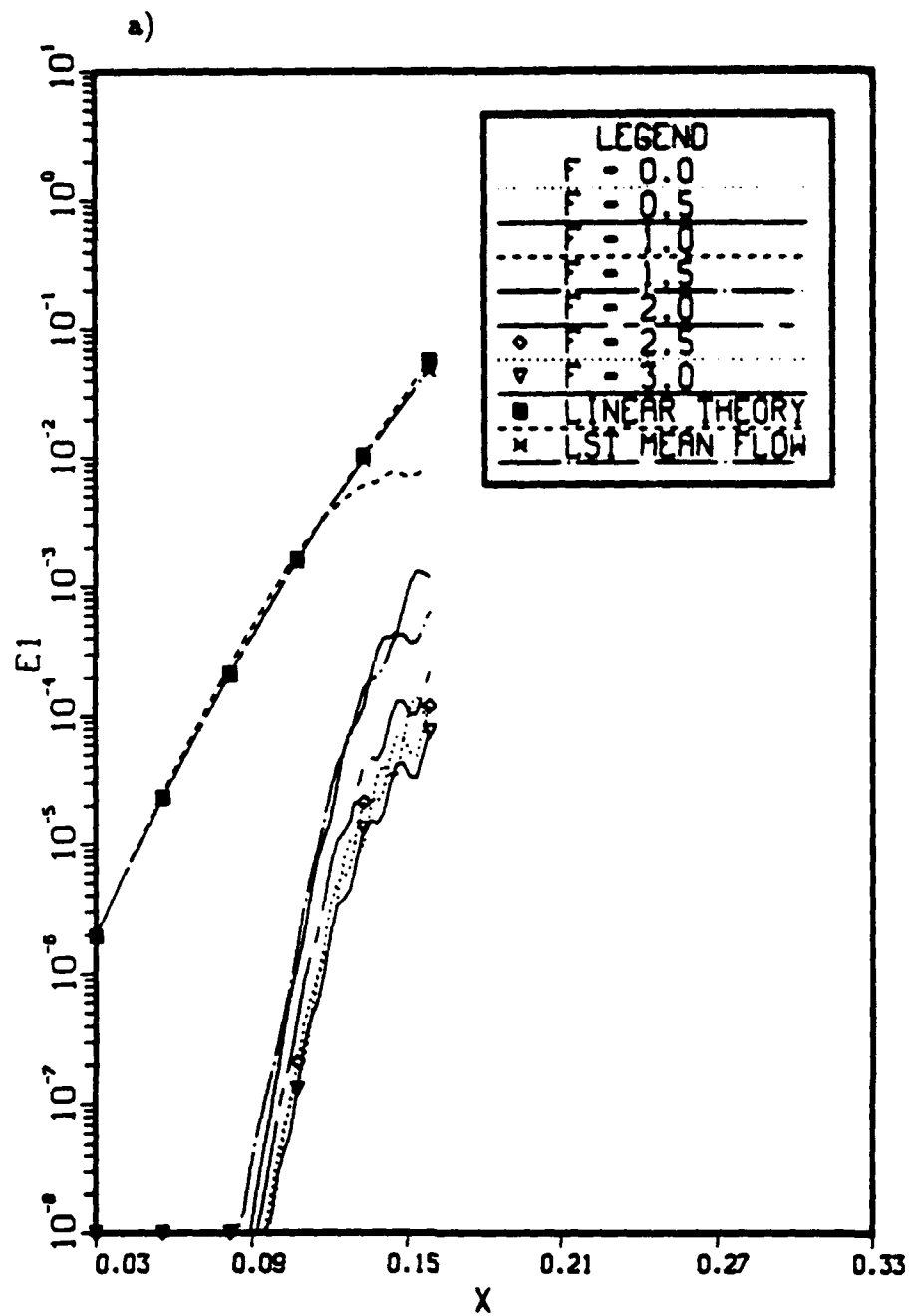


Figure 6.35 Amplification curves of the kinetic energy  $\hat{E}^1(x, F)$ . Case-7:  $A_2 = 0$ ,  $A_3 = .001$ ,  $\beta = .51$ , and  $\gamma = .5$ . a)  $6T_F < t \leq 8T_F$ , b)  $8T_F < t \leq 10T_F$ .

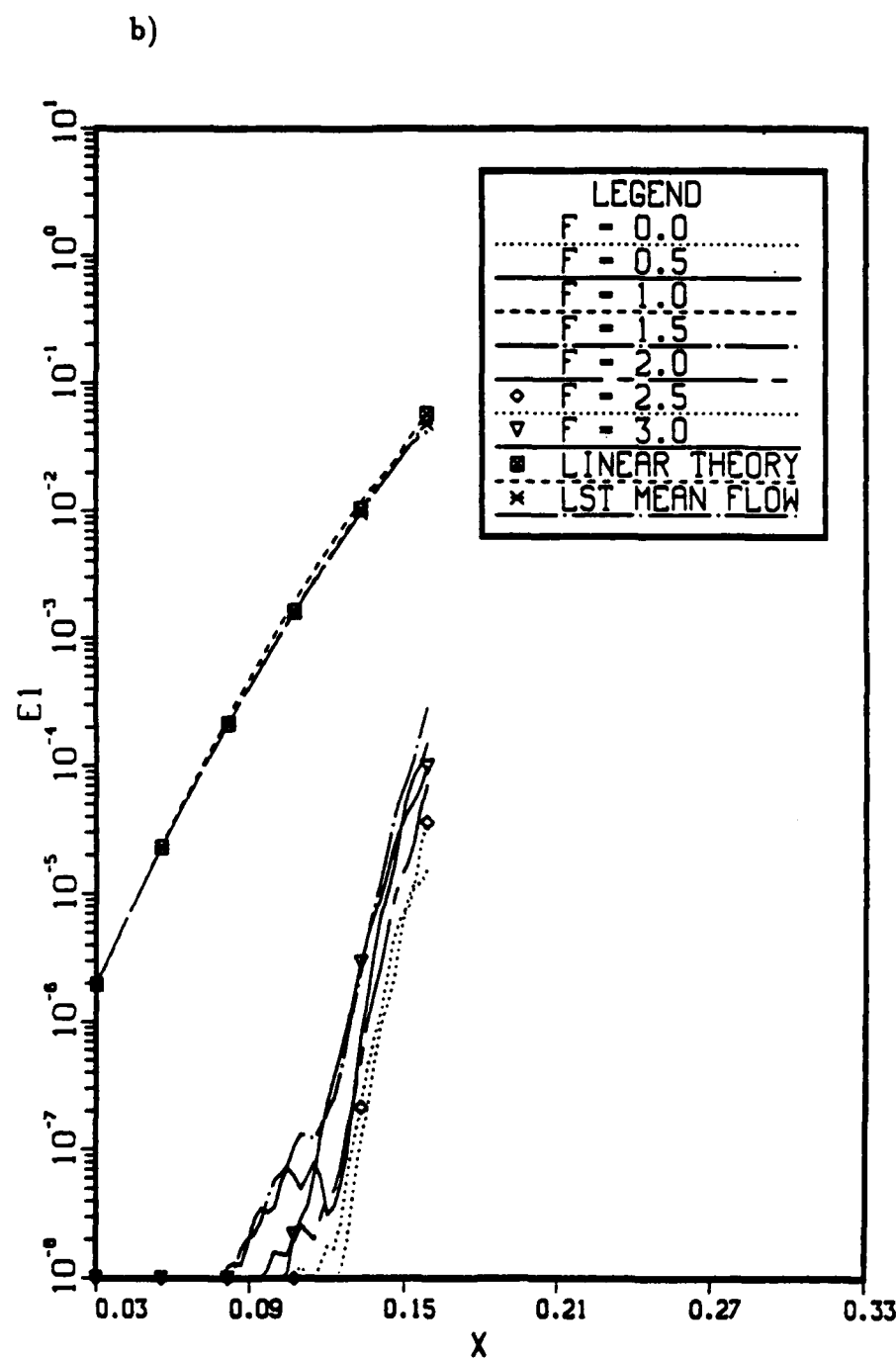
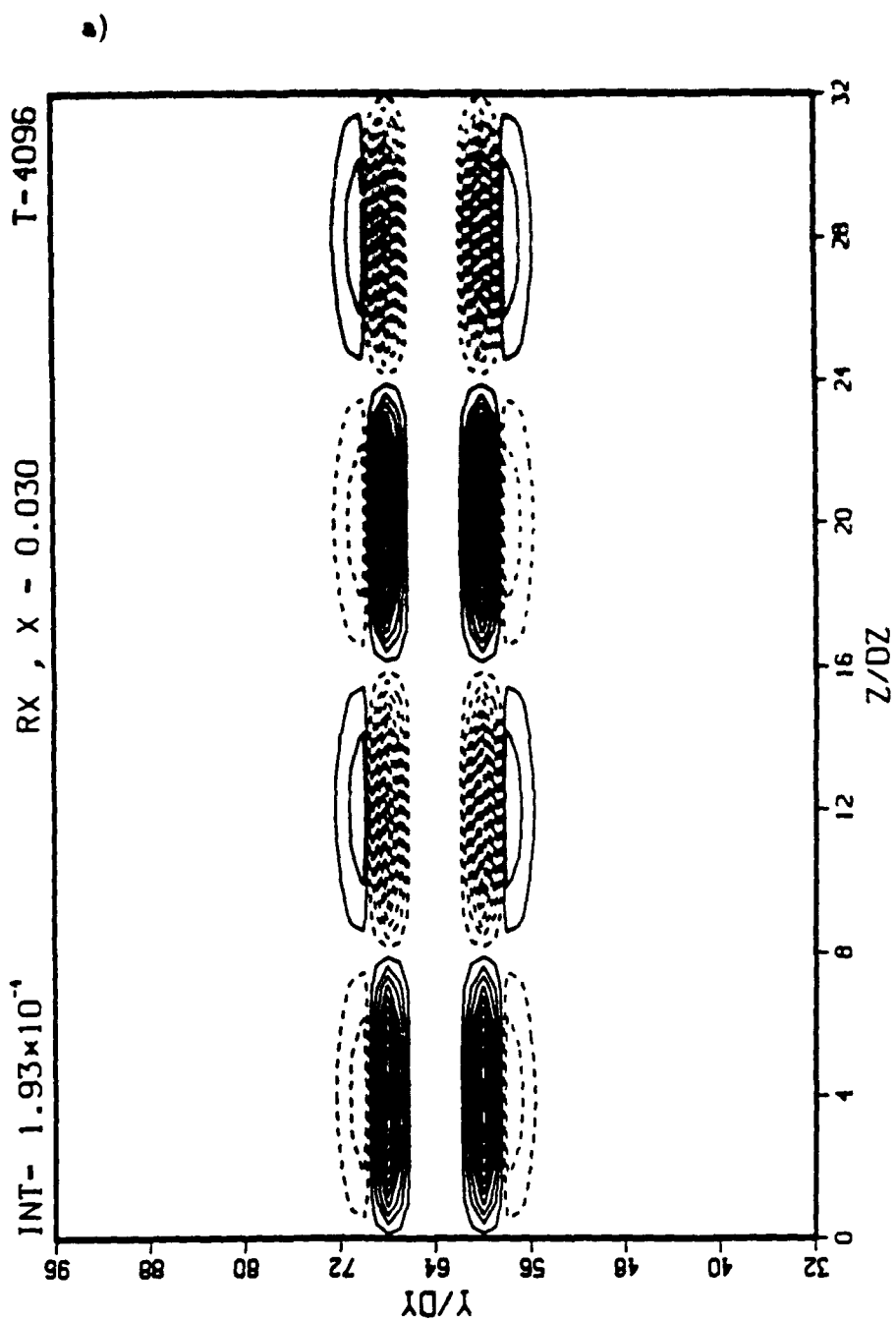


Figure 6.35 Continued.



**Figure 6.36** Contours of streamwise vorticity  $\omega_x$  in the  $yz$ -plane for  $t = 4096\Delta t$ .  
Case-7:  $A_2 = 0$ ,  $A_3 = .001$ ,  $\beta = .51$ , and  $\gamma = .5$ . Twenty contour intervals between the minimum and maximum values. Solid lines denote positive vorticity and dashed lines denote negative vorticity. a)  $x = .030$ , b)  $x = .146$ .

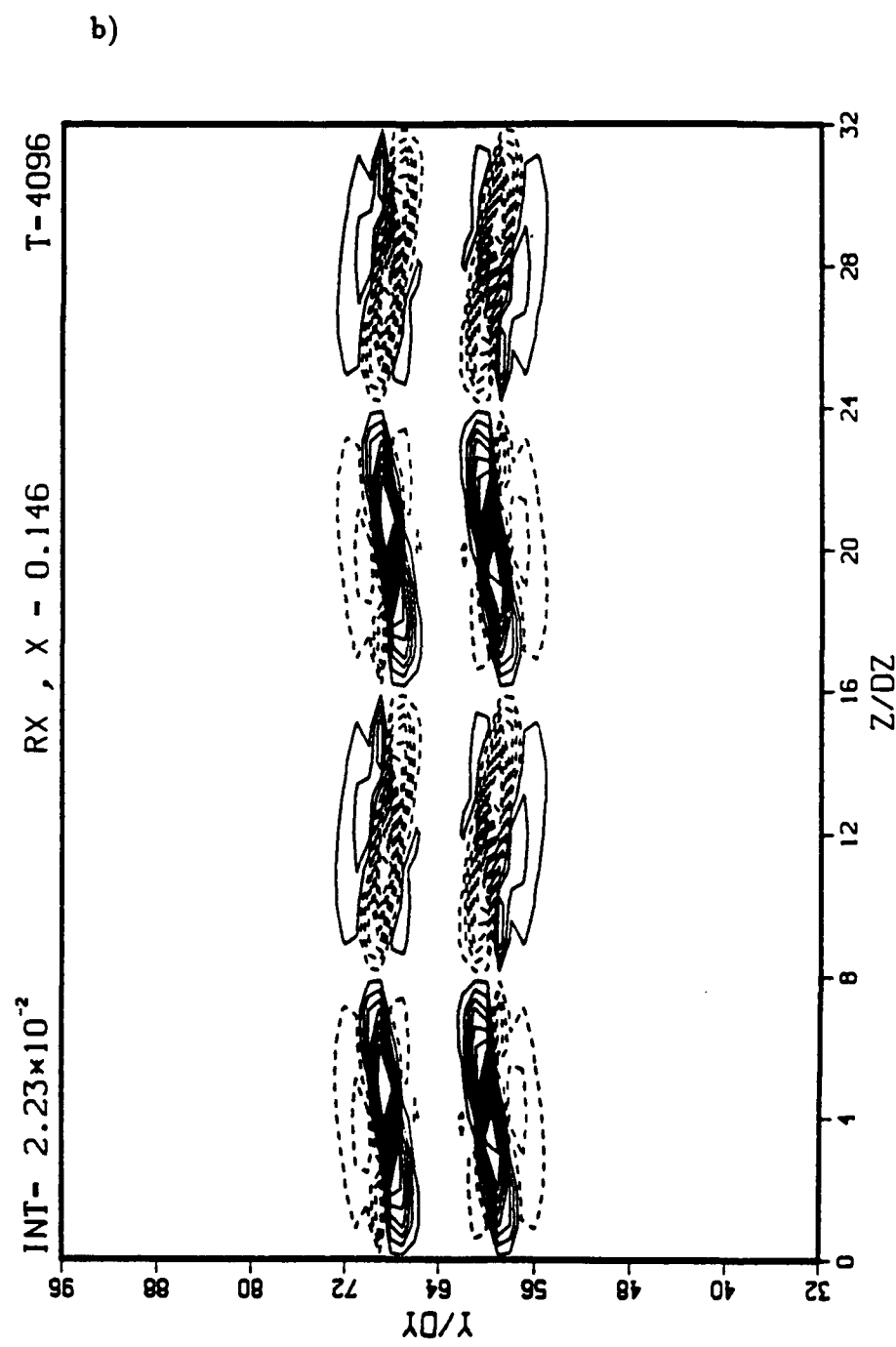


Figure 6.36 Continued.

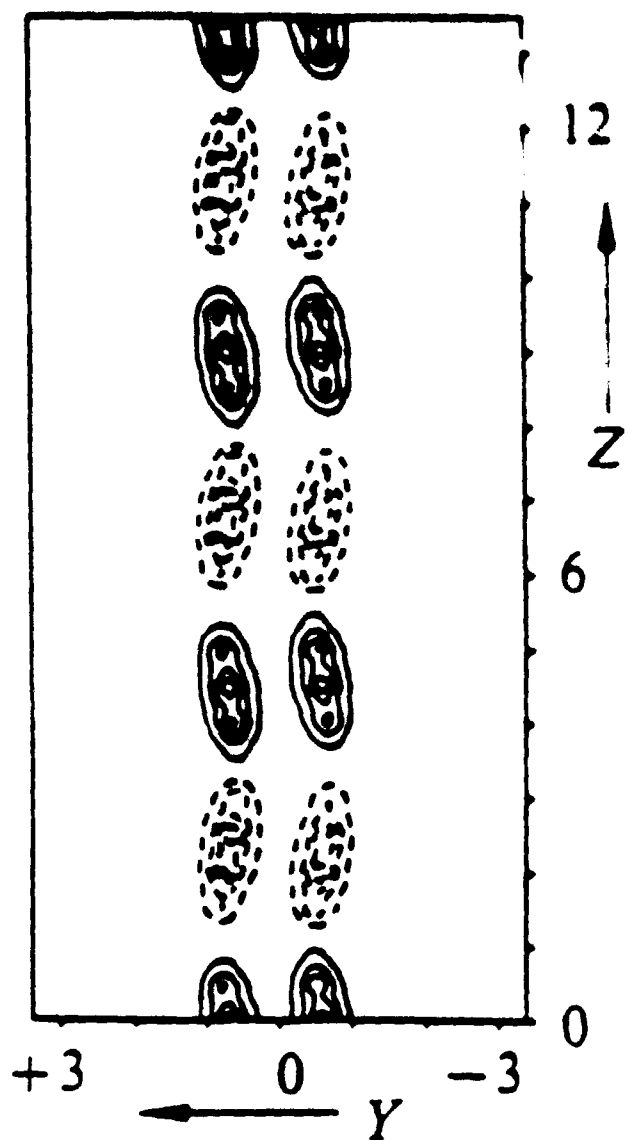


FIGURE 5. Top and side views of all vortex filaments at time  $t = 80$ . The filaments of the upper layer are drawn as solid lines, those of the lower layer are represented by dashed lines. In addition lines of constant streamwise vorticity are plotted for a vertical ( $Y, Z$ )-plane at  $z = 4.6$ .

Figure 6.37 Contours of streamwise vorticity  $\omega_x$  in the  $yz$ -plane, reproduced from Meiburg and Lasheras (1988).

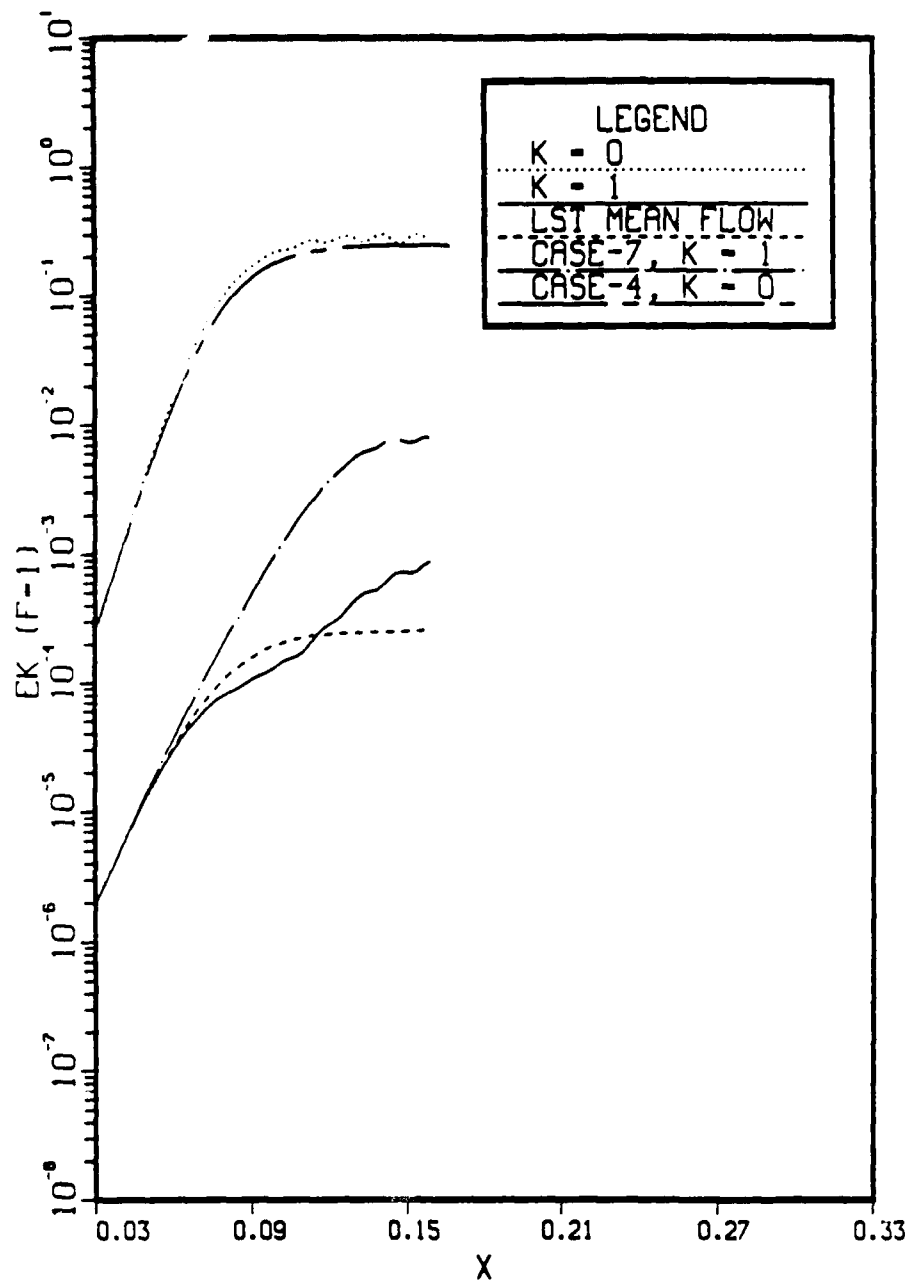


Figure 6.38 Amplification curves of the kinetic energy  $\hat{E}^k(x,1)$ . Case-8:  $A_2 = .01$ ,  $A_3 = .001$ ,  $\beta = .51$ , and  $\gamma = .5$ .

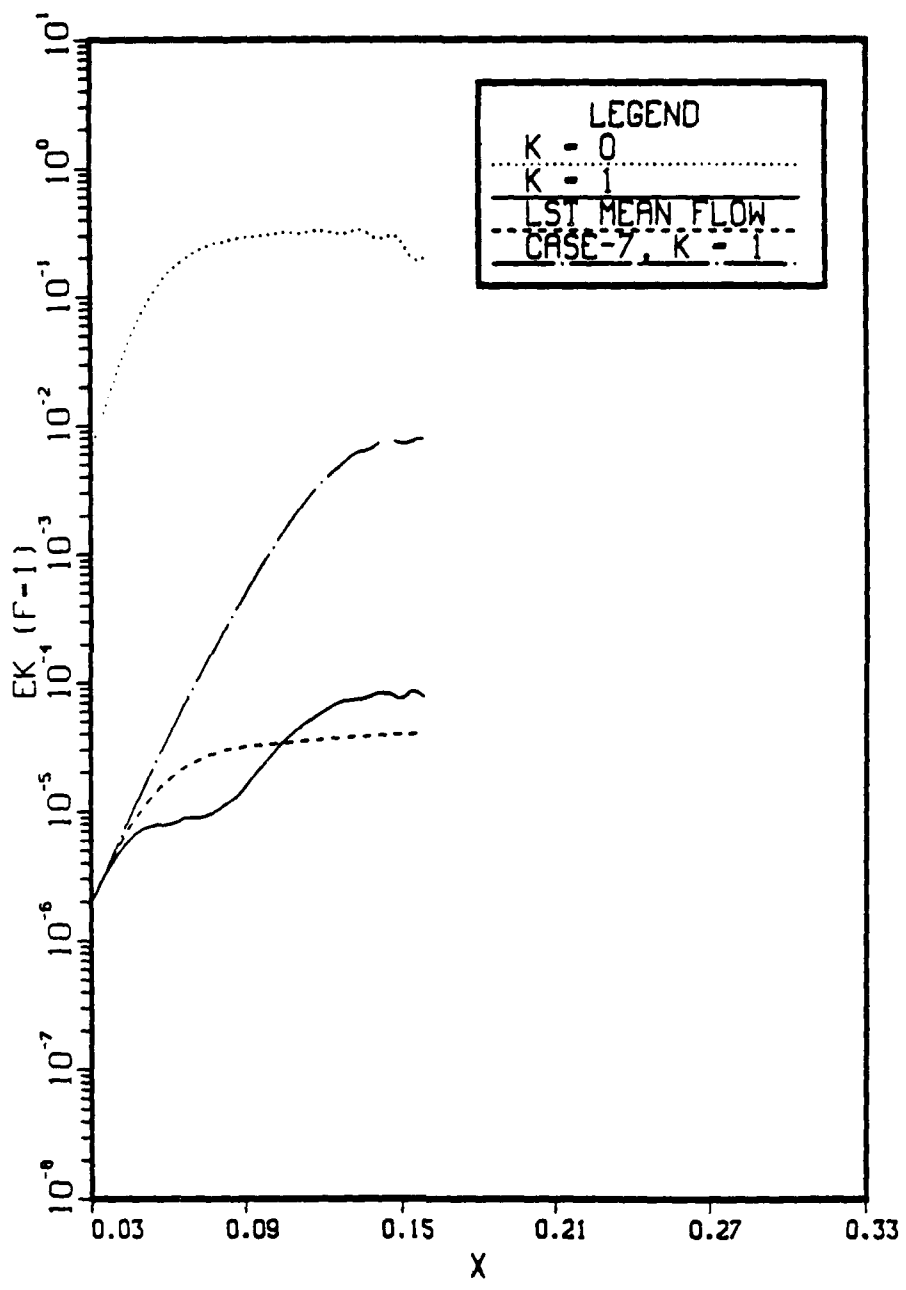


Figure 6.39 Amplification curves of the kinetic energy  $\hat{E}^k(x,1)$ . Case-9:  $A_2 = .05$ ,  $A_3 = .001$ ,  $\beta = .51$ , and  $\gamma = .5$ .

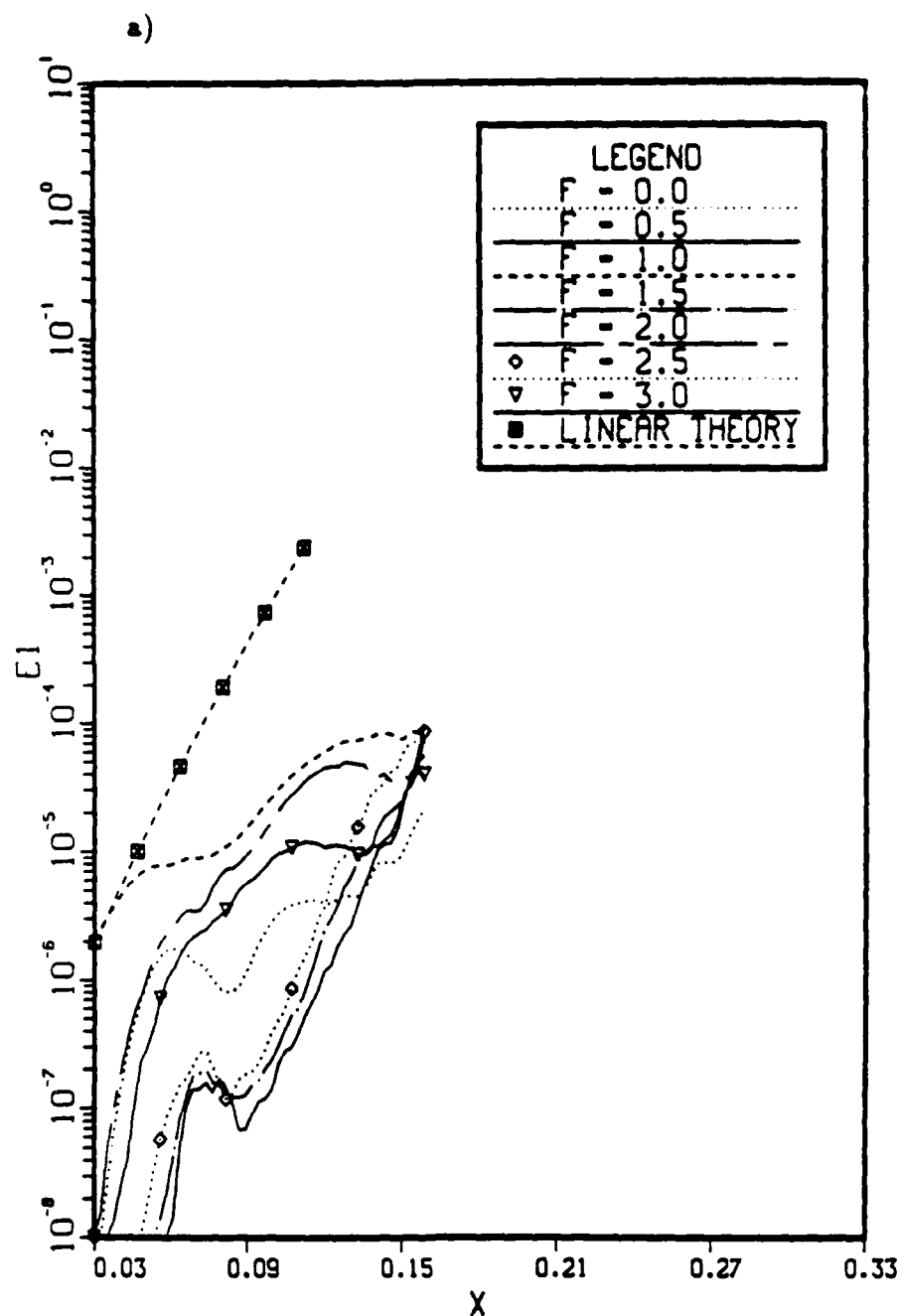


Figure 6.40 Amplification curves of the kinetic energy  $\hat{E}^1(x, F)$ . Case-9:  $A_2 = .05$ ,  $A_3 = .001$ ,  $\beta = .51$ , and  $\gamma = .5$ . a)  $N = 256$ , b)  $N = 512$ .

b)

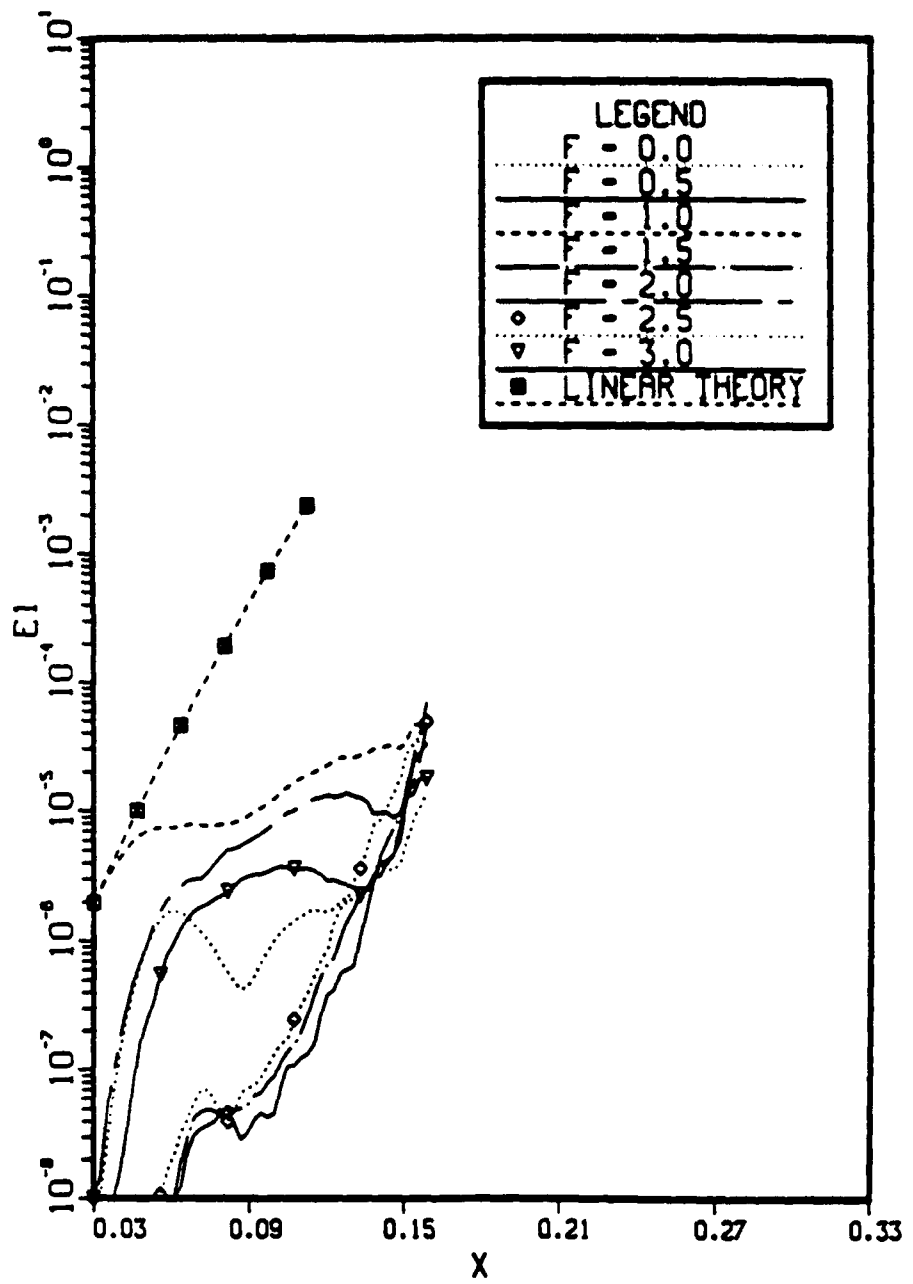


Figure 6.40 Continued.

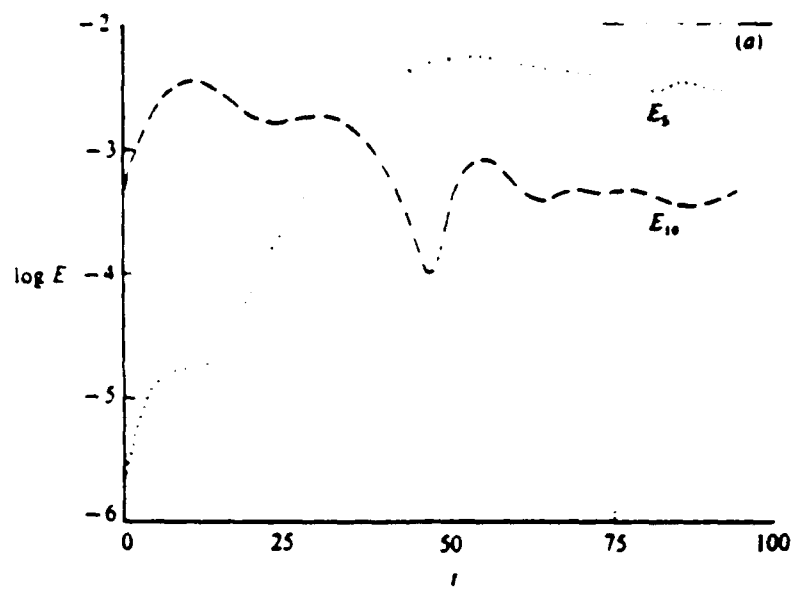


FIGURE 14. (a) A plot of the evolution of the modal energies as functions of time  $E_5 = E_{01} + E_{11} + E_{21}$ , i.e. the three lowest spanwise modes with the same  $x$ -wavelength as the fundamental.  $R = 100$ ,  $a = 0.4446$ ,  $A_{10} = 0.22$ ,  $A_{11} = 0$  and  $A_{21} = 10^{-5}$ .  $M = N = P = 64$ . (b) A three-dimensional perspective plot of the vorticity field as in figure 10 at  $t = 96$ . (c) As (a) but  $A_{10} = 0.14$ . (d) As (b) but  $A_{10} = 0.14$ .

Figure 6.41 Temporal variation of two-dimensional and three-dimensional disturbance kinetic energy in a free shear layer, reproduced from Metcalfe et. al (1987).

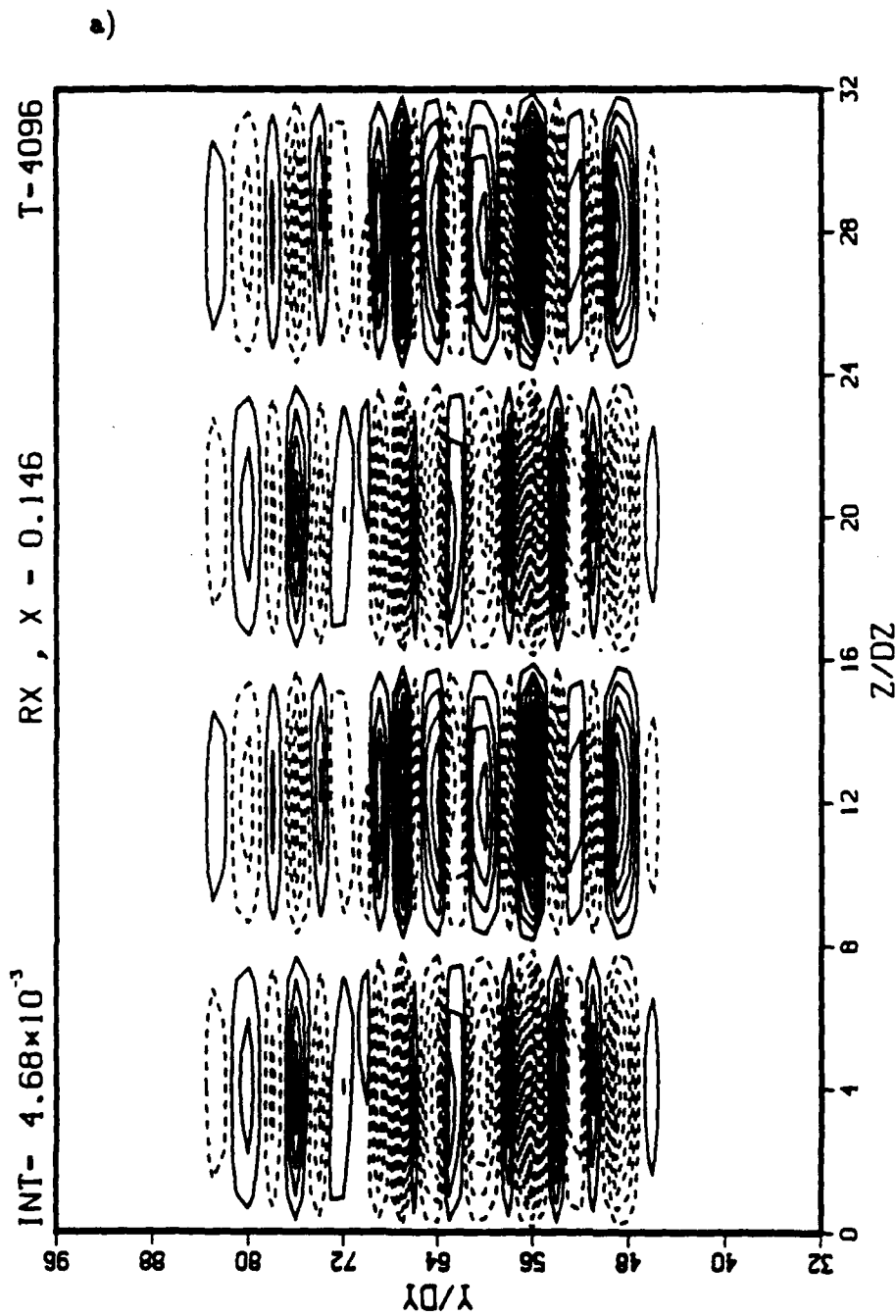


Figure 6.42 Contours of streamwise vorticity  $\omega_x$  in the  $yz$ -plane for  $t = 4096\Delta t$ .  $x = .146$ . Twenty contour intervals between the minimum and maximum values. Solid lines denote positive vorticity and dashed lines denote negative vorticity. a) Case-8,  $A_2 = 0.01$  and  $A_3 = 0.001$ ; b) Case-9,  $A_2 = 0.05$  and  $A_3 = 0.001$ .

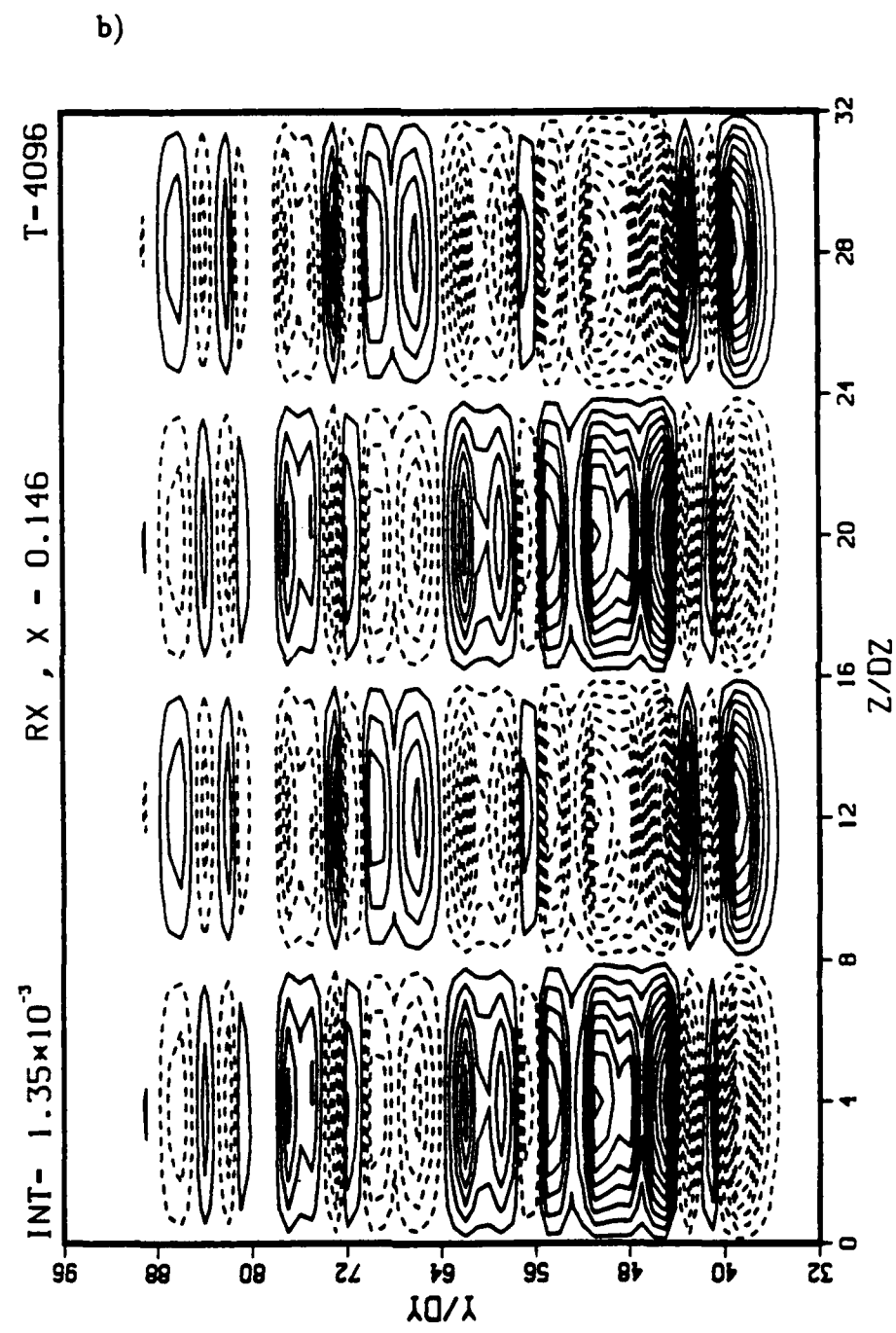
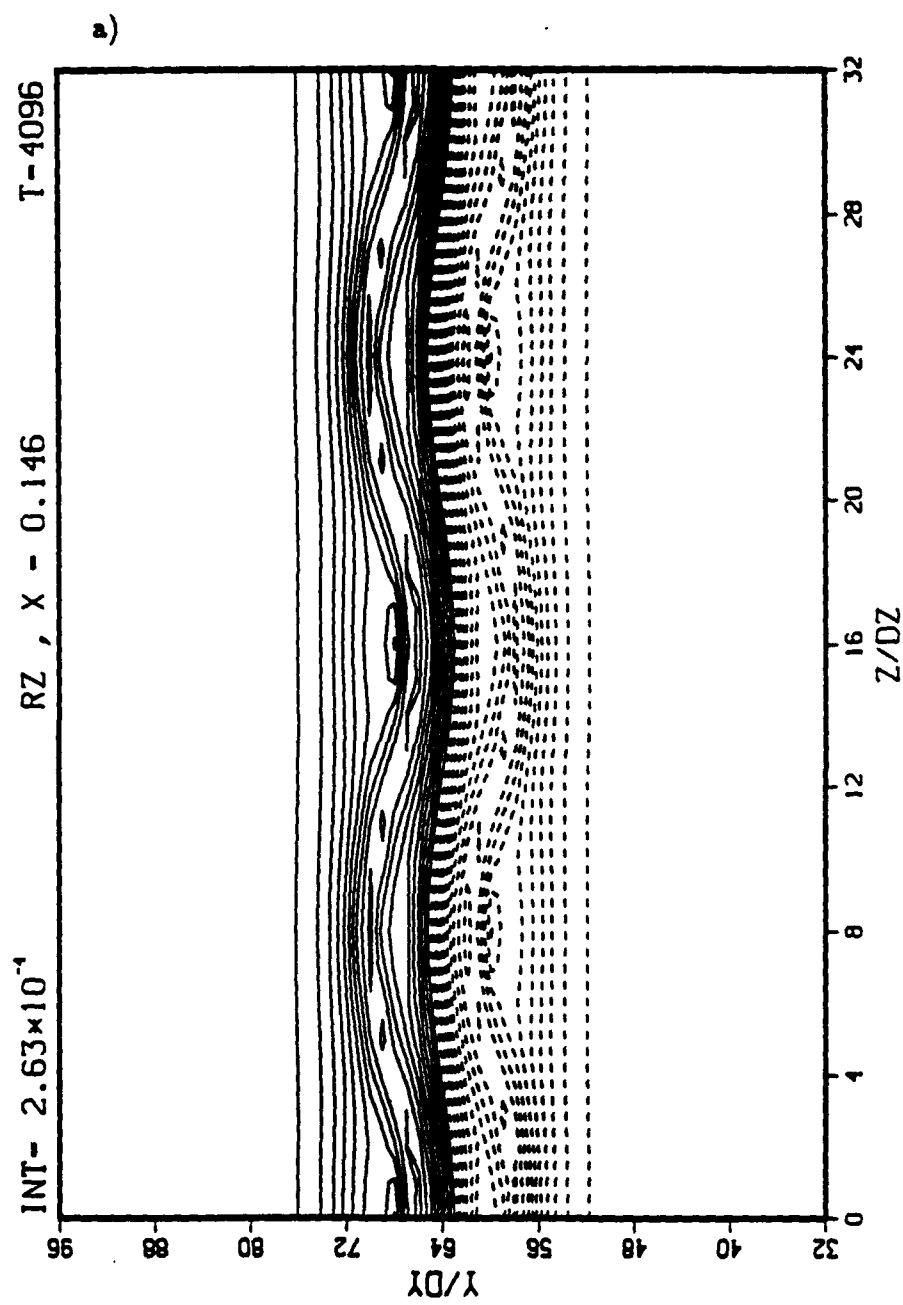


Figure 6.42 Continued.



**Figure 6.43** Contours of spanwise vorticity  $\omega_z$  in the  $yz$ -plane for  $t = 4096\Delta t$ ,  $x = .146$ . Twenty contour intervals between the minimum and maximum values. Solid lines denote positive vorticity and dashed lines denote negative vorticity. a) Case-7,  $A_2 = 0.00$  and  $A_3 = 0.001$ ; b) Case-8,  $A_2 = 0.01$  and  $A_3 = 0.001$ ; c) Case-9,  $A_2 = 0.05$  and  $A_3 = 0.001$ .

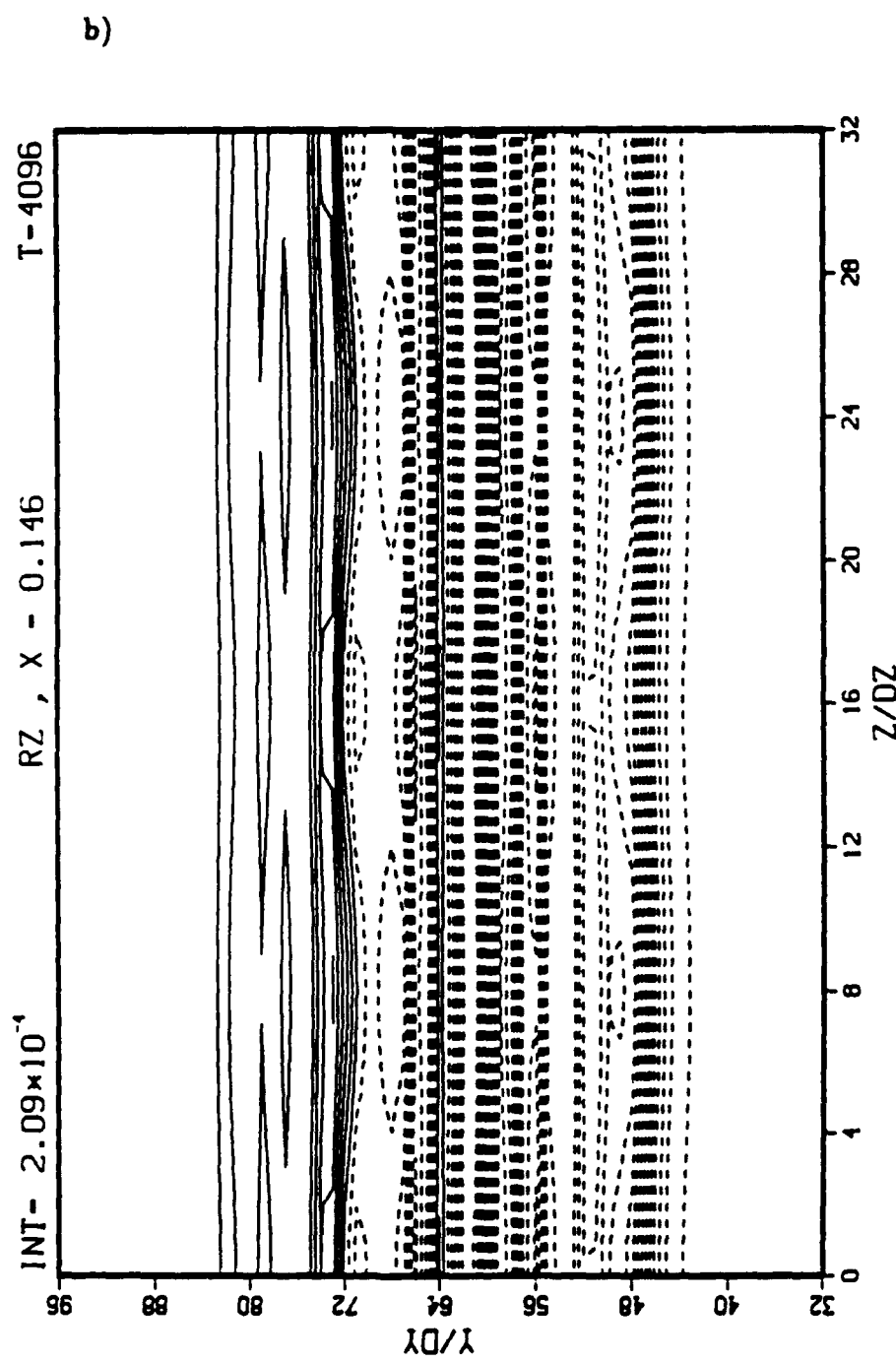


Figure 6.43 Continued.

c)

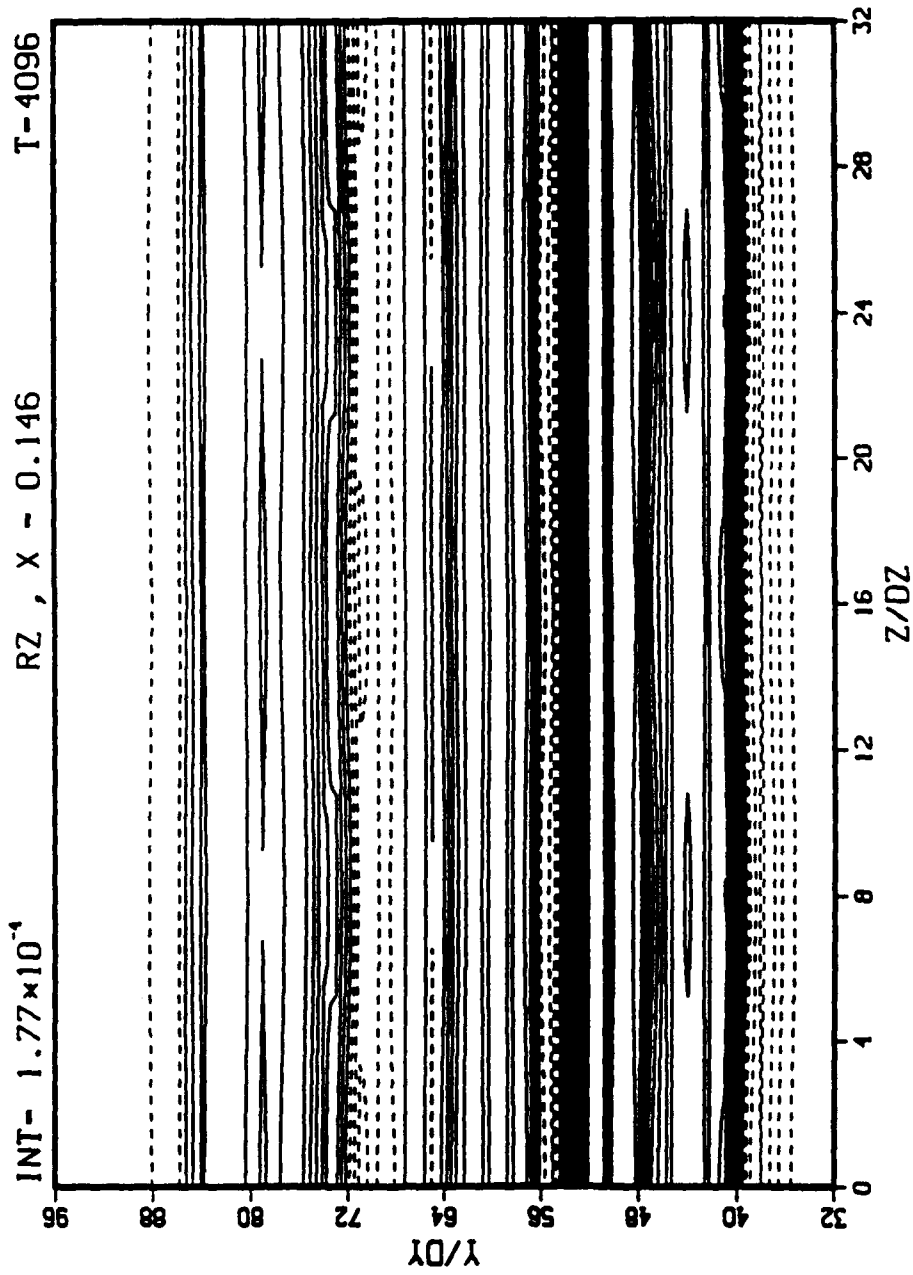
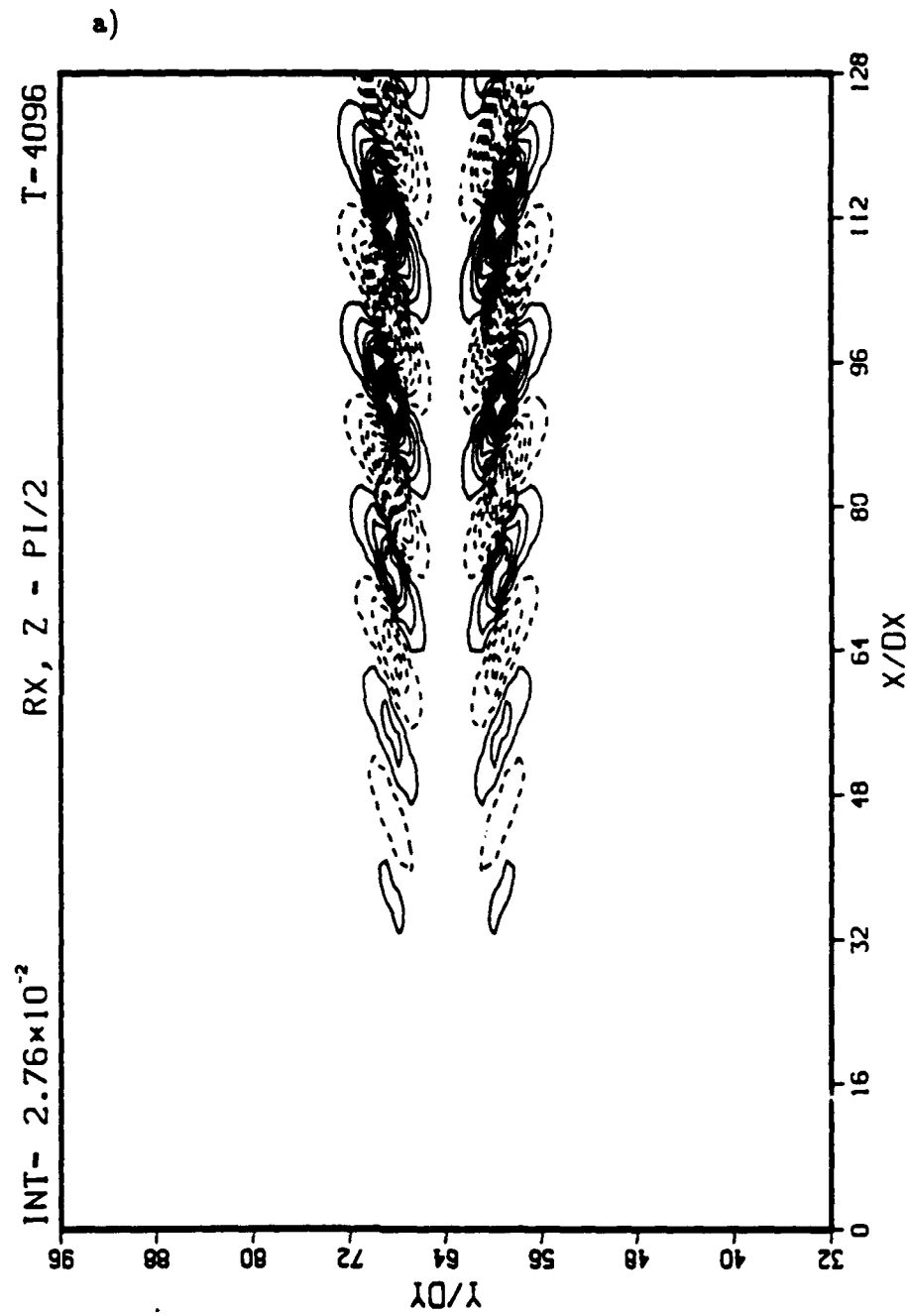


Figure 6.43 Continued.



**Figure 6.44** Contours of streamwise vorticity  $\omega_x$  in the  $xy$ -plane for  $t = 4096\Delta t$ ,  $z = \pi/2$ . Twenty contour intervals between the minimum and maximum values. Solid lines denote positive vorticity and dashed lines denote negative vorticity. a) Case-7,  $A_2 = 0.00$  and  $A_3 = 0.001$ ; b) Case-8,  $A_2 = 0.01$  and  $A_3 = 0.001$ ; c) Case-9,  $A_2 = 0.05$  and  $A_3 = 0.001$ .

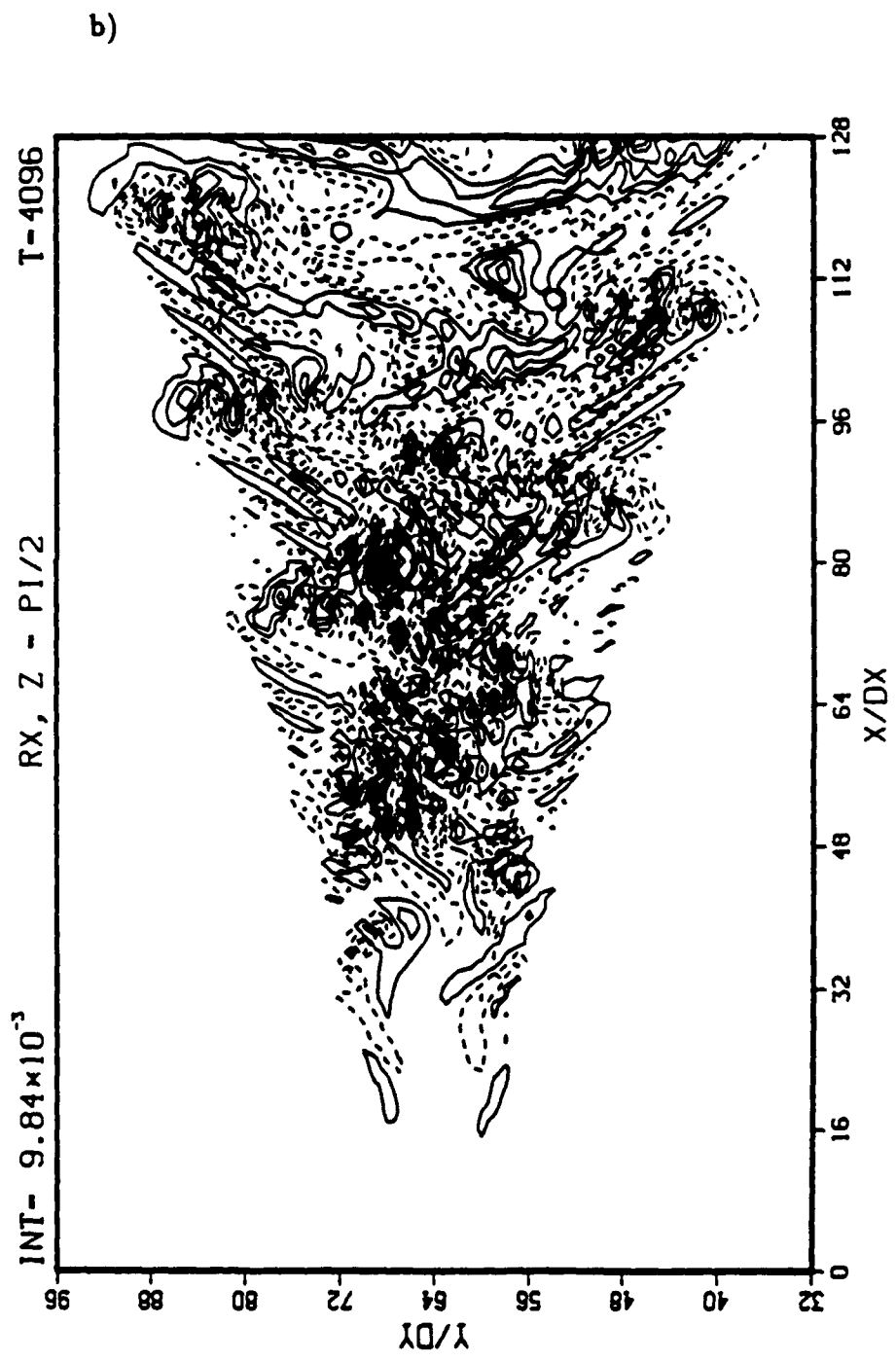


Figure 6.44 Continued.

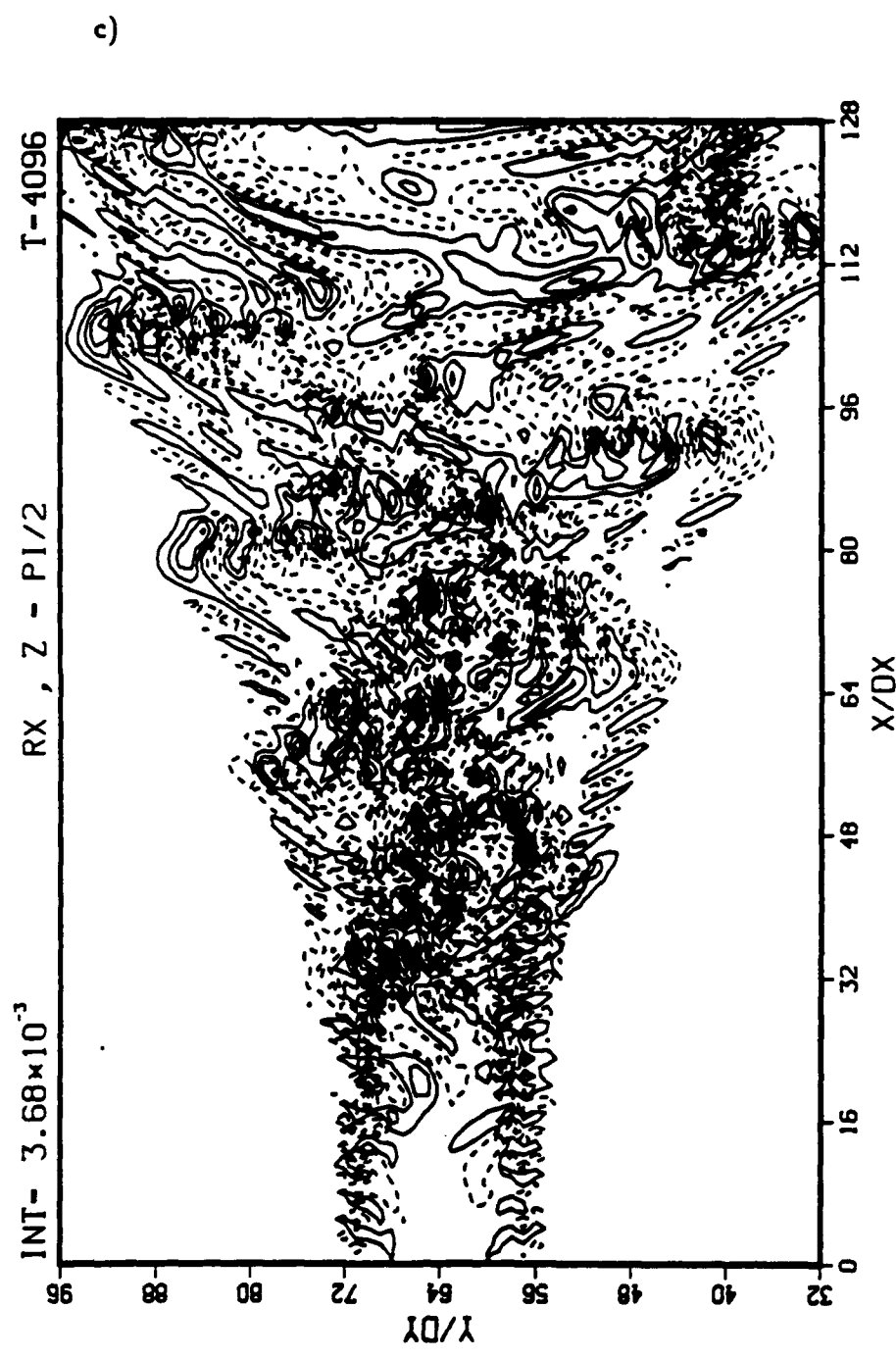


Figure 6.44 Continued.

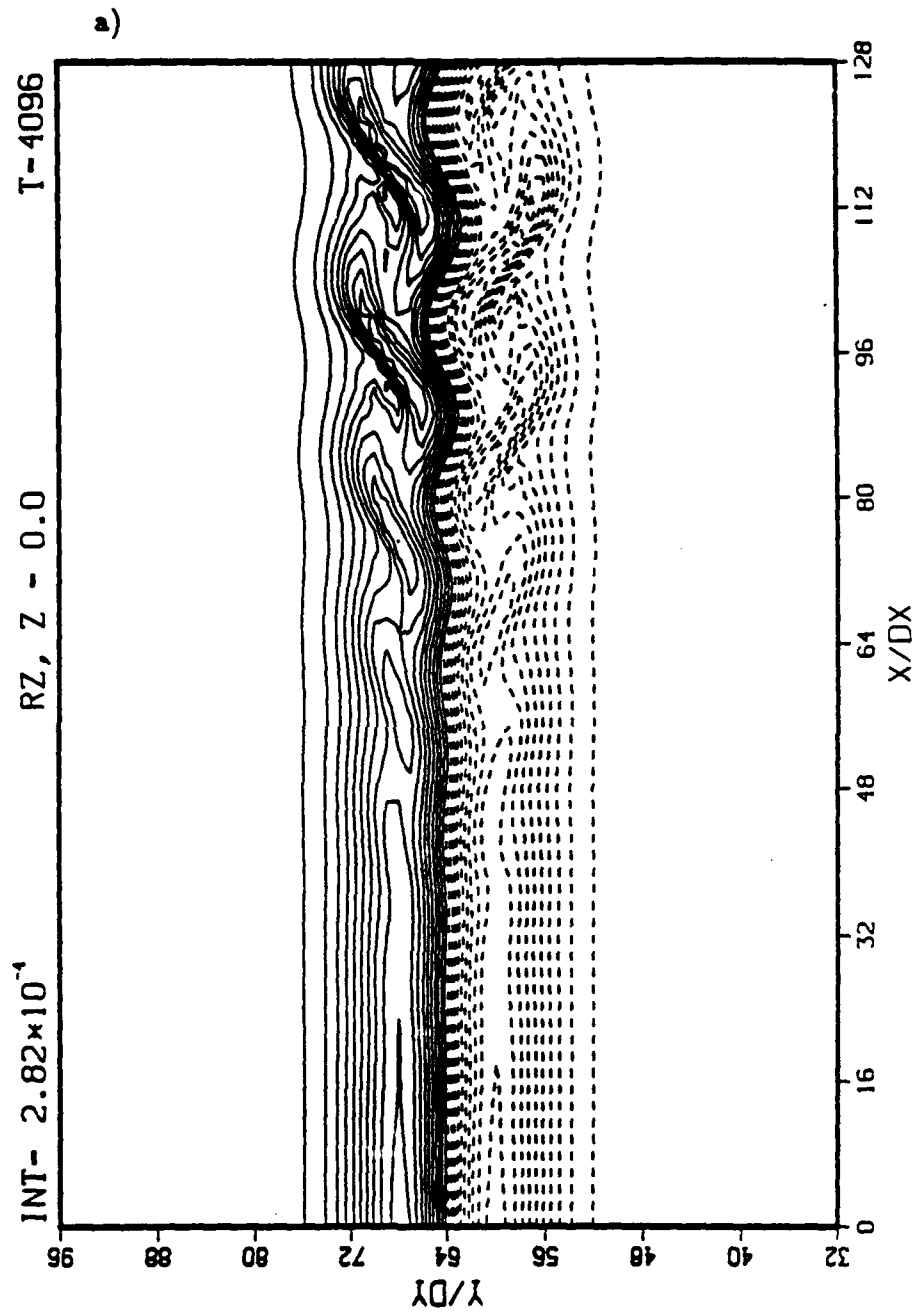


Figure 6.45 Contours of spanwise vorticity  $\omega_z$  in the  $xy$ -plane for  $t = 4096\Delta t$ .  $z = 0$ . Twenty contour intervals between the minimum and maximum values. Solid lines denote positive vorticity and dashed lines denote negative vorticity. a) Case-7,  $A_2 = 0.00$  and  $A_3 = 0.001$ ; b) Case-8,  $A_2 = 0.01$  and  $A_3 = 0.001$ ; c) Case-9,  $A_2 = 0.05$  and  $A_3 = 0.001$ .

b)

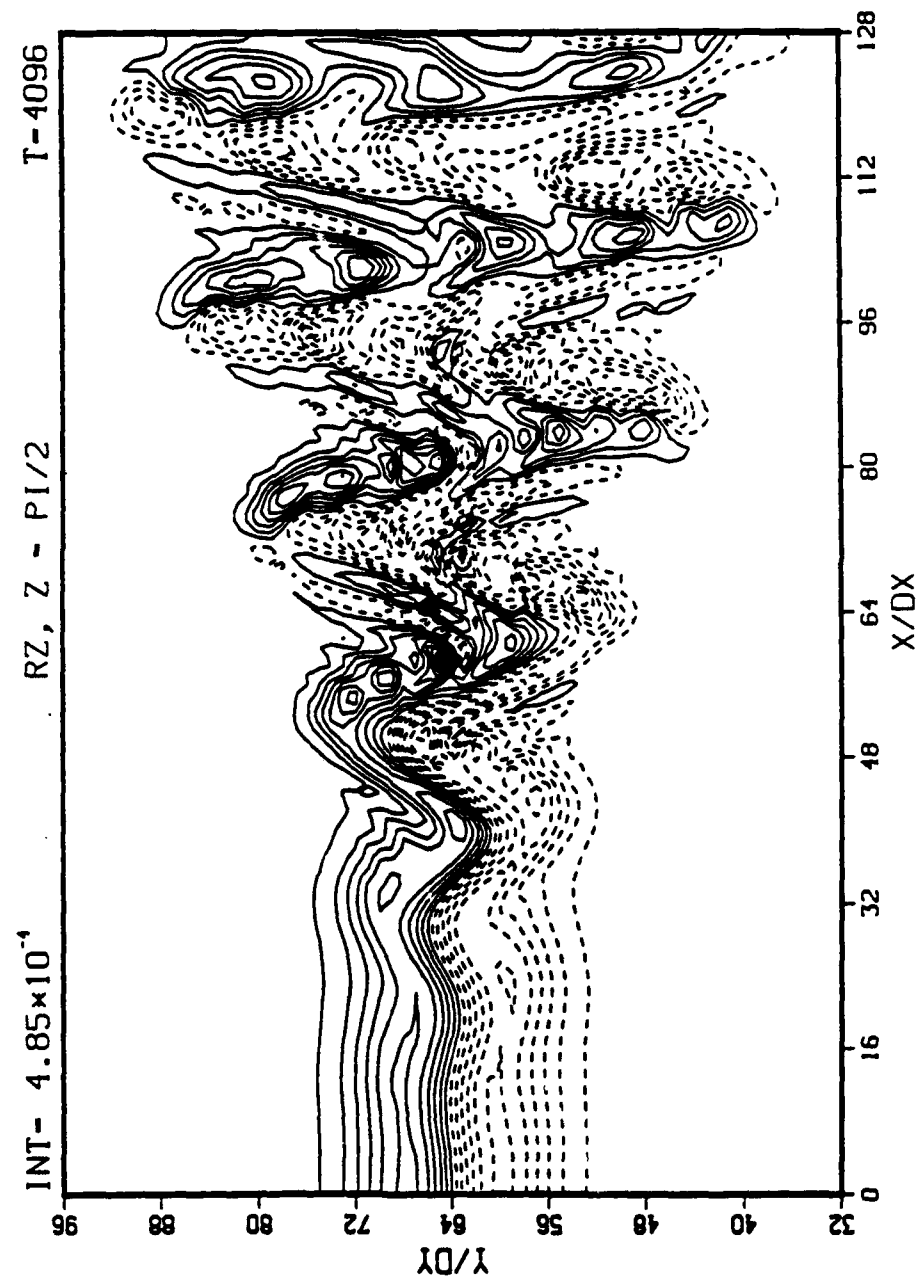


Figure 6.45 Continued.

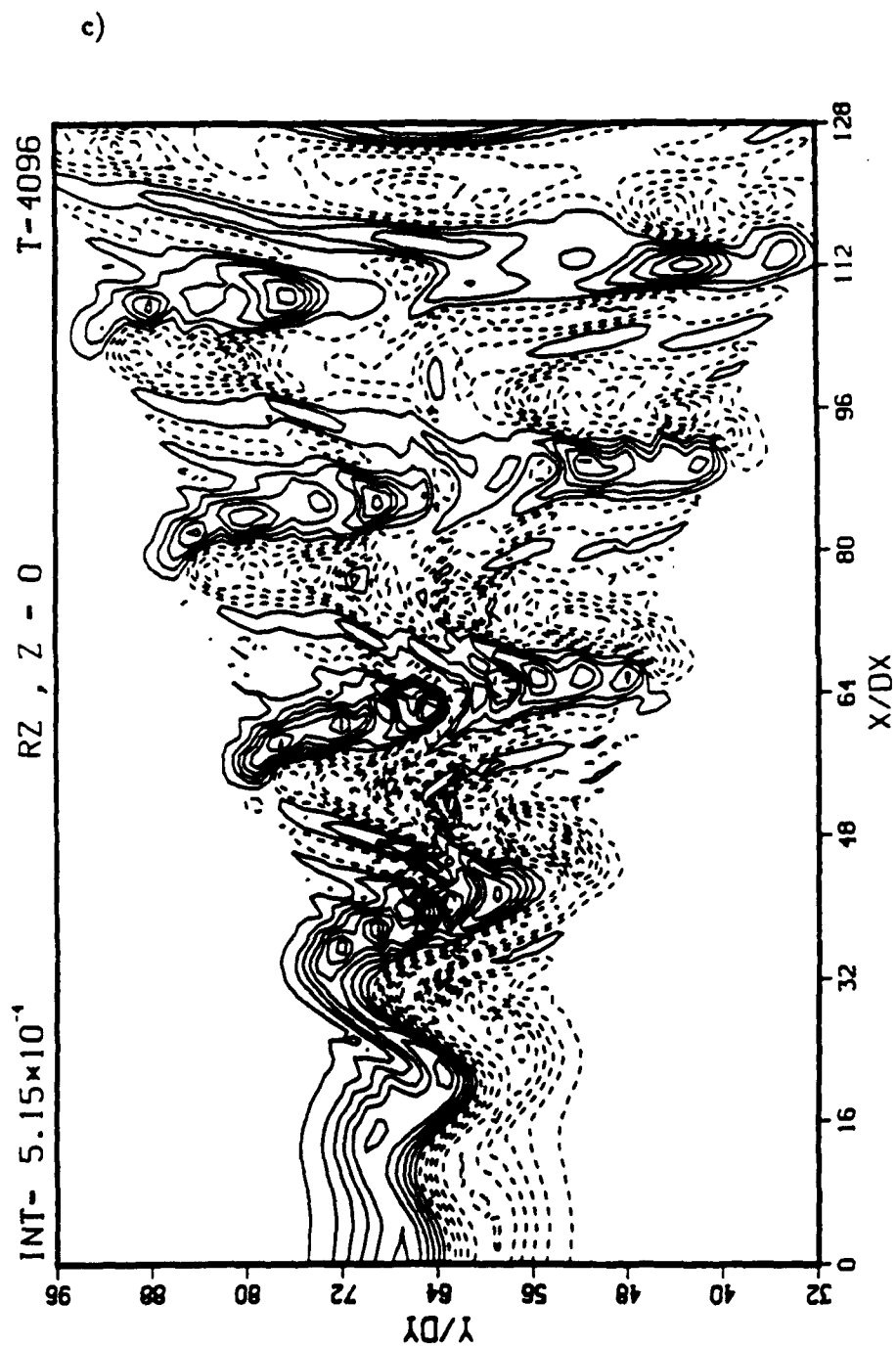


Figure 6.45 Continued.

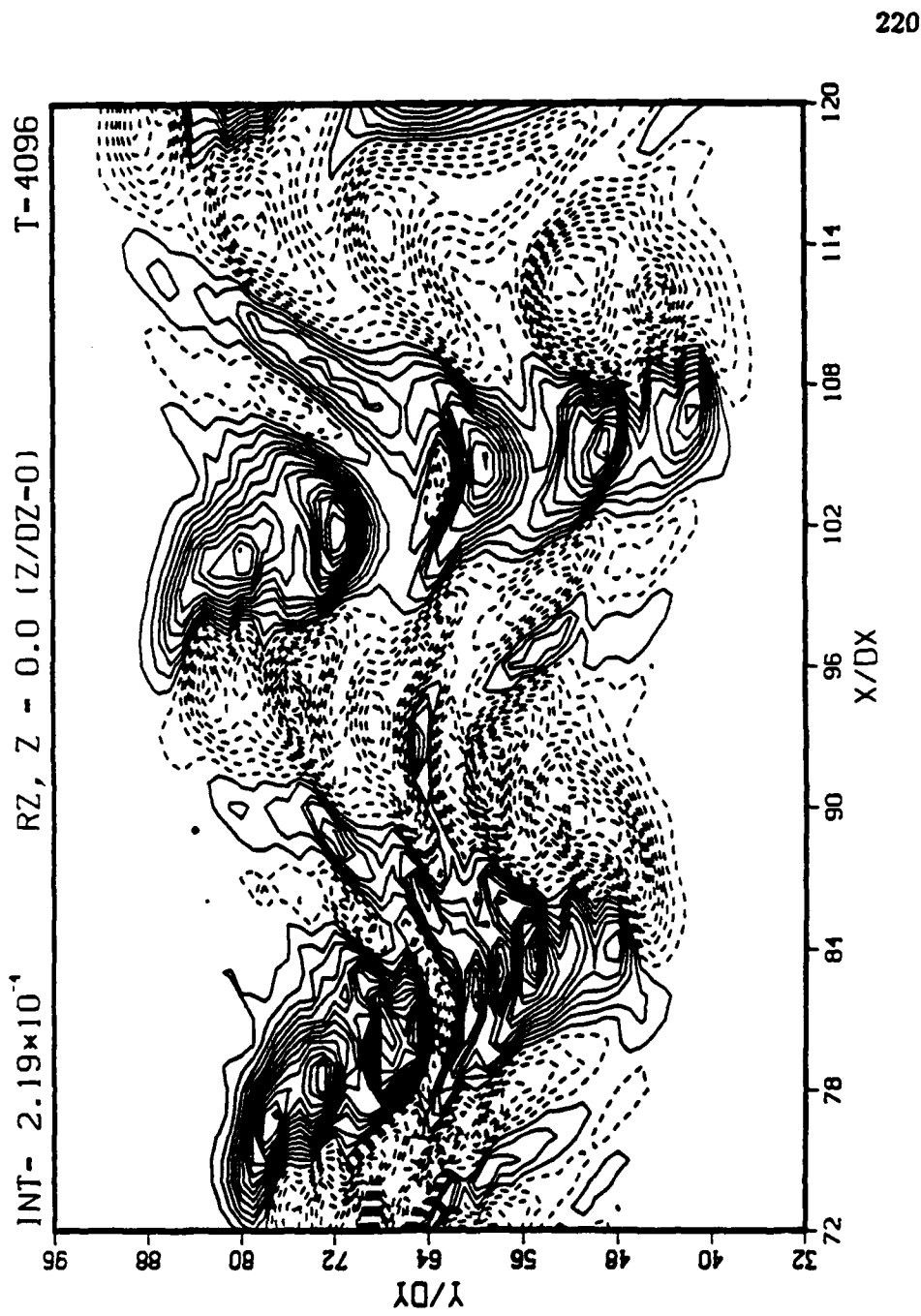


Figure 6.46 Contours of spanwise vorticity  $\omega_z$  in the  $zy$ -plane for  $t = 4096\Delta t$  and  $z = 0$ . Case-8:  $A_2 = .01$ ,  $A_3 = .001$ ,  $\beta = .51$ , and  $\gamma = .5$ . Thirty contour intervals between the minimum and maximum values. Solid lines denote positive vorticity and dashed lines denote negative vorticity.

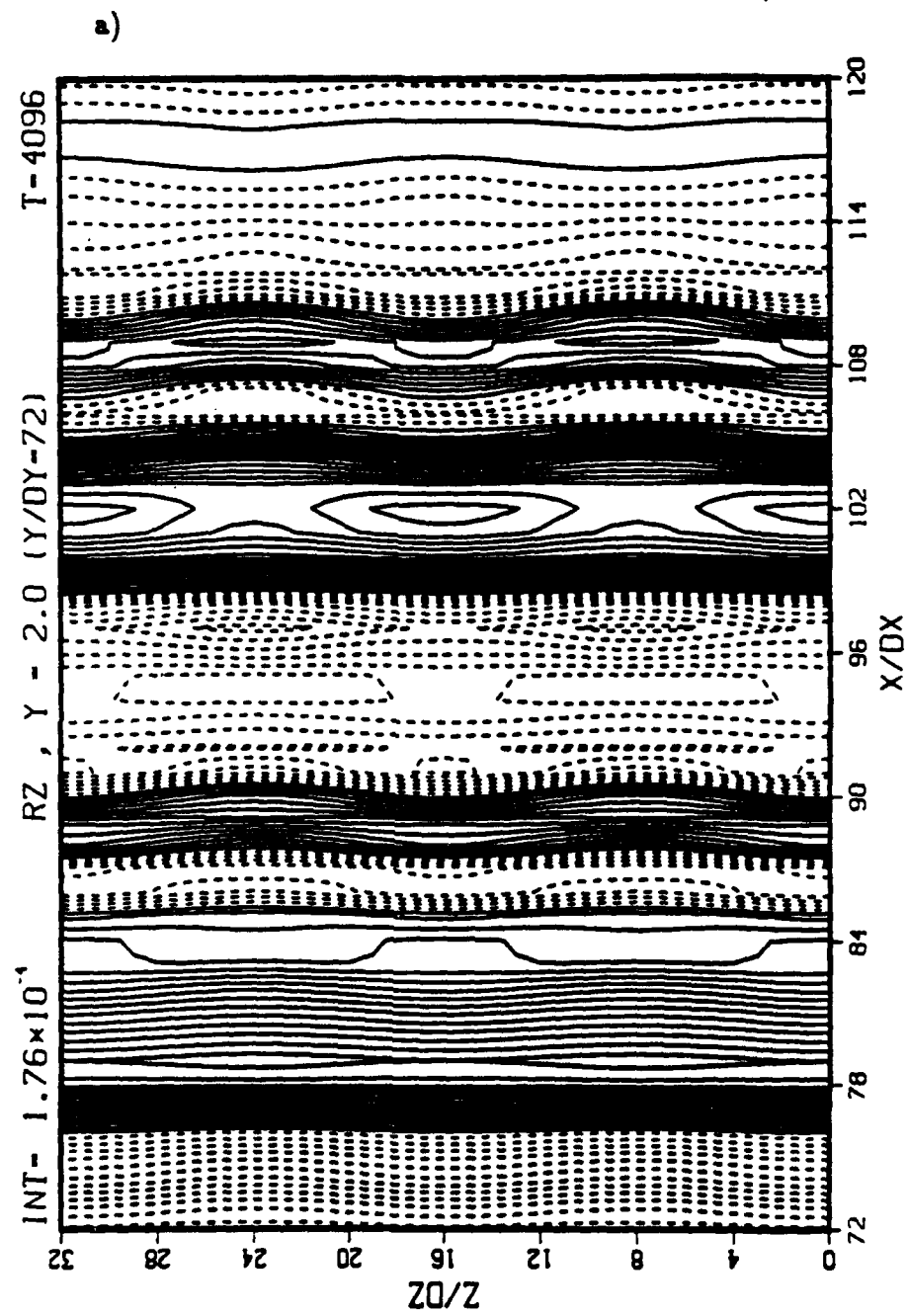


Figure 6.47 Contours of spanwise vorticity  $\omega_z$  in the  $zz$ -plane for  $t = 4096\Delta t$ . Case-8:  $A_2 = .01$ ,  $A_3 = .001$ ,  $\beta = .51$ , and  $\gamma = .5$ . Thirty contour intervals between the minimum and maximum values. Solid lines denote positive vorticity and dashed lines denote negative vorticity. a)  $y = 2$  ( $y/\Delta y = 72$ ), b)  $y = -2$  ( $y/\Delta y = 56$ ).

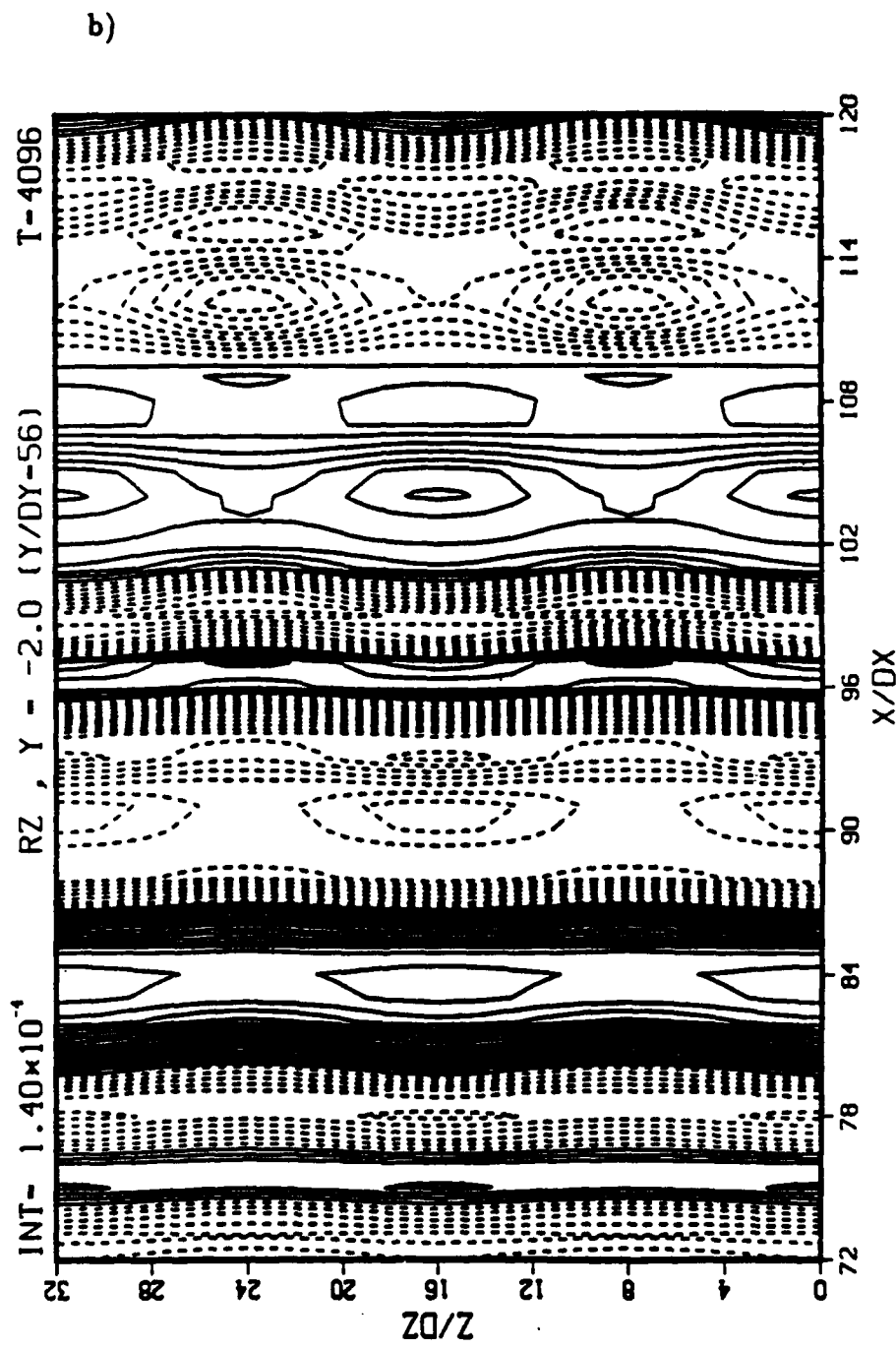
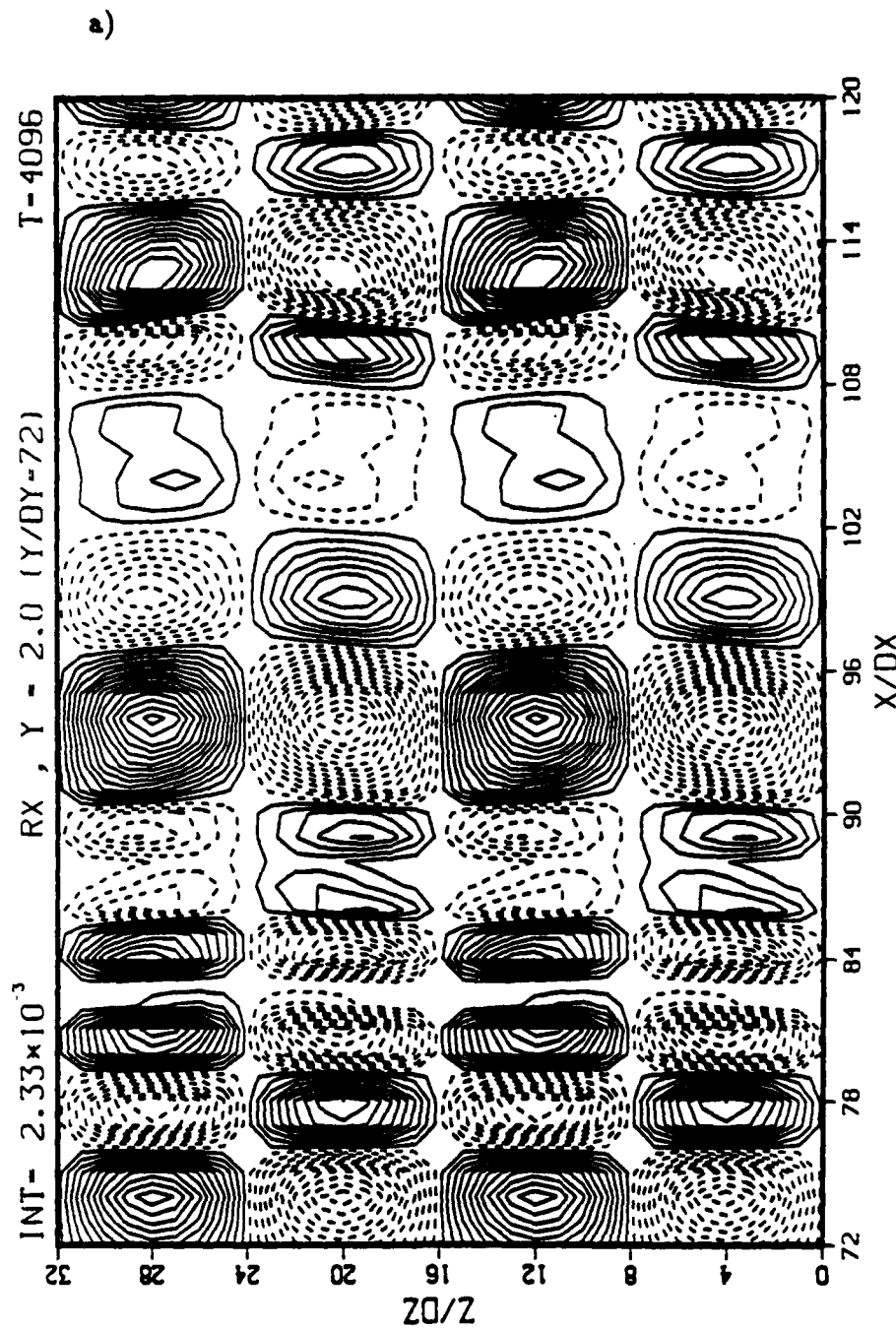


Figure 6.47 Continued.



**Figure 6.48** Contours of streamwise vorticity  $\omega_x$  in the  $zz$ -plane for  $t = 4096\Delta t$ .  
**Case-8:**  $A_2 = .01$ ,  $A_3 = .001$ ,  $\beta = .51$ , and  $\gamma = .5$ . Thirty contour intervals between the minimum and maximum values. Solid lines denote positive vorticity and dashed lines denote negative vorticity. a)  $y = 2$  ( $y/\Delta y = 72$ ), b)  $y = -2$  ( $y/\Delta y = 56$ ).

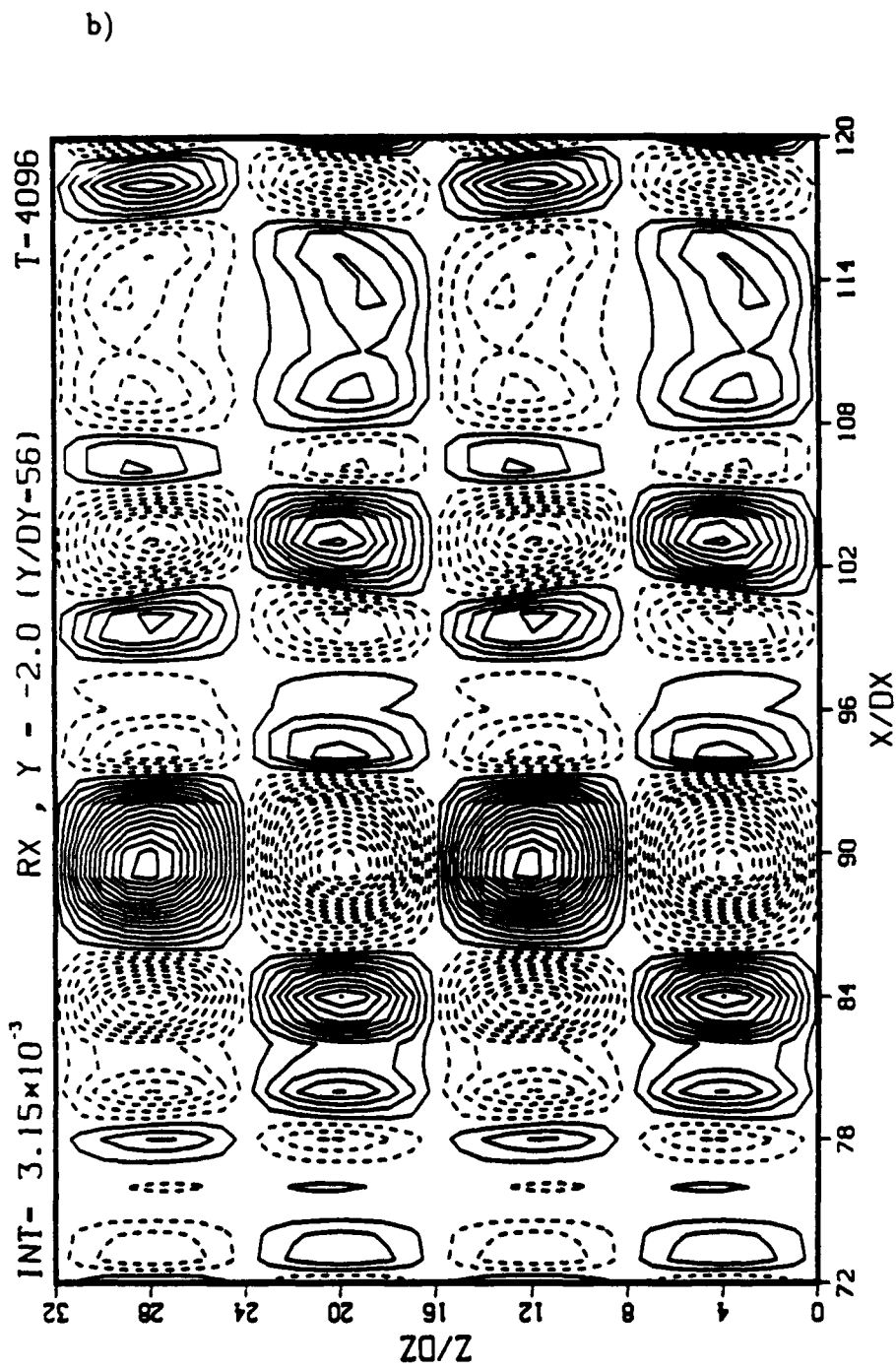


Figure 6.48 Continued.

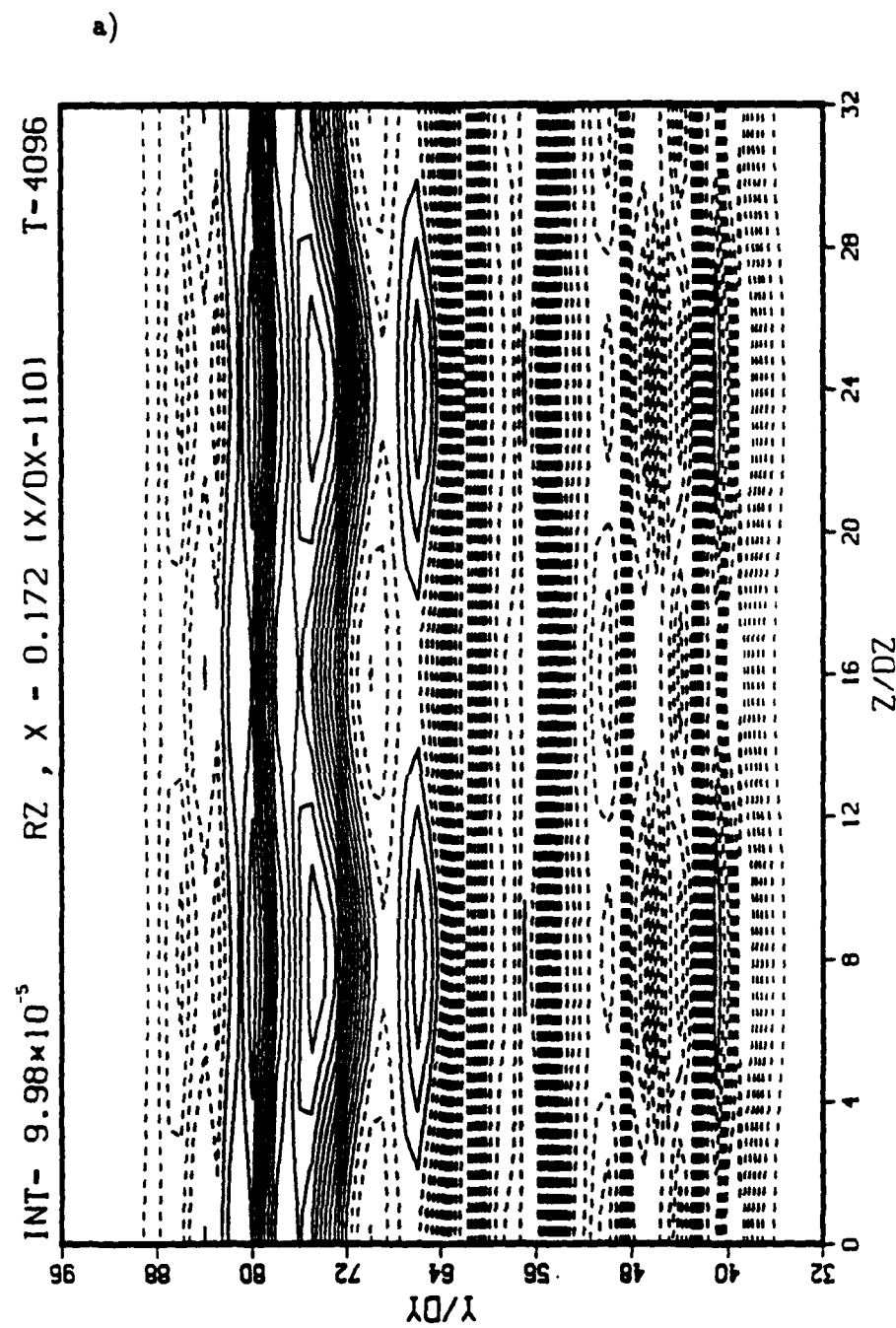


Figure 6.49 Contours of spanwise vorticity  $\omega_z$  in the  $yz$ -plane for  $t = 4096\Delta t$ . Case-8:  $A_2 = .01$ ,  $A_3 = .001$ ,  $\beta = .51$ , and  $\gamma = .5$ . Thirty contour intervals between the minimum and maximum values. Solid lines denote positive vorticity and dashed lines denote negative vorticity. a)  $x = .172$  ( $x/\Delta x = 110$ ), b)  $x = .160$  ( $x/\Delta x = 101$ ).

b)

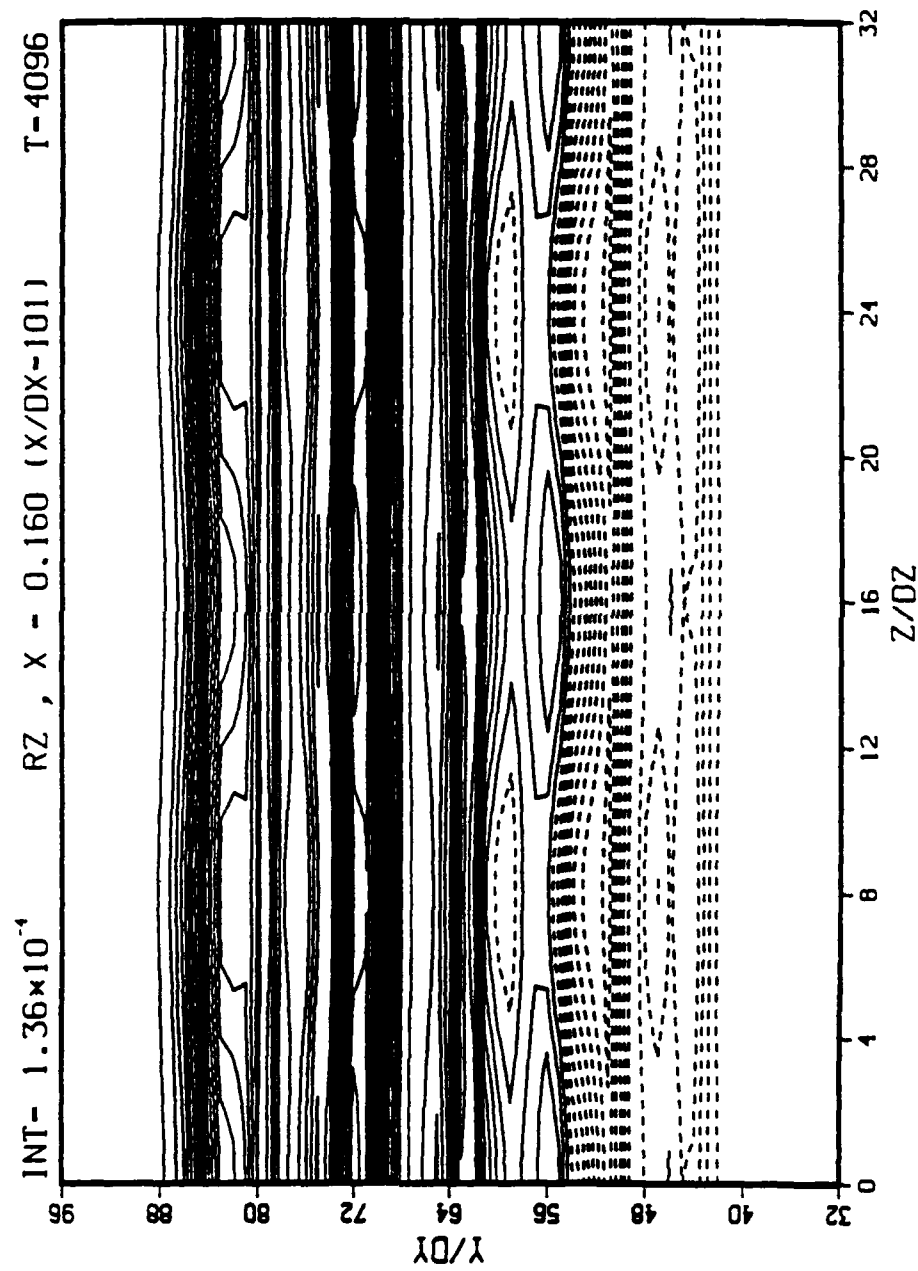


Figure 6.49 Continued.

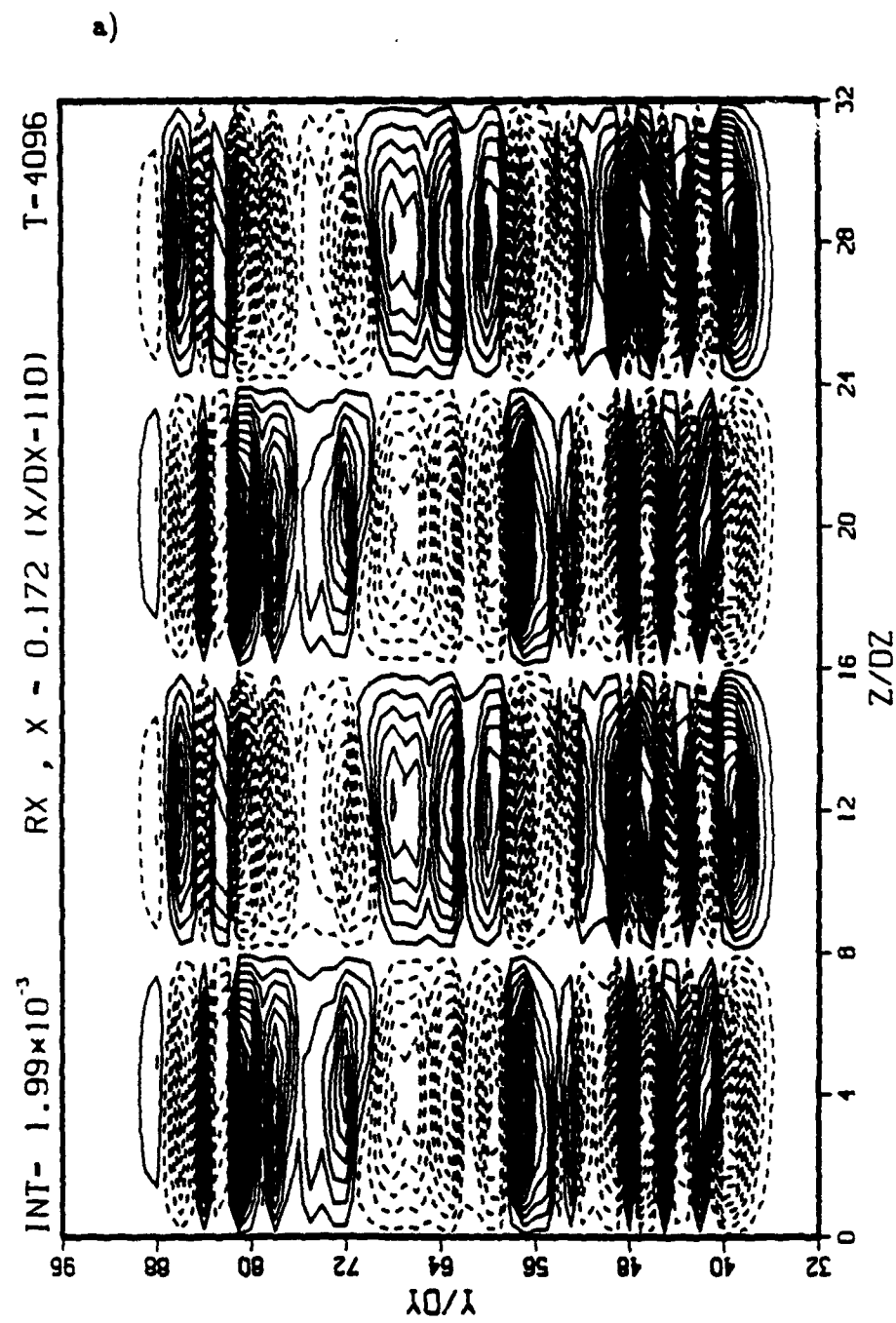


Figure 6.50 Contours of streamwise vorticity  $\omega_x$  in the  $yz$ -plane for  $t = 4096\Delta t$ .  
Case-8:  $A_2 = .01$ ,  $A_3 = .001$ ,  $\beta = .51$ , and  $\gamma = .5$ . Thirty contour intervals between the minimum and maximum values. Solid lines denote positive vorticity and dashed lines denote negative vorticity. a)  $x = .172$  ( $x/\Delta x = 110$ ), b)  $x = .160$  ( $x/\Delta x = 101$ ).

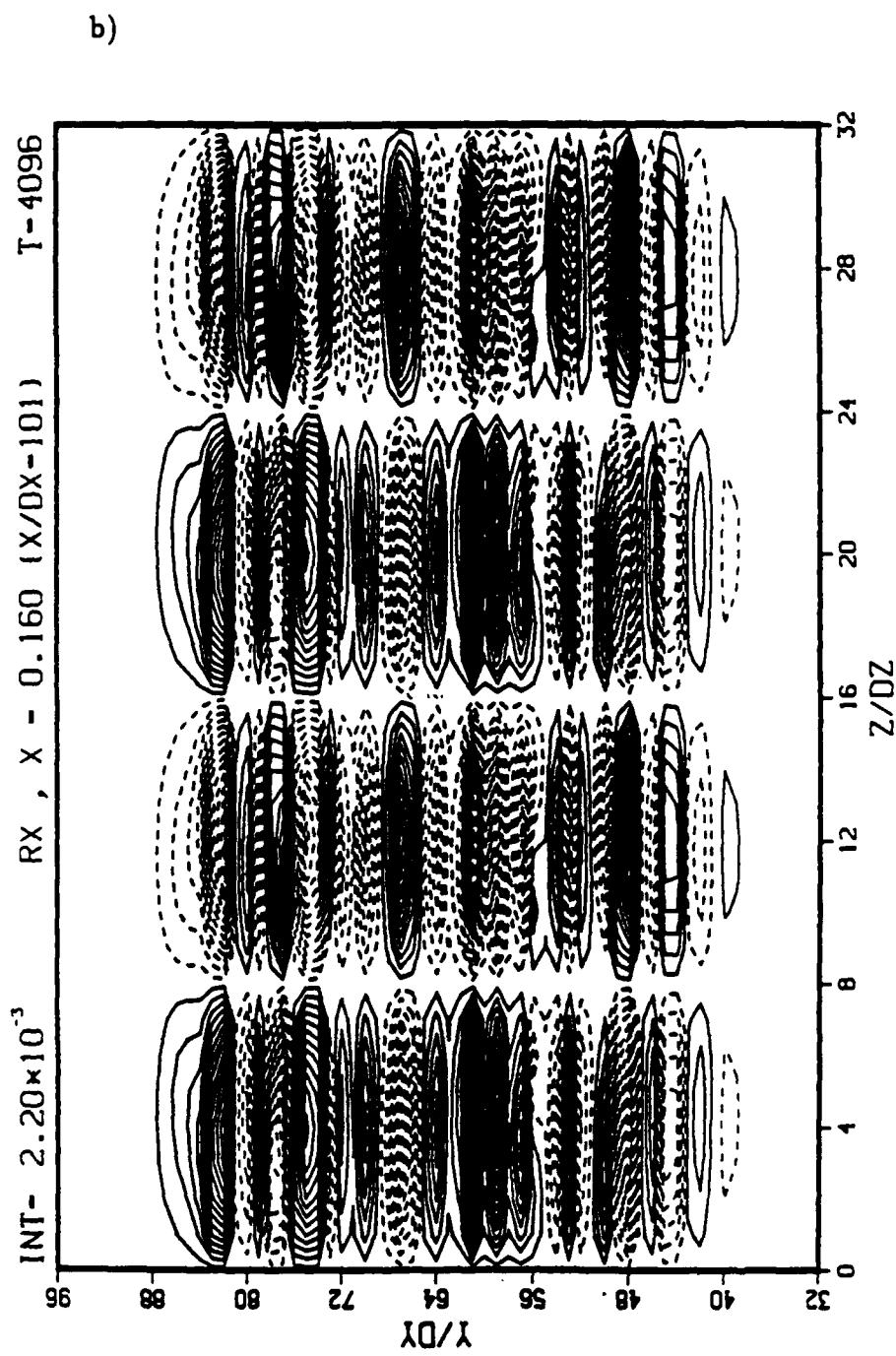


Figure 6.50 Continued.

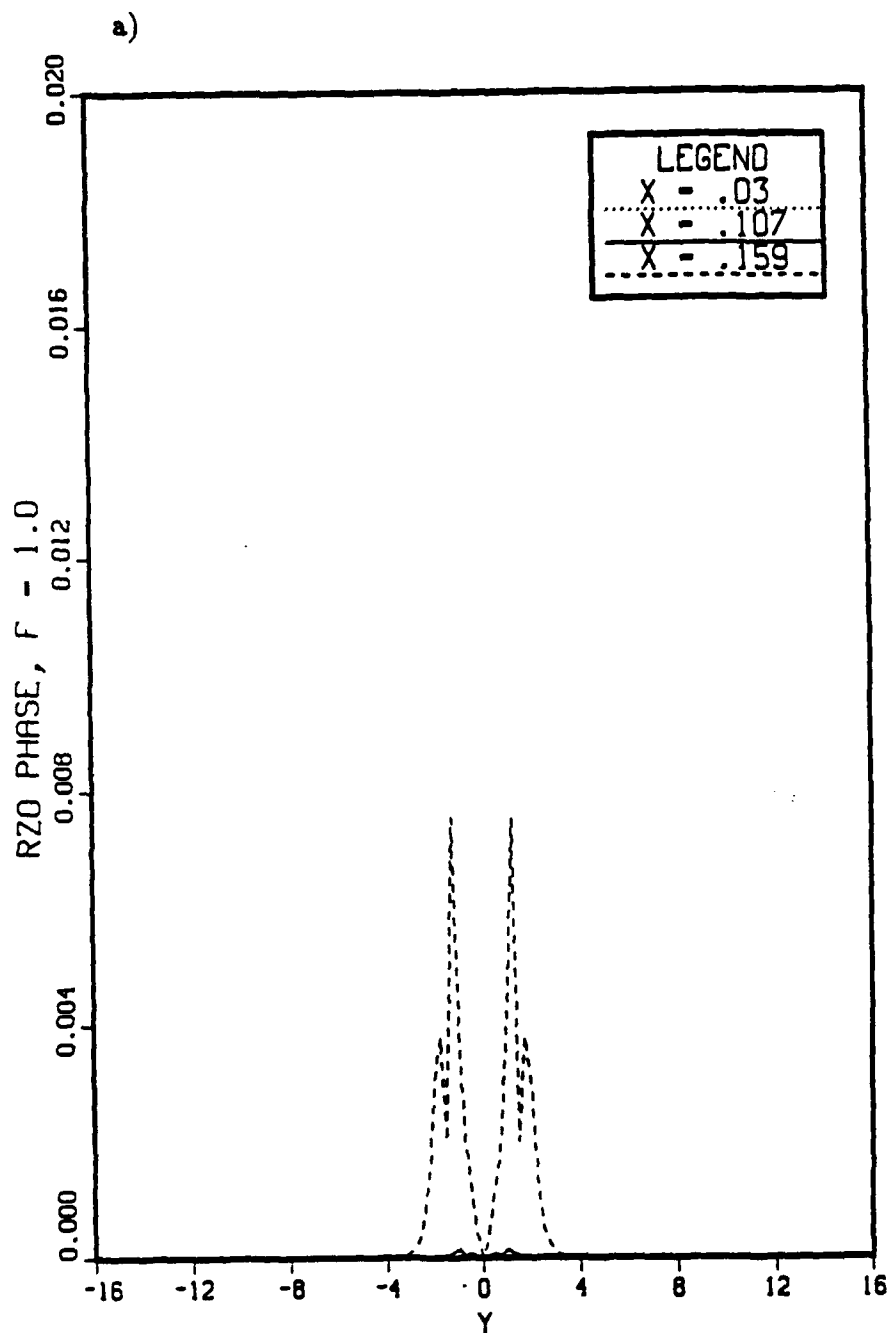


Figure 6.51 Vorticity amplitude distributions for  $F = 1$ . Case-7:  $A_2 = 0$ ,  $A_3 = .001$ ,  $\beta = .51$ , and  $\gamma = .5$ . a) spanwise vorticity,  $\Omega_z^0$ ; b) spanwise vorticity,  $\Omega_z^1$ ; c) streamwise vorticity,  $\Omega_x^1$ .

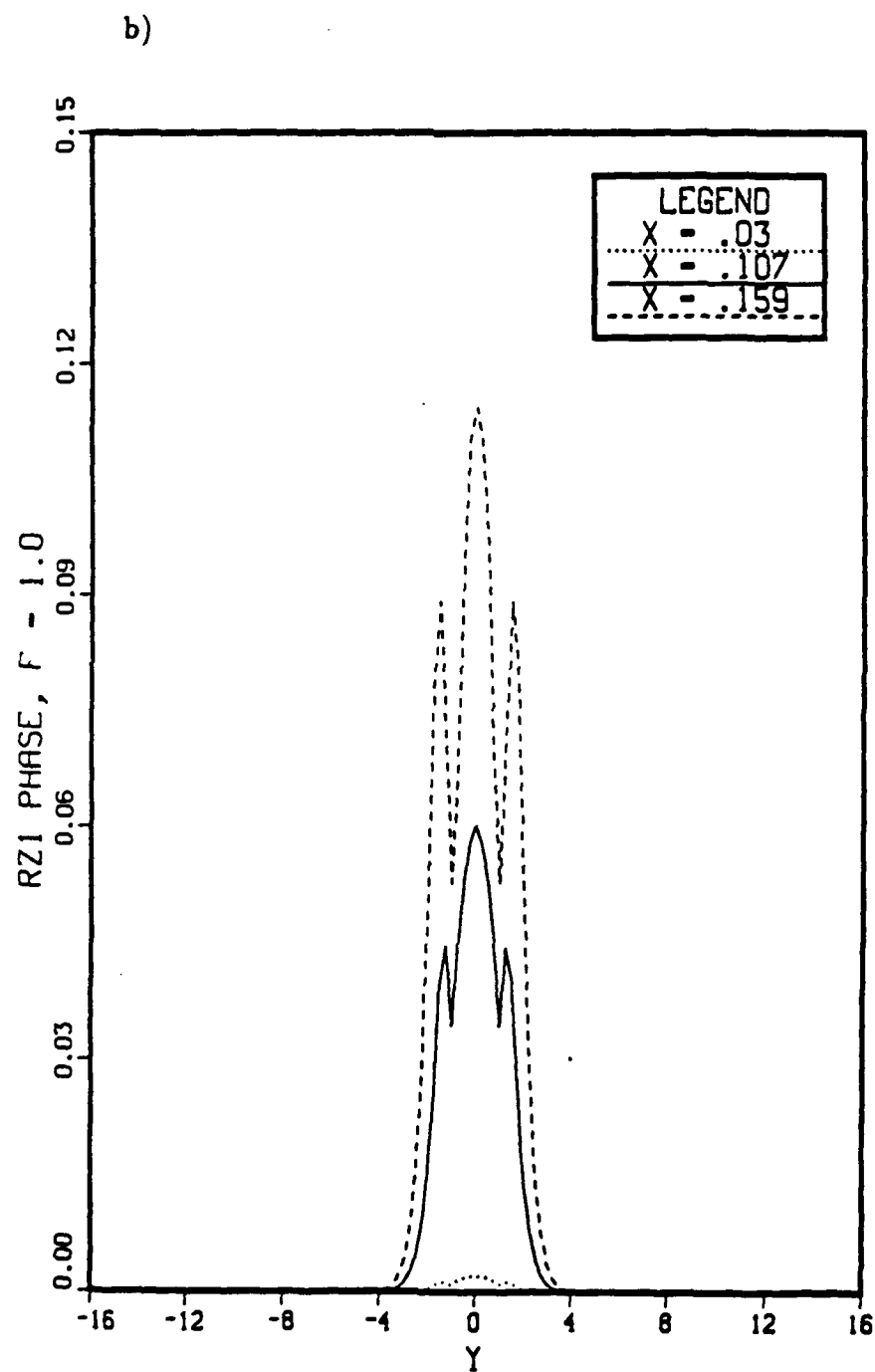


Figure 6.51 Continued.

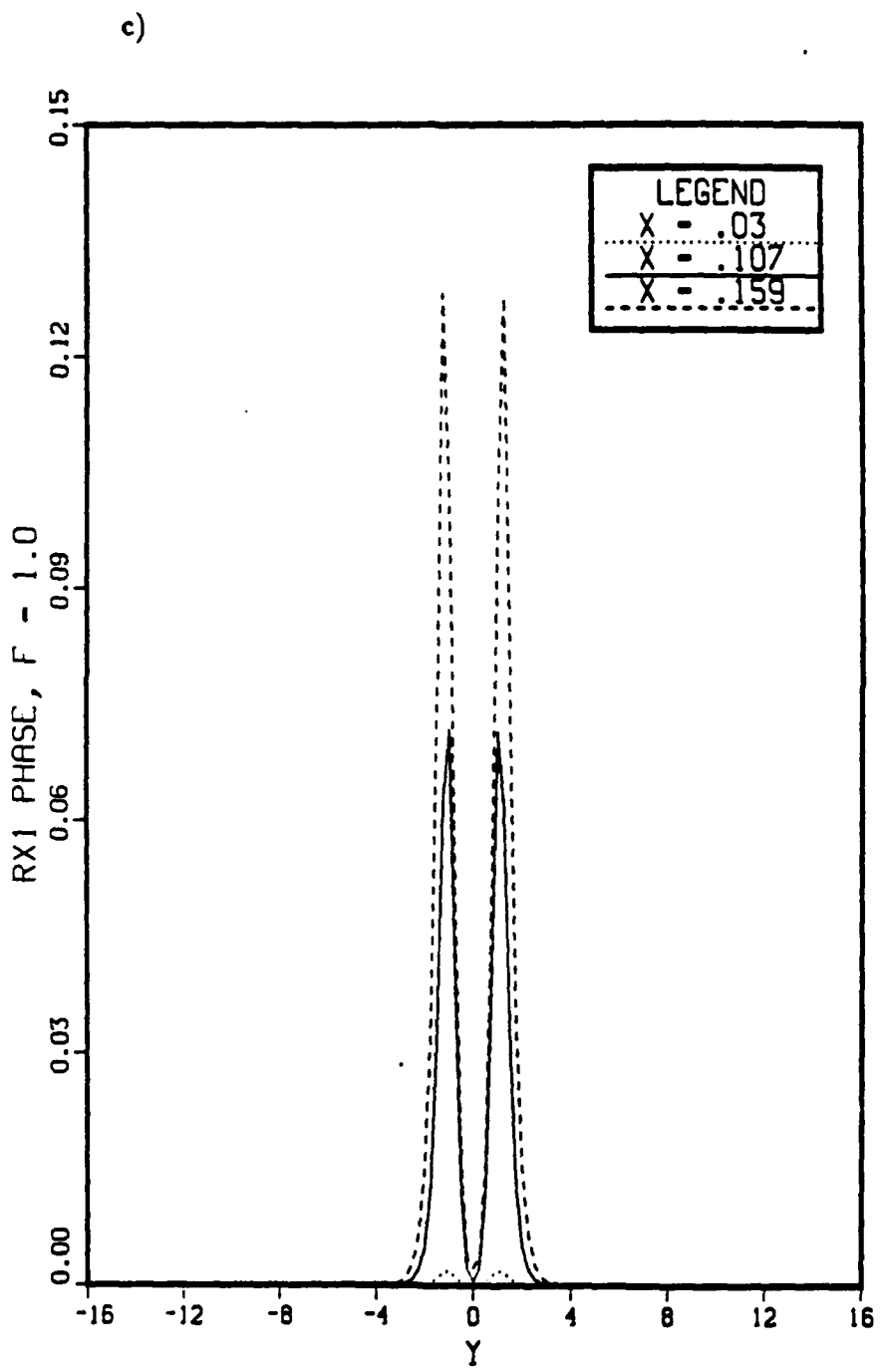


Figure 6.51 Continued.

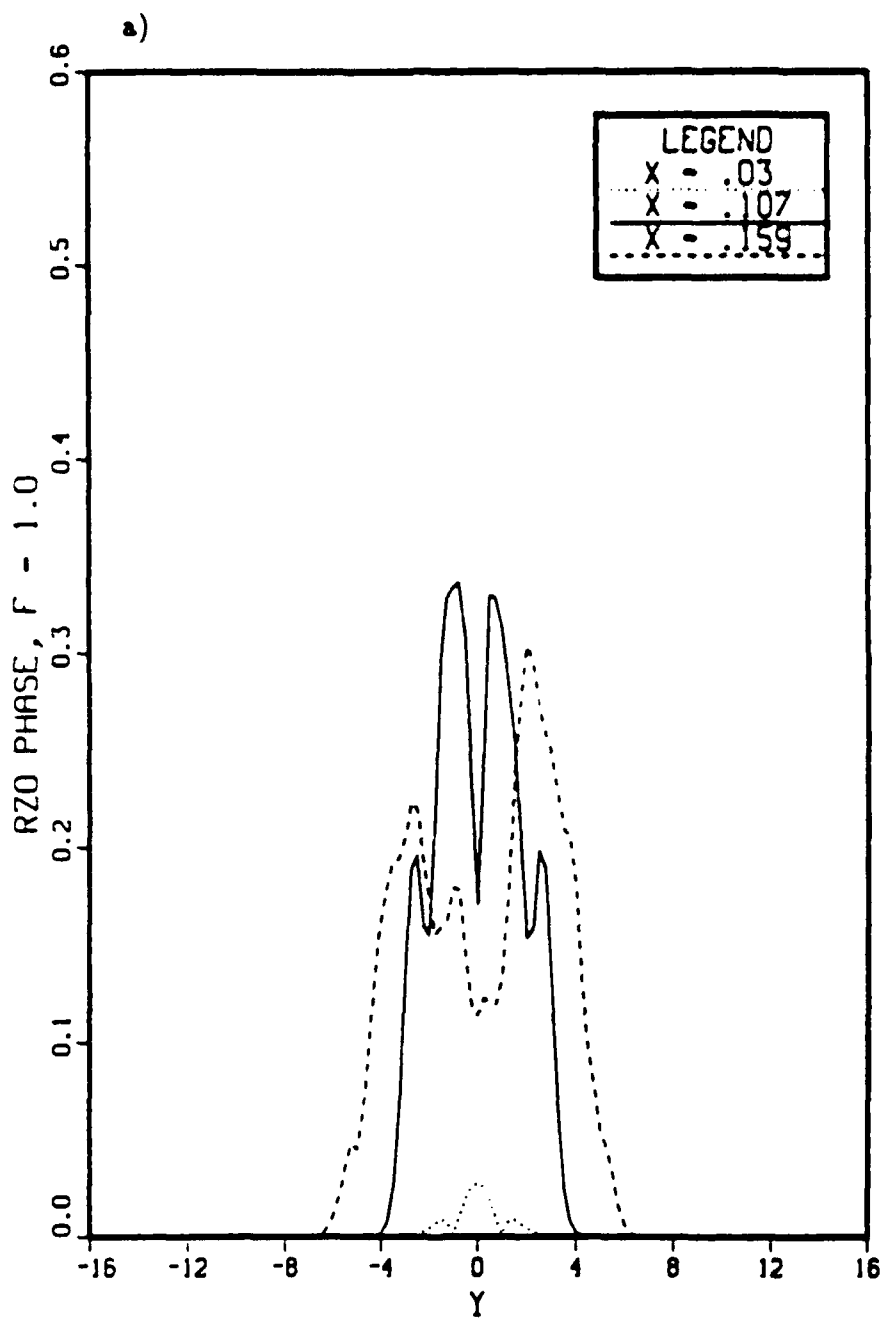


Figure 6.52 Vorticity amplitude distributions for  $F = 1$ . Case-8:  $A_2 = .01$ ,  $A_3 = .001$ ,  $\beta = .51$ , and  $\gamma = .5$ . a) spanwise vorticity,  $\Omega_z^0$ ; b) spanwise vorticity,  $\Omega_z^1$ ; c) streamwise vorticity,  $\Omega_x^1$ .

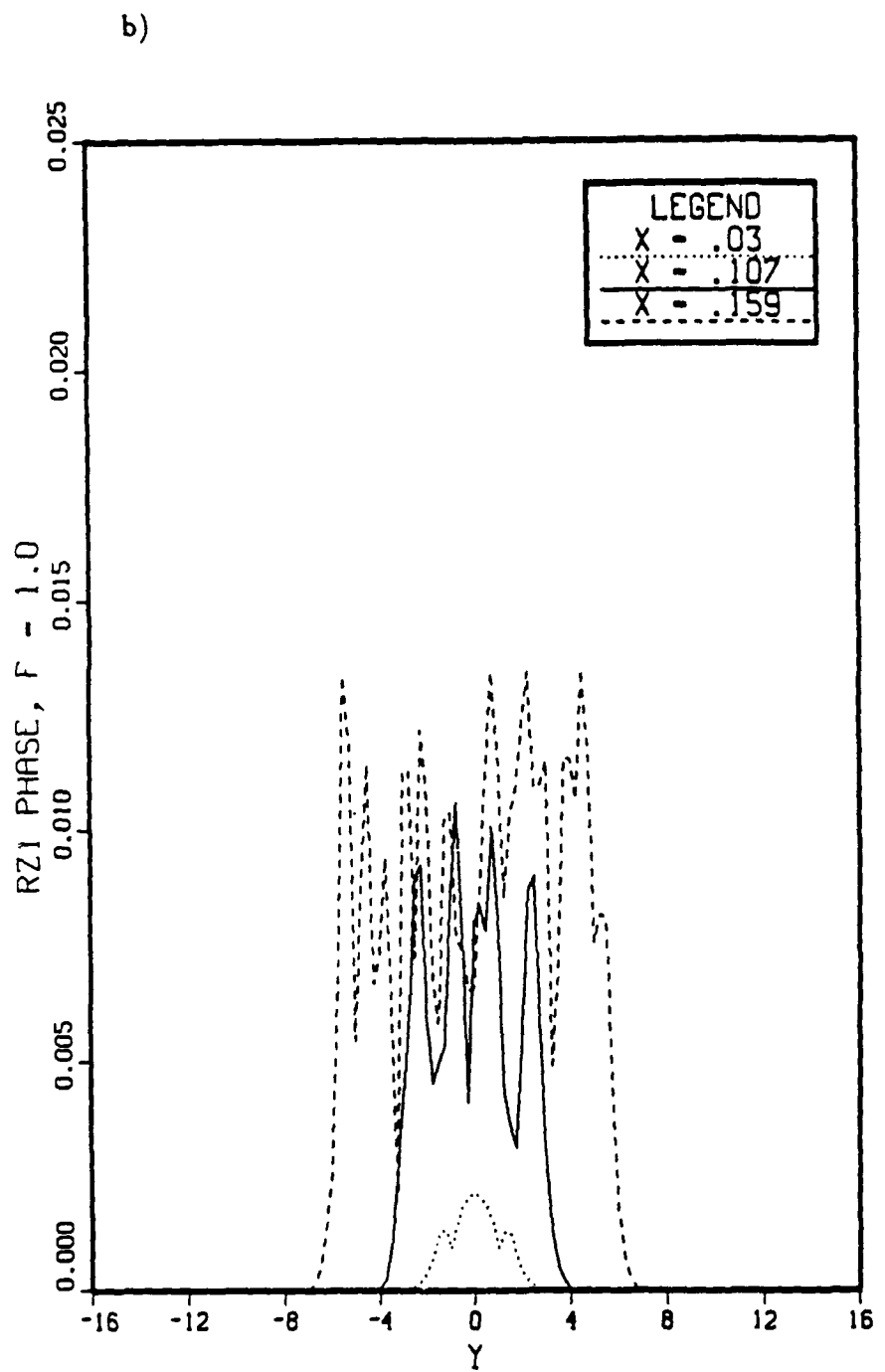


Figure 6.52 Continued.

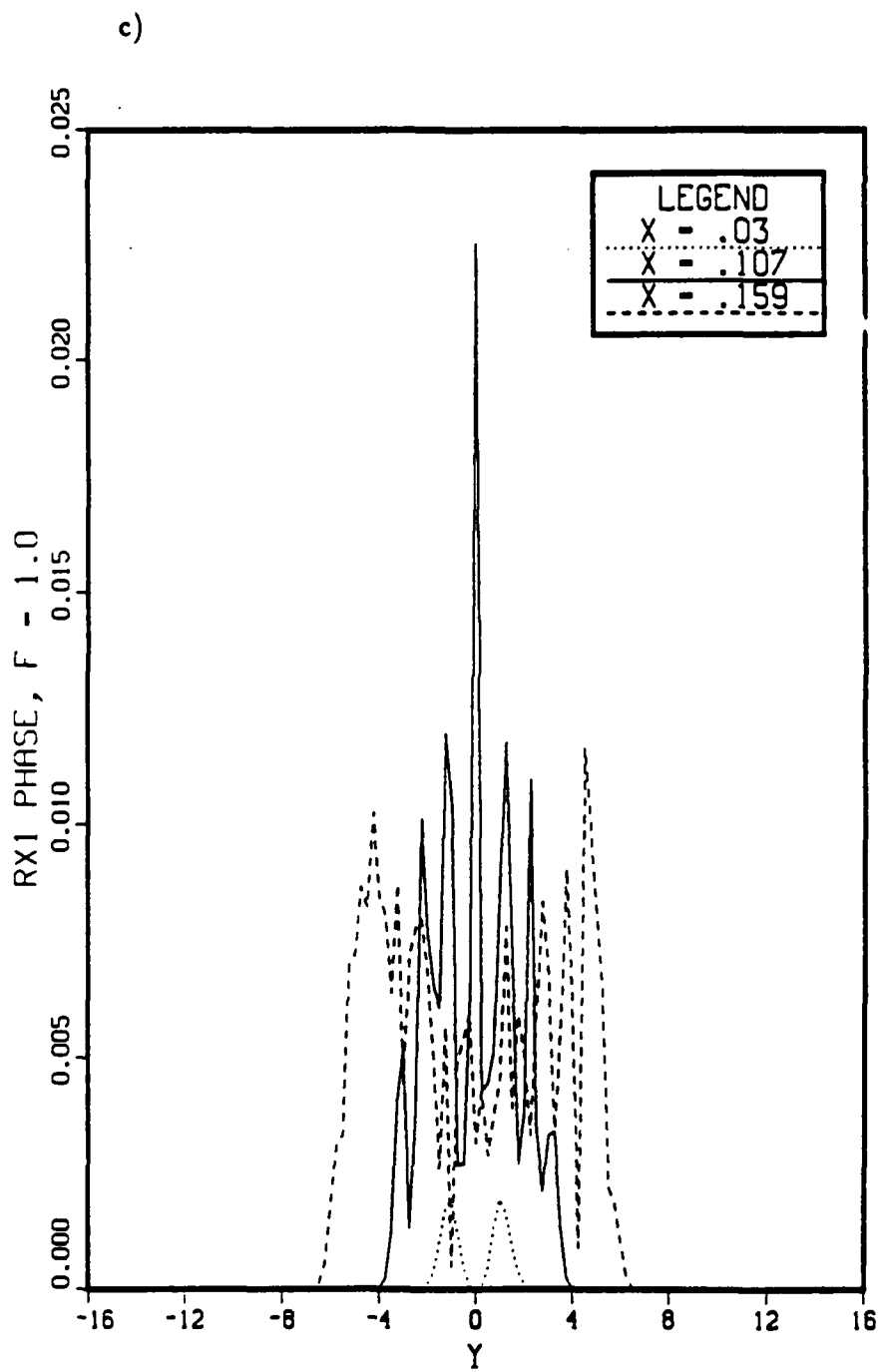


Figure 6.52 Continued.

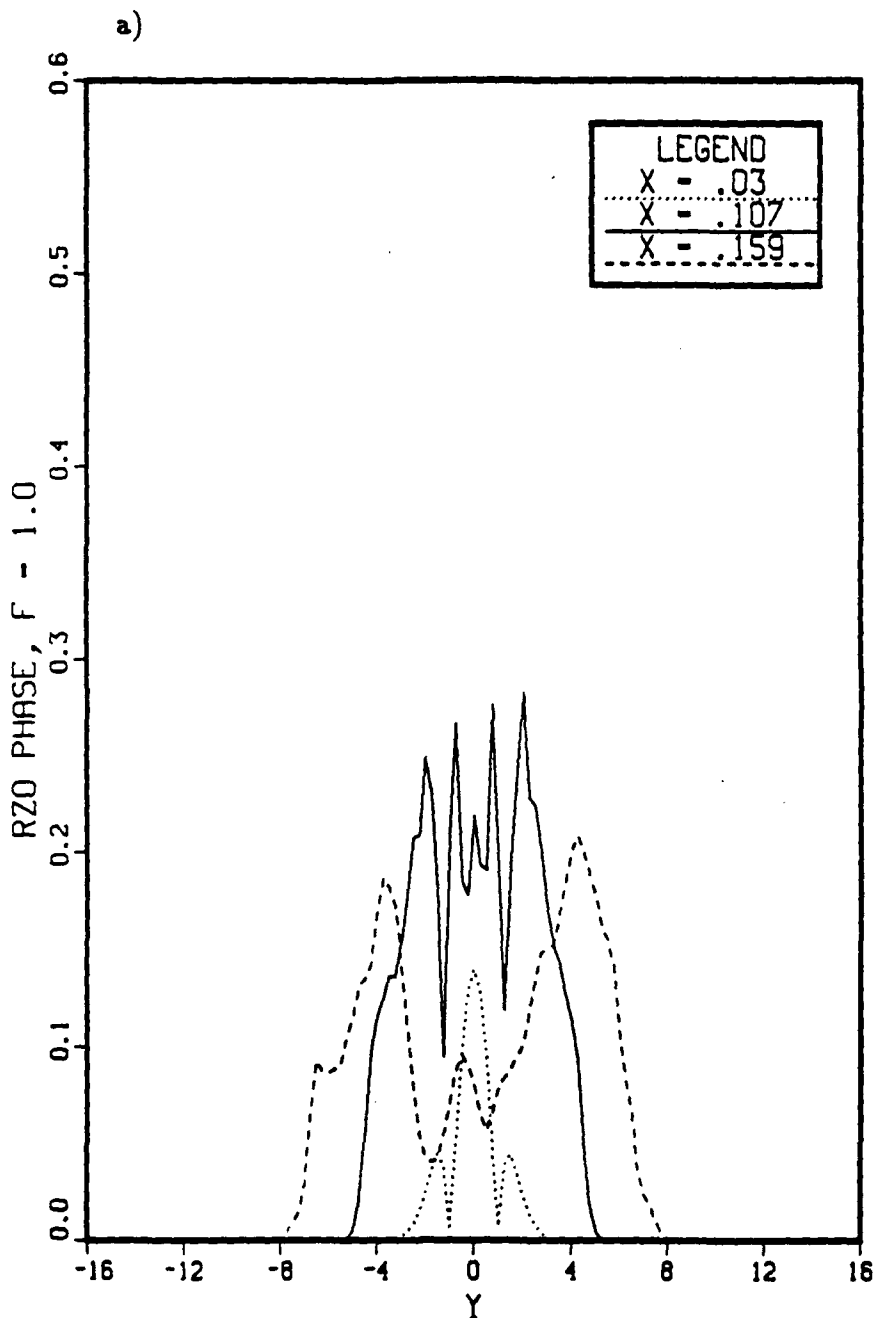


Figure 6.53 Vorticity amplitude distributions for  $F = 1$ . Case-9:  $A_2 = .05$ ,  $A_3 = .001$ ,  $\beta = .51$ , and  $\gamma = .5$ . a) spanwise vorticity,  $\Omega_z^0$ ; b) spanwise vorticity,  $\Omega_z^1$ ; c) streamwise vorticity,  $\Omega_x^1$ .

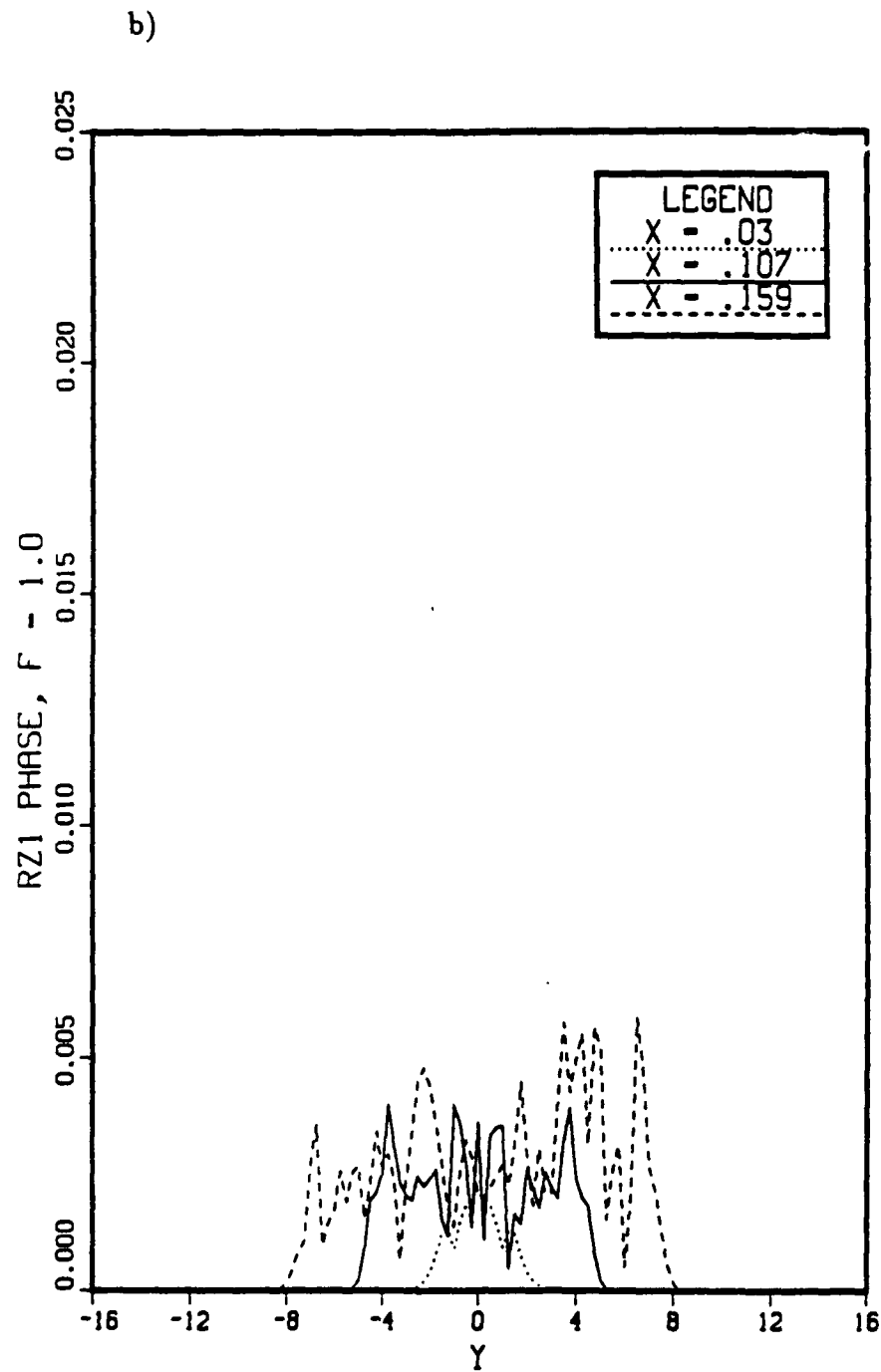


Figure 6.53 Continued.

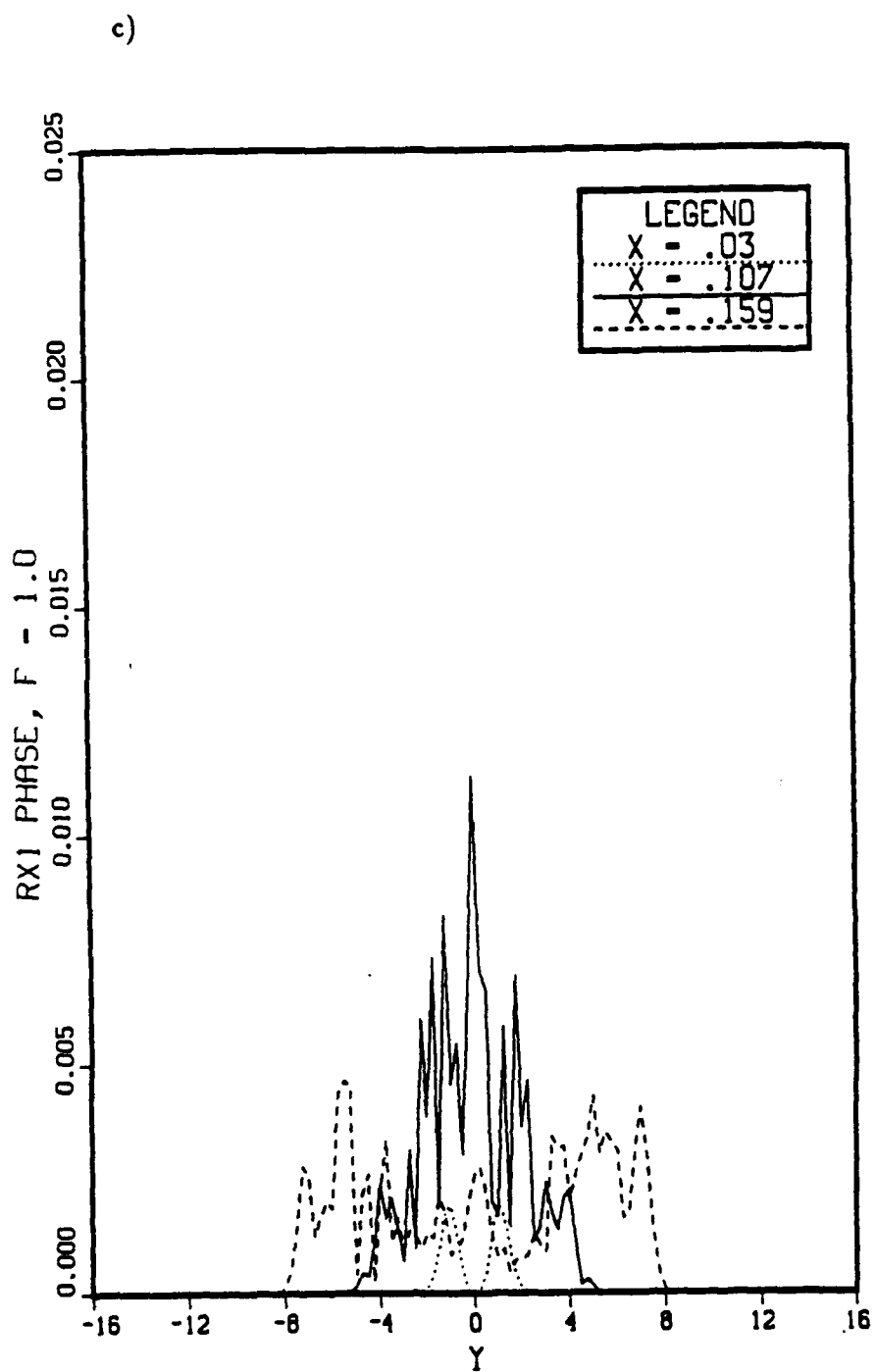


Figure 6.53 Continued.

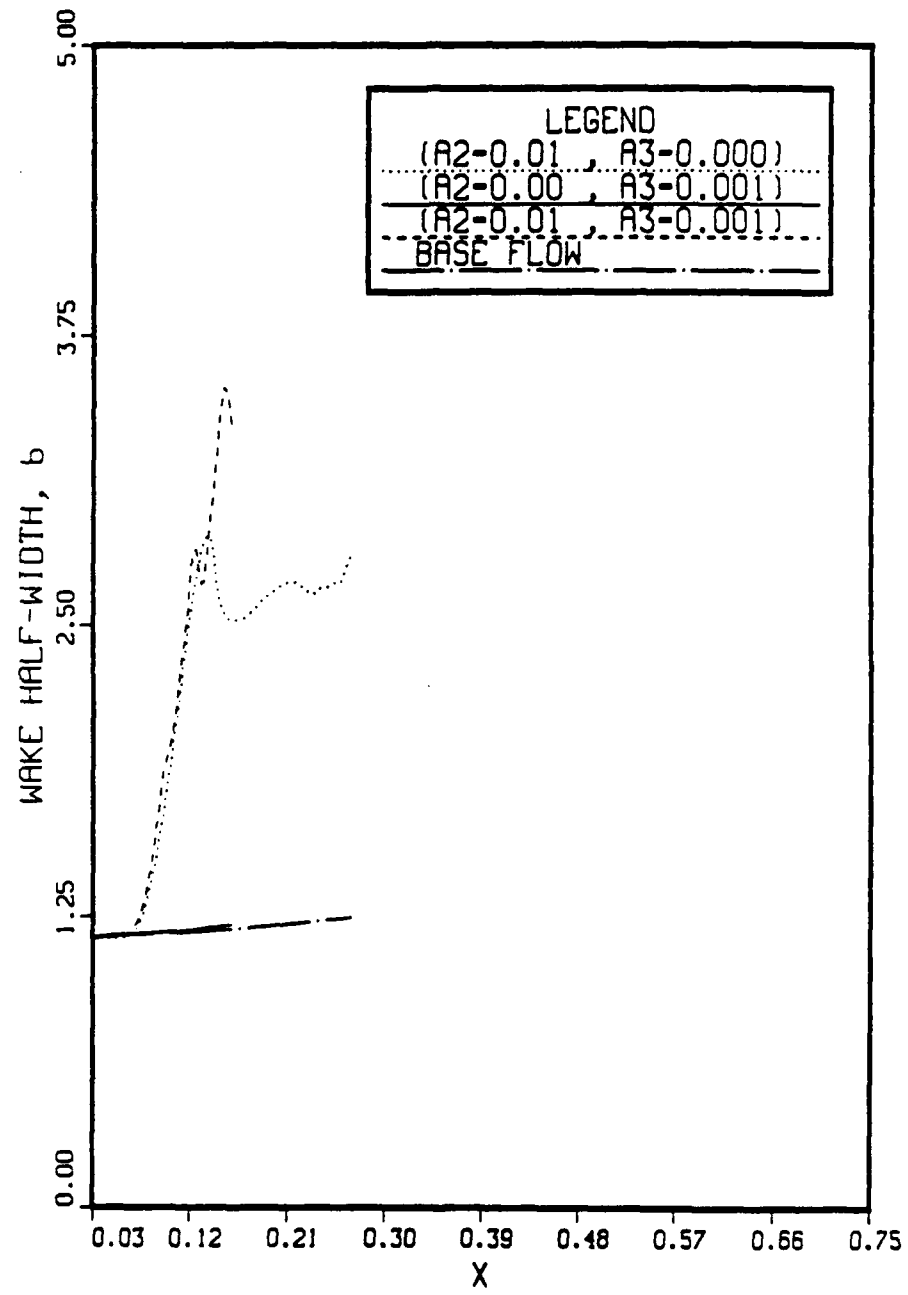


Figure 6.54 Streamwise variation of the wake half-width  $b$  for Case-4,  $A_2 = 0.01$ ,  $A_3 = 0.00$ ; Case-7,  $A_2 = 0.00$ ,  $A_3 = 0.001$ ; and Case-8,  $A_2 = 0.01$ ,  $A_3 = 0.001$ .

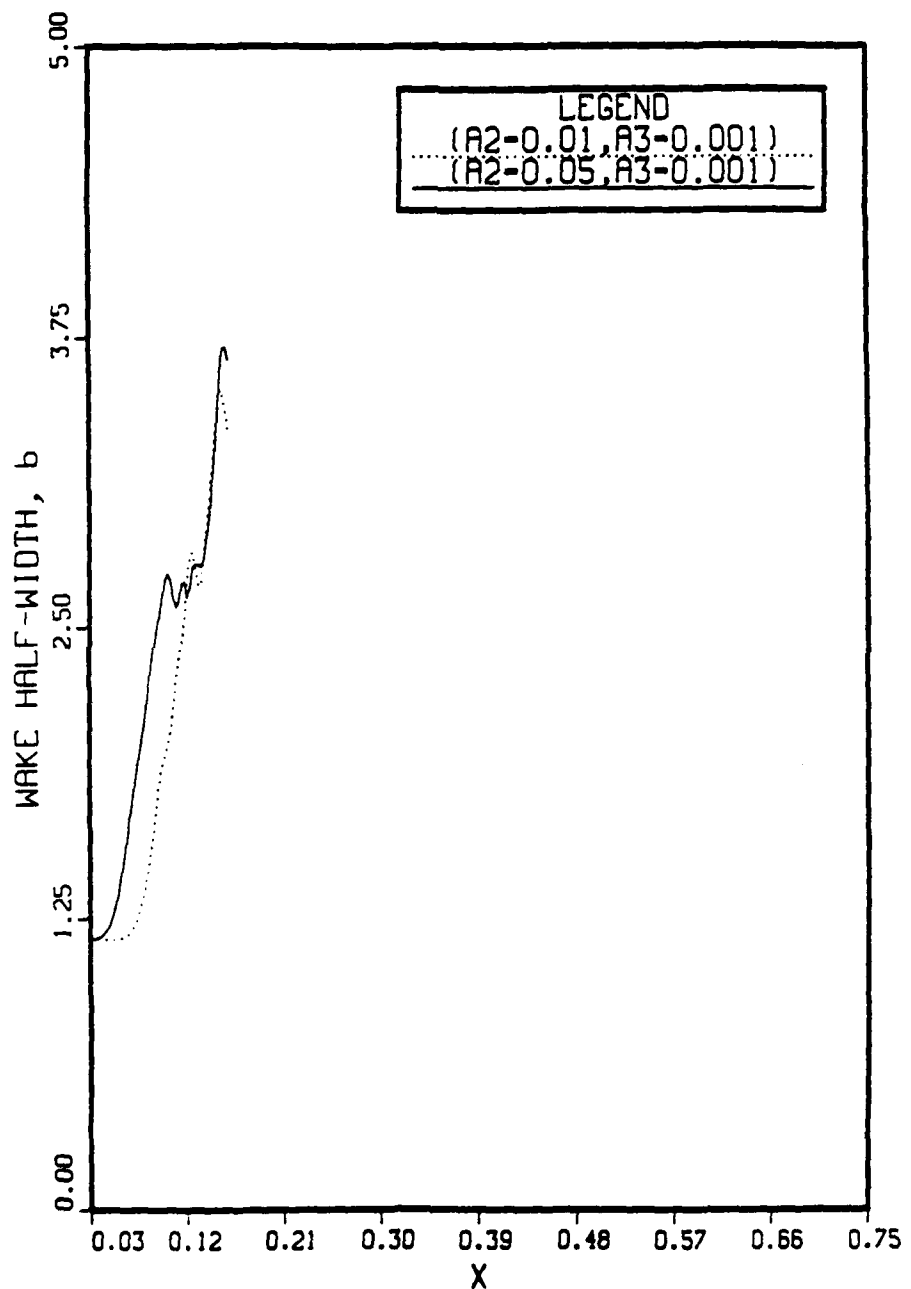


Figure 6.55 Streamwise variation of the wake half-width  $b$  for Case-8,  $A_2 = 0.01$ ,  $A_3 = 0.001$ ; and Case-9,  $A_2 = 0.05$ ,  $A_3 = 0.001$ .

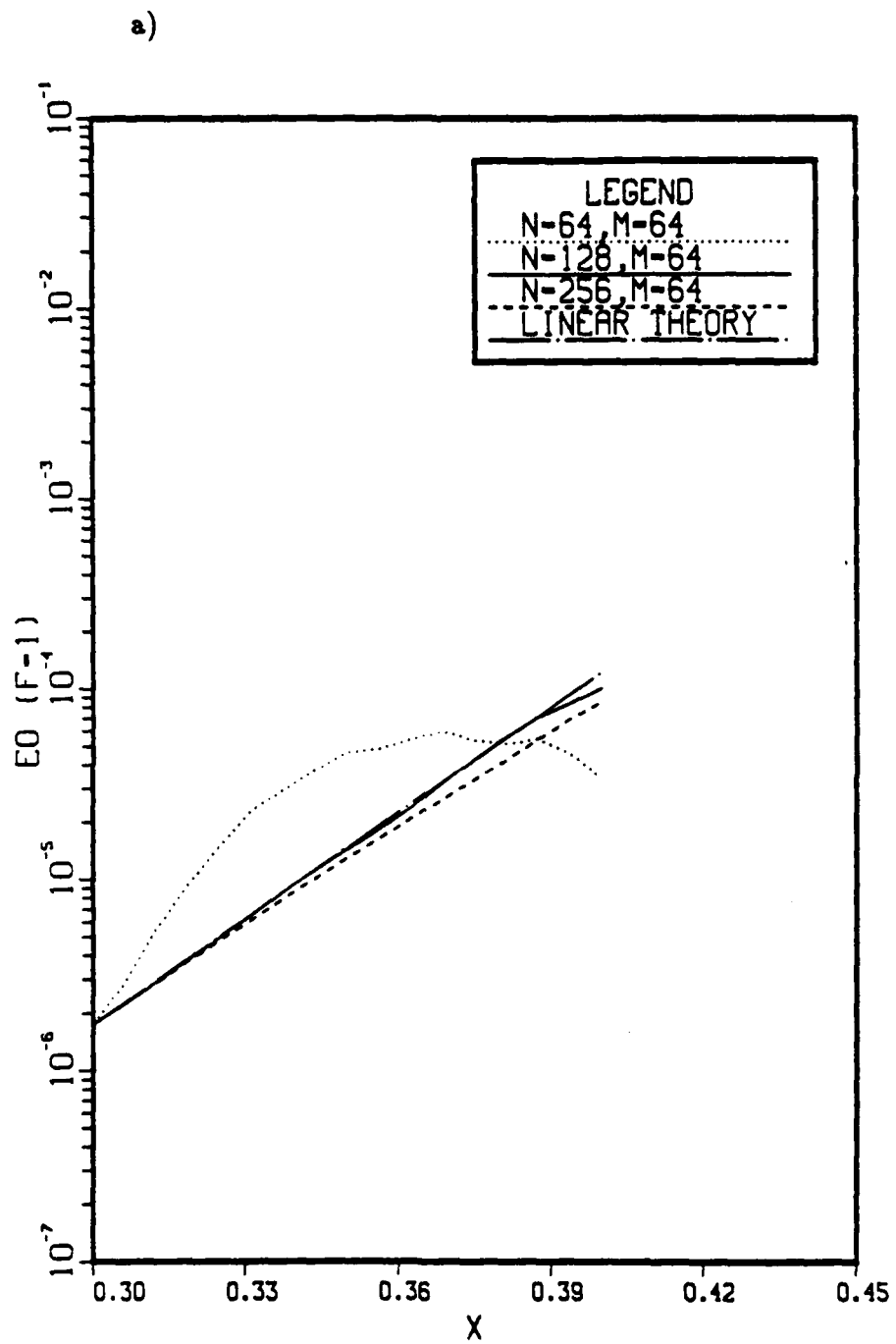


Figure B.1 Influence of the grid increment on the amplification of the kinetic energy  $\dot{E}^0(x, F = 1)$  for Case-1. a)  $M = 64$  with  $N = 64$ ,  $N = 128$ , and  $N = 256$ ; b)  $N = 128$  with  $M = 32$ ,  $M = 64$ , and  $M = 128$ .

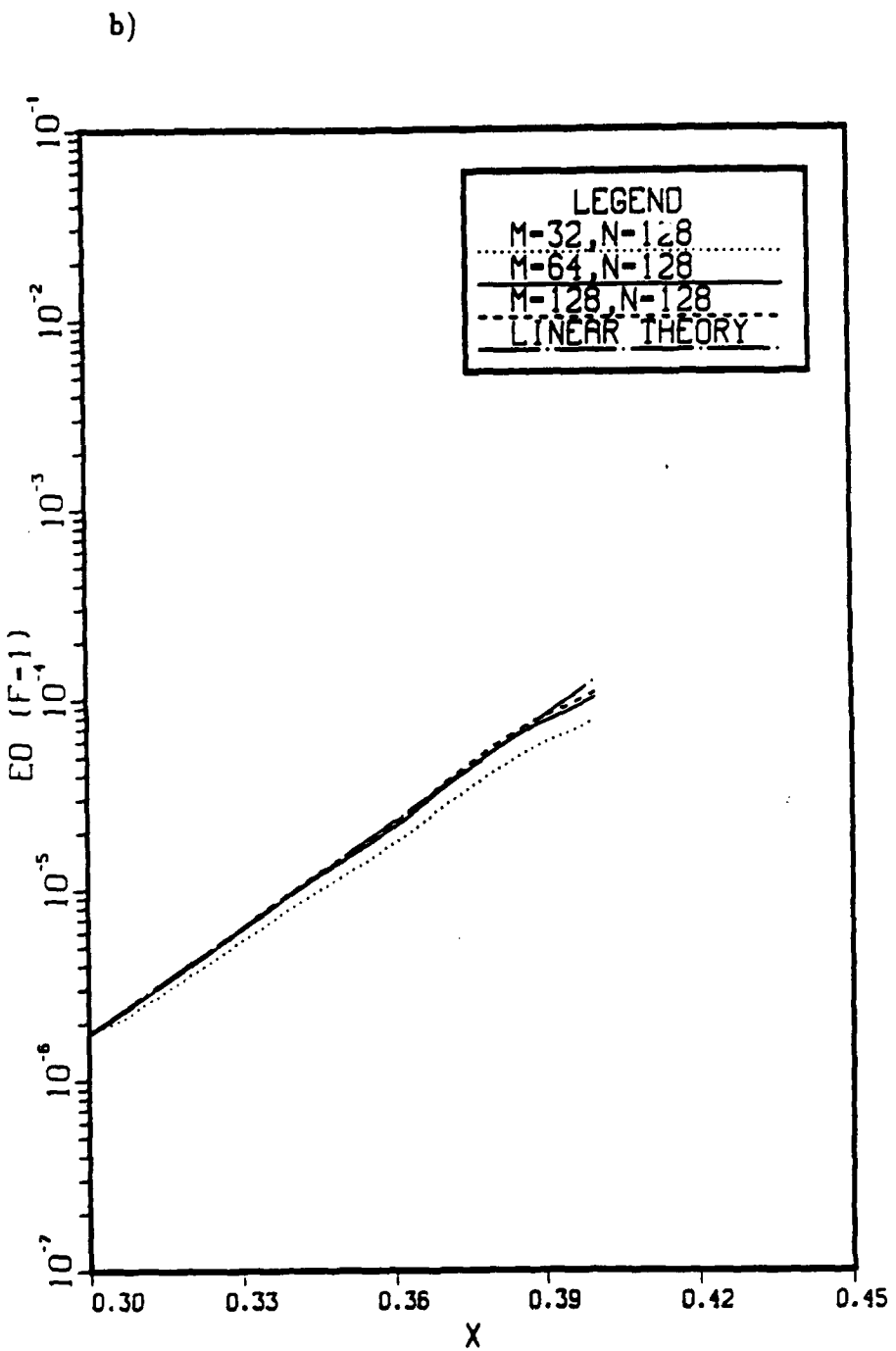


Figure B.1 Continued.

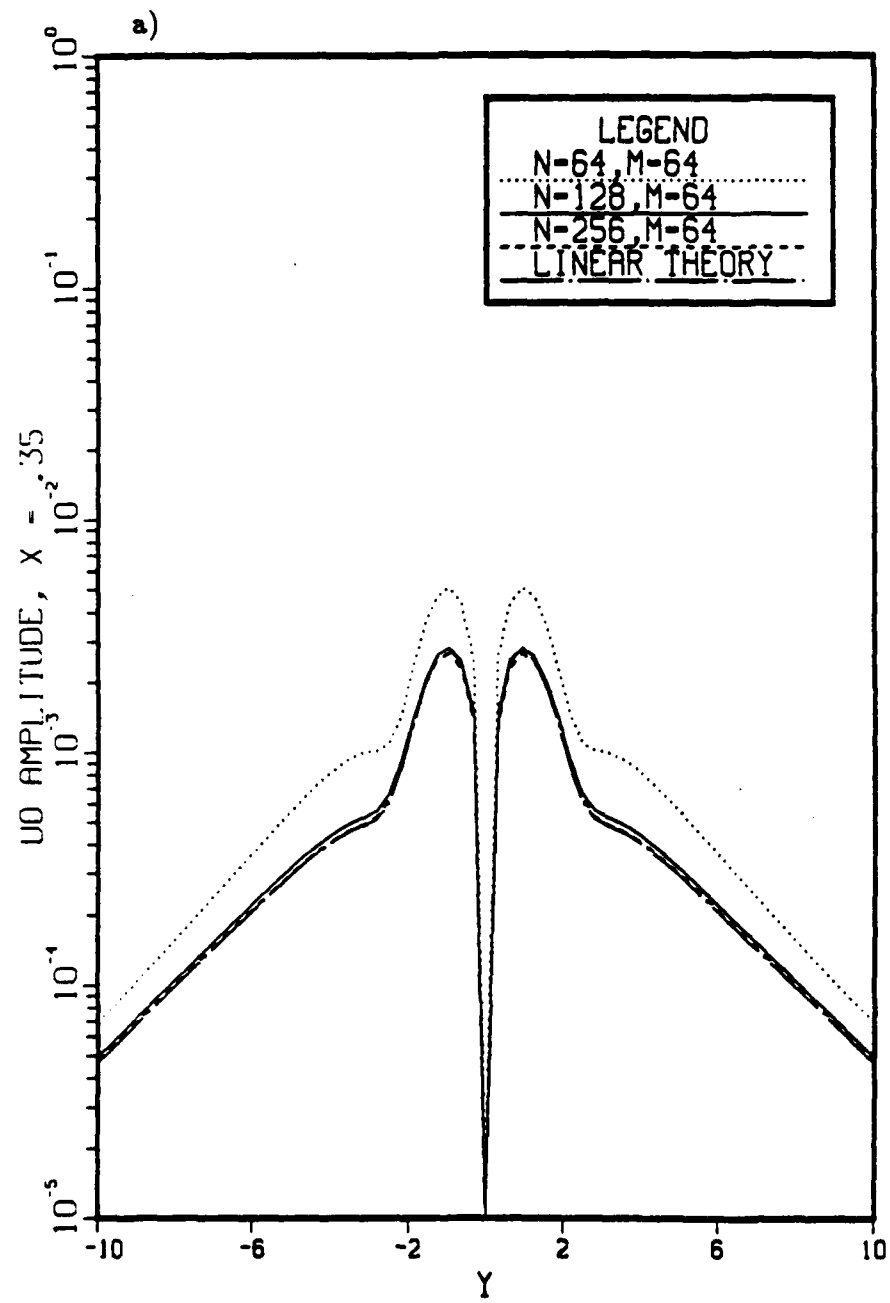


Figure B.2 Influence of the grid increment on the amplitude distributions of the fundamental disturbance ( $F = 1$ ) of the streamwise velocity.  
 a)  $M = 64$  with  $N = 64$ ,  $N = 128$ , and  $N = 256$ ; b)  $N = 128$  with  $M = 32$ ,  $M = 64$ , and  $M = 128$ .

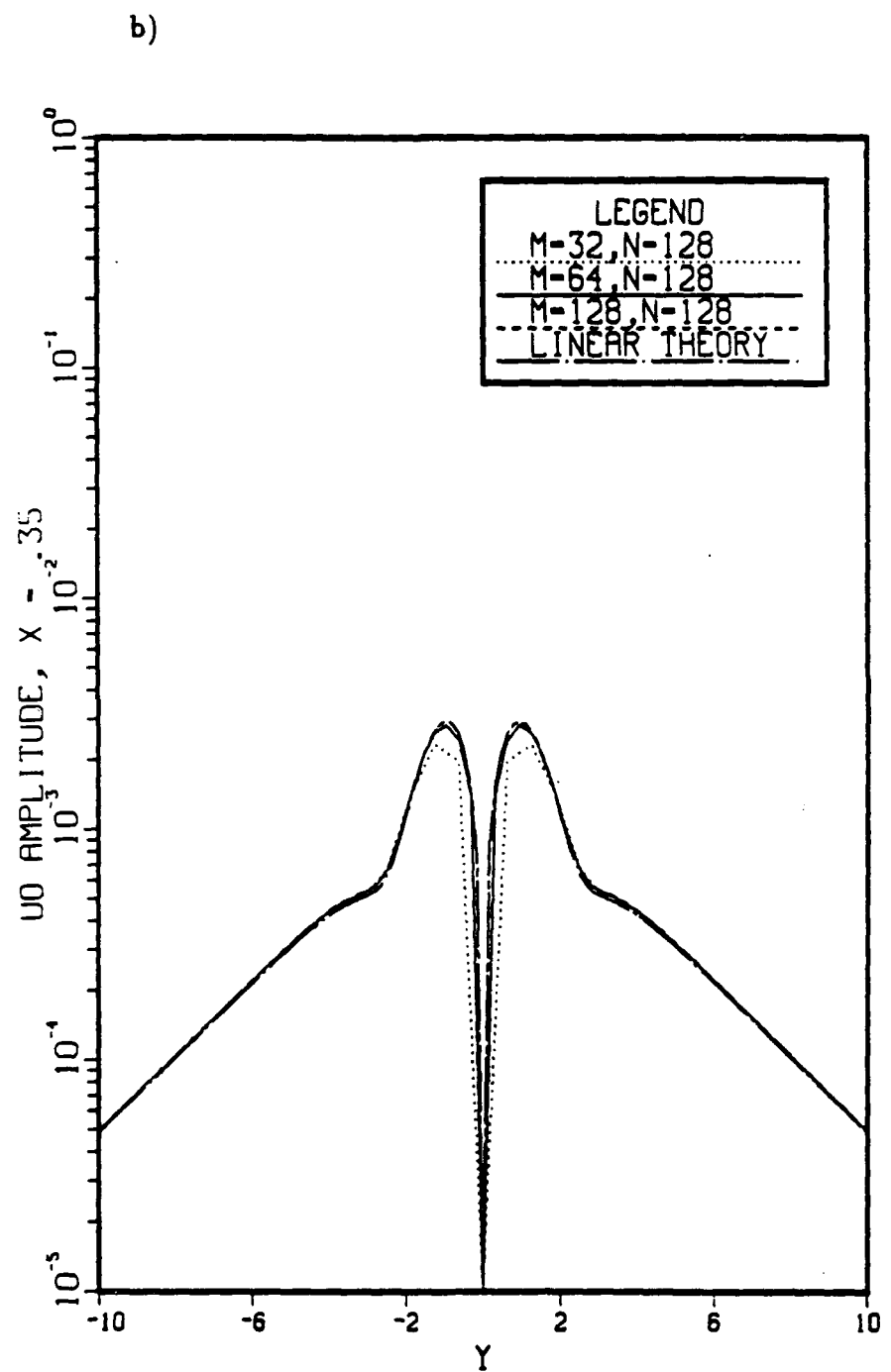


Figure B.2 Continued.

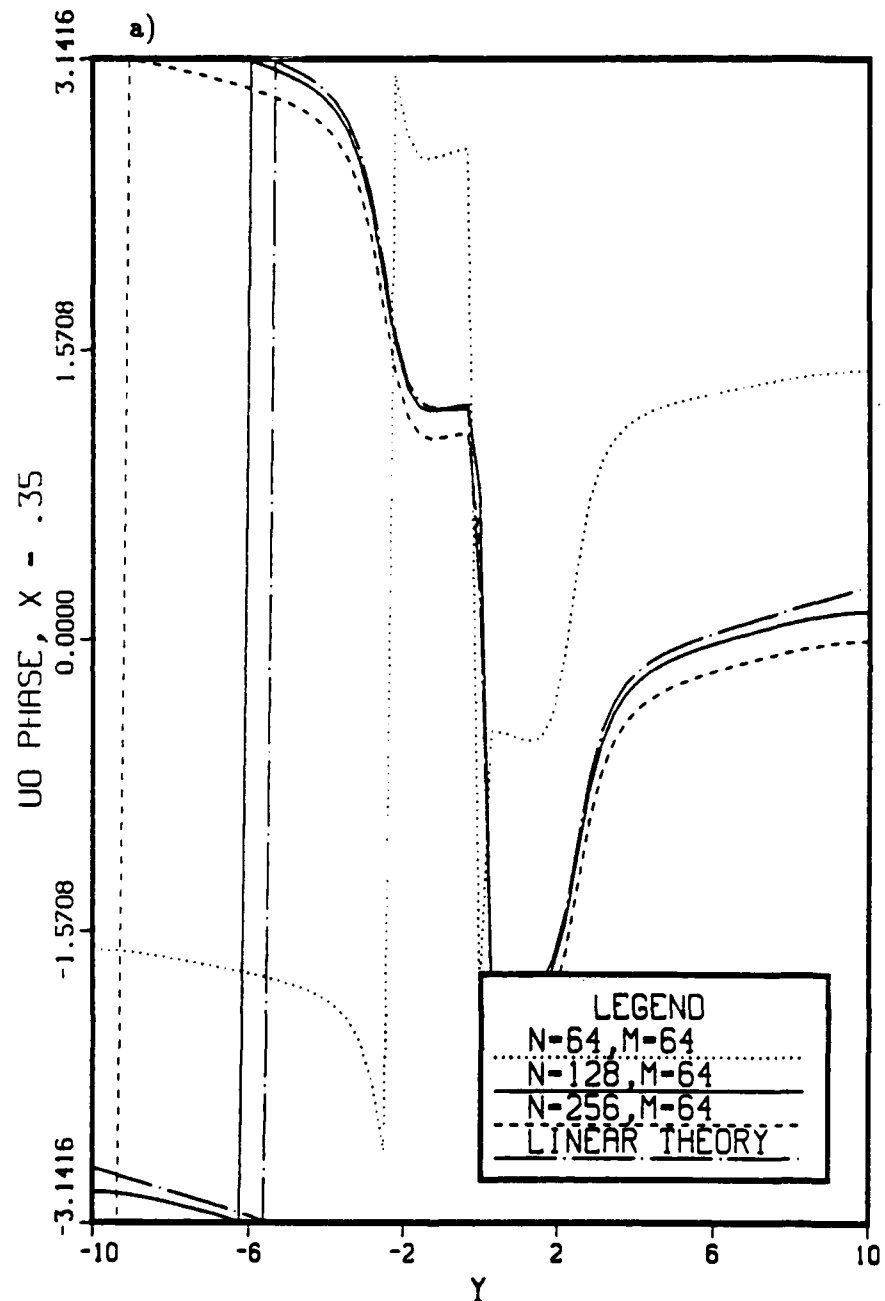


Figure B.3 Influence of the grid increment on the phase distributions of the fundamental disturbance ( $F = 1$ ) of the streamwise velocity. a)  $M = 64$  with  $N = 64$ ,  $N = 128$ , and  $N = 256$ ; b)  $N = 128$  with  $M = 32$ ,  $M = 64$ , and  $M = 128$ .

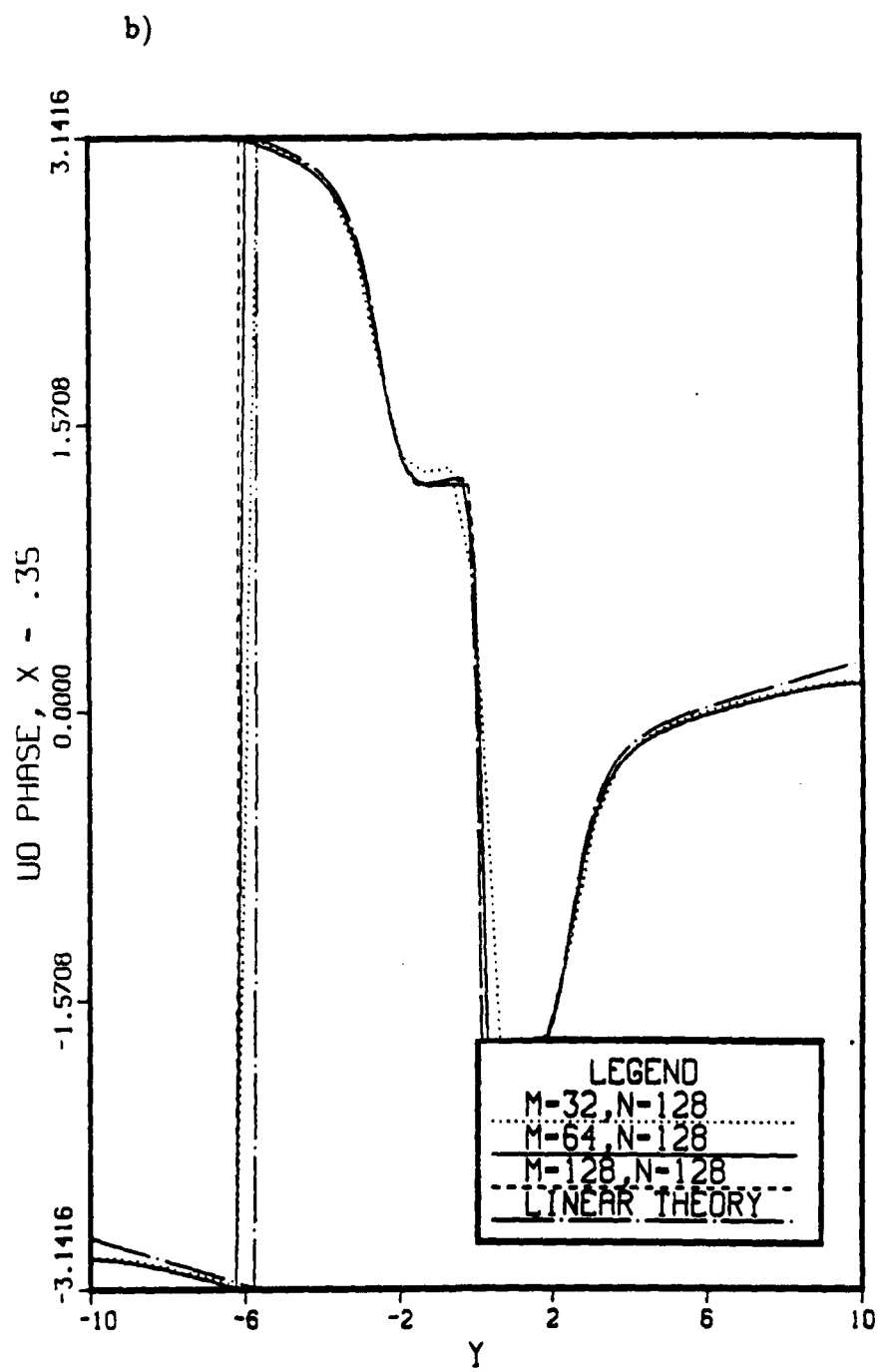


Figure B.3 Continued.

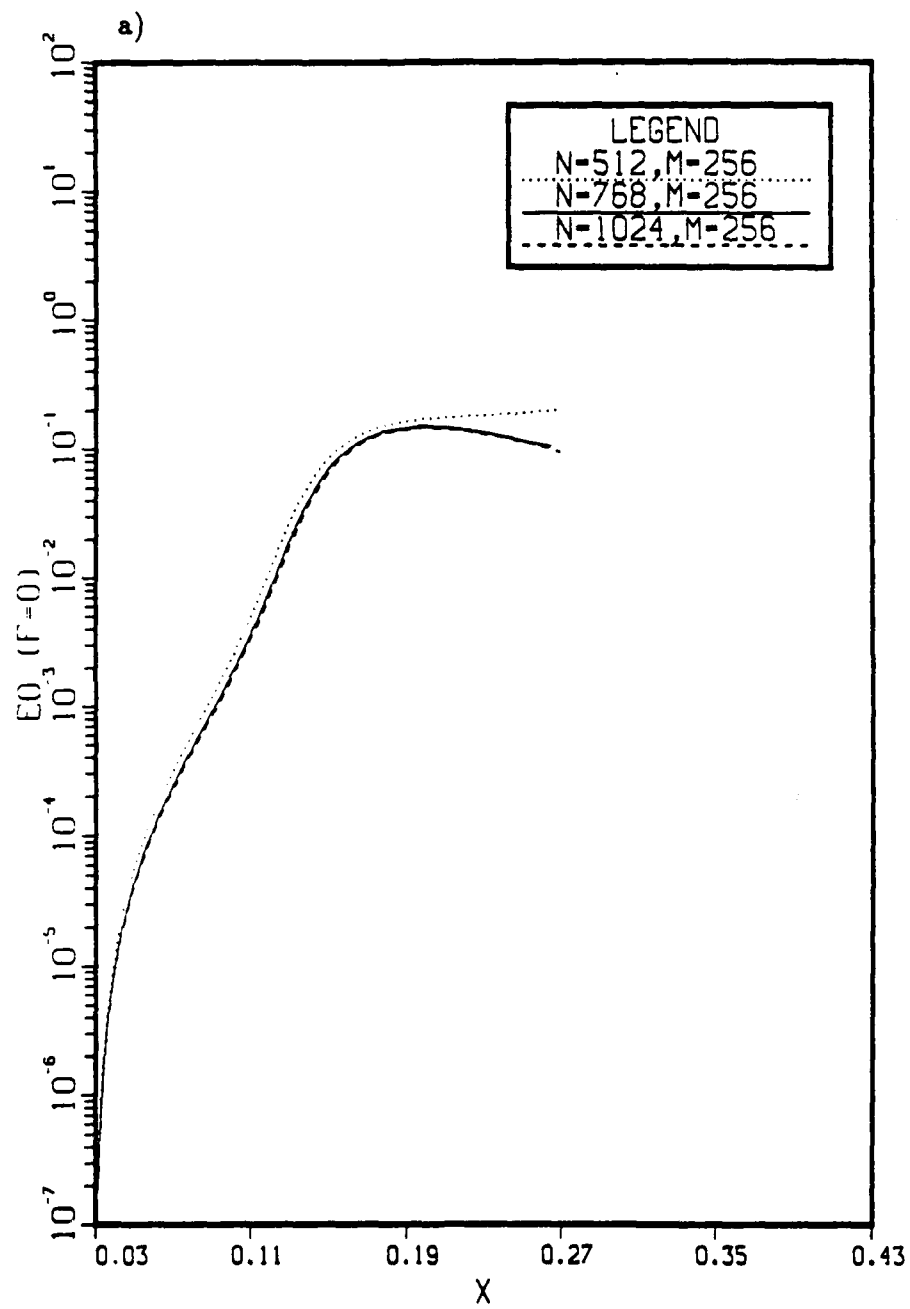


Figure B.4 Influence of the streamwise grid increment on the amplification of the kinetic energy  $\hat{E}^0(x, F)$ . Case-2:  $M = 256$  with  $N = 512$ ,  $N = 768$ , and  $N = 1024$ . a) the mean component,  $F = 0$ ; b) the fundamental component,  $F = 1$ ; c) the second harmonic,  $F = 2$ .

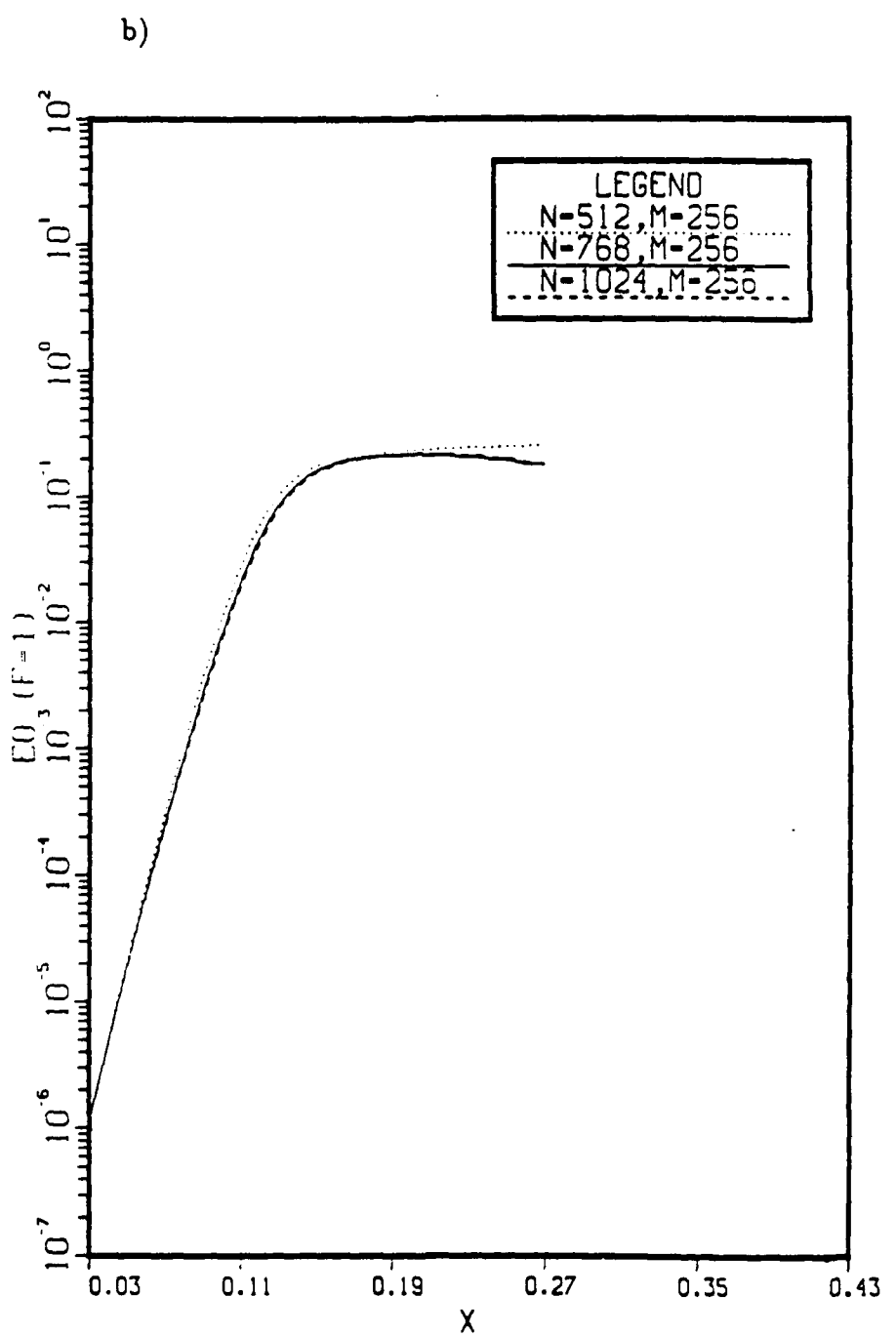


Figure B.4 Continued.

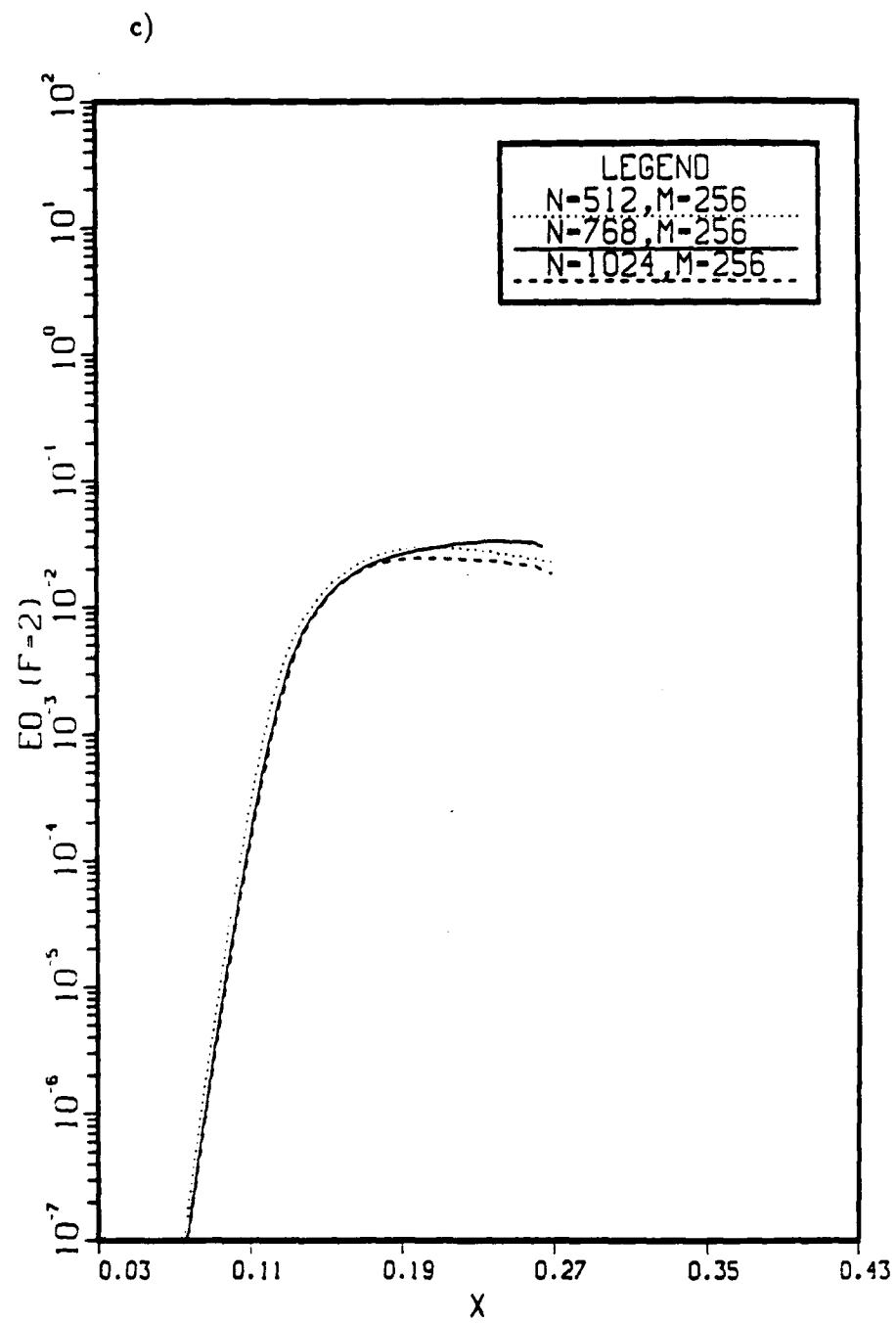


Figure B.4 Continued.

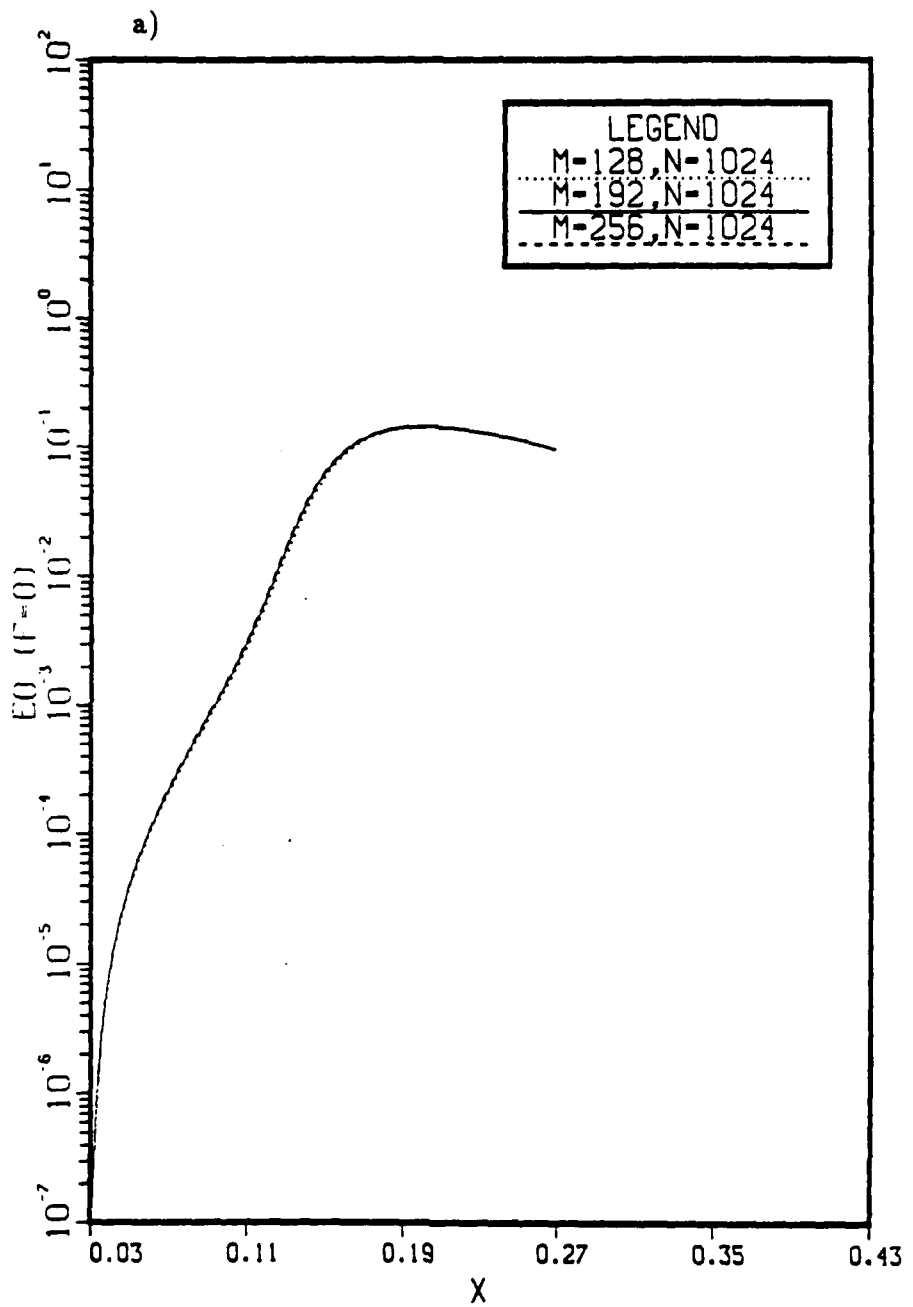


Figure B.5 Influence of the transvere grid increment on the amplification of the kinetic energy  $\hat{E}^0(x, F)$ . Case-2:  $N = 1024$  with  $M = 128$ ,  $M = 192$ , and  $M = 256$ . a) the mean component,  $F = 0$ ; b) the fundamental component,  $F = 1$ ; c) the second harmonic,  $F = 2$ .

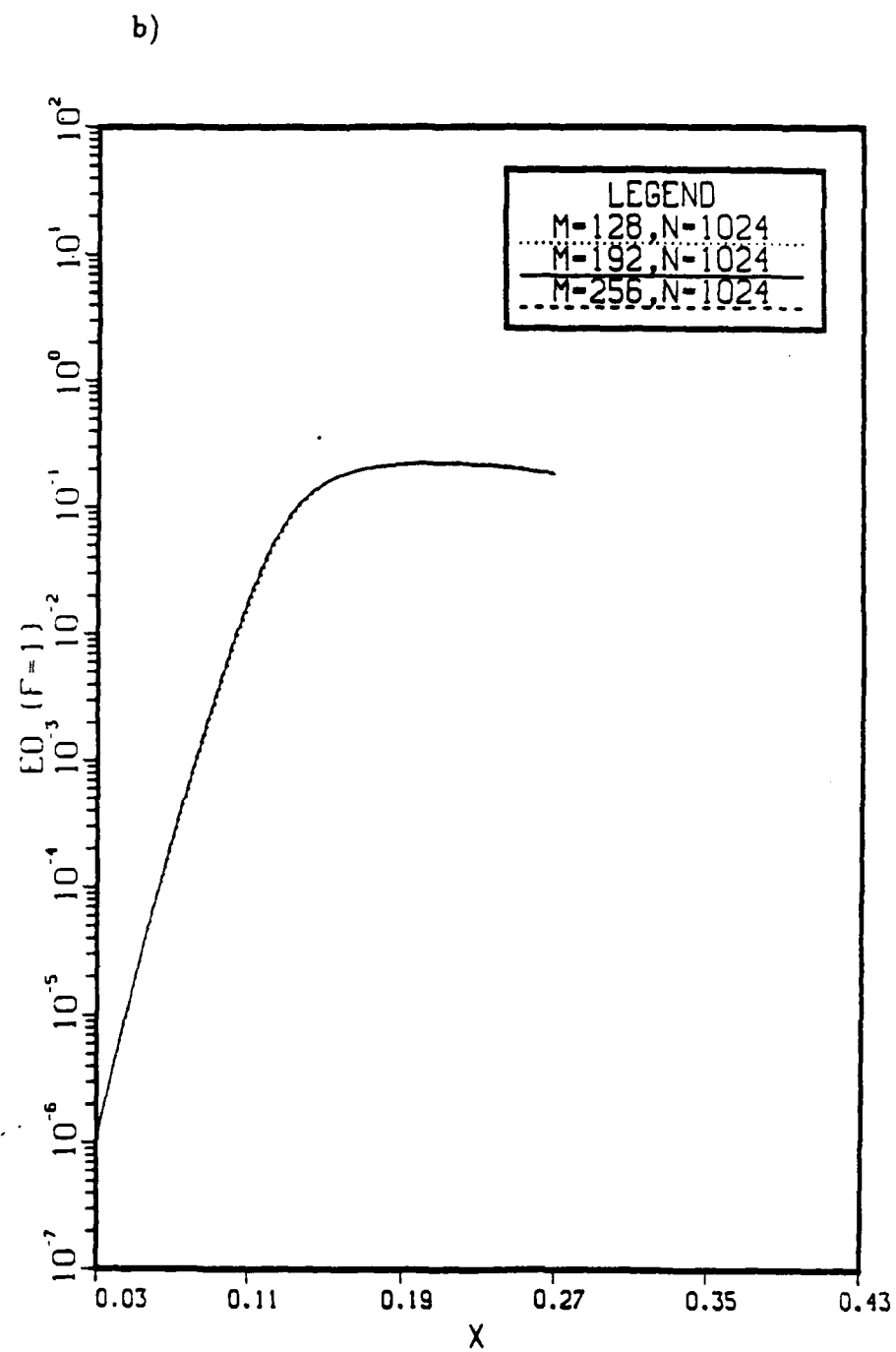


Figure B.5 Continued.

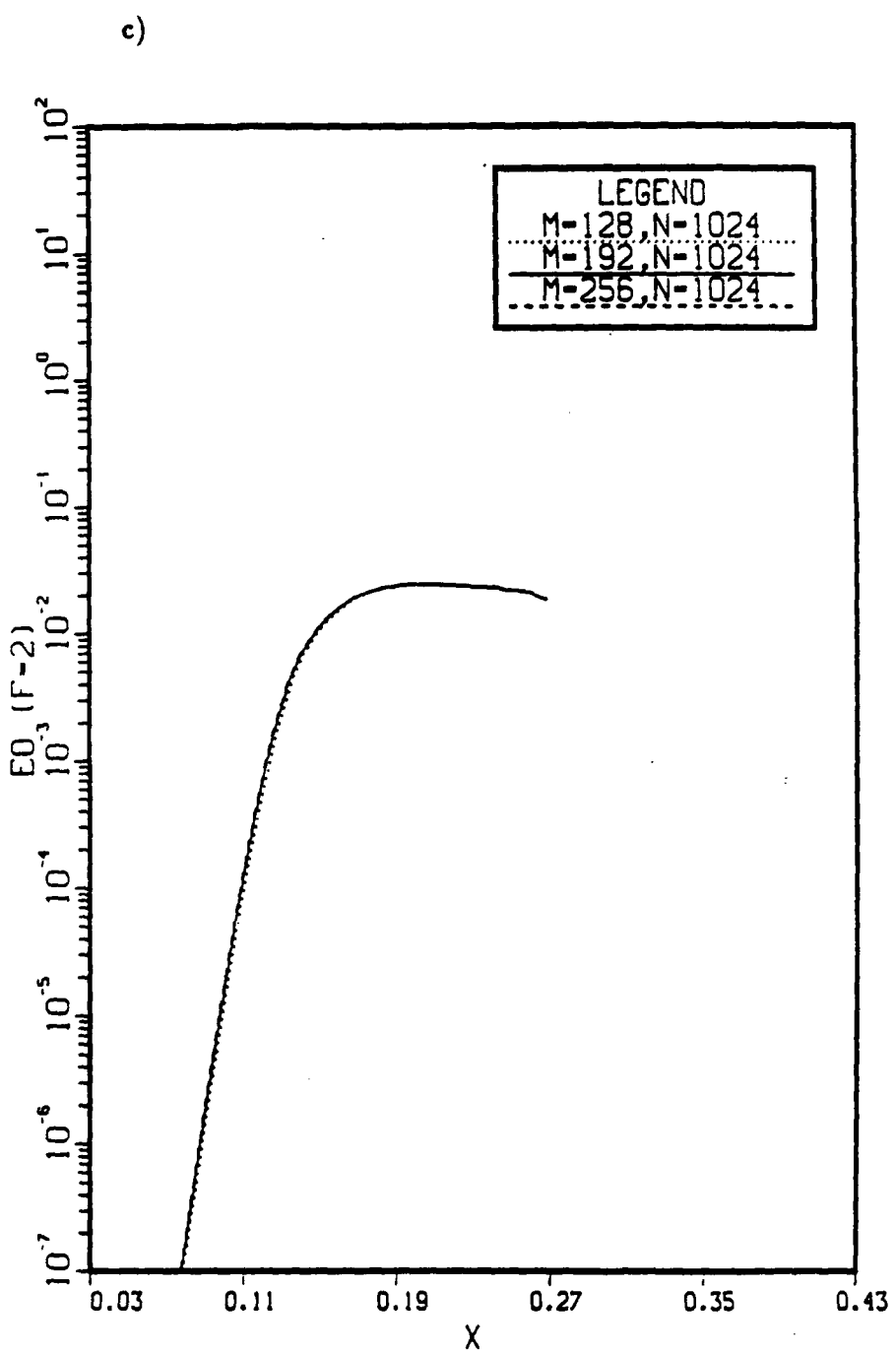


Figure B.5 Continued.

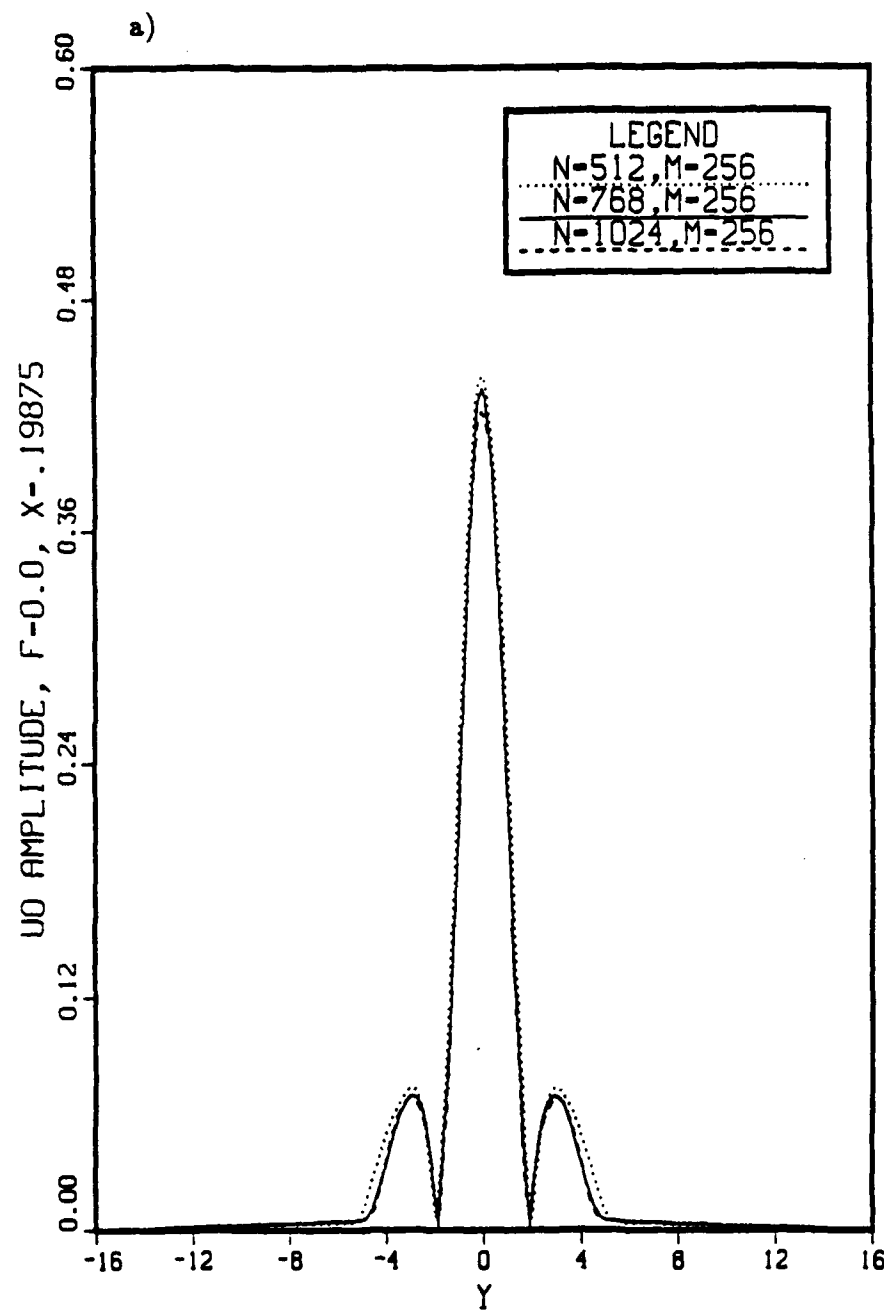


Figure B.6 Influence of the streamwise grid increment on the amplitude distributions of the streamwise velocity. Case-2:  $M = 256$  with  $N = 512$ ,  $N = 768$ , and  $N = 1024$ . a) the mean component,  $F = 0$ ; b) the fundamental component,  $F = 1$ ; c) the second harmonic,  $F = 2$ .

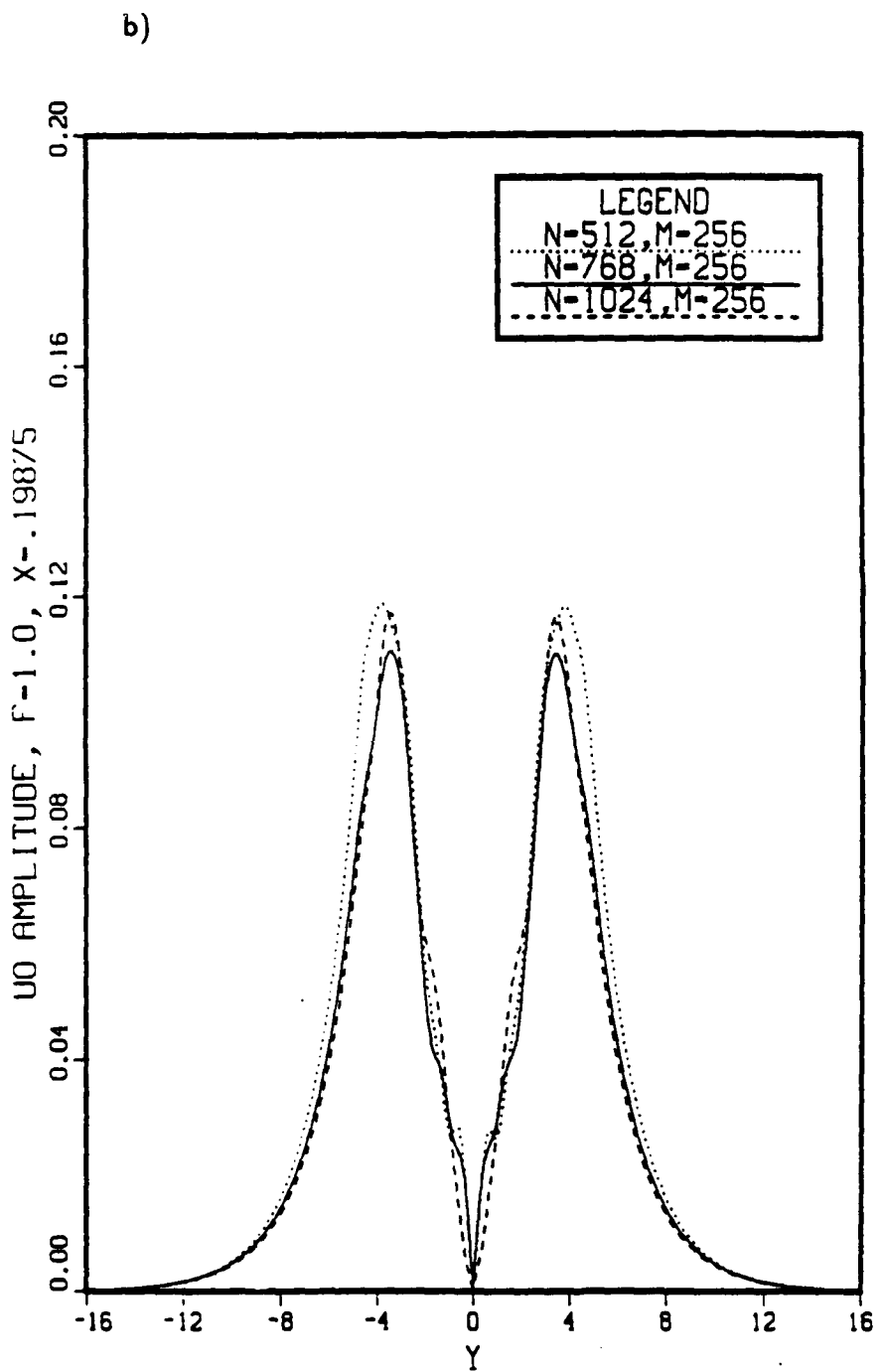


Figure B.6 Continued.

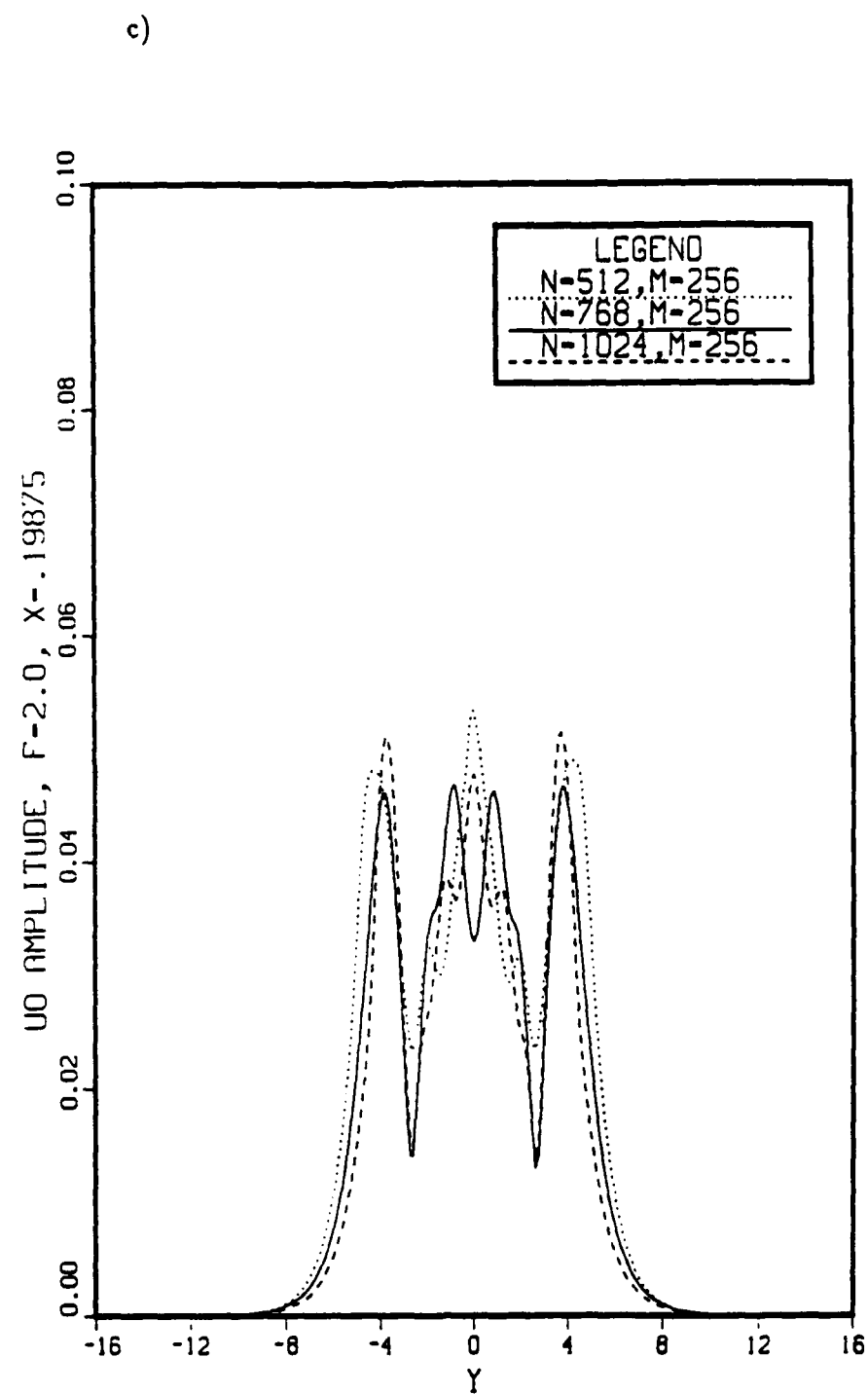


Figure B.6 Continued.

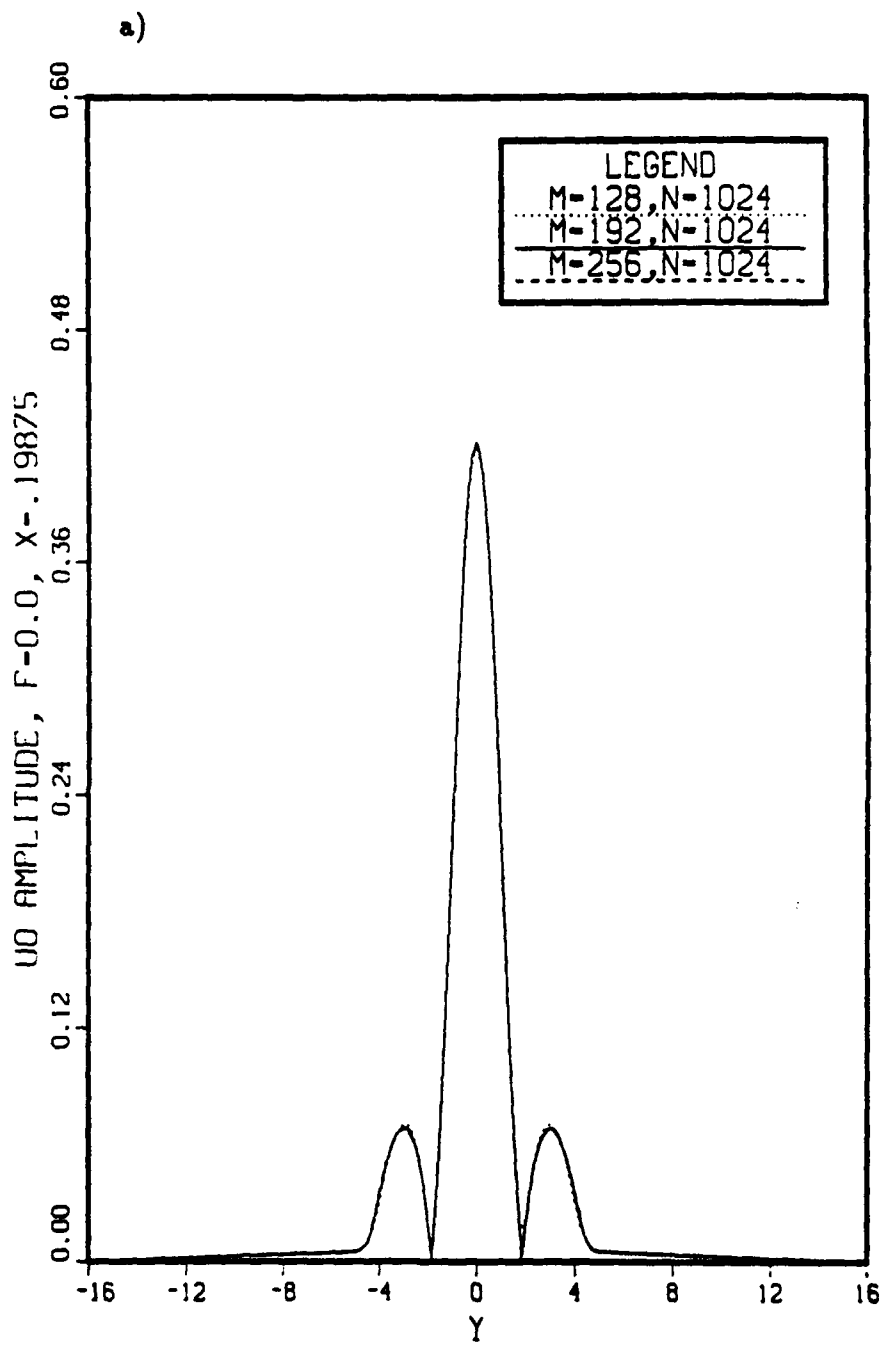


Figure B.7 Influence of the transverse grid increment on the amplitude distributions of the streamwise velocity. Case-2:  $N = 1024$  with  $M = 128$ ,  $M = 192$ , and  $M = 256$ . a) the mean component,  $F = 0$ ; b) the fundamental component,  $F = 1$ ; c) the second harmonic,  $F = 2$ .

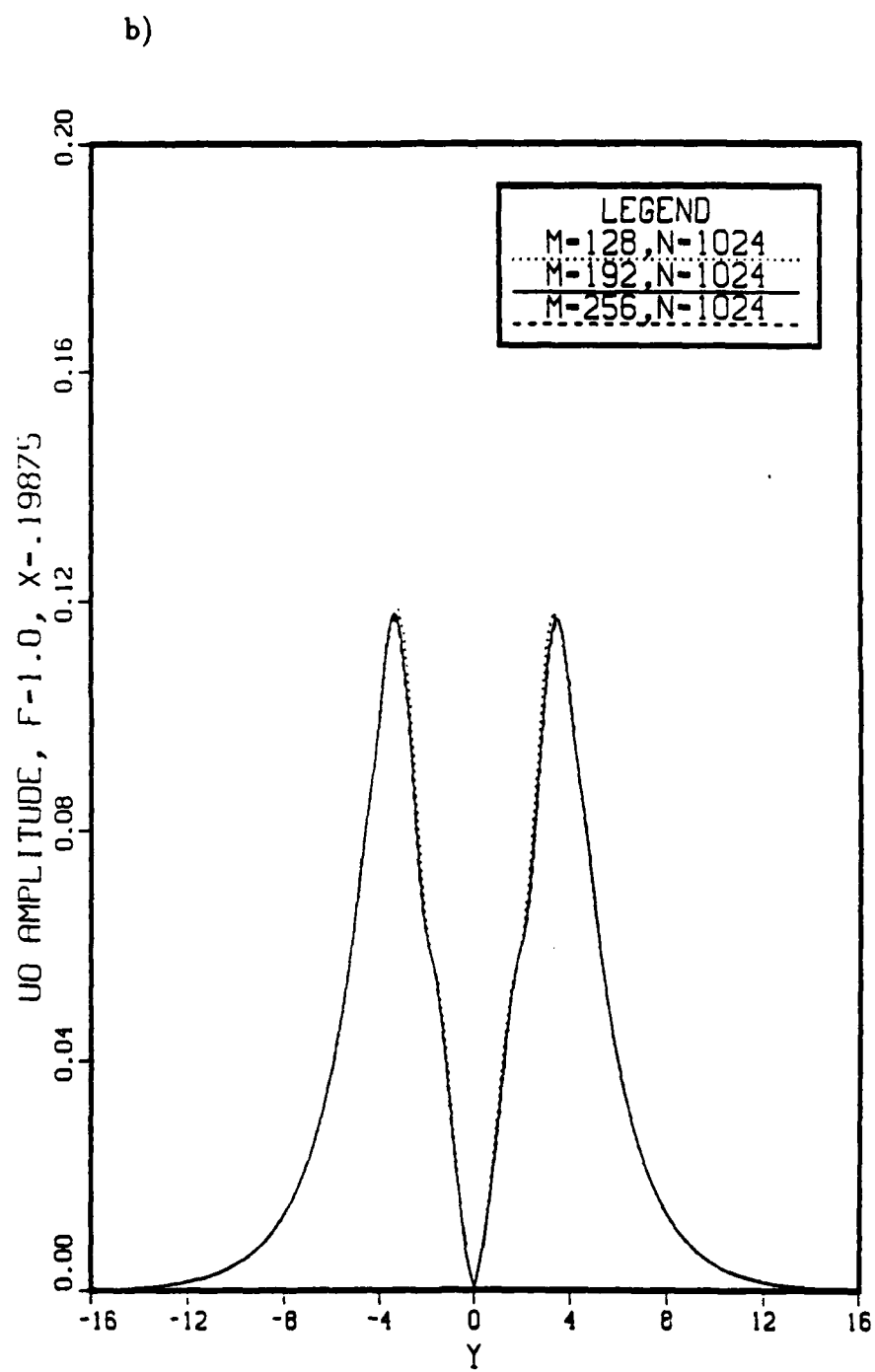


Figure B.7 Continued.

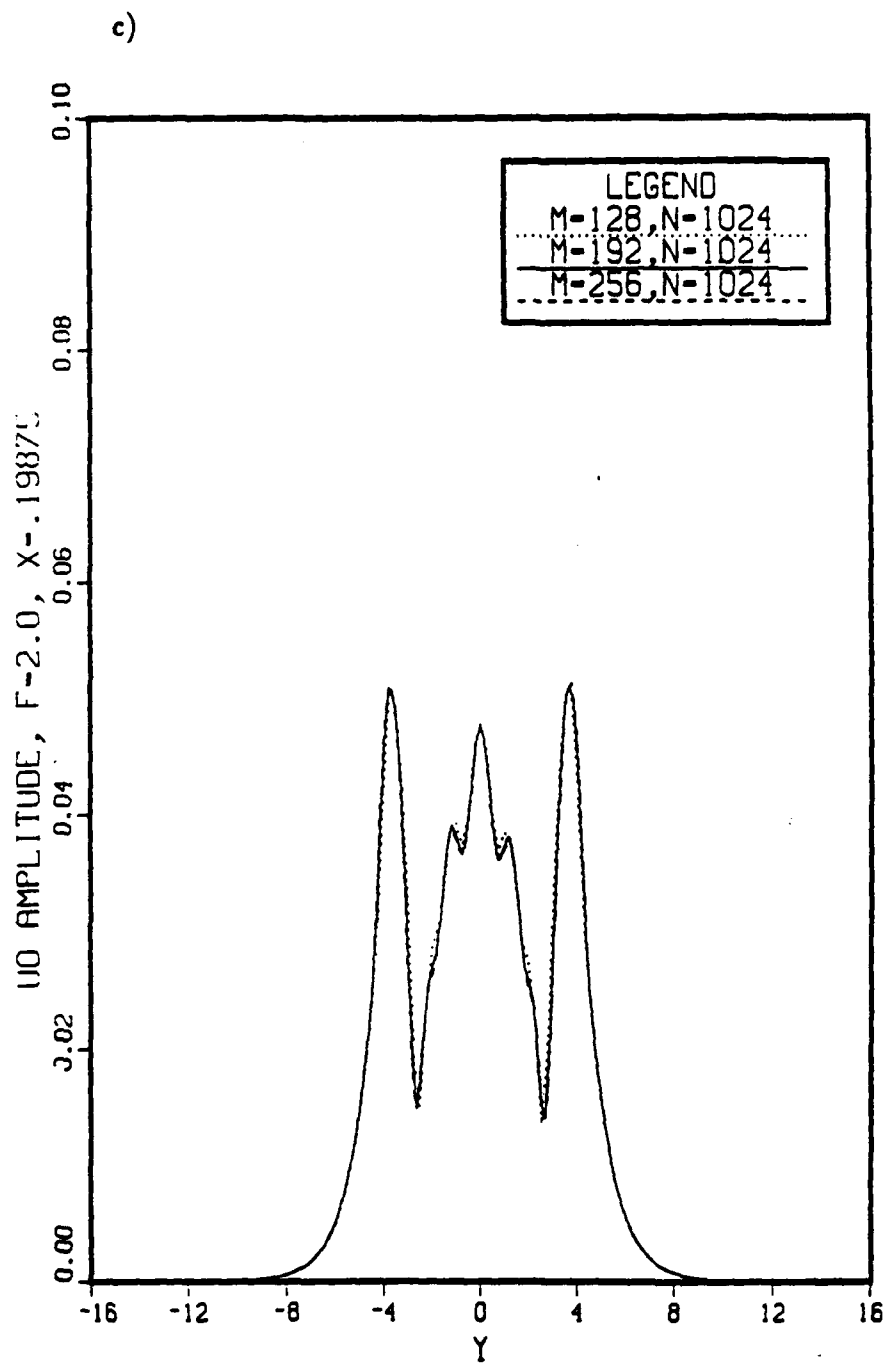


Figure B.7 Continued.

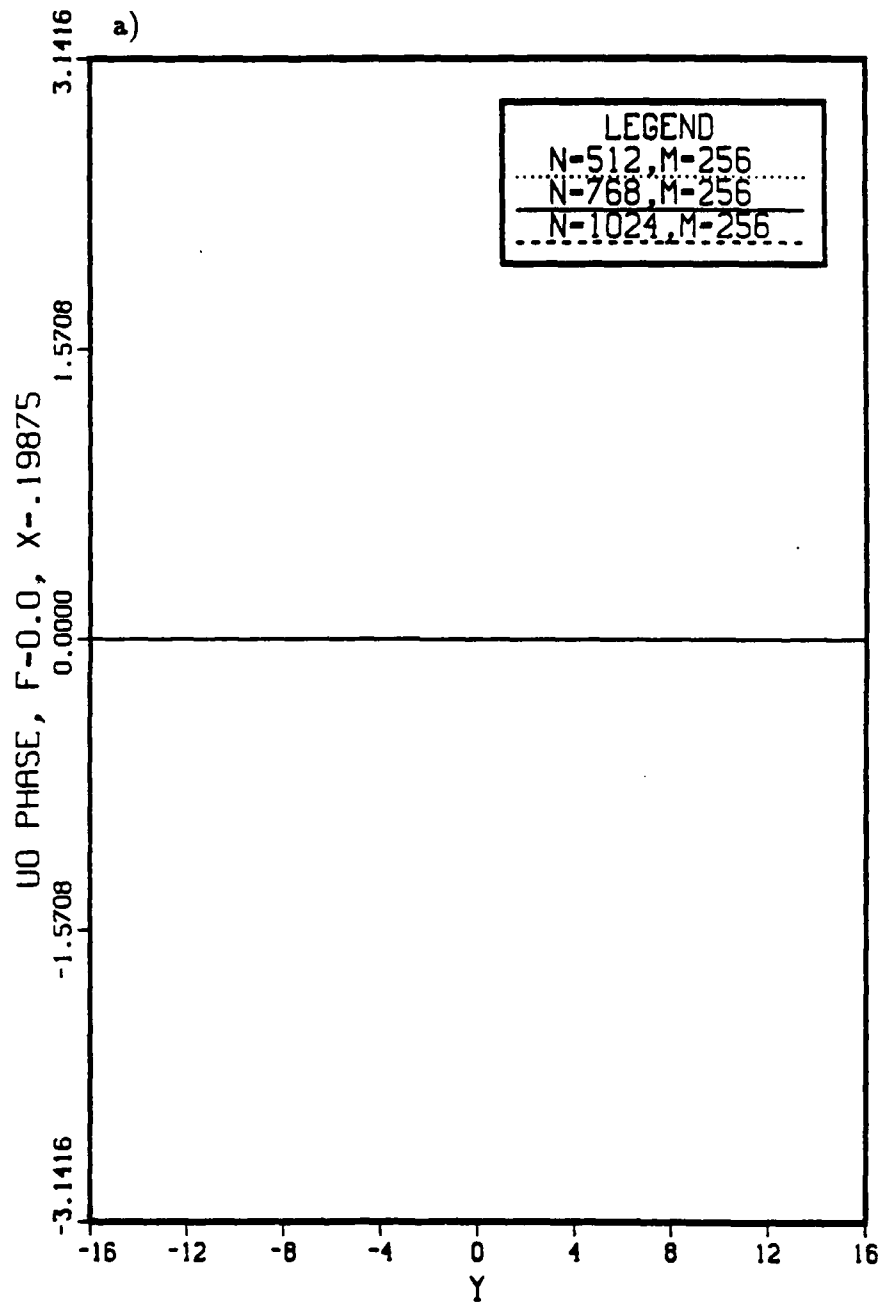


Figure B.8 Influence of the streamwise grid increment on the phase distributions of the streamwise velocity. Case-2:  $M = 256$  with  $N = 512$ ,  $N = 768$ , and  $N = 1024$ . a) the mean component,  $F = 0$ ; b) the fundamental component,  $F = 1$ ; c) the second harmonic,  $F = 2$ .

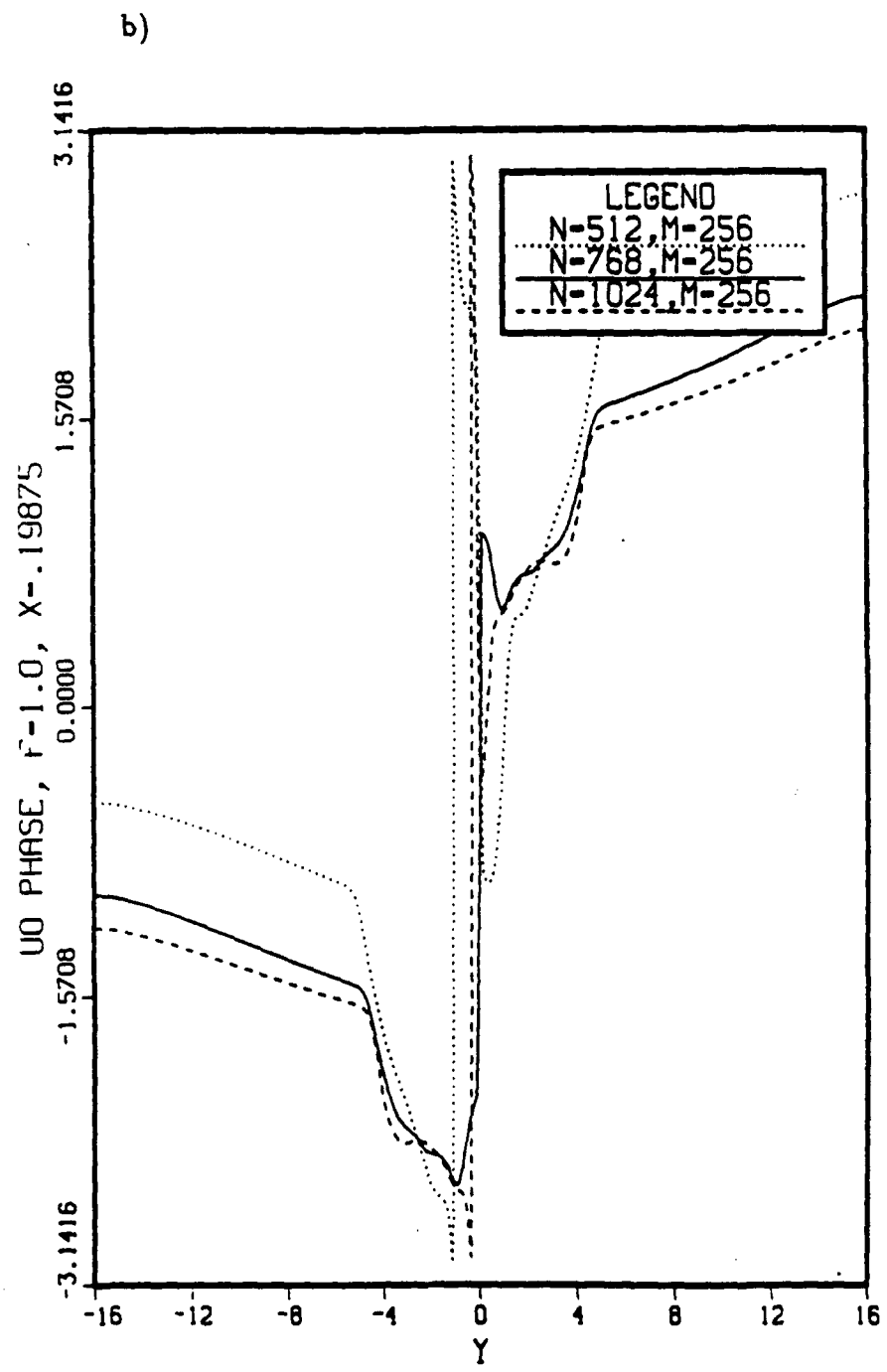


Figure B.8 Continued.

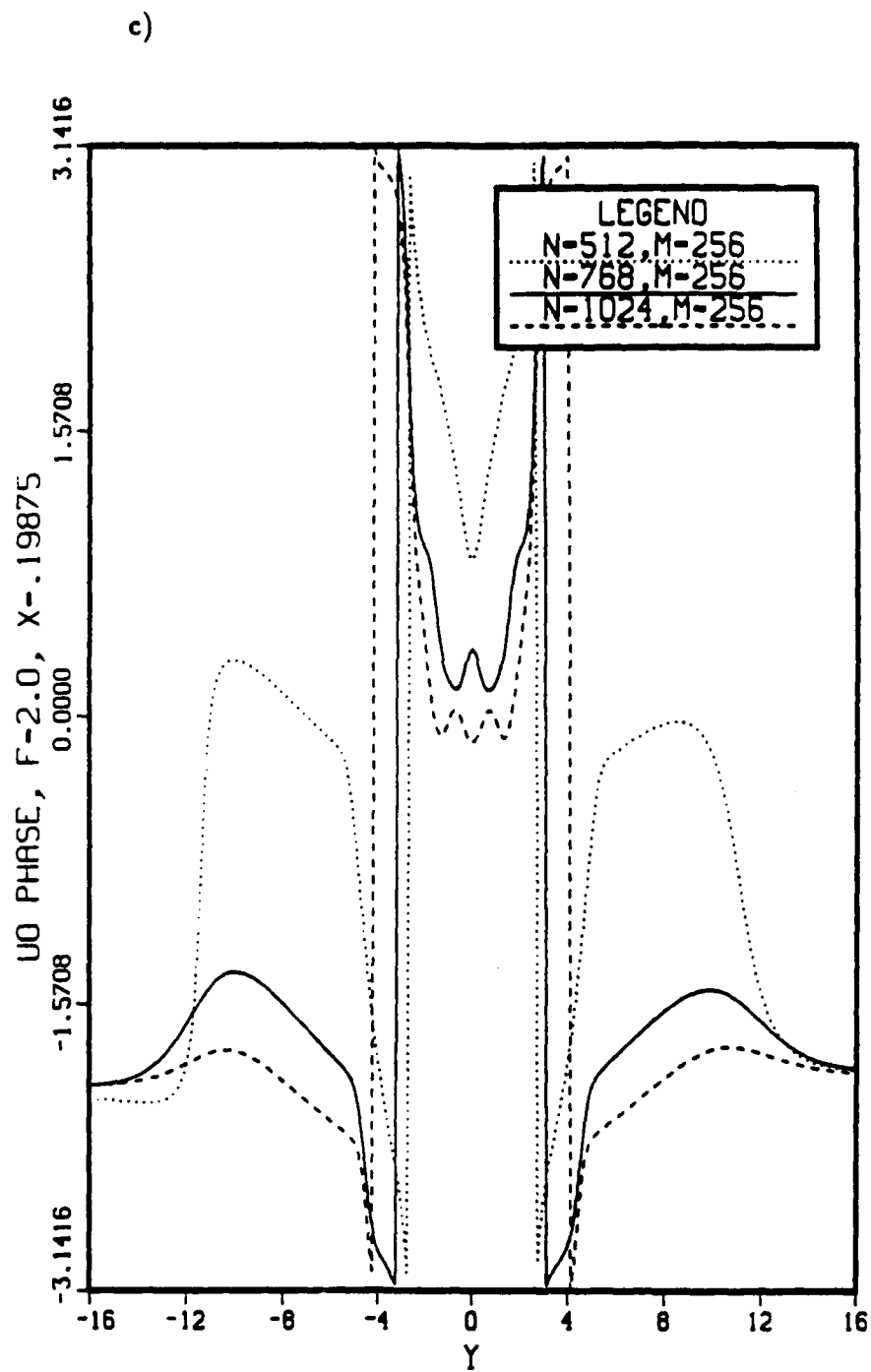
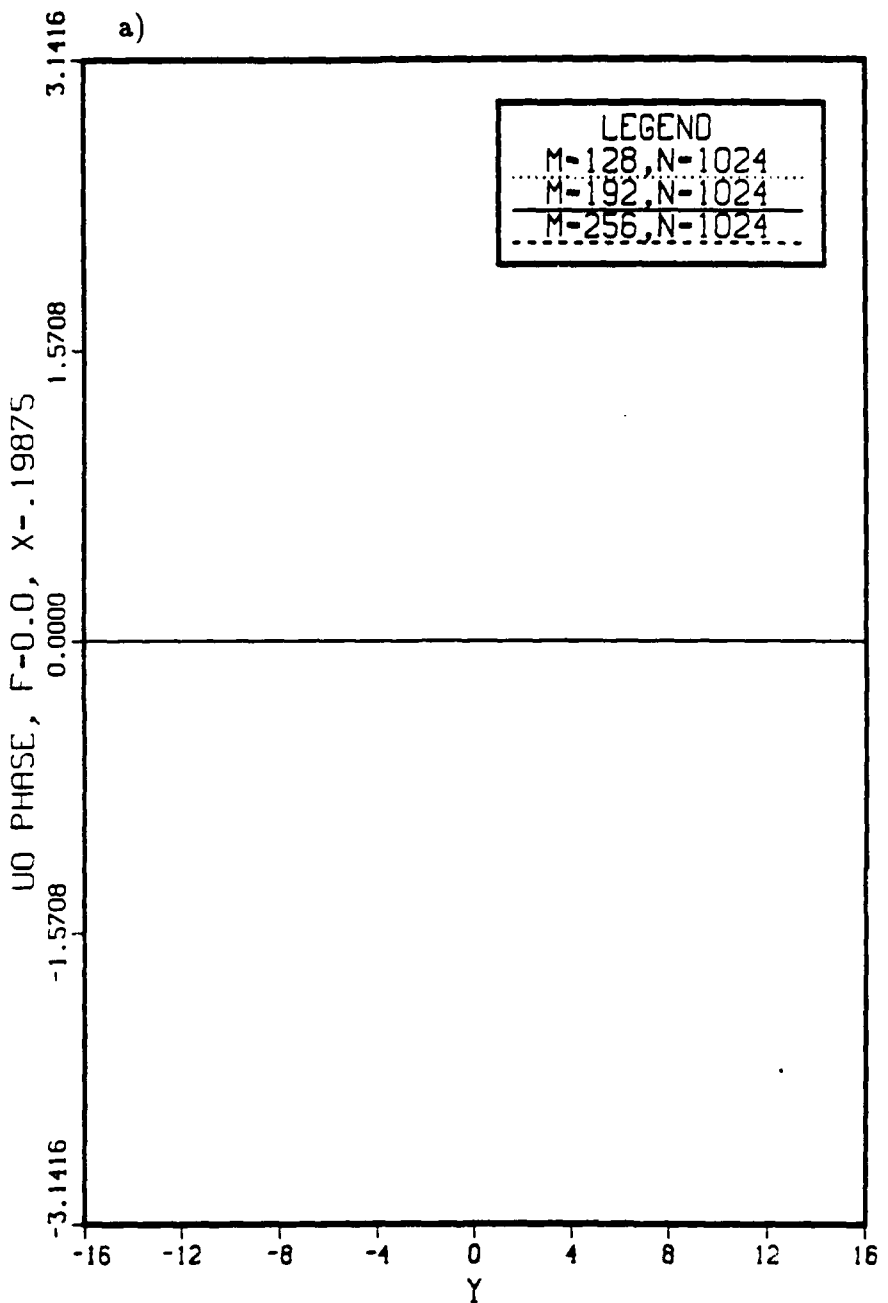


Figure B.8 Continued.



**Figure B.9** Influence of the transverse grid increment on the phase distributions of the streamwise velocity. Case-2:  $N = 1024$  with  $M = 128$ ,  $M = 192$ , and  $M = 256$ . a) the mean component,  $F = 0$ ; b) the fundamental component,  $F = 1$ ; c) the second harmonic,  $F = 2$ .

b)

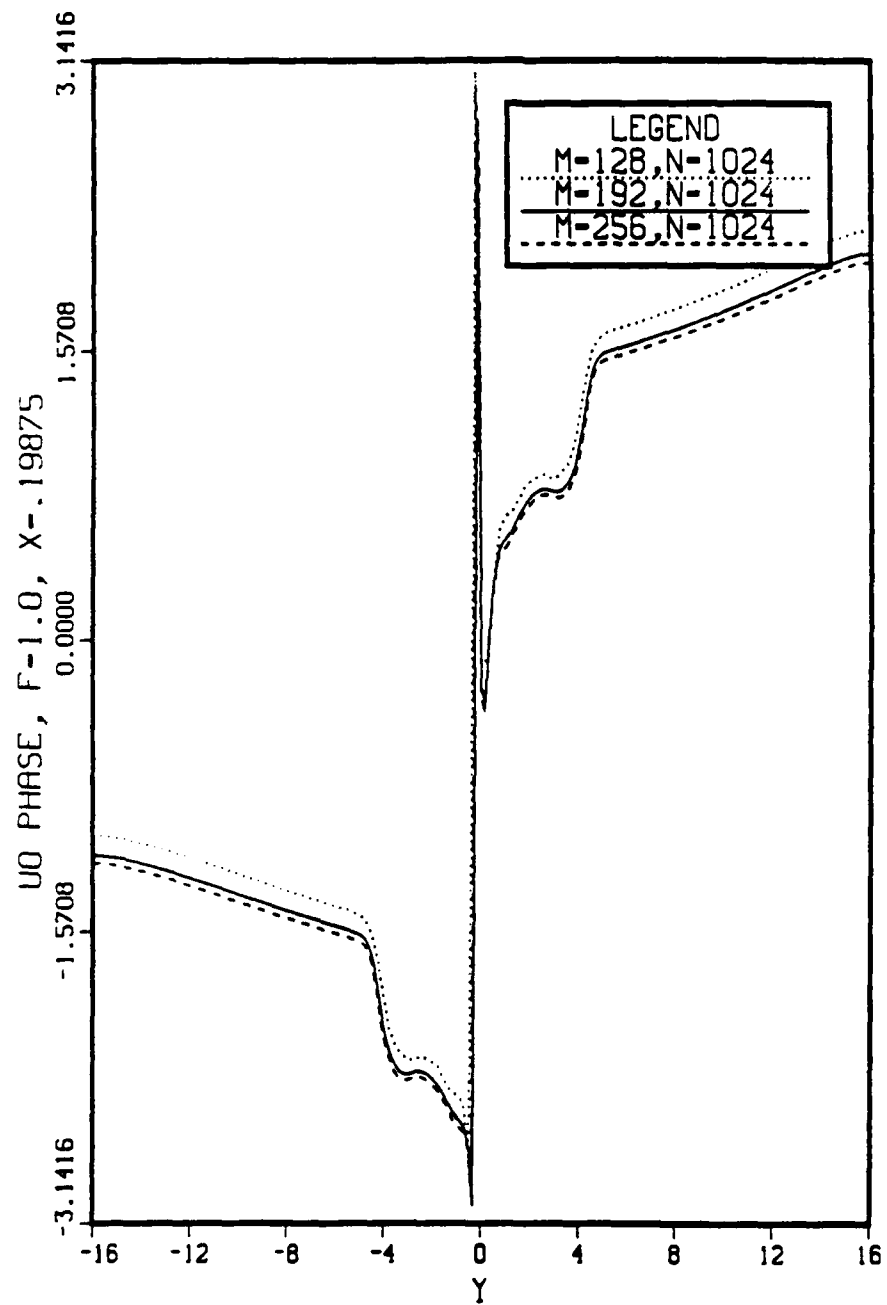


Figure B.9 Continued.

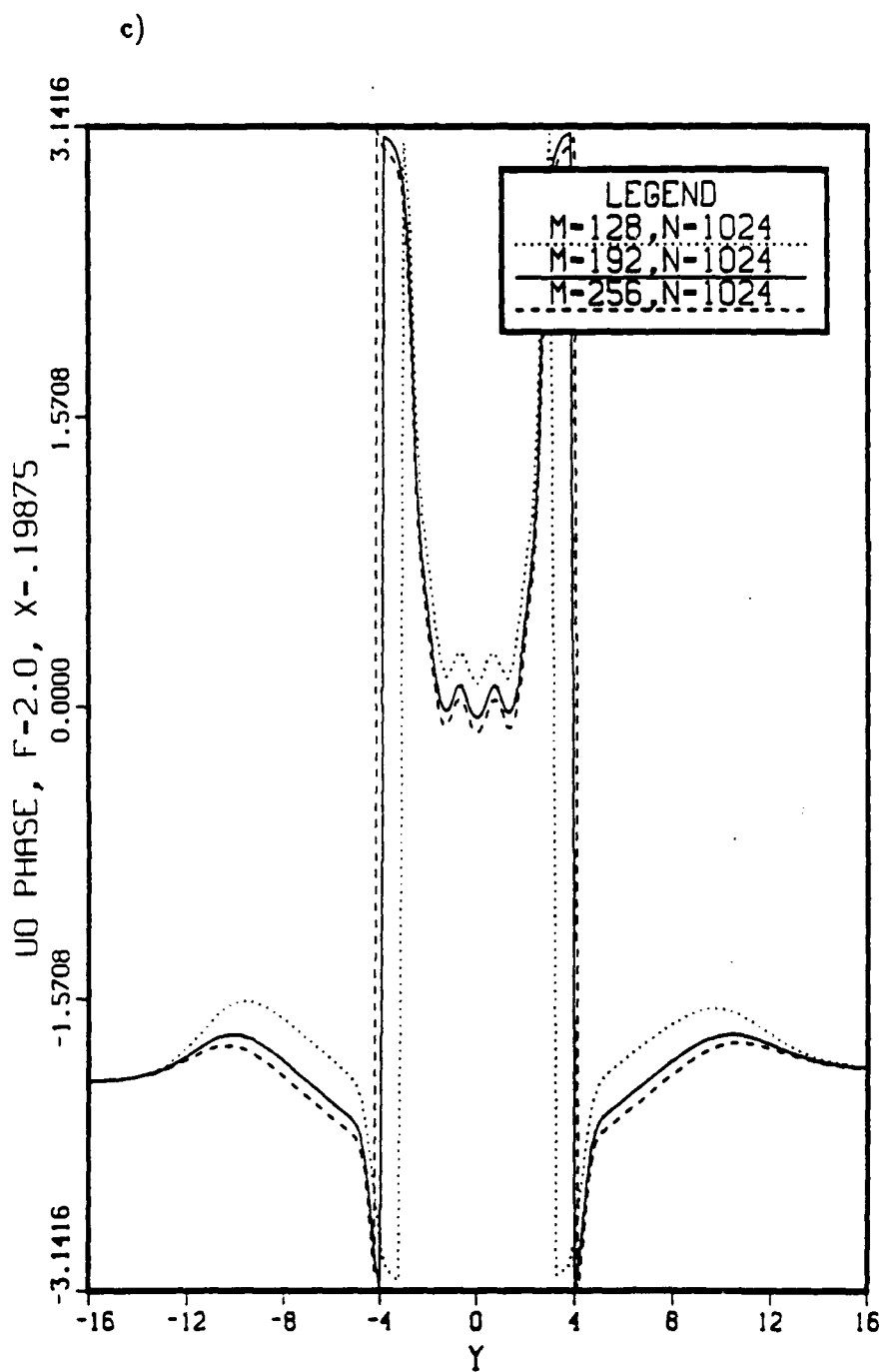


Figure B.9 Continued.

## APPENDIX A

SOLUTION OF THE THREE-DIMENSIONAL  
ORR-SOMMERFELD EQUATION

In this appendix, the finite-difference method used to obtain the eigenvalues and eigenfunctions of the three-dimensional Orr-Sommerfeld equation for the spatial stability problem is discussed. Both the Orr-Sommerfeld equation and the related Squire's equation are solved using fourth-order finite-differences.

For a small amplitude disturbance with velocity and vorticity components

$$u(x, y, z, t) = \text{Real}(\hat{u}(y)e^{i(\alpha z + \gamma z - \beta t)}) , \quad (A.1a)$$

$$v(x, y, z, t) = \text{Real}(\hat{v}(y)e^{i(\alpha z + \gamma z - \beta t)}) , \quad (A.1b)$$

$$w(x, y, z, t) = \text{Real}(\hat{w}(y)e^{i(\alpha z + \gamma z - \beta t)}) , \quad (A.1c)$$

$$\omega_x(x, y, z, t) = \text{Real}(\hat{\omega}_x(y)e^{i(\alpha z + \gamma z - \beta t)}) , \quad (A.1d)$$

$$\omega_y(x, y, z, t) = \text{Real}(\hat{\omega}_y(y)e^{i(\alpha z + \gamma z - \beta t)}) , \quad (A.1e)$$

$$\text{and } \omega_z(x, y, z, t) = \text{Real}(\hat{\omega}_z(y)e^{i(\alpha z + \gamma z - \beta t)}) , \quad (A.1f)$$

the amplitude  $\hat{v}(y)$  of the transverse velocity is an eigenfunction of the Orr-Sommerfeld equation

$$(U - c)(\hat{v}'' - (\alpha^2 + \gamma^2)\hat{v}) - U''\hat{v} + \frac{i}{\alpha Re}(\hat{v}''' - 2(\alpha^2 + \gamma^2)\hat{v}'' + (\alpha^2 + \gamma^2)^2\hat{v}) = 0 . \quad (A.2)$$

In equation (A.2),  $U = U(y)$  is the streamwise velocity of the undisturbed flow and is assumed to be independent of  $x$  and  $z$ . Furthermore,  $\alpha$  is the streamwise wavenumber of the disturbance,  $\gamma$  is the spanwise wavenumber of the disturbance,  $c = \beta/\alpha$  is the phase velocity of the disturbance where  $\beta$  is the temporal frequency,

$Re$  is the Reynolds number, and  $i = \sqrt{-1}$  is the imaginary number. The notation  $(\ )'$  denotes differentiation with respect to  $y$ .

Solutions of equation (A.2) are sought in the transverse interval  $y_{min} \leq y \leq y_{max}$ . For wakes, equation (A.2) is subject to boundary conditions at  $y = y_{min}$  and  $y = y_{max}$  of the form

$$\hat{v}''(y_{min}) = \alpha^2 \hat{v}(y_{min}) , \quad (A.3a)$$

$$\hat{v}'(y_{min}) = \alpha \hat{v}(y_{min}) , \quad (A.3b)$$

$$\hat{v}''(y_{max}) = \alpha^2 \hat{v}(y_{max}) , \quad (A.3c)$$

$$\text{and } \hat{v}'(y_{max}) = -\alpha \hat{v}(y_{max}) . \quad (A.3d)$$

Equation (A.2), coupled with the boundary conditions (A.3), is an eigenvalue problem of the form

$$L_1 \hat{v} = c L_2 \hat{v} \quad (A.4a)$$

where

$$\begin{aligned} L_1 = & U \left( \frac{d^2}{dy^2} - \alpha^2 - \gamma^2 \right) - U'' \\ & + \frac{i}{\alpha Re} \left( \frac{d^4}{dy^4} - 2(\alpha^2 + \gamma^2) \frac{d^2}{dy^2} + (\alpha^2 + \gamma^2)^2 \right) \end{aligned} \quad (A.4b)$$

and

$$L_2 = \frac{d^2}{dy^2} - \alpha^2 - \gamma^2 . \quad (A.4c)$$

For specified parameters  $\alpha$ ,  $\gamma$ ,  $Re$ , and the base flow velocity  $U$ , equation (A.4a) can be solved for the eigenvalue  $c$  and the eigenfunction  $\hat{v}$ .

For spatially amplifying disturbances,  $\alpha$  is obtained as a function of  $\beta$ ,  $Re$ , and  $\gamma$  by iteratively solving equation (A.4a) for the eigenvalue  $c$ , subject to the constraint,

$$F(\alpha) = \frac{\beta}{\alpha} - c = 0 . \quad (A.5)$$

Subsequent values of  $\alpha$  are obtained by applying the secant method to equation (A.5) to get

$$\alpha^{j+1} = \alpha^j - F(\alpha^j) \left( \frac{\alpha^{j+1} - \alpha^j}{F(\alpha^j) - F(\alpha^{j-1})} \right) \quad (A.6)$$

where  $j$  denotes the iteration level. The iteration scheme is repeated until  $\alpha(\beta, Re, \gamma)$  is obtained for the desired accuracy. For each iteration level  $j$ , the Orr-Sommerfeld equation (A.4a) is solved using a finite-difference method.

The eigenfunction  $\hat{v}(y)$  of equation (A.4a) is sought at the discrete points

$$y_m = y_0 + m\Delta y \text{ for } m = 0, \dots, M \quad (A.7)$$

where  $y_0 = y_{min}$ ,  $y_M = y_{max}$ ,  $\Delta y$  is the spacing between grid points, and  $M + 1$  is the total number of points in the domain. The function  $\hat{v}(y)$  and its derivatives can be approximated to fourth-order accuracy (Kurtz and Crandall, 1962) using

$$\hat{v}_m = \frac{1}{360}g_{m-2} + \frac{7}{45}g_{m-1} + \frac{41}{60}g_m + \frac{7}{45}g_{m+1} + \frac{1}{360}g_{m+2} , \quad (A.8a)$$

$$\hat{v}'_m = \frac{1}{h} \left( -\frac{1}{2}g_{m-1} + \frac{1}{2}g_{m+1} \right) , \quad (A.8b)$$

$$\hat{v}''_m = \frac{1}{h^2} \left( \frac{1}{12}g_{m-2} + \frac{2}{3}g_{m-1} - \frac{3}{2}g_m + \frac{2}{3}g_{m+1} + \frac{1}{12}g_{m+2} \right) , \quad (A.8c)$$

$$\text{and } \hat{v}'''_m = \frac{1}{h^4} (g_{m-2} - 4g_{m-1} + 6g_m - 4g_{m+1} + g_{m+2}) \quad (A.8d)$$

where  $\hat{v}_m = \hat{v}(y_m)$ .

Using equations (A.8) to approximate the derivatives in the Orr-Sommerfeld equation (A.4a) and the boundary conditions (A.3), the following matrix

eigenvalue problem

$$\left( \begin{array}{ccccc}
 d_1 & d_2 & d_3 & d_4 & d_1 \\
 d_5 & d_6 & d_7 & d_6 & d_5 \\
 A_1 & B_1 & C_1 & D_1 & E_1 \\
 \ddots & \ddots & \ddots & \ddots & \ddots \\
 \ddots & \ddots & \ddots & \ddots & \ddots \\
 \ddots & \ddots & \ddots & \ddots & \ddots \\
 \ddots & \ddots & \ddots & \ddots & \ddots \\
 A_M & B_M & C_M & D_M & E_M \\
 d_5 & d_6 & d_7 & d_6 & d_5 \\
 d_1 & d_2 & d_3 & d_4 & d_1 \\
 \end{array} \right) \begin{pmatrix} g_{-2} \\ g_{-1} \\ g_0 \\ \vdots \\ \vdots \\ \vdots \\ g_M \\ g_{M+1} \\ g_{M+2} \end{pmatrix} = 0$$
  

$$c \left( \begin{array}{ccccc}
 0 & 0 & 0 & 0 & 0 \\
 0 & 0 & 0 & 0 & 0 \\
 \hat{A}_1 & \hat{B}_1 & \hat{C}_1 & \hat{D}_1 & \hat{E}_1 \\
 \ddots & \ddots & \ddots & \ddots & \ddots \\
 \ddots & \ddots & \ddots & \ddots & \ddots \\
 \ddots & \ddots & \ddots & \ddots & \ddots \\
 \hat{A}_M & \hat{B}_M & \hat{C}_M & \hat{D}_M & \hat{E}_M \\
 0 & 0 & 0 & 0 & 0 \\
 0 & 0 & 0 & 0 & 0 \\
 \end{array} \right) \begin{pmatrix} g_{-2} \\ g_{-1} \\ g_0 \\ \vdots \\ \vdots \\ \vdots \\ g_M \\ g_{M+1} \\ g_{M+2} \end{pmatrix} = 0 \quad (A.9)$$

is obtained. The coefficients of the matrices in equation (A.9) are

$$A_m = U(y_m) + a_1 U''(y_m) + a_2 + b_1 , \quad (A.10a)$$

$$B_m = U(y_m) + a_3 U''(y_m) + a_4 + b_2 , \quad (A.10b)$$

$$C_m = U(y_m) + a_5 U''(y_m) + a_6 + b_3 , \quad (A.10c)$$

$$D_m = B_m , \quad (A.10d)$$

$$E_m = A_m , \quad (A.10e)$$

and

$$\hat{A}_m = a_7 , \quad (A.11a)$$

$$\hat{B}_m = a_8 , \quad (A.11b)$$

$$\hat{C}_m = a_9 , \quad (A.11c)$$

$$\hat{D}_m = a_8 , \quad (A.11d)$$

$$\hat{E}_m = a_7 , \quad (A.11e)$$

and

$$d_1 = \frac{\Delta y}{360} \sqrt{\alpha^2 + \gamma^2} , \quad (A.12a)$$

$$d_2 = \frac{7\Delta y}{45} \sqrt{\alpha^2 + \gamma^2} + \frac{1}{2} , \quad (A.12b)$$

$$d_3 = \frac{41\Delta y}{60} \sqrt{\alpha^2 + \gamma^2} , \quad (A.12c)$$

$$d_4 = \frac{7\Delta y}{45} \sqrt{\alpha^2 + \gamma^2} - \frac{1}{2} , \quad (A.12d)$$

$$d_5 = \frac{1}{12} - \frac{\Delta y}{360} (\alpha^2 + \gamma^2) , \quad (A.12e)$$

$$d_6 = \frac{2}{3} - \frac{7\Delta y}{45} (\alpha^2 + \gamma^2) , \quad (A.12f)$$

$$d_7 = -\frac{3}{2} - \frac{41\Delta y}{60} (\alpha^2 + \gamma^2) . \quad (A.12g)$$

The constants in equations (A.10) and (A.11) are

$$a_1 = \frac{1}{12\Delta y^2} - \frac{1}{360} (\alpha^2 + \gamma^2) , \quad (A.13a)$$

$$a_2 = -\frac{1}{360} , \quad (A.13b)$$

$$a_3 = \frac{2}{3\Delta y^2} - \frac{7}{45} (\alpha^2 + \gamma^2) , \quad (A.13c)$$

$$a_4 = -\frac{7}{45} , \quad (A.13d)$$

$$a_5 = -\frac{3}{2\Delta y^2} - \frac{41}{60} (\alpha^2 + \gamma^2) , \quad (A.13e)$$

$$a_6 = -\frac{41}{60} , \quad (A.13f)$$

$$a_7 = -\frac{1}{360} (\alpha^2 + \gamma^2) + \frac{1}{12\Delta y^2} , \quad (A.13g)$$

$$a_8 = -\frac{7}{45} (\alpha^2 + \gamma^2) + \frac{2}{3\Delta y^2} , \quad (A.13h)$$

$$a_9 = -\frac{41}{60} (\alpha^2 + \gamma^2) - \frac{3}{2\Delta y^2} , \quad (A.13i)$$

and

$$b_1 = \frac{i}{\alpha Re} \left( \frac{1}{\Delta y^4} - \frac{1}{6\Delta y^2} (\alpha^2 + \gamma^2) + \frac{1}{360} (\alpha^2 + \gamma^2)^2 \right) , \quad (A.14a)$$

$$b_2 = \frac{i}{\alpha Re} \left( -\frac{4}{\Delta y^4} - \frac{4}{3\Delta y^2} (\alpha^2 + \gamma^2) + \frac{7}{45} (\alpha^2 + \gamma^2)^2 \right) , \quad (A.14b)$$

$$b_3 = \frac{i}{\alpha Re} \left( \frac{6}{\Delta y^4} - \frac{3}{\Delta y^2} (\alpha^2 + \gamma^2) + \frac{41}{60} (\alpha^2 + \gamma^2)^2 \right) . \quad (A.14c)$$

The eigenvalues and eigenfunctions of equation (A.9) are obtained using the IMSL routine EIGZC. As equation (A.9) is a  $M+5$  dimensional matrix eigenvalue problem,  $M+5$  eigenvalues and eigenfunctions are obtained. However, only two eigenvalues and two eigenfunctions have physical meaning.

Of the  $M+5$  values of the complex eigenvalue  $c$ , only those for which the real part of  $c$ ,

$$c_r = \text{Real} \left( \frac{\beta}{\alpha} \right) = \beta \left( \frac{\alpha_r}{\alpha_r^2 + \alpha_i^2} \right) , \quad (A.15)$$

satisfies

$$c_r < 1 \text{ for } \beta < 1 \quad (A.16)$$

are considered to be physically meaningful. In this work,  $\beta$  is always less than one. Of the eigenvalues that satisfy (A.16), one corresponds to a sinuous mode disturbance and one corresponds to a varicose mode disturbance. The sinuous mode eigenvalue is the one for which

$$c_i = \text{Imag} \left( \frac{\beta}{\alpha} \right) = -\frac{\beta \alpha_i}{\alpha_r^2 + \alpha_i^2} \quad (A.17)$$

attains its maximum value and for which the corresponding centerline transverse velocity is nonzero. Alternatively, the varicose mode eigenvalue is the one for

which  $c_i$  attains its maximum value and for which the corresponding centerline transverse velocity is zero.

Once  $\alpha$  is obtained for the given parameters  $\beta$ ,  $\gamma$ , and  $Re$ , it remains to construct the velocity and vorticity components from the eigenfunction  $g_m$ . For each transverse location  $y_m$ , the transverse velocity  $\hat{v}_m$  is obtained from

$$\hat{v}_m = \frac{1}{360}g_{m-2} + \frac{7}{45}g_{m-1} + \frac{41}{60}g_m + \frac{7}{45}g_{m+1} + \frac{1}{360}g_{m+2} . \quad (A.18)$$

Procedures to obtain the remaining velocity and vorticity components depend on whether the disturbance is two-dimensional or three-dimensional.

For two-dimensional disturbances ( $\gamma = 0$ ), the streamwise velocity is obtained from the continuity equation

$$\hat{u}_m = \frac{i}{\alpha} \hat{v}'_m \quad (A.19)$$

where  $\hat{v}'_m$  is given by equation (A.8b). The spanwise vorticity component  $\hat{\omega}_z$  is obtained from

$$\hat{\omega}_{zm} = \frac{i}{\alpha} (\hat{v}''_m - \alpha^2 \hat{v}_m) \quad (A.20)$$

where  $\hat{v}''_m$  is given by equation (A.8c). The remaining velocity and vorticity components are

$$\hat{w}_m = \hat{\omega}_{zm} = \hat{\omega}_{ym} = 0 . \quad (A.21)$$

For three-dimensional disturbances ( $\gamma \neq 0$ ), the velocity and vorticity components are obtained in the following manner. The transverse vorticity  $\hat{\omega}_y$  is obtained from Squire's equation

$$\hat{\omega}_y'' - (\alpha^2 + \gamma^2 + i\alpha Re(U - c)) \hat{\omega}_y = -i Re U' \gamma \hat{v} . \quad (A.22)$$

Squire's equation is solved in the transverse interval  $y_{\min} \leq y \leq y_{\max}$  subject to the Dirichlet boundary conditions

$$\hat{\omega}_y(y_{\min}) = 0 , \quad (A.23a)$$

$$\text{and } \hat{\omega}_y(y_{\max}) = 0 . \quad (A.23b)$$

Fourth-order finite-differences are used to discretize the derivatives in equation (A.22). The resulting system of equations,

$$\left( \begin{array}{cccccc} G_0 & 16 & -1 & & & & \\ 16 & G_1 & 16 & -1 & & & \\ -1 & 16 & G_2 & 16 & -1 & & \\ \ddots & \ddots & \ddots & \ddots & \ddots & & \\ \ddots & \ddots & \ddots & \ddots & \ddots & & \\ \ddots & \ddots & \ddots & \ddots & \ddots & & \\ & & & & & -1 & 16 & G_{M-2} & 16 & -1 \\ & & & & & -1 & 16 & G_{M-1} & 16 & -1 \\ & & & & & -1 & 16 & G_M & & \end{array} \right) \begin{pmatrix} \hat{\omega}_{y0} \\ \hat{\omega}_{y1} \\ \hat{\omega}_{y2} \\ \vdots \\ \vdots \\ \vdots \\ \hat{\omega}_{yM-2} \\ \hat{\omega}_{yM-1} \\ \hat{\omega}_{yM} \end{pmatrix} =$$

$$\begin{pmatrix} f_0 \\ f_1 \\ f_2 \\ \vdots \\ \vdots \\ \vdots \\ f_{M-2} \\ f_{M-1} \\ f_M \end{pmatrix} , \quad (A.24)$$

is solved for the transverse vorticity  $\hat{\omega}_y$ . The coefficients of the matrix in equation (A.24) are

$$G_m = -12\Delta y^2 (\alpha^2 + \gamma^2 + i\alpha Re(U(y_m) - c)) - 30 \quad (A.25)$$

and the right hand side of equation (A.24) is composed of the elements

$$f_m = -iU'(y_m)\gamma\hat{v}_m 12\Delta y^2 . \quad (A.26)$$

The remaining velocity and vorticity components can be obtained from the transverse velocity  $\hat{v}$  and the transverse vorticity  $\hat{\omega}_y$ . The spanwise vorticity  $\hat{\omega}_z$  is obtained from the equation

$$\hat{\omega}_{z,m} = -i\alpha \frac{((\alpha^2 + \gamma^2) \hat{v}_m + \hat{v}_m'' - c\hat{\omega}'_{y,m})}{\alpha^2 + \gamma^2} . \quad (A.27)$$

Equation (A.27) is derived from the  $v$  Poisson equation and the relationship

$$i\alpha\hat{\omega}_z + \hat{\omega}'_y + i\gamma\hat{\omega}_z = 0 . \quad (A.28)$$

In equation (A.27), the derivative  $\hat{v}_m''$  is obtained from equation (A.8c) and  $\hat{\omega}'_{y,m}$  is obtained using the fourth-order finite-difference formula

$$\hat{\omega}'_{y,m} = \frac{1}{12h} (\hat{\omega}_{y,m-2} - 8\hat{\omega}_{y,m-1} - 8\hat{\omega}_{y,m+1} + \hat{\omega}_{y,m+2}) . \quad (A.29)$$

The streamwise vorticity is obtained from equation (A.28), rewritten as

$$\hat{\omega}_{z,m} = -\frac{i\gamma\hat{\omega}_{z,m} + \hat{\omega}'_{y,m}}{i\alpha} , \quad (A.30)$$

where  $\hat{\omega}'_{y,m}$  is obtained from equation (A.29). The streamwise velocity is obtained from the relation

$$\hat{u}_m = \left( \frac{i\alpha}{\alpha^2 + \gamma^2} \right) \left( \hat{\omega}_{y,m} + \frac{\alpha}{\gamma} \hat{v}'_m \right) \quad (A.31)$$

which is derived from the definition of the transverse vorticity. Finally, the spanwise velocity is obtained from the continuity equation

$$\hat{w}_m = -\frac{i\alpha\hat{u}_m + \hat{v}'_m}{i\gamma} . \quad (A.32)$$

In both equations (A.31) and (A.32), the velocity derivative  $\hat{v}'_m$  is obtained from equation (A.8b).

## APPENDIX B

INFLUENCE OF THE GRID INCREMENT  
ON THE NUMERICAL SOLUTION

For the calculations that are discussed in Chapter 6, it is desired to determine the influence of the grid increment on the numerical solutions. This is done by repeating the calculations of Case-1 and Case-2 for several different computational grids. For Case-1, small amplitude disturbances are calculated and therefore, this case is used to test the influence of the grid increment when nonlinear effects are unimportant. For Case-2, larger amplitude disturbances, as compared to Case-1, are calculated. This case is used to test the influence of the grid increment when nonlinear effects are significant.

For both Case-1 and Case-2, the streamwise and transverse grid increments are varied independently so that the variation of the calculated flow field with the grid increment may be observed. With the domain size held constant, the grid increments are varied by changing the number of grid points. For the temporal discretization, numerical stability considerations require that a much smaller time step be used than is required based solely on temporal accuracy. Therefore, the time step is not varied for either Case-1 or Case-2.

Case-1 is recalculated using the grids

$$M = 64, N = 64, \quad (B.1a)$$

$$M = 64, N = 256, \quad (B.1b)$$

$$N = 128, M = 32, \quad (B.1c)$$

$$\text{and } N = 128, M = 128. \quad (B.1d)$$

In addition, the results of Case-1 that are described in Chapter 6, for which

$$N = 128 \text{ and } M = 64 , \quad (B.2)$$

are compared with the calculations described here. All other parameters for these calculations are identical to those discussed in Chapter 6 with regard to Case-1.

Figures B.1 show amplification curves of the fundamental disturbance for various grid increments. In Figure B.1a, the amplification curves corresponding to  $N = 128$  and  $N = 256$  are relatively close together and exhibit exponential growth. However, for  $N = 64$  the amplification curve is significantly different from those corresponding to  $N = 128$  and  $N = 256$  and does not exhibit exponential growth as would be expected for a small amplitude disturbance. In Figure B.1b, the amplification curves corresponding to  $M = 64$  and  $M = 128$  are almost identical while the amplification curve corresponding to  $M = 32$  exhibits small differences with the other two curves. For all values of  $M$ , the fundamental disturbance grows exponentially.

Figures B.2 display the amplitude distribution of the fundamental disturbance component of the streamwise velocity for various grid increments. In Figure B.2a, the amplitude distributions for  $N = 128$  and  $N = 256$  are quite close and compare well to linear stability theory. For  $N = 64$ , the shape of the amplitude distribution is similar to those for  $N = 128$  and  $N = 256$ , but its amplitude level is significantly higher than for the other curves. In Figure B.2b, the amplitude distributions for  $M = 64$  and  $M = 128$  are quite close. For  $M = 32$ , the amplitude distribution is similar in shape to those for  $M = 64$  and  $M = 128$  but clearly requires a smaller transverse grid increment.

Figures B.3 display the phase distribution of the fundamental disturbance component of the streamwise velocity for various grid increments. In Figure B.3a,

the phase distributions for  $N = 256$  and  $N = 128$  are similar in shape and reasonably close together. For  $N = 64$ , a significant phase difference between this curve and those for  $N = 128$  and  $N = 256$  is present. In Figure B.3b, the phase distributions for all values of  $M$  are in reasonable agreement.

From these results it is apparent that the size of the grid increment has significant influence on the calculated flow field. However, it appears that for the grid used for Case-1 in Chapter 6, for which

$$M = 64 \quad \text{and} \quad N = 128 , \quad (B.3)$$

the calculated flow field is reasonable well resolved and is not significantly altered when the finer grids ( $N = 256, M = 64$  and  $N = 128, M = 128$ ) are employed.

Case-2 is recalculated using the grids

$$M = 256 , \quad N = 512 , \quad (B.4a)$$

$$M = 256 , \quad N = 768 , \quad (B.4b)$$

$$N = 1024 , \quad M = 128 , \quad (B.4c)$$

$$\text{and} \quad N = 1024 , \quad M = 192 . \quad (B.4d)$$

In addition, the results of Case-2 that are discussed in Chapter 6, for which

$$M = 256 \quad \text{and} \quad N = 1024 , \quad (B.5)$$

are compared with the calculations discussed here. All other parameters for these calculations are identical to those discussed in Chapter 6 with regard to Case-2.

Since nonlinear effects are important for this flow field, the fundamental disturbance as well as the mean and second harmonics components are displayed for various grid increments. Figures B.4 and B.5 display the amplification curves for

the mean component  $F = 0$ , the fundamental disturbance  $F = 1$ , and the second harmonic  $F = 2$ . In Figure B.4a ( $F = 0$ ) and B.4b ( $F = 1$ ), the amplification curves corresponding to  $N = 768$  and  $N = 1024$  are virtually identical. Beyond the point of saturation, the amplification curves for  $N = 512$  deviate from those corresponding to  $N = 768$  and  $N = 1024$ . In Figure B.4c, the second harmonic ( $F = 2$ ) appears to be more sensitive to the streamwise grid increment than the other harmonic components and appears to require greater streamwise resolution than was used in these calculations. In Figures B.5, the amplification curves for all three harmonic components,  $F = 0$ ,  $F = 1$ , and  $F = 2$ , are virtually identical regardless of the transverse grid increment.

Figures B.6 through B.9 display the amplitude and phase distributions of the streamwise velocity for  $F = 0$ ,  $F = 1$ , and  $F = 2$ . As was observed for the amplification curves, the amplitude and phase distributions vary more with the streamwise grid increment than with the transverse grid increment. In particular, the second harmonic component displays the most sensitivity with respect to the streamwise grid increment.

From the results presented in Figures B.4 through B.9, it would appear that for  $M = 256$ , the transverse grid increment is sufficiently small so that the mean component, the fundamental component, and the second harmonic component are adequately represented. However, for the streamwise grid increment corresponding to  $N = 1024$ , the results are not quite as conclusive. It appears that the mean component and the fundamental component are adequately represented with this grid increment. However, it is not quite as clear whether the second harmonic is adequately resolved as it displays a significant variation with the streamwise grid increment.

## REFERENCES

- Aref, H. and E. D. Siggia (1981). "Evolution and Breakdown of a Vortex Street in Two Dimensions," *J. Fluid Mech.*, **109**, pp. 435-463.
- Batchelor, G. K. (1967). *An Introduction to Fluid Mechanics*, Cambridge University Press.
- Breidenthal, R. (1980). "Response of Plane Shear Layers and Wakes to Strong Three-Dimensional Disturbances," *Phys. Fluids*, **23**, No. 10, pp. 1929-1934.
- Fasel, H. F. (1976). "Investigation of the Stability of Boundary Layers by a Finite-Difference Model of the Navier-Stokes Equations," *J. Fluid Mech.*, **78**, pp. 355-383.
- Gaster, M. (1962). "A Note on the Relation Between Temporally-Increasing and Spatially-Increasing Disturbances in Hydrodynamic Stability," *J. Fluid Mech.*, **14**, pp. 222-224.
- Gaster, M. (1974). "On the Effects of Boundary-Layer Growth on Flow Stability," *J. Fluid Mech.*, **66**, pp. 465-480.
- Goldstein, M. (1929). "Concerning Some Solutions of the Boundary Layer Equations in Hydrodynamics," *Proc. Camb. Phil. Soc.*, **26**, pp. 1-30.
- Kurtz, E. F. and S. H. Crandall (1962). "Computer-Aided Analysis of Hydrodynamic Stability," *J. Math. Phys.*, **41**, pp. 264-279.
- Mattingly, G. E. and W. O. Criminale (1972). "The Stability of an Incompressible Two-Dimensional Wake," *J. Fluid Mech.*, **51**, pp. 233-273.
- Meiburg, E. and J. C. Lasheras (1987). "Comparison between Experiments and Numerical Simulations of Three-Dimensional Plane Wakes," *Phys. Fluids*, **30**, No. 3, pp. 623-625.
- Meiburg, E. and J. C. Lasheras (1988). "Experimental and Numerical Investigation of the Three-Dimensional Transition in Plane Wakes," *J. Fluid Mech.*, **190**, pp. 1-37.
- Metcalfe, R. W., S. A. Orszag, M. F. Brachet, S. Menon, and J. J. Riley (1987). "Secondary Instability of a Temporally Growing Mixing Layer," *J. Fluid Mech.*, **184**, pp. 207-243.
- Miksad, R. W., F. L. Jones, E. J. Powers, Y. C. Kim and L. Khadra (1982). "Experiments on the Role of Amplitude and Phase Modulation during Transition to Turbulence," *J. Fluid Mech.*, **123**, pp. 1-29.

- Motohashi, T. (1979). "A Higher-Order Nonlinear Interaction among Spectral Components," *Phys. Fluids*, **22**, No. 6, pp. 1212-1213.
- Pruett, C. D. (1986). "Numerical Simulations of Nonlinear Waves in Free Shear Layers," Ph.D. Dissertation, University of Arizona.
- Robinson, A. C. and P. G. Saffman (1982). "Three-Dimensional Stability of Vortex Arrays," *J. Fluid Mech.*, **125**, pp. 411-427.
- Sato, H. and K. Kuriki (1961). "The Mechanism of Transition in the Wake of a Thin Flat Plate Placed Parallel to a Uniform Flow," *J. Fluid Mech.*, **11**, pp. 321-352.
- Sato, H. (1970). "An Experimental Study of Non-Linear Interaction of Velocity Fluctuations in the Transition Region of a Two-Dimensional Wake," *J. Fluid Mech.*, **44**, pp. 741-765.
- Sato, H. and Y. Onda (1970). "Detailed Measurements in the Transition Region of a Two-Dimensional Wake," Report No. 453, Institute of Space and Aeronautical Science, University of Tokyo, pp. 317-377.
- Sato, H. and H. Saito (1975). "Fine-Structure of Energy Spectra of Velocity Fluctuations in the Transition Region of a Two-Dimensional Wake," *J. Fluid Mech.*, **67**, pp. 539-559.
- Smith, G. D. (1985). *Numerical Solution of Partial Differential Equations: Finite Difference Methods*, Oxford University Press.
- Swarztrauber, P. N. (1977). "The Methods of Cyclic Reduction, Fourier Analysis and The FACR Algorithm for the Discrete Solution of Poisson's Equation on a Rectangle," *SIAM Review*, **19**, No. 3, pp. 490-501.
- White, F. (1974). *Viscous Fluid Flow*, McGraw-Hill.
- Zabusky, N. J. and G. S. Deem (1971). "Dynamical Evolution of Two-Dimensional Unstable Shear Flows," *J. Fluid Mech.*, **47**, pp. 353-379.